Continuum model for nanocolumn growth during low-pressure vapour deposition

Yicun Huang

Department of Mechanical Engineering
University of Canterbury

August 2019

Preface

This thesis describes work carried out from June 2016 to October 2019 in the Department of Mechanical Engineering, University of Canterbury. This dissertation is the result of my own work and includes nothing which is the outcome of work done in collaboration, except where appropriately indicated in the text. No part of this work has been previously published, or is being submitted for any other qualification at this or any other university. The author of this thesis however, at the time of this writing is in the process of preparing manuscripts and clearing the backlog of work for the dissemination of material contained in the thesis. Some of the results in Ch. 6 of the thesis have been included in the following conference presentations, in which the talks were either given by the author or his supervisor Dr. Catherine Bishop.

- Yicun Huang, *A mesoscale model of faceted titania film growth*, XVI ECerS Conference, 16-20 Jun 2019, Turin, Italy

Acknowledgements

I am grateful for my College of Engineering PhD Scholarship which provided me with stipend and tuition fees for the majority of my PhD. I would like to thank my supervisor Dr. Catherine Bishop for providing me with the opportunity to further my research topic, engaging in interminable arguments and the endless redoing of work, which now seems to be all worth it. I am thankful for the help and support from the pp-MOCVD group, in particular from Prof. Susan Krumdieck, Dr. Sarah Masters, Dr. Alexandra Gardecka, Rukmini Gorthy and Johann Land. Special thanks to my fellow officemate Dr. James Hewett for the insightful discussions and my flatmate Dr. Aaron Beardsley for the helpful guide to EBSD.

I would also like to extend my appreciation to Dr. Daniel Lewis who has given me free tutorials on basic aspects in materials science. A huge thanks to my Kiwi gang and equally friends from abroad, as far away as England and Germany, my loyal YAMAHA UX30 and Cannondale Saeco, as well as the many memorable Kiwi experiences. Finally I would like to extend my deepest gratitude to mum and dad, without whose love I would have not been able to get here.

Abstract

Controlling the interfaces, including the free surfaces, of nanostructured thin films is of crucial importance for applications such as photocatalysis, single-crystalline substrates and energy materials. Some polycrystalline TiO_2 thin films grown by chemical vapour deposition at low pressures possess unusual anatase nanocolumns with well-aligned, faceted, secondary features. One variant grown by pulsed pressure metalorganic vapour deposition has excellent photocatalytic and antimicrobial activity. The striking anatase morphology has a $\langle 110 \rangle$ growth direction, and the activity is thought to be related to the crystallography of the exposed surfaces and nanostructure.

The unusual microstructure is hypothesised to result from the interplay between the kinetics of preferential deposition caused by the shadowing effect at low pressures and finite surface diffusion driven by highly anisotropic surface energies. There is no existing modelling work that explores these detailed effects and the resulting exposed surfaces for realistic, material-specific deposition systems. In this thesis, a continuum model that incorporates both process-specific and materials-specific effects is developed. A spectral method is used to solve coupled partial differential equations for the 3D evolution of structure.

The model was validated for a well-known MgO microstructure produced by oblique angle deposition. A long-standing discrepancy between the existing theories and experimental observations regarding the column tilt angle and in-plane texturing in this cubic $\{100\}$-habit material is resolved with the new model. A finite surface diffusion, together with shadowing due to ballistic transport, is shown to give rise to the biaxial texture and the roof-tile surface morphology experimentally observed for MgO.

The evolution of anatase-TiO_2 nanocolumns during low pressure chemical vapour deposition was studied. The anisotropic interfacial energies for important surfaces in this tetragonal material were calculated using density functional theory. A numerical perturbation study showed the influence of the initial condition and growth regime on stabilising experimentally consistent morphologies. Plate-like branched structures were stabilised with large surface areas of high energy free surfaces such as $\{116\}$. Plate growth directions consistent with available scanning electron microscopy were predicted.

Many nanostructured materials with interesting morphologies and surface-dominated properties are made using low pressure chemical or physical vapour deposition. The model developed and validated here can be applied to understand how to select processing parameters such as temperature and pressure in order to control the resultant morphologies and engineering properties.

Contents

1. Overview

1.1 Motivation

In thin film applications, columnar microstructures usually lead to films with special properties, such as photocatalysis [1] superconductivity [2], optical [3], ferromagnetic [4] and electrochemical [5] properties. The performance of these thin films depends on the quality of texturing and the nature of the columnar morphology. Using low-pressure deposition techniques, the columnar structures grown usually show inter-columnar voids due to the effect known as shadowing. Many existing theories for the origin of formation of columnar microstructures have focused on this process-specific effect [6, 7, 8, 9, 10, 11, 3, 12]. However, the resulting columnar structures exhibit different nanostructured morphologies, due to the different materials deposited. For example, biaxially textured Mo [13], CaF_2 [14, 15], Mg [16, 17] and MgO [18] columnar structures, fabricated using the same oblique angle deposition (OAD) technique, take on different morphologies. It is for this reason, a new material-specific model is needed to study the specific deposition processes, for the applications in which the thin film properties are linked to the columnar morphology. Prototypical applications of such include the oblique angle deposited, biaxially textured MgO thin films and the low-pressure vapour deposited, fibre textured anatase-TiO_2 thin films.

1.2 Biaxially textured MgO

1.2.1 Oblique angle deposition

The origin of morphological development of columnar structures during OAD has been the subject of prolific and ongoing research in both areas of experimental and theoretical practice [19, 20]. In general, the columnar morphology is sensitive to the degree of deposition asymmetry, introduced by the directional flux. This asymmetry induces anistropic growth of the columnar structures, which results in well-aligned, tilted nanocolumns. As best demonstrated by the characterisation of a Mo thin film [13], shown in Fig. 1.1b and Fig. 1.1c. Mo thin film has a {110}-faceted crystal habit and it was fabricated using OAD with directional flux indicated by arrow on figure. The nanocolumns are well aligned in terms of the their crystal orientation. This is known as an in-plane texture, characterised by the surface reflection high-energy electron diffraction (RHEED) pole figure measurement shown in Fig. 1.1a. The nanocolumns are isolated with no true grain boundary formed, due to the shadowing effect. Furthermore, the columnar structures are tilted at an angle with respect to the substrate. Intra-columnar branches are also observed on the sidewalls on the nanocolumns. These common microstructural features of obliquely deposited films are evident on the scanning electron microscopy (SEM) images in Fig. 1.1b and Fig. 1.1c.

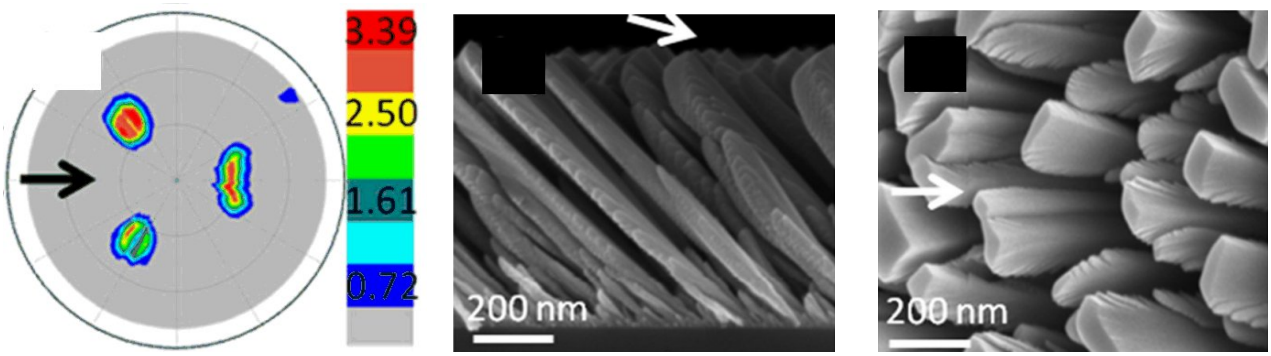

(a) (b) (c)

Figure 1.1: (a) surface RHEED pole figure with diffraction intensity (arb. units) indicated by the colour bar, SEM images of a biaxially textured Mo thin film (b) the side profile and (c) the top view (all taken from [13]). The arrows indicate the direction of the vapour flux.

The in-plane texture disappears if the thin film is deposited on a rotating substrate. The tilting of the nanocolumns becomes vertical to the substrate. This is indicated by the surface RHEED pole figure in Fig. 1.2a. Compared with Fig. 1.1a which informs an in-plane texture, a fibre texture of the columnar microstructure is developed for Mo nanocolumns grown on rotating substrate, shown in Fig. 1.2b and Fig. 1.2c.

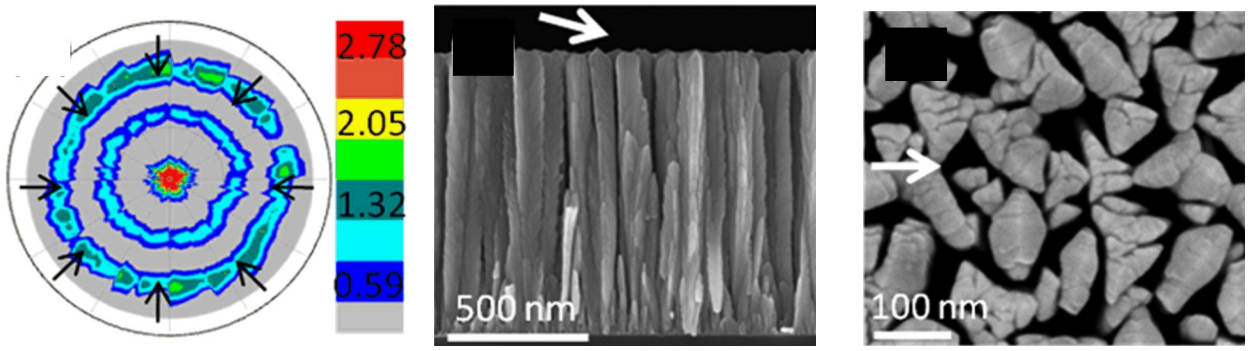

(a) (b) (c)

Figure 1.2: (a) surface RHEED pole figure using the the breaking of in-plane texture on a rotating substrate, (b) SEM top view and (c) SEM side view of the resultant fibre textured Mo thin film (all taken from [13]). The arrows indicate the direction of the vapour flux.

1.2.2 Multi-faceted morphology

It is the knowledge of this alignment in biaxially textured thin films that enables the detailed characterisation of their morphologies, such as the terminating facets of the individual nanocolumns. Shown in Fig. 1.3 are two MgO thin films fabricated using OAD, both exhibiting the same biaxial texture [21, 18]. The terminating top facets are of {100} type and they are well aligned both vertically and horizontally, as shown by the SEM top view in Fig. 1.3a. This is known as the 'roof-tile' surface morphology. It allows for the growth of high-quality superconducting coated conductors (such as DyBCO) in the application of MgO buffer layers [21] and it has helped build the world's first superconducting wind turbines [22]. The columnar morphology of biaxially textured MgO is multi-faceted. Very little is known, however, about the nature of the terminating facets of the sidewalls of MgO nanocolumns shown on Fig. 1.3b. In Ch. 5, a material-specific model is developed to study the detailed morphology of obliquely deposited MgO nanoclumns.

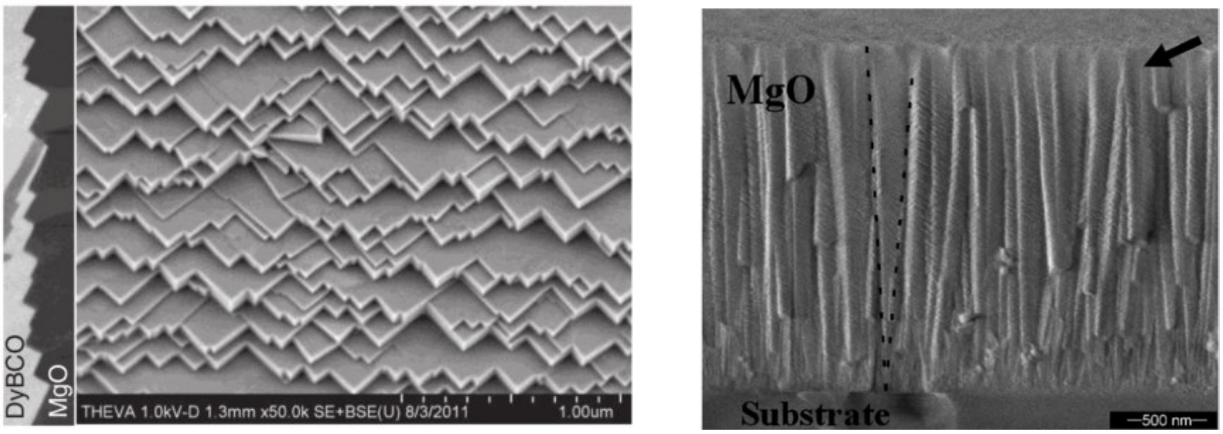

(a) (b)

Figure 1.3: Biaxially textured MgO thin films with multi-faceted morphology (a) SEM top view of a high-quality MgO coating [21] (b) SEM side profile of a MgO thin film [18]

1.3 Nanostructured anatase-TiO_2

1.3.1 pp-MOCVD grown anatase-TiO_2

Titanium dioxide TiO_2 is one of the most popular ceramic materials, owing to its association with technologically important applications, such as photocatalysts [23, 24, 25, 26, 27, 28, 29] and semiconductors [30, 31]. Black Titania polycrystalline thin films deposited on various substrates using pulsed pressure metal-organic chemical vapour deposition (pp-MOCVD) exhibit extraordinary photocatalytic and antimicrobial properties, such as high photocatalytic activity [32] and high kill rate [1]. Fig. 1.4a shows a black titania thin film deposited on metal substrate. The anti-fouling, anti-scratch and various other mechanical properties of the thin film make the production particularly suitable for applications in health care, water and air purification industries [28, 29, 33]. The scalibility of this deposition technique is superior [34] when compared with other techniques, such as evaporation, sol-gel, pulsed laser and sputtering. For instance, the thin films grown by molecular beam epitaxy (MBE) has a typical growth rate of the order of $1\,\text{Å}\,\text{s}^{-1}$, whereas the pp-MOCVD can achieve three orders of magnitude greater average growth rate [33].

The polycrystalline thin films fabricated by pp-MOCVD are $\langle 110 \rangle$-fibre-textured [1], shown in Fig. 1.4b. They feature a faceted, prismatic surface morphology. Furthermore, SEM and transmission electron microscopy (TEM) studies reveal that the resulting columnar microstructure of the anatase-TiO_2 nanocolumns exhibits large exposed surface area, due to the presence of a network of secondary structures developed on the sidewalls [1]. These faceted secondary structures extend all the way to the film surface and appear to show a plate-like morphology, as shown in Fig. 1.5. The photocatalytic and antimicrobial properties are thought to be related to this unusual microstructure [1].

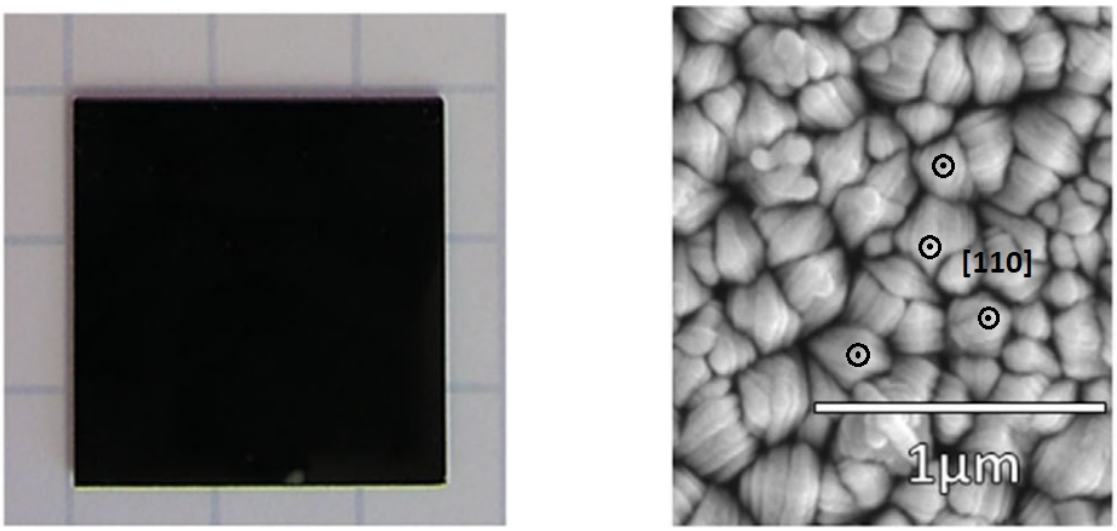

(a) (b)

Figure 1.4: 3 µm anatase-TiO_2 thin film on fused silica substrate deposited at 525°C, (a) photograph and (b) SEM top view of the thin film sample (images taken and edited from [35]).

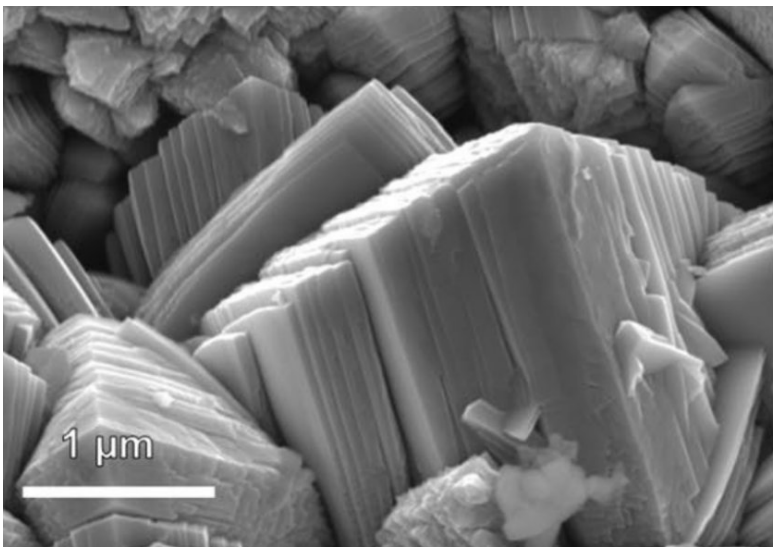

Figure 1.5: SEM micrograph showing the distinct surface morphology of anatase nanocolumns (image taken from [1]).

pp-MOCVD processes

In order to deposit a uniform thin film onto a substrate, techniques such as carrier gas MOCVD and rotating substrate deposition are commonly used. The pp-MOCVD reactor employs a carrier gas-free pulsed injection system [1]. A liquid precursor solution of TTIP and toluene is injected into the reactor chamber which induces a pressure change and leads to rapid expansion of the gaseous species. This expansion in combination with the use of an eclipser enables macroscopically uniform transport of the gas species to the surface of the heated substrate and hence it produces a conformal layer of coating on the substrate [28, 29, 33, 36].

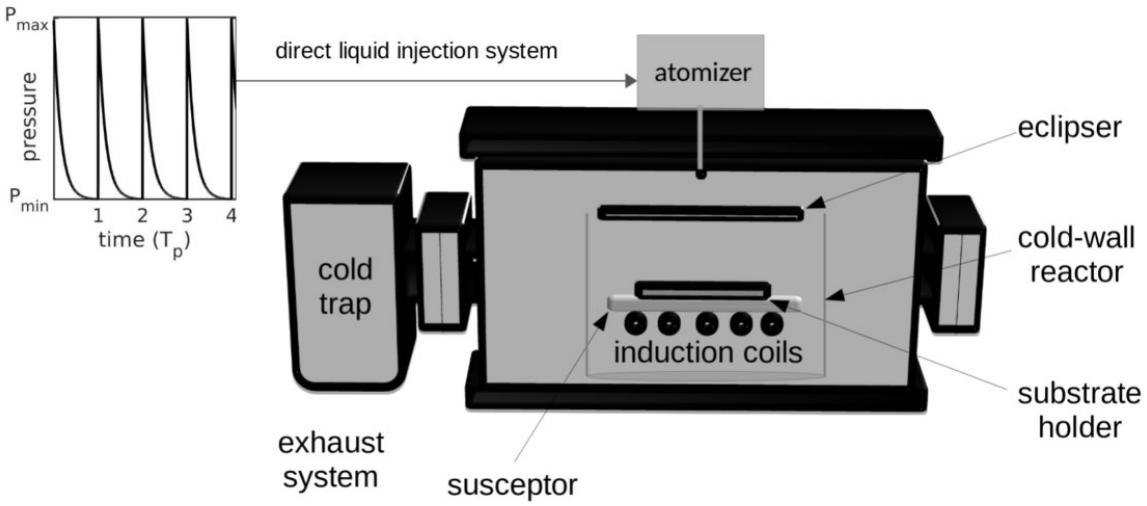

Figure 1.6: pp-MOCVD reactor schematic diagram.

Fig. 1.6 shows a schematic of the pp-MOCVD setup and a direct liquid injection system which pumps a controlled volume of a liquid solution of TTIP in toluene. TTIP is one of the most commonly used precursors for depositing titania thin films. The injected droplet is instantly evaporated once entering the reactor due to the low pressure the reactor operates in. The TTIP molecule then undergoes complex thermal decomposition [37] and the resulting ligands and complexes participate in surface reactions, e.g. adsorption, desorption and surface diffusion. The substrate is inductively heated to a range of temperatures 350 °C $\sim$ 550 °C. Gas species are continuously pumped out of the reactor, keeping the reactor chamber in a lower pressure for the subsequent pulsing cycle.

A semi-analytical model has been developed for this system to study the pressure response of a droplet evaporation process during the injection [38]. The macroscopic pressure profile (shown in Fig. 1.6) of the source is tunable with parameters P_{max}, P_{min} the maximum and minimum pulsing pressure, and T_p the pulse time [36]. These parameters have a direct influence on the pressure induced vapour flux onto the substrate, which has not so far been modelled for this system. In Sec. 2.2, a one-dimensional numerical model is presented for a moving boundary problem with pulsing pressure.

1.3.2 Other processes

In many vapour deposition techniques, pressure is important processing parameter. In particular, it determines the transport mechanisms for the adparticles from the source to the substrate. For a single species at fixed pressure, the Knudsen number Kn, the ratio between mean free path of the species and the feature dimension, characterises the transport regime. At low pressure, the mean free path is large compared with the dimensions of the reactor (typically for Kn $>$ 10), the species particles arrive at the substrate without bumping into each other, this is commonly referred to as continuum breakdown or ballistic transport. On the other hand if Kn $\ll$ 1, collisions occur at a high rate before making contact to the substrate, the mass transport becomes diffusive and classical continuum descriptions of a fluid can be applied.

For a conservative estimate of the pp-MOCVD process, one assumes a molecular diameter of $d = 0.3\,\text{nm}$ of the precursor, lowest temperature used $T = 773\,\text{K}$ and peak pressure $P = 500\,\text{Pa}$. The mean free path is estimated to be

$$\lambda = \frac{RT}{\sqrt{2}\pi d^2 N_A P} \approx 53\,\mu\text{m}$$

where $R = 8.3145\,\mathrm{J\,mol^{-1}\,K^{-1}}$ is the gas constant and $N_A = 6.022 \times 10^{23}\,\mathrm{mol^{-1}}$ is the Avogadro number. As far as the surface features of the thin film are concerned (sub-micro dimensions), it can be ensured by this rough estimate that the local Kn is greater than 10. This informs that the mass transport is ballistic in the region of deposited surfaces.

Many of the anatase-TiO_2 deposition systems in literature share the same processing condition, i.e. low pressure, with the pp-MOCVD process. Despite the variety in how reactors are designed or what deposition techniques are used, there are a number of research groups that produced a same $\langle 110 \rangle$-fibre-textured anatase-TiO_2 thin film with a visually similar film morphology. The commonality in these deposition techniques is low pressure under which mass transport can be considered as ballistic. Therefore, it is helpful to look at other reported antase-TiO_2 columnar structures deposited using low-pressure techniques.

LPMOCVD

The nano-structured anatase-TiO_2 thin film having good photocatalytic activity has been reported as early as 2001 by Jung et al. [24] using conventional low pressure MOCVD (LPMOCVD). They attributed the high photocatalytic decomposition rate of methylene blue in aqueous solution to the specific surface area [25]. The typical operating pressure and temperature they used for the deposition process are $P = 1\,\mathrm{Torr} \approx 133\,\mathrm{Pa}$ and $T = 500\,^{\circ}\mathrm{C}$ respectively. Despite the strikingly similar film morphology this process obtained, Fig. 1.7 Left, they have not reported the texture of the thin film or the terminating surfaces.

The first report of a $\langle 110 \rangle$-textured anatase-TiO_2 polycrystalline thin film to the author's knowledge appears in Wu et al. [39]. They produced similar nano-structured morphology (shown in Fig. 1.7) using a constant-flow CVD process, with a similar processing pressure and temperature. The X-ray diffraction (XRD) analysis in this paper confirms that the anatase polycrystalline thin film is $\langle 110 \rangle$-textured.

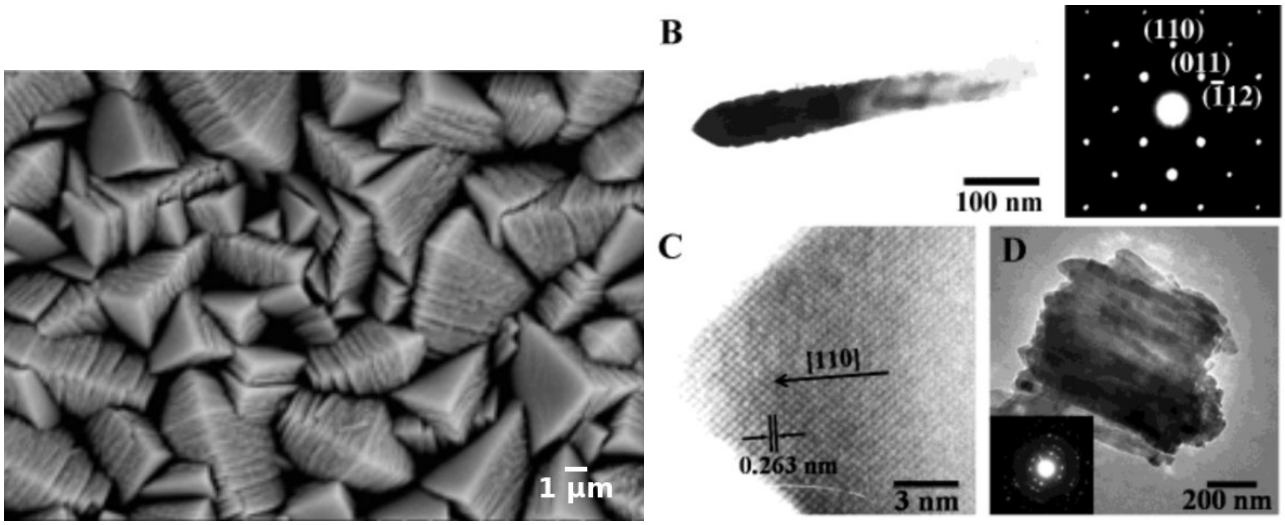

Figure 1.7: Left: SEM surface morphologies of LPMOCVD anatase-TiO_2 thin film (cf. [26]) and Right: (B) the tip of the nanorod, (C) the high resolution TEM and (D) the TEM images of the nanorods scraped off from the thin film (cf. [39]). It is noted here that the SAED labelling in (B) and the annotations on TEM image in (C) are in disagreement.

Vertical-flow MOCVD

In a pioneering work, Chen et al. isolated one of the single nanorods (Fig. 1.8 Left) of the $\langle 110 \rangle$-textured anatase-TiO_2 thin film (Fig. 1.8 Right) in TEM and studied the selected area electron diffraction (SAED) pattern, as shown in Fig. 1.8 Left. They also suggested a growth mechanism [40, 27] that has nothing to do with ballistic transport of the species. By the help of an atomic model for visualisation, they proposed a periodic boundary chain (PBC) model, according to which the exposed surfaces are bounded by {112} and {001} microfacets truncated by steps. However very little is known of the stepped surfaces for this particular solid-vapour interface whose nature is much more complex than the authors suggest. The processing parameters used in their work include a constant flow of O_2 gas with pressure maintained at $P = 1.5\,\text{mbar} = 150\,\text{Pa}$ in a cold-wall reactor with substrate temperature $T = 550\,^\circ\text{C}$. It has not been acknowledged in any way that the low pressure plays a role in the kinetic process of the deposition but a PBC self-assemble of the units consisting of {112} and {001} microfacets is attributed to the resultant microstructure. A criticism here would be that this growth mechanism proposed is only feasible for particles grown in aqueous solutions, e.g. the nano-necklace of Penn and Banfield [41].

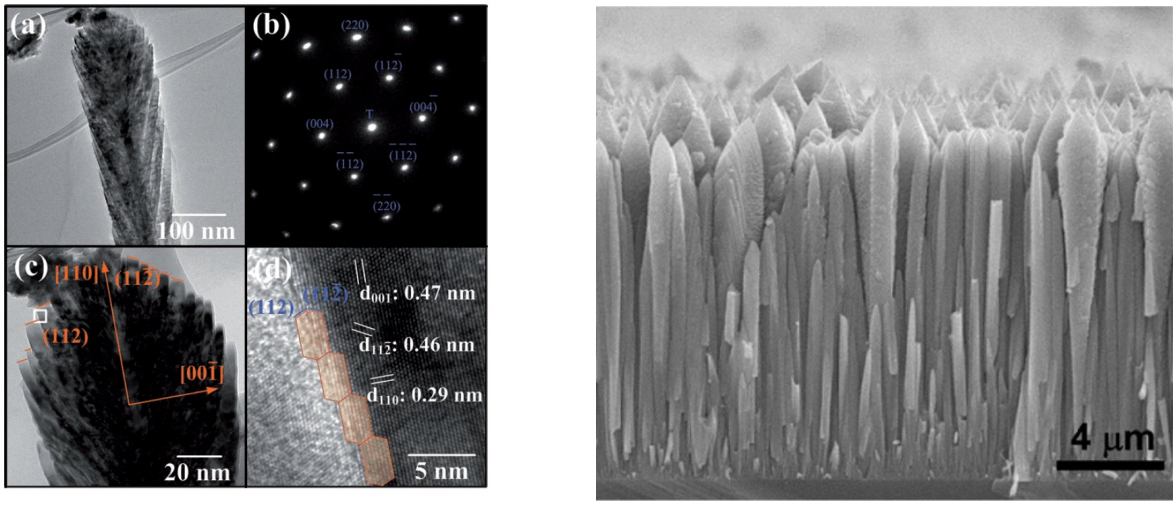

Figure 1.8: Left: (a) TEM image of a single-crystal anatase-TiO_2 nanorod (b) SAED along the $[1\bar{1}0]$ zone axis (c) TEM and (d) high resolution TEM (cf. [40]) Right: SEM side profile of the columnar microstructure (cf. [27]).

Sputter deposition

A different fabrication technique for making nano-structured anatase-TiO_2 thin films was reported in an experimental work, with a $\langle 110 \rangle$ texture (shown in Fig. 1.9), using sputtering deposition [42]. In this vacuum physical vapour deposition (PVD) process, the film morphologies are controlled by the source-to-substrate distance. It is found that the nano-structured microstructure is only obtained with a separation distance below a certain threshold. The source-to-substrate distance is an important parameter that alters the flux distribution at the material surface. The result of this work suggests that the flux distribution controls the film morphology.

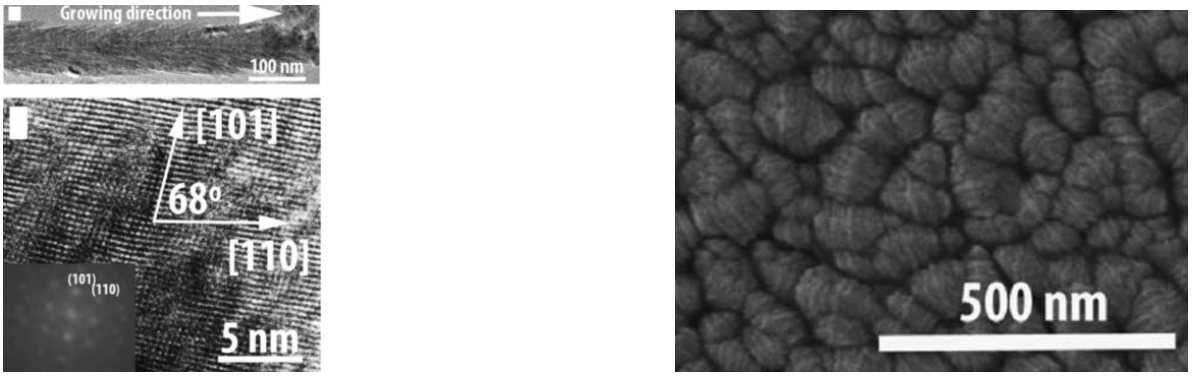

(a) (b)

Figure 1.9: (a) High resolution TEM of a single nanorod with lattice fringes showing the ⟨110⟩ growth direction and (b) SEM top view of the nano-structured film morphology (taken from [42]).

1.4 Thesis outline

Looking ahead, the remainder of this thesis is organised as follows: Ch. 2 reviews the classical problems of phase transition. A one-dimensional (1-D), deposition problem is introduced to extend the classical problems to incorporate an unsteady boundary condition. General theories involving dimension larger than 1 are reviewed. Basic materials science concepts such as surface energy density γ, capillarity ξ-vector, equilibrium shape of a crystal and well-known thin film growth theories are also introduced for general materials. Ch. 3 provides an extensive review on the existing modelling methodologies. Ch. 4 considers a construction method and employs it in the calculations of γ and ξ for realistic materials anatase-TiO_2 and MgO.

In Ch. 4 surface diffusion of realistic materials, as modelled by an energy minimisation calculation, is implemented and realised for anatase-TiO_2 and MgO. The equilibrium shapes of anatase-TiO_2 and MgO reached by the energy minimisation calculations are obtained and benchmarked against the convexified ξ-plots calculated in Ch. 4. The implementation of surface diffusion with highly anisotropic surface energy for anatase-TiO_2 and MgO provides the necessary tool for the development of materials-specific deposition models in the subsequent chapters.

Ch. 5 discusses the origin of texture formation and the discrepancy between existing theories and experimental observations. An alternative theory is proposed for the texture formation of biaxially textured nanocolumns. A continuum model is developed for a prototype OAD-MgO system and the theory is demonstrated by means of three-dimensional (3-D) numerical simulations of the model. Ch. 6 is centred around making a prediction of candidates of the exposed surfaces, based on the model developed in Ch. 5 and similar assumptions made for an OAD-MgO system. New representations for exposed surfaces are also developed in Chapters 5 and 6 for the analysis of results. Ch. 7 reviews the thesis, draws together the main ideas developed in Ch. 5 and Ch. 6, and compares them with existing continuum models.

2. Classical theories of crystal growth

The purpose of this chapter is to review the theoretical underpinning of classical theories of crystal growth. As an overview, the basic mathematical description and special solutions to the classical Stefan problem are detailed in Sec. 2.1. An extension of the theory to incorporate unsteady boundary condition is followed in Sec. 2.2, considering a 1-D gas-solid phase transition problem. Analysis for this particular problem related to the pp-MOCVD system is provided. General theories involving dimension larger than 1 are reviewed in Sec. 2.3, together with existing thin film growth theories in Sec. 2.4. In later chapters, the formulation involved in solving these problems numerically will be reviewed in depth in Ch. 3, following the 3-D concepts given in 2.3.3 and 2.3.4. To facilitate the reading, a list of notations used throughout the chapter is given in Tab. 10.1 in the Appendix.

2.1 Moving boundary problem

In 1D, it is well known that the phase transition problem of a pure material can be described by the moving boundary problem which involves a moving interface located at $h(t)$ and two changing domains $V^+(t)$ and $V^-(t)$ representing the bulk phases. Here the prototype phases are liquid and solid. The classical Stefan Problem is a special type of moving boundary problem. It arises from solving simultaneously the heat equations in two bulk phases which have different thermal diffusivities* α^i, separated by a moving planar interface whose normal velocity v_n is a function of the local gradients of temperature $\nabla T|_i$ and surface normal $\vec{n}$ pointing outwards. The interface location h(t) and its normal velocity v_n are *a priori* unknown. Considering a solid V^s growing into liquid V^l:

$$T_t^i = \alpha^i \nabla^2 T^i \qquad \text{in} \quad V(t) \tag{2.1}$$

$$\rho^s L_f v_n = (k^s \nabla T|_s - k^l \nabla T|_l) \cdot \vec{n} \qquad \text{on} \quad h(t) \tag{2.2}$$

The temperature at the interface T^{I} is equal to equilibrium melting temperature T_m for planar interface. The Stefan condition Eqn. 2.2 is a result of energy balance at the interface in which the latent heat is released so that the interface advances at a speed v_n. ρ is the material density, $T_t = {}^{\partial T}/_{\partial t}$ and L_f is the specific latent heat of fusion.

For the simplest Stefan problem of solidification concerning a planar boundary and an undercooled solid in $V^s(t)$ growing into its melt $V^l(t)$. Assuming plane symmetry the temperature field $T = T(x,t)$ needs to be solved everywhere except where it is constant $T(h,t) = T_m$. Boundary condition at the domain wall $T(0,t) = T_\infty$ is imposed so that the amount of undercooling can be found as $\Delta T = T_m - T_\infty$. Moreover the temperature must be continuous at the

*$i = s, l$

interface, i.e.,

$$\lim_{x \to h(t)^-} T^s(x,t) = \lim_{x \to h(t)^+} T^l(x,t) = T_m$$

These are summarised below with the initial temperature profile in domain $[0, L]$ shown in Fig. 2.1. The governing equations are given by

in solid	$T_t^s = \alpha^s T_{xx}^s$	$0 < x < h(t)$	(2.3)
in liquid	$T^l(x,t) = T_m$	$h(t) < x < L$	(2.4)
on interface	$T^{\mathrm{I}} = T_m$	$x = h(t)$	(2.5)
	$\rho^s L_f \cdot v_n = k^s T_x^s$		

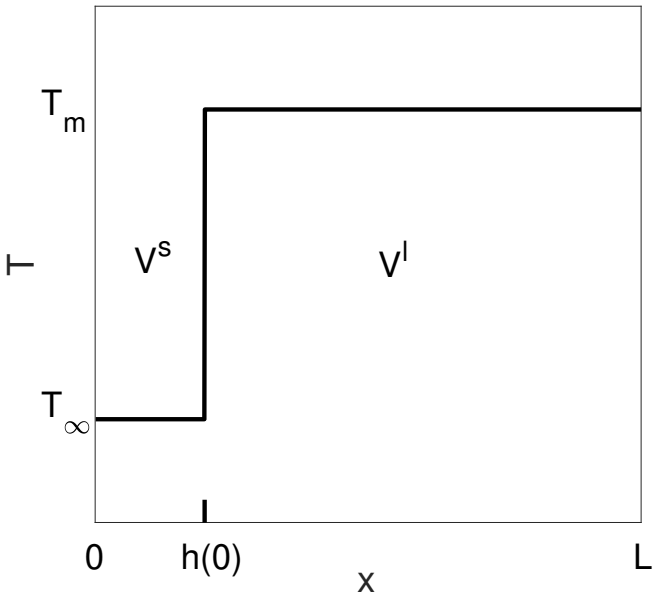

Figure 2.1: Temperature profile in domain [0,L] at $t = 0$ with boundary condition $T(0,t) = T_\infty$

By appropriately rescaling the problem and combining the variables, the heat equation is transformed into a nonlinear ordinary differential equation. Detailed derivation can be found in for instance [43]. There also exists a study of the accuracy and performance of various numerical approximations compared with the similarity solution [44]. The solution of the dimensionless undercooling S^{-1} is shown in Eqn. 2.6 and plotted against the dimensionless front velocity $\widehat{v}_n$ in Fig. 2.2, where c_p^s is the specific heat capacity of the solid phase.

$$\sqrt{\pi} e^{\widehat{v}_n^2} \mathrm{erf}\left(\widehat{v}_n\right) = S^{-1} = \frac{c_p^s \Delta T}{L_f} \tag{2.6}$$

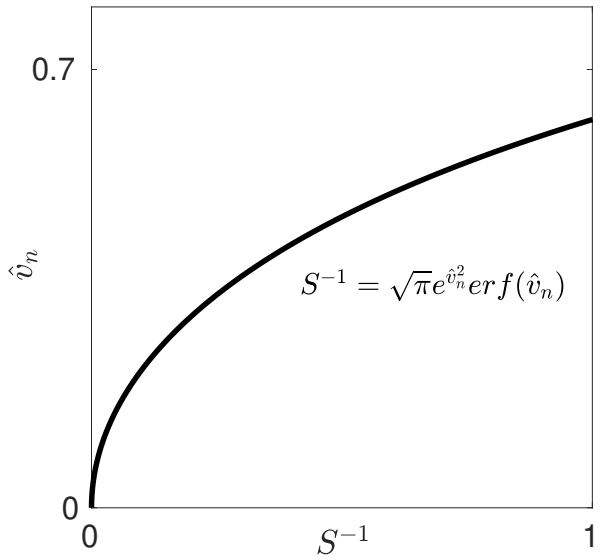

Figure 2.2: Similarity solution for the problem of undercooled solid growing into its melt

For comparison, a system of solid kept at temperature T_m growing into its undercooled melt at temperature T_∞ can be described below using the same set of notation as before and initial temperature field plotted in Fig. 2.3:

$$\begin{array}{lll} \text{in solid} & T^s(x,t) = T_m & x < h(t) \quad (2.7) \\ \text{in liquid} & T_t^l = \alpha^l T_{xx}^l & x > h(t) \quad (2.8) \\ \text{on interface} & T^{\mathrm{I}} = T_m & x = h(t) \quad (2.9) \\ & \rho_s L_f \cdot v = -k^l T_x^l & \end{array}$$

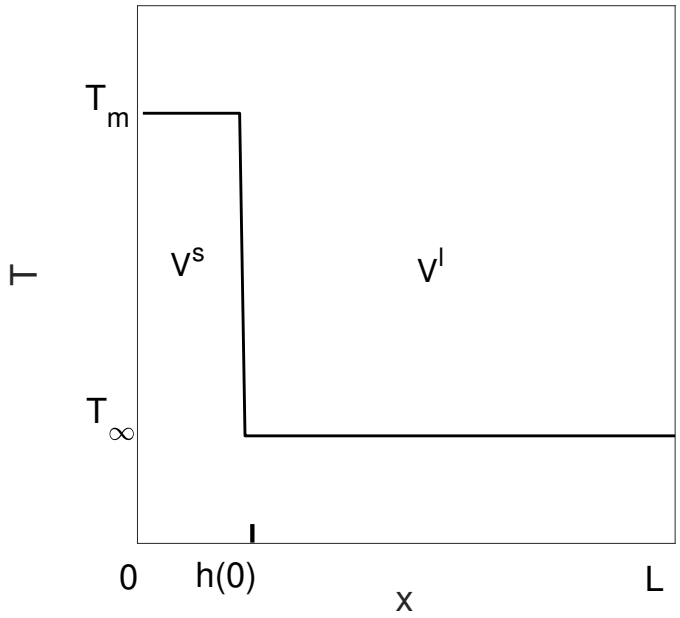

Figure 2.3: Temperature profile with boundary condition $T(L,t) = T_\infty$

However the deceptively similar system yields a totally different solution $S^{-1} = \sqrt{\pi} e^{\widehat{v}_n^2} \mathrm{erfc}\,(\widehat{v}_n)$, where erfc is the complementary error function. As shown in Fig. 2.4 the similarity solution

dictates that there exists a critical undercooling at which no resistance is against the increase of front velocity. But one should also include the effect of kinetic undercooling so that the advance in the interface front is damped.

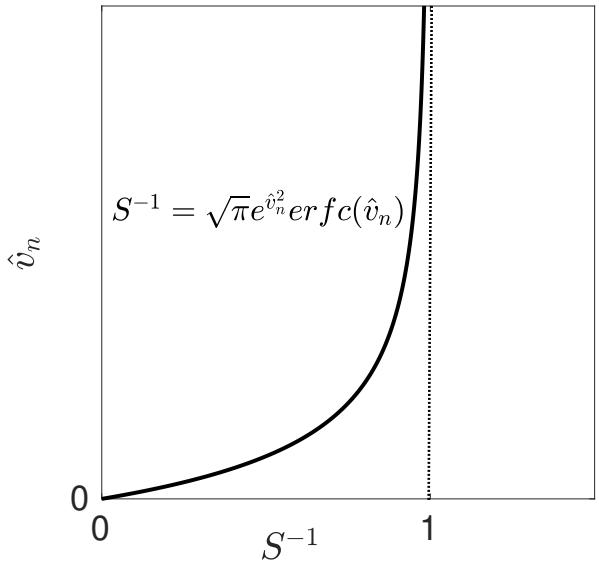

Figure 2.4: Solution to the problem of planar interface kept at T_m growing into its undercooled melt.

2.2 1-D deposition

The aim of this section is to extend the classical theory reviewed above to a gas-solid phase transition problem, with a special attention to the unsteady boundary condition featured by a typical pp-MOCVD system. A full description of the deposition system includes gas-phase dynamics, deposition and re-emission events and surface diffusion, with complications of geometric shadowing, attachment kinetics and crystalline anisotropy. It is very difficult, if not impractical, to consider all these effects altogether in a model, as far as continuum approach is concerned. It is however common to make assumptions and simplifications of the unknowns and the less significant contributions to the growth of an interface. The simplification made in this chapter is the one spacial dimension, i.e. a planar interface. A 1-D deposition model is presented, with an unsteady boundary condition mimicking the pulsing pressure at far field. The chapter starts with the physics of the problem. Assumptions are followed to simplify the problem. Finally, numerical methods applicable to the problem are implemented for the evaluation of the model.

In one spacial dimension there is only one direction of growth, namely unidirectional growth. This implies that anisotropy in any forms does not exist. Moreover the gas phase transport is limited to diffusion as ballistic transport is trivial in one spacial dimension. With the above complications lifted it is numerically tractable to retain the sharp interface description (rather than a variational approximation of it) and hence making it easier to work on physical parameters, as listed in Tab. 10.1. This allows the model to associate processing parameters of the pp-MOCVD deposition system with model parameters and to include processing features, such as pulsing pressure into the model. Another implication is that, inherently it is infeasible to model a material-specific system in 1D which would significantly complicate the problem. Material-specific systems are explored in Chapters 4, 5 and 6.

2.2.1 Problem statement

Deposition is a surface reaction whose rate depends upon the degree of supersaturation that drives it. In the moving-boundary problem Eqns. 2.10-2.16 three different boundary conditions $f(t)$ are posed in which (i) is static and (ii) is time-dependent and (iii) is periodic. In addition, the size of the domain L enters the equation because of the boundary effects imposed by the finite domain. This effect is evident in the case of 1-D static pressure in Sec. 2.2.2 but is shown to be not well-posed.

$$c_t = Dc_{xx} \quad \text{in} \quad V_{apour}(t) \tag{2.10}$$
$$(c_{sol} - c_{sat})\dot{h} = Dc_x \quad \text{on} \quad h(t) \tag{2.11}$$
$$c = c_{sat} \quad \text{on} \quad h(t) \tag{2.12}$$
$$c = f(t) \quad \text{on} \quad x = L \tag{2.13}$$

$$(i) \quad f_1(t) = c_0 \tag{2.14}$$

$$(ii) \quad f_2(t) = \begin{cases} c_0 + c_{max}\mathrm{e}^{-\alpha t} & t \geq 0 \\ 0 & t < 0 \end{cases} \tag{2.15}$$

$$(iii) \quad f_3(t) = \sum_{k=0}^{\infty} f_2(t - kT_p) \tag{2.16}$$

where the boundary conditions f_2 is a right-sided exponential decay and f_3 a pulse train of f_2 with period T_p. The three functions f_1, f_2 and f_3 are plotted in Fig. 2.5.

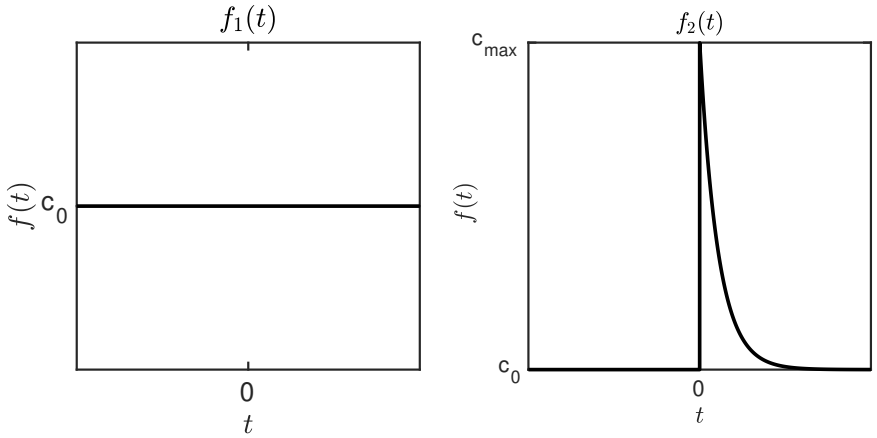

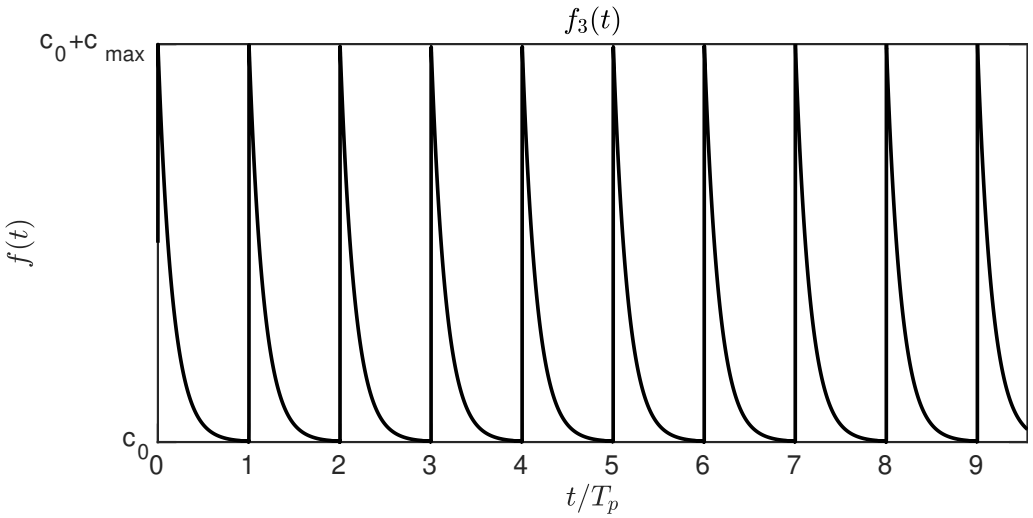

Figure 2.5: three different boundary conditions discussed in this report

Compared with solute diffusion problems (e.g. [45], Eqn. 1) the Stefan condition Eqn. 2.11 describing the mass balance at the interface can be approximated by $c_{sol}\dot{h} = Dc_x$ for deposition systems, given that $c_{sol} \gg c_{sat}$. The Stefan condition also induces non-linearity associated with the moving-boundary problem. Consider the parametric form of the moving boundary $\boldsymbol{r}(t) = \big(h(t), t\big)$ and its velocity $\boldsymbol{v}(t) = \big(\dot{h}(t), 1\big)$, the gradient of field $c(x,t)$ along $\boldsymbol{v}$ is equal to 0 subject to mass conservation on a moving reference frame fixed at the front h, that is

$$\boldsymbol{v} \cdot \boldsymbol{\nabla} c = \frac{\partial c}{\partial x}\frac{dh}{dt} + \frac{\partial c}{\partial t} = 0$$

where

$$\boldsymbol{\nabla} c \equiv \begin{pmatrix} \partial_x \\ \partial_t \end{pmatrix} c(x,t)$$

therefore, the spatial gradient c_x is now a function of h and t, i.e. $c_x = c_x(h,t) = -c_t/\dot{h} \implies \dot{h} = -c_t/c_x$. Substitute this back into Eqn. (3):

$$-\frac{D}{c_{sol}}c_x^2(h,t) = c_t(h,t) = Dc_{xx} \tag{2.17}$$

which implies that the problem is non-linear.

2.2.2 Static pressure

By the virtue of a self-similarity transformation a solution is found for a deposition system of finite domain with constant Dirichlet boundary condition Eqn. 2.14 at $x = L$. Analogous to the Stefan number for the thermal system a characteristic number for deposition is defined as $\mathcal{S}_d = {}^{c_{sol}}/_{(c_0 - c_{sat})}$. The scaled deposition front and domain are also defined analogous to the thermal system as $\eta_h = {}^{h}/_{2\sqrt{Dt}}$ and $\eta_L = {}^{L}/_{2\sqrt{Dt}}$ respectively. The solution amounts to Eqn. 2.18 plotted in Fig. 2.6.

$$\begin{cases} c(x,t) & = c_0 + (c_{sat} - c_0)\frac{erf(\frac{x}{2\sqrt{Dt}}) - erf(\eta_L)}{erf(\eta_h) - erf(\eta_L)} \\ h(t) & = 2\,\eta_h\sqrt{Dt} \\ \mathcal{S}_d^{-1} & = \sqrt{\pi}\,\eta_h e^{\eta_h^2}[erf(\eta_L) - erf(\eta_h)] \end{cases} \tag{2.18}$$

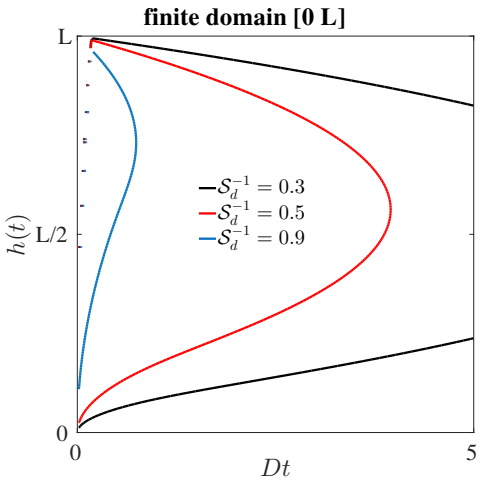

Figure 2.6: h v.s. t for a finite deposition system

The solution generalises the semi-infinite solution when $L \to \infty$. However as shown in Fig. 2.6 the problem is not *well-posed* as the solution is not unique. In order to ensure the well-posedness for the numerical analysis that follows, assumption is made so that the domain L is far greater than the length scale of growth l, i.e. $L \gg l$, as far as the deposition system is concerned.

2.2.3 Right-sided exponential decay

The individual pulse in a periodic pulse train can be modelled as function f_2 in Eqn. 2.15 where c_0, c_{max} and α are processing parameters which control the base concentration, maximum concentration and the width of the pulse respectively. Here a more convenient expression is chosen for f_2 to suit the dimensional analysis:

$$c = c_0 + c_{max}\theta_L, \qquad \theta_L \equiv \mathrm{e}^{-\alpha t}, \qquad c_{max} \equiv \delta\Delta c = \delta(c_{sat} - c_0) \qquad \text{on} \qquad x = L$$

The introduction of a time-dependent boundary condition complicates the previous problem for which similarity solutions cannot be constructed. Exact solutions only exist for the kinetics limited case where the quasi-steady-state approximation stands, similar to the ice crystal growth model in [46]. However it is also useful to study the diffusion limited growth for which a numerical solution to the sharp interface equations can be sought. First nondimensionalisation of the problem is done by scaling time and length as follows to include α and the inverse Stefan number ϵ:

$$\zeta = \frac{x}{l} \qquad \tau = \frac{t}{t_0} \qquad \mathcal{S}'_d = -\frac{c_{sol}}{\delta\Delta c}$$

$$l = \sqrt{\frac{D}{\alpha}} \qquad t_0 = \frac{l^2}{D} \qquad \epsilon = \frac{1}{\mathcal{S}'_d}$$

$$c = c_0 - \delta(\Delta c)\theta \qquad \mathcal{H}(\tau) = \frac{h(t)}{l} \qquad \zeta_L = \frac{L}{l} \to \infty$$

The moving boundary descriptions (2)-(5) then becomes:

$$\theta_\tau = \theta_{\zeta\zeta} \qquad \mathcal{H}(\tau) < \zeta < \infty \tag{2.19}$$
$$\theta = f(\tau) = \mathrm{e}^{-\tau} \qquad \zeta \to \infty \tag{2.20}$$
$$\theta = \frac{1}{\delta} \qquad \zeta = \mathcal{H}(\tau) \tag{2.21}$$
$$\mathcal{H}_\tau = \epsilon\theta_\zeta \qquad \zeta = \mathcal{H}(\tau) \tag{2.22}$$

2.2.4 Pulsing pressure

The pulse train of Eqn. 2.20 can be approximated in terms of a Fourier series Eqn. 2.23 to suit the following numerical analysis:

$$f_3'(\tau) = \sum_{k=0}^{\infty} f_2'(\tau - kT_p') = \sum_{n=-\infty}^{\infty} C_n \mathrm{e}^{in\tau} \tag{2.23}$$
$$C_n = \tfrac{1}{T_p'}\tfrac{in-1}{n^2+1}\left(\mathrm{e}^{-(in+1)T_p'} - 1\right) \tag{2.24}$$

where $T_p' = \alpha T_P$ is the dimensionless period of pulsing which is an additional processing parameter introduced by pulsing. It can be shown that, $\frac{df_3'(\tau)}{d\tau} \to \infty$ as $\tau \to kT_p'$. It is for this reason, f_3 boundary condition is not included in the analysis below. In the context of a pulsing pressure deposition, this means that only one cycle is considered (modelled by the f_2 boundary condition).

2.2.5 Numerical analysis

Numerical methods

As seen in the problem statement only the case (i) of the boundary condition Eqn. 2.13 has an exact solution in closed form. In fact it is more common to apply numerical methods to Stefan-like problems, notably, the enthalpy method [47], boundary immobilisation method (BIM) [48], perturbation method and nodal integral method. The standard boundary immobilisation method for a fixed domain is followed here and then due to the semi-infinite domain defined in the formulation Eqns. 2.19-2.22 a mapping is required to transform the semi-infinite domain into a fixed number of grid points to facilitate the numerical calculations.

Under the transformation

$$\xi = \frac{\zeta}{\mathcal{H}(\tau)}, \qquad T(\xi, \tau) = \theta(\zeta, \tau)$$

Eqns. 2.19-2.22 are transformed into a domain fixed at one end where $\xi = 1$ corresponding to $\zeta = \mathcal{H}(\tau)$ at the moving boundary:

$$\mathcal{H}^2 T_\tau = T_{\xi\xi} + \xi\mathcal{H}\cdot\mathcal{H}_\tau T_\xi \qquad 1 < \xi < \infty \tag{2.25}$$
$$T = \mathrm{e}^{-\tau} \qquad \xi \to \infty \tag{2.26}$$
$$T = \frac{1}{\delta} \qquad \xi = 1 \tag{2.27}$$
$$\mathcal{H}\cdot\mathcal{H}_\tau = \epsilon T_\xi \qquad \xi = 1 \tag{2.28}$$

Discretisation

Following for example [49, 50] the unbounded end of the domain can be transformed by using an algebraic map defined as follows so that the unbounded domain in Eqns. 2.19-2.22 becomes bounded:

$$\xi \to c\,\frac{z}{1-z}, \qquad T(\xi,\tau) \to u(z,\tau), \qquad \mathcal{H}(\tau) \to c\,\frac{s(\tau)}{1-s(\tau)}$$

where c is a control parameter for relative grid size of the so-called quasi-uniform grids and the z value at fixed boundary in the new coordinate is defined as $z_s \equiv {}^1\!/\!_{(1+c)}$. The Eqns. 2.25-2.28 then become

$$\frac{c^4}{(1-z)^4}\,\frac{s^2}{(1-s)^2}u_\tau = u_{zz} + \left[\frac{c^4 z}{(1-z)^3}\,\frac{s}{(1-s)^3}\,\frac{ds}{d\tau} - \frac{2}{1-z}\right]u_z \qquad z_s < z < 1 \tag{2.29}$$

$$u = f(\tau) \qquad z = 1 \tag{2.30}$$

$$u = \frac{1}{\delta} \qquad z = z_s \tag{2.31}$$

$$\frac{c^3 s}{(1-s)^3}\,\frac{ds}{d\tau} = \epsilon(1-z)^2\,u_z \qquad z = z_s \tag{2.32}$$

The discretisations of partial differential equation (PDE) 2.29 and 2.32 when applying the Crank-Nicolson scheme which involves a central difference at $\tau^{n+\frac{1}{2}}$ on s and u, e.g. $s^{n+\frac{1}{2}} = \frac{1}{2}(s^n + s^{n+1})$ are therefore

$$\frac{c^4}{(1-z_i)^4}\,\frac{\left(s^{n+\frac{1}{2}}\right)^2}{\left(1-s^{n+\frac{1}{2}}\right)^2}\,\frac{u_i^{n+1}-u_i^n}{\Delta\tau} = \frac{1}{2}\left(\frac{u_{i+1}^{n+1}-2u_i^{n+1}+u_{i-1}^{n+1}}{(\Delta z)^2}\right) + \frac{1}{2}\left(\frac{u_{i+1}^{n}-2u_i^{n}+u_{i-1}^{n}}{(\Delta z)^2}\right)$$
$$+\left[\frac{c^4 z_i}{(1-z_i)^3}\,\frac{s^{n+\frac{1}{2}}}{\left(1-s^{n+\frac{1}{2}}\right)^3}\,\frac{s^{n+1}-s^n}{\Delta\tau} - \frac{2}{1-z_i}\right]\left[\frac{1}{2}\left(\frac{u_{i+1}^{n+1}-u_{i-1}^{n+1}}{2\Delta z}\right) + \frac{1}{2}\left(\frac{u_{i+1}^{n}-u_{i-1}^{n}}{2\Delta z}\right)\right] \tag{2.33}$$

$$\frac{c^3 s^{n+\frac{1}{2}}}{\left(1-s^{n+\frac{1}{2}}\right)^3}\,\frac{s^{n+1}-s^n}{\Delta\tau} = \epsilon(1-z_i)^2\left[\frac{1}{2}\left(\frac{u_{i+1}^{n+1}-u_{i-1}^{n+1}}{2\Delta z}\right) + \frac{1}{2}\left(\frac{u_{i+1}^{n}-u_{i-1}^{n}}{2\Delta z}\right)\right]\Bigg|_{i=1} \tag{2.34}$$

where i and n hold for $i = 2, 3, ..., m-1$ and $n = 0, 1, 2, ...$ The ghost values u_0^{n+1} and u_0^n in Eqn. 2.34 can be eliminated by substituting $i = 1$ into Eqn. 2.33 and 2.34:

$$\begin{cases} \left[\dfrac{c^4 z_1}{(1-z_1)^3}\,\dfrac{s^{n+\frac{1}{2}}}{\left(1-s^{n+\frac{1}{2}}\right)^3}\,\dfrac{s^{n+1}-s^n}{\Delta\tau} - \dfrac{2}{1-z_1}\right]\dfrac{s^{n+\frac{1}{2}}}{\left(1-s^{n+\frac{1}{2}}\right)^3}\,\dfrac{s^{n+1}-s^n}{\Delta\tau}\,\dfrac{-2c^3(\Delta z)^2}{\epsilon(1-z_1)^2} \\ \qquad\qquad = u_2^{n+1} + u_2^n + u_0^{n+1} + u_0^n - \frac{4}{\delta} \\ \\ \dfrac{s^{n+\frac{1}{2}}}{\left(1-s^{n+\frac{1}{2}}\right)^3}\,\dfrac{s^{n+1}-s^n}{\Delta\tau}\,\dfrac{4c^3\Delta z}{\epsilon(1-z_1)^2} = u_2^{n+1} + u_2^n - u_0^{n+1} - u_0^n \end{cases} \tag{2.35}$$

in which $u_1^n = u_1^{n+1} = \frac{1}{\delta}$ at $z_1 = z_s$ due to the boundary condition 2.31. This results in a quintic equation for s^{n+1}:

$$\frac{s^{n+\frac{1}{2}}}{\left(1-s^{n+\frac{1}{2}}\right)^3}\frac{s^{n+1}-s^n}{\Delta\tau}\frac{2c^3\Delta z}{\epsilon(1-z_s)^2}\left[\frac{2\Delta z}{1-z_s}-\frac{c^4(\Delta z)z_s}{(1-z_s)^3}\frac{s^{n+\frac{1}{2}}}{\left(1-s^{n+\frac{1}{2}}\right)^3}\frac{s^{n+1}-s^n}{\Delta\tau}+2\right] = 2(u_2^{n+1}+u_2^n-\frac{2}{\delta}) \tag{2.36}$$

Initialisation

So far the initial conditions of $s(\tau)$ and $u(z,\tau)$ are not specified since the system is degenerate when $t \to 0$ subject to simple constant initial condition for u, e.g. $u(z,0) = 0$ combined with $s(0) = 0$. A interesting work addressed the issues associated with the initialisation of numerical schemes for Stefan-like problems [51]. The method described in the work requires that $u(z_s,\tau) = 0$ which does not apply for the system Eqns. 2.29-2.32. A more common approach to initialise the system (not necessarily correct) is to analytically find the approximate solution in the small time limit and use it as the initial condition in the numerical scheme. However this has to be done on a case-by-case basis to the different problems described in Sections 2.2.2, 2.2.3 and 2.2.4. Here it can be tentatively assumed that all the three systems behave in a similar way at small time and use the exact solution for the problem with boundary condition f_1 Eqn. 2.18 in Sec. 2.2.2 to initialise the systems using boundary conditions given by f_2 and f_3.

A finite-difference direct solver

The discretisations Eqn. 2.33 and 2.36 allow both the field u^{n+1} and front position z^{n+1} in the next time step to be solved linearly. To achieve this matrices are assembled to suit fast algorithms for solving the inverse of a sparse matrix. The resulted linear system Eqn. 2.37

$$\left(\mathbf{A}-\frac{\left(s^{n+\frac{1}{2}}\right)^2}{\left(1-s^{n+\frac{1}{2}}\right)^2}\mathbf{B}+\frac{s^{n+\frac{1}{2}}\left(s^{n+1}-s^n\right)}{\left(1-s^{n+\frac{1}{2}}\right)^3}\mathbf{C}-\mathbf{D}\right)\mathbf{u^{n+1}} = \left(-\mathbf{A}-\frac{\left(s^{n+\frac{1}{2}}\right)^2}{\left(1-s^{n+\frac{1}{2}}\right)^2}\mathbf{B} - \frac{s^{n+\frac{1}{2}}\left(s^{n+1}-s^n\right)}{\left(1-s^{n+\frac{1}{2}}\right)^3}\mathbf{C}+\mathbf{D}\right)\mathbf{u^n}-\mathbf{2E} \tag{2.37}$$

is solved for the next time step $(n+1)$ given the initial values of field and front position at n, in which $\mathbf{A}, \mathbf{C}$ and $\mathbf{D}$ are tridiagonal matrix, and $\mathbf{E}$ the vector due to boundary conditions Eqn. 2.30 and 2.31.

$$\mathbf{A} = \begin{bmatrix} -2 & 1 & 0 & \cdots & \cdots & \cdots & 0 \\ 1 & -2 & 1 & 0 & \cdots & \cdots & 0 \\ 0 & 1 & -2 & 1 & 0 & \cdots & 0 \\ \vdots & \ddots & & & & \ddots & \vdots \\ 0 & \cdots & \cdots & 0 & 1 & -2 & 1 \\ 0 & \cdots & \cdots & \cdots & 0 & 1 & -2 \end{bmatrix}_{(i=m-2)\times(j=m-2)} \qquad \mathbf{u} = \begin{bmatrix} u_2 \\ u_3 \\ u_4 \\ \vdots \\ u_{m-1} \end{bmatrix}_{m-2}$$

$$\mathbf{B} = \begin{bmatrix} \mathbf{b_2} & 0 & 0 & \cdots & 0 \\ 0 & \mathbf{b_3} & 0 & \cdots & 0 \\ 0 & 0 & \mathbf{b_4} & \cdots & 0 \\ \vdots & & & \ddots & \\ 0 & 0 & 0 & \cdots & \mathbf{b_{m-1}} \end{bmatrix}_{(m-2)\times(m-2)} \quad \mathbf{C} = \begin{bmatrix} 0 & \mathbf{c_2} & 0 & \cdots & \cdots & 0 \\ -\mathbf{c_3} & 0 & \mathbf{c_3} & \cdots & \cdots & 0 \\ 0 & -\mathbf{c_4} & 0 & \mathbf{c_4} & \cdots & 0 \\ \vdots & \ddots & \ddots & \ddots & \ddots & \vdots \\ 0 & \cdots & \cdots & -\mathbf{c_{m-2}} & 0 & \mathbf{c_{m-2}} \\ 0 & \cdots & \cdots & 0 & -\mathbf{c_{m-1}} & 0 \end{bmatrix}_{(m-2)\times(m-2)}$$

$$\mathbf{D} = \begin{bmatrix} 0 & \mathbf{d_2} & 0 & \cdots & \cdots & 0 \\ -\mathbf{d_3} & 0 & \mathbf{d_3} & \cdots & \cdots & 0 \\ 0 & -\mathbf{d_4} & 0 & \mathbf{d_4} & \cdots & 0 \\ \vdots & \ddots & \ddots & \ddots & \ddots & \vdots \\ 0 & \cdots & \cdots & -\mathbf{d_{m-2}} & 0 & \mathbf{d_{m-2}} \\ 0 & \cdots & \cdots & 0 & -\mathbf{d_{m-1}} & 0 \end{bmatrix}_{(m-2)\times(m-2)}$$

$$\mathbf{E} = \begin{bmatrix} \frac{1}{\delta}\left(1 - \frac{c^4(\Delta z) z_2}{2\Delta\tau(1-z_2)^3}\frac{s^{n+\frac{1}{2}}(s^{n+1}-s^n)}{\left(1-s^{n+\frac{1}{2}}\right)^3} + \frac{2}{1-z_2}\right) \\ 0 \\ 0 \\ \vdots \\ 0 \\ f(\tau)\left(1 + \frac{c^4(\Delta z) z_{m-1}}{2\Delta\tau(1-z_{m-1})^3}\frac{s^{n+\frac{1}{2}}(s^{n+1}-s^n)}{\left(1-s^{n+\frac{1}{2}}\right)^3} - \frac{2}{1-z_{m-1}}\right) \end{bmatrix}_{m-2}$$

Matrix elements $\mathbf{b_i}, \mathbf{c_i}, \mathbf{d_i}$ are given by:

$$\mathbf{b_i} \equiv \frac{2c^4(\Delta z)^2}{\Delta\tau(1-z_i)^4}, \quad \mathbf{c_i} \equiv \frac{c^4(\Delta z) z_i}{2\Delta\tau(1-z_i)^3}, \quad \mathbf{d_i} \equiv \frac{2}{1-z_i}$$

2.2.6 Numerical results

Algorithm 1 BIM-Crank-Nicolson

procedure SOLVE LINEAR SYSTEMS OF EQUATIONS
    assemble matrices **A**, **B**, **C** and **D**
    initialise vector u^1 according to Sec. 2.2.5
loop:
    for $n = 0$ to some time interval **do**
        calculate vector **E** using current and old values of s
        while $|temp - s(n+1)| < 1e-13$ **do**
            solve Eqn. 2.37 to obtain $u^{(n+1)}$
            calculate the value of $s(n+1)$ for the next time step using Eqn. 2.36
            let temp $= s(n+1)$
        update the value of $s(n+1)$
procedure ERROR ANALYSIS
    calculate η_h in Eqn. 2.18 using the Newton-Raphson method
    convert back $s \to \mathcal{H}$, $u \to T$ and $z \to \xi$
    convert back $T \to \theta$ and $\xi \to \zeta$
    compare the exact solutions and numerical solutions

By employing the direct finite difference solver detailed above it is possible to study the unsteady in-flow condition f_2 which has no exact solution. However $f1$ is also solved numerically to benchmark the direct solver. In Algorithm 1 a pseudocode of the algorithm involved in solving this 1-D, one-sided Stefan problem is summarised.

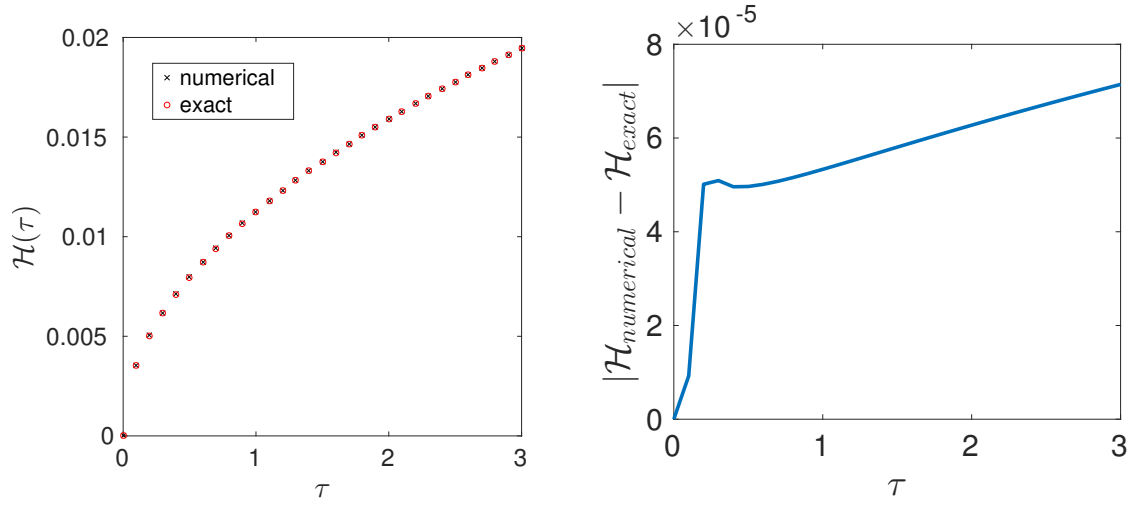

(a) (b)

Figure 2.7: (a) $\mathcal{H}$ v.s. τ for a semi-infinite domain deposition system. (b) Error of $\mathcal{H}$ as a function of τ

Numerical results for $\mathcal{H}(\tau)$ with f_1 boundary condition obtained using Algorithm 1 and the direct solver are shown in Figures 2.7a. The exact solutions exist for $f(\tau) = f_1$ and are used to calculate errors for $\mathcal{H}$ and c, plotted in Figures 2.7b and 2.8a respectively. The numerical method is used to approximate solutions for $f(\tau) = f_2$, plotted in Fig. 2.8b, which makes up of the more complex form f_3. It can be seen in the numerical solution that the difference in response to an exponential decay f_2 is small, compared with steady condition f_1.

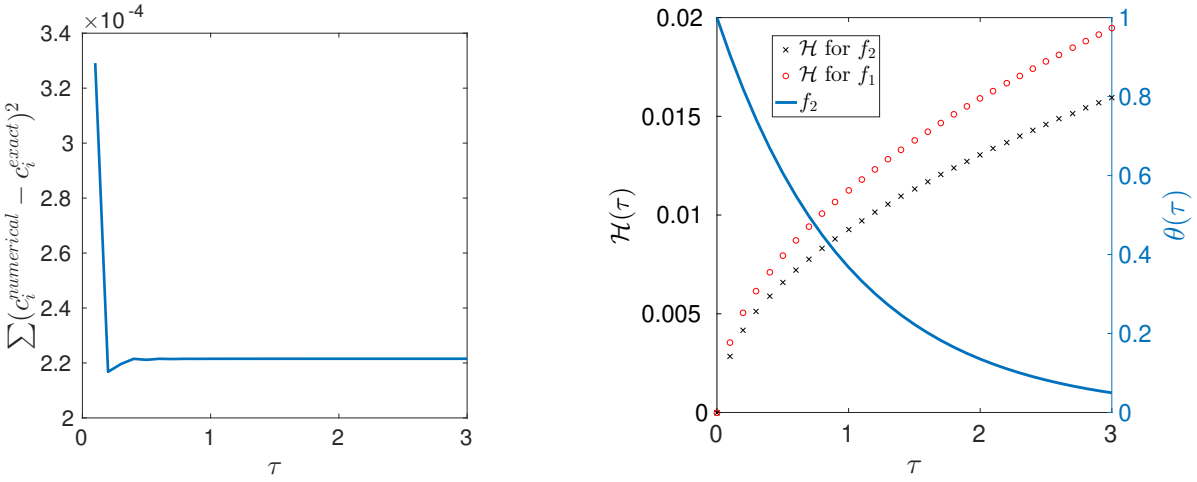

(a) (b)

Figure 2.8: (a) L^2 error of c as a function of τ. (b) Response of $\mathcal{H}$ with boundary condition given by $f(\tau) = f_2$.

To summarise, a vapour deposition system is modelled as a moving boundary problem. Dimensional analysis is done to the moving boundary formulation and it is found that the domain is semi-infinite. In addition, the moving boundary problem requires that the other boundary of the 1-D domain to be determined as part of the solution. The correct numerical method therefore has to account for both the unknowns due to the time-varying domain and the semi-infinite domain individually. To solve the problem, a novel BIM method is adapted to transform the time-varying domain to a fixed domain. An algebraic mapping is subsequently used to map the fixed semi-infinite domain into a bounded domain. Logarithmic mapping results in non-linear systems of equations. A direct finite difference solver is built and the numerical method is benchmarked against a system with static pressure and found to be accurate. A numerical solution for system featuring a right-sided exponential decay function, the f_2 boundary condition, is obtained. It is noted lastly here that, this accurate method is only applicable for systems of dimension $d = 1$. Complications of the moving boundary problem arise for $d > 1$, e.g. the crystal anisotropy. In Chapters 4.3, 5 and 6, a diffuse interface approach will be adopted to accommodate a 3-D interface and crystal anisotropy. The diffuse interface approach is introduced in the next chapter.

2.3 General theories

2.3.1 Curved interface

Considering a curved 1-D interface in a 2-D domain for which the curvature $H = {}^1/_R \neq 0$. The energy balance at the interface Eqn. 2.39 differs from the one used to obtain Eqn. 2.2 due to the stretching of the area $A = h \times \delta h$ so that the identity

$$\frac{1}{A}\frac{dA}{dt} = -2Hv_n = \kappa v_n \tag{2.38}$$

holds (curvature by convention is positive for interface expanding and negative for interface shortening and therefore I denote $\kappa = -2H$). The energy balance is performed below with geometries and notations illustrated in Fig. 2.9.

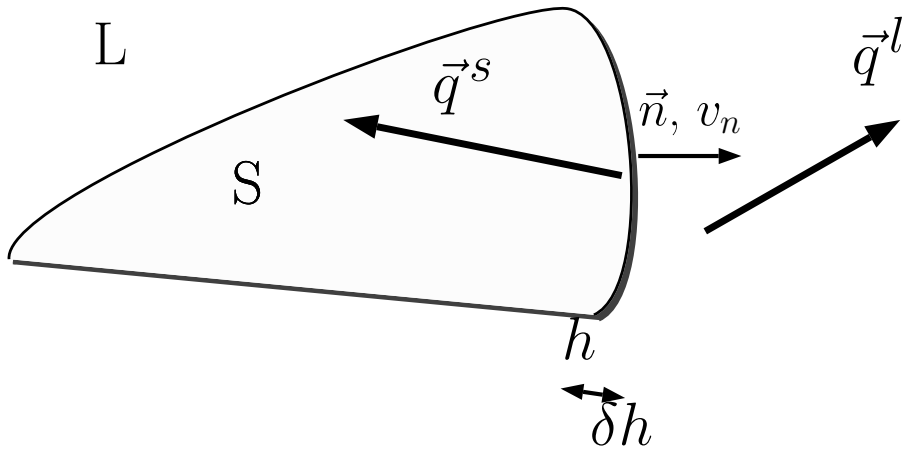

Figure 2.9: Energy balance of curved interface between solid phase S and liquid phase L.

$$\rho^s L v_n A\delta t - \gamma A|_{h+\delta h} + \gamma A|_h = (\vec{q}^l - \vec{q}^s)\cdot\vec{n}A\delta t \tag{2.39}$$

$$\rho^s L_f v_n - \frac{1}{A}\frac{d}{dt}(\gamma A) = (k^s\nabla T^s - k^l\nabla T^l)\cdot\vec{n} \tag{2.40}$$

$$\rho^s L_f v_n(1 - \kappa\frac{\gamma}{\rho^s L_f}) = (k^s\nabla T^s - k^l\nabla T^l)\cdot\vec{n} \tag{2.41}$$

where γ is the isotropic surface energy density in units of Jm^{-2} and Eqn. 2.40 is the generalised Stefan condition for curved interface with isotropic surface energy. If the surface energy is anisotropic, i.e. $\gamma = \gamma(\vec{n})$, a weighted mean curvature κ_γ should be defined (as will be introduced in Sec. 2.3.3) so that the L.H.S. of Eqn. 2.40 becomes

$$\rho^s L_f v_n - \frac{1}{A}\frac{d}{dt}\int_{h(t)}\gamma(\vec{n})dA = \rho^s L_f v_n - \frac{1}{A}\int_{h(t)}\kappa_\gamma\cdot v_n dA \tag{2.42}$$

The second term on the left hand side in Eqns. 2.40 and 2.42 represents the rate of energy expended by interface stretching and is usually ignored in the usual form of heat balance [52].

2.3.2 Gibbs-Thompson effect

In the previous section it is shown that how part of the energy liberated by phase transition is used to create the interface. However, to calculate the speed v_n one has to know the heat flux $\vec{q}$ in and out of the interface which is related by Fourier's law to the temperature gradient ∇T evaluated at both sides of the interface. The computing of ∇T^s or ∇T^l requires the knowledge of the interface temperature T^{I} which is not T_m for a curved interface illustrated in Fig. 2.10.

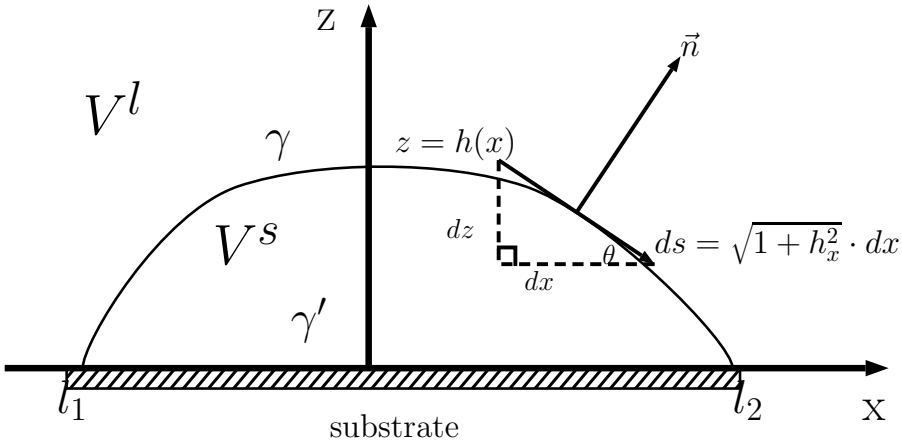

Figure 2.10: A curved interface $h(x)$ joining point l_1 and l_2 on the substrate in a 2-D domain.

Consider a curved interface $z = h(x)$ bounded by l_1 and l_2. The total Helmholtz free energy $\mathcal{F}$ and volume $\mathcal{A}$ are defined as:

$$\begin{aligned} \mathcal{F} &= \int_{l_1}^{l_2} \gamma \sqrt{(1 + h_x^2)} dx + \gamma'(l_2 - l_1) \\ \mathcal{A} &= \int_{l_1}^{l_2} h(x) dx \end{aligned} \tag{2.43}$$

where γ and γ' here for simplicity are the interfacial energy $\gamma_{interface}$ and $\gamma_{substrate}$ previously defined for solid-liquid and solid-substrate interfaces. Combining the two to form an unconstrained variational problem we get:

$$\begin{aligned} E &= \mathcal{F} + \lambda \mathcal{A} \\ &= \int_{l_1}^{l_2} \left[\gamma (1 + h_x^2)^{1/2} + \lambda h(x) \right] dx + \gamma'(l_2 - l_1) \end{aligned} \tag{2.44}$$

by setting $\delta E = 0$ and identify that the $\kappa = \left[\frac{h_x}{(1 + h_x^2)^{1/2}} \right]_x = -2H \quad \Longrightarrow$

$$\begin{aligned} -\gamma \left[\frac{h_x}{(1 + h_x^2)^{1/2}} \right]_x + \lambda &= 0 \\ \lambda &= 2H\gamma \\ 2H &= \frac{h_{xx}}{(1 + h_x^2)^{3/2}} \end{aligned} \tag{2.45}$$

and that the Lagrange multiplier λ is the change in Gibbs energy, i.e. $\lambda = \Delta G = \dfrac{\rho^s L_f \Delta T^{\mathrm{I}}}{T_m}$ for small ΔT, we have[†] :

[†] ΔT^{I} is the undercooling of the interface below T_m (c.f., [53] Eqn. 4.25).

$$-\kappa\gamma = \frac{\rho^s L_f \Delta T^{\mathrm{I}}}{T_m}$$
$$T^{\mathrm{I}} = T_m\Big(1 - \frac{\gamma}{\rho^s L_f}\kappa\Big) \tag{2.46}$$

Eqn. 2.46 is the Gibbs-Thompson expression and it defines the surface tension undercooling. Follow Mullins' treatment [54] on anisotropic surface energy density in 2D $\gamma = \gamma(\theta)$ where $\theta = \tan^{-1}(-h_x)$, we obtain

$$\lambda = -\kappa(\gamma + \gamma_{\theta\theta}) \tag{2.47}$$

and therefore the interface temperature for curved interface $h(x)$ with anisotropic surface energy is:

$$T^{\mathrm{I}} = T_m\Big(1 - \frac{\gamma + \gamma_{\theta\theta}}{\rho^s L_f}\kappa\Big) \tag{2.48}$$

2.3.3 Capillarity vector

The $\vec{\xi}$ vector, more formally known as the capillarity vector was introduced by Gibbs and its properties were developed by Hoffman and Cahn to suit anisotropy applications for planar interface [55] and for curved interface [56]. It is used to extend the anisotropic surface energy which is dependent on Cartesian coordinates due to the normalisation $\sqrt{n_x^2 + n_y^2 + n_z^2} = 1$ of the unit normal $\vec{n} = \vec{N}/|\vec{N}|$ [57].

$$\vec{\xi} := \nabla_{\vec{N}}\Big(|\vec{N}|\gamma(\vec{n})\Big) = \nabla_{\vec{N}}\,\gamma(\vec{N}) \tag{2.49}$$

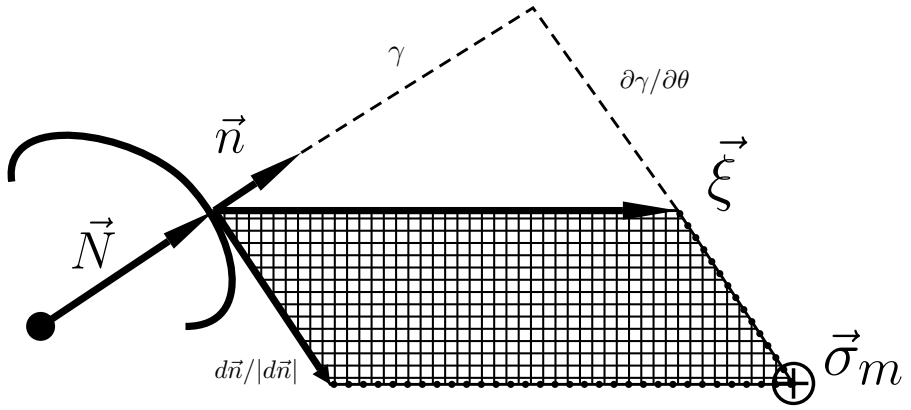

Figure 2.11: Force $\vec{\xi}$ and torque $\vec{\sigma}_m$ acting on a surface element with the shaded area dA and orientation $\vec{n}$.

It has a normal component $\xi_n = \gamma\vec{n}$ describing the expansion or contraction and a tangential component $\xi_t = (^{\partial\gamma}/_{\partial\theta})_{max}\,\hat{t}_0$ denoting the tendency of rotation to minimise the free energy. Unit vector $\hat{t}_0$ lies in the plane normal to $\vec{n}$ and points to the direction with maximum changing in γ with respect to the polar angle $\theta = atan(^{n_y}/_{n_x})$. This is illustrated in Fig. 2.11.

Following the definition of $\vec{\xi}$ and its properties, Cahn and Hoffman derived the expression for the work done $\delta(\gamma dA)$ to the incremental deflection $\delta(d\vec{A})$ by the force $\vec{\xi}$ that resembles the

classical form of external work required to change shape of the surface by effects of expansion or contraction combined with rotation $\delta(\gamma dA) = \vec{\xi} \cdot \delta(d\vec{A})$ [55]. Torque per unit length $\hat{l}$ can also be expressed as $\vec{\sigma}_m = \vec{\xi} \times \hat{l}$ for the representation of moment acting on the surface edges [56]. The effects on the surface are all encoded in $\vec{\xi}$ as its two components. The component of rotation ξ_t is zero in the case of isotropic surface energy leaving only ξ_n in the normal direction of magnitude γ. Similar to mean curvature $\kappa = \nabla \cdot \vec{n}$, the weighted mean curvature κ_γ is defined as $\kappa_\gamma := \nabla \cdot \vec{\xi}$ which embodies the crystallographic anisotropy together with the geometric property of the surface. Moreover the rate of change in total surface energy can be written succinctly by the use of divergence theorem and Reynolds transport theorem as:

$$\begin{aligned}
\boxed{\frac{d}{dt}\int_{h(t)} \gamma(\vec{n}) dA} &= \frac{d}{dt}\int_{h(t)} \vec{\xi}(\vec{n}) \cdot \vec{n} dA \\
&= \frac{d}{dt}\int_{V_+(t)} \nabla_s \cdot \vec{\xi} dV \\
&= \frac{d}{dt}\int_{\Omega_+(t)} \nabla_s \cdot \vec{\xi} \cdot h dA \\
&= \int_{\Omega_+(t)} \frac{\partial}{\partial t}(\nabla_s \cdot \vec{\xi} \cdot h) dA \\
&= \int_{h(t)} \nabla_s \cdot \vec{\xi} \cdot v_n dA \\
\boxed{= \int_{h(t)} \kappa_\gamma \cdot v_n dA}
\end{aligned} \tag{2.50}$$

This formulation of the anisotropic mean curvature will suit particularly well with calculations of the asymptotics of a diffuse interface model incorporating anisotropy in the gradient energy coefficient term [58], as well as defining anisotropy in the approximating of a sharp interface model using parametric finite element method [59, 60]. The ξ-vector also appears ubiquitously in the formalisms of phase field models for energy minimising calculations [58, 61, 62, 63].

2.3.4 Equilibrium crystal shapes

The ξ-vector formalism reviewed in Sec. 2.3.3 is convenient in linking a given γ-function to a specific Wulff shape W, in particular the ξ-vector traces W and it can be analytically expressed in terms of the vector derivatives of γ. This section demonstrates this relationship with examples.

For a toy-type anisotropy γ-function with constants γ_0 and γ_4 that controls the magnitude and strength of the anisotropy of γ respectively* is plotted in Fig. 2.12a:

$$\gamma(\vec{N}) = N\gamma_0 + \frac{\gamma_4}{N^3}\sum_{d=1}^{3} N_d^4 \tag{2.51}$$

The ξ-vector is defined as the gradient of $\gamma(\vec{N})$ in the $\vec{N}$-space:

*It is convenient to parameterise γ in terms of normal vector $\vec{N}$ rather than the unit normal $\vec{n}$ for taking the gradient in of γ in $\vec{N}$-space.

$$\nabla_{\vec{N}}\gamma(\vec{N}) = \vec{n}\gamma(\vec{n}) + 4\gamma_4\left[(n_x^3\vec{i} + n_y^3\vec{j} + n_z^3\vec{k}) - \vec{n}(n_x^4 + n_y^4 + n_z^4)\right] \tag{2.52}$$

For a big enough γ_4 value the ξ-plot develops the so-called 'ears' and 'flaps' as shown in Fig. 2.12b. These features correspond to the missing orientations on the Wulff shape.

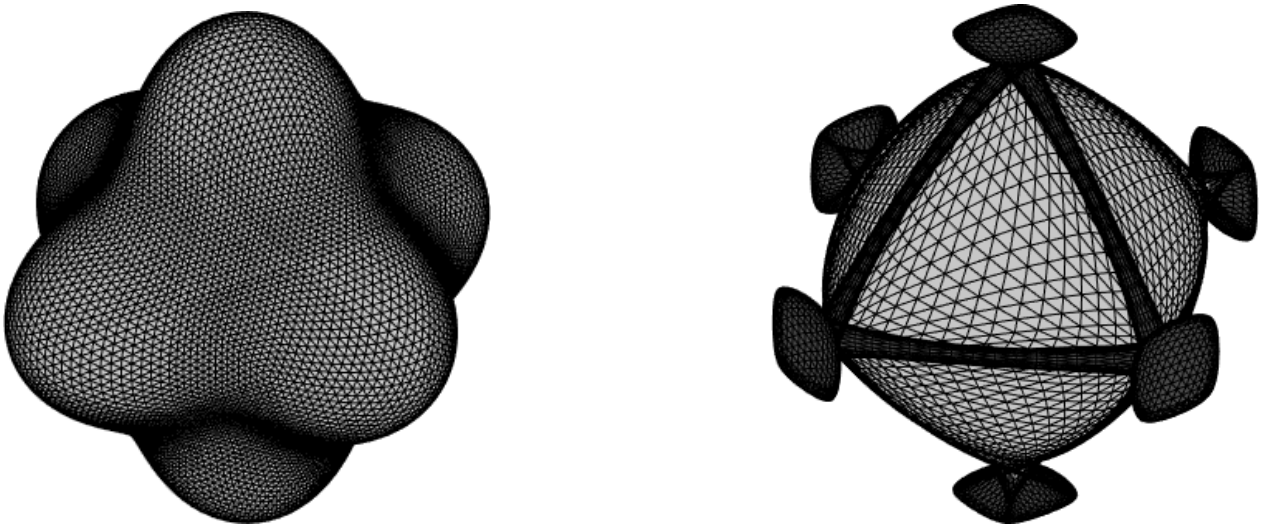

(a) (b)

Figure 2.12: (a) γ-plot and (b) the corresponding ξ-plot (with 'ears' and 'flaps' coloured black) of a toy-type anisotropy with constants $\gamma_0 = 1$ and $\gamma_4 = 1.2$.

The missing orientations can be identified on a $1/\gamma$-plot (Fig. 2.13a) using a well-known criterion given by Sekerka [64]. It follows that the remaining orientations on a convexified ξ-plot correspond to the Wulff shape as plotted in Fig. 2.13b.

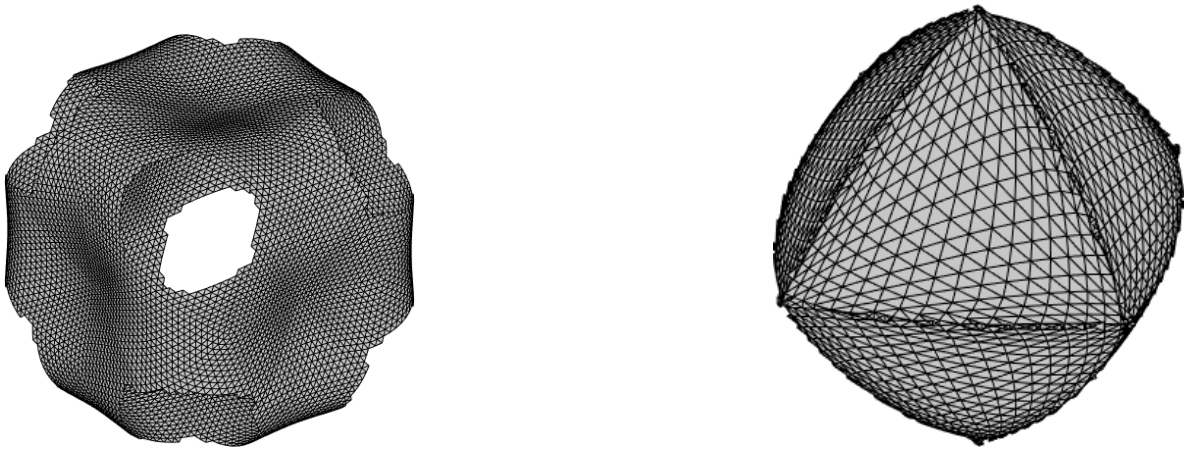

(a) (b)

Figure 2.13: (a) The missing orientations shown on a $1/\gamma$-plot and (b) the corresponding convexified ξ-plot consisted of the remaining orientations, which gives the Wulff shape.

2.4 Thin film theories

2.4.1 Epitaxial growth morphologies

Epitaxially films are single-crystal thin films deposited usually in an ultra-high vacuum with the whole film being a single crystal. Because of the single-crystal characteristics, the epitaxial thin films develop different growth morphologies that can be explained by a simple energetics argument: the surface excess Gibbs free energy ΔG is minimised in equilibrium conditions. Considering only equilibrium thermodynamics, i.e. excluding the kinetics, surface energy of the substrate $E_{substrate}$[†] can differ from the combined surface energy of the film E_{film} and the interface $E_{interface}$. Different mechanisms of growth are therefore followed. For $E_{substrate} > E_{film} + E_{interface}$, a full contact of wetting adlayers is favoured. This results in an atomically flat surface and is called the Frank-van der Merwe mode or the layer-by-layer deposition as illustrated in Fig. 2.14a.

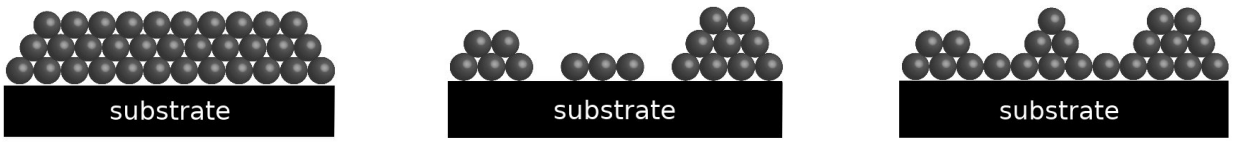

(a) (b) (c)

Figure 2.14: Different modes of thin film formation: (a) Frank-van der Merwe mode, (b) Volmer-Weber mode and (c) Stranski-Krastanov mode.

As shown in Fig. 2.14b when $E_{substrate} < E_{film} + E_{interface}$, islands are formed and this is known as the Volmer-Weber mode, in which the system favours less contact between adsorbate and substrate. In addition, for the island/non-wetting mode, elastic strain is induced by the lattice mismatch for heterogeneous nucleation. The lattice misfit is a function of the lattice constants of two materials from which the elastic strain can be calculated. Droplet-like islands are formed due to the relaxation of the elastic strain. Fig. 2.14c shows the interpolation, the Stranski-Krastanov mode which is a combination of aforementioned two distinct types. The driving force for all these three modes is the minimisation of ΔG of the system.

2.4.2 Texturing in polycrystalline thin films

The simple picture depicted by the energetics argument above assumes equilibrium or near equilibrium conditions. For thin films deposited in conditions far from equilibrium, the growth mechanism and the resulting film structure are independent of the nature of the substrate which result in either amorphous or polycrystalline thin films. The growth morphologies can be vastly different depending on the deposition conditions and here the polycrystalline thin films grown in low pressure is reviwed. A texture is developed as a result of two competing effects, i.e. surface diffusion and preferential deposition. The famous van der Drift theory of texture formation [65] gives a simplistic survival-of-the-fittest guideline of the texture selection during the film deposition: the crystallites with the fastest growth direction perpendicular to the substrate outgrow the neighbouring grains through grain boundary impingement, hence dominate the film thickness and define the texture. The terminating planes are determined by the crystal growth habit. However it is much more complicated to determine the fastest growth

[†] $E_{substrate}$ and E_{film} are the excess energies of an interface between vapour phase and the solid specified by the subscripts.

direction of a faceted single crystal when subject to two competing effects of surface diffusion and preferential deposition, besides the effect of grain boundary impingement. To simplify the problem van der Drift discussed some deposition scenarios, and all the limiting cases in which the film morphologies can be distinguished. These are summarised below with references to existing modelling works that use similar assumptions.

i) infinite surface diffusion even along the substrate
The film evolution follows the 'survival of the fittest' and an out-of-plane texture is formed. The selection mechanism is dependent on the grain boundary impingement. The resulting film morphology was shown by means of geometric simulation in [65], shown in Fig. 2.15. Assuming that when the grains meet they consume each other, tetragonal systems with the ratio of lattice parameters $\frac{c}{a} < \sqrt{2}$ result in a $\langle 110 \rangle$ fibre textured polycrystalline thin film.

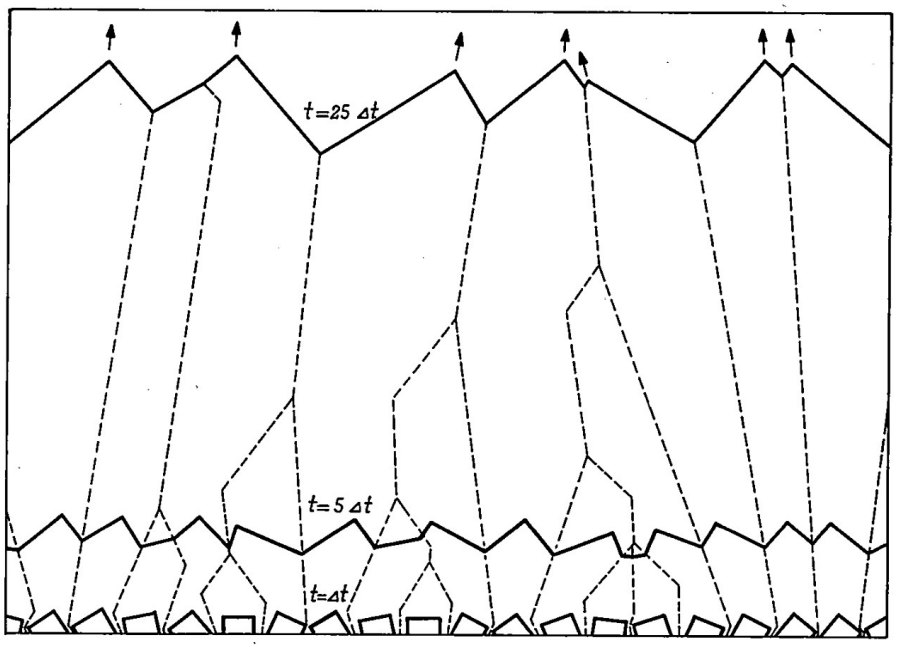

Figure 2.15: In this geomotric simulation van der Drift considered randomly oriented seeds with cubic symmetry and they evolve according to scenario i. At late stage of growth ($t = 25\Delta t$), the grains with the fastest growth direction (corner pointing direction) nearly perpendicular to the substrate survive.

ii) infinite surface diffusion, but restricted to the individual crystals
This is similar to case (i) but with a different grain impingement mechanism as when the grain boundaries meet they do not consume into each other. Existing models incorporating infinite surface diffusion result in fully morphologies with no inter-columnar voids formed (zero porosity) [66, 67].

iii) infinite surface diffusion, but restricted to the individual crystal faces
Now each facet on the single crystallites collects its own adparticles and there is a barrier for the adparticles to diffuse across the edges and corners. As a consequence, the shadowing plays a big role here in the morphological development because of this limited case

of surface diffusion. The barrier can be related to an atomistic effect called 3-D Ehrlich-Schwoebel barrier which is the energy barrier for the surface diffusion across two facets associated with different surface energies [68].

iv) no surface diffusion
Under this assumption the surface evolves according to Huygens' principle for an advancing wave front subject to the preferential depositing due to shadowing [69]. The faceted shape is lost and texture is not developed assuming nucleation of grains with random orientation.

v) finite surface diffusion
Adparticles incorporated into the material interface have different mobility, depending on the crystallographic orientation of the interface. The anisotropy in surface energies plays a central role in the surface diffusion. For a realistic material deposited under complex flux, the resulting morphology is elusive to predict. Very few study has considered this growth scenario.

2.4.3 Structural zone model

The limiting cases of the interplay between two competing mechanisms, i.e. surface diffusion and deposition result in three different texturing regimes for the polycrystalline thin films. For random (no preferred orientation) and fibre textures (only one preferred orientation), and assuming directional flux, empirical models have been developed as an indication of what film morphology may result for a given set of deposition rate and temperature. These sophisticated qualitative models (e.g. [70, 71, 72, 73, 74]) use similar but inconsistent terminologies for the resulting microstructures and film morphologies called zones. The control parameters taken into account in these models are not only specific to the materials (e.g., metals and metal oxides) but also the process, such as the target-to-substrate distance and adparticle energy in sputter deposition. However there are parameters that are universal among all the thin films and deposition techniques, i.e. pressure and the homologous temperature. Under low pressure there are four distinct zones which are characterised by adparticle mobility:

I) At low homologous temperature the adparticle mobility is limited so that the competitive growth does not take place, and randomly oriented or even amorphous grains are formed.

II) Analogous to case (i) of the van der Drift's model, at high temperature the adparticle mobility allows the facets to form edges and corners which are each associated with a speed and a direction. The grains undertake competitive growth and the result is a fiber textured, polycrystalline thin film that is determined by the minimal energy planes of the crystal (i.e. crystal growth habit).

III) At very high temperature the bulk diffusion occurs and results in equiaxed grains.

T) A transition between zone I and II in which the shadowing becomes influential and takes part in the orientation selection. A fibre texture is formed but different from that of zone II because of the effect of shadowing.

Mahieu et al. [75] modified the idea in a more detailed extended structural zone model and to include the biaxially textured thin films (two preferred orientations). Their explanation of the in-plane orientation selection is akin to the survival-of-the-fittest type argument and they have not considered the case (v) with finite surface diffusion with the lack of grain boundary impingement.

3. Existing modelling methods

3.1 Modelling strategies

Modelling and simulation work have been done in different areas of structure evolution for a single-phase polycrystalline material, such as crystallisation, grain boundary migration [76], polycrystalline growth [66, 67] and solidification [77, 78, 79, 80]. These mesoscale models gave insight into the collective behaviour of the polycrystalline thin film that a microscopic model is not capable of, hence the studies of micron-sized multi-grain structure by means of computer simulation are possible. On the other hand, a typical atomistic molecular dynamics (MD) model for instance has time step of the order $10^{-9}s$ which makes it unrealistic to study even single grain growth. The level-set approach by Smereka et al. [66] and Ophus et al. [67] uses the formulation of kinetic Wulff shape derived from geometric arguments [81] and fast level-set algorithms. But it assumes velocity limited growth, spatially and temporally uniform impingement that are not the case for CVD. In CVD there are a number of atomic processes taking place at different rates in the vicinity of substrate accompanied by chemical reactions and composition changes. Furthermore, material-specific anisotropy is not accounted for in these mesoscale models. A Monte Carlo (MC) modelling technique [82] on the other hand incorporates different reactions at different rates and has the advantages to work on both mesoscale and atomic scale and to tackle material-specific systems.

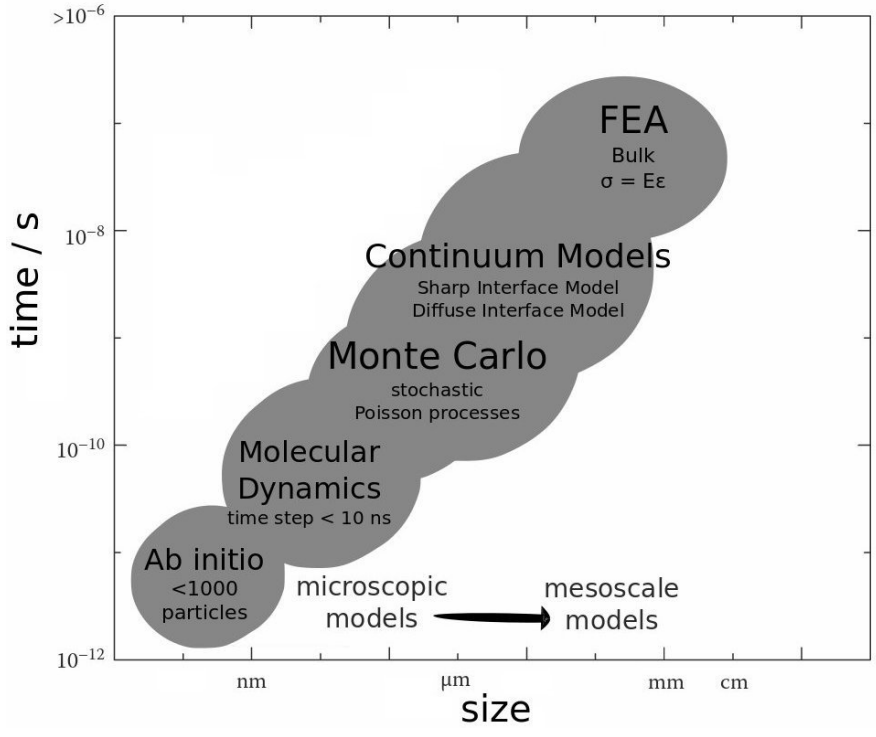

Figure 3.1: Time and length scales of various modelling methodologies.

In a review paper by Atkinson [83] numerical models are classified as statistical, probabilistic and deterministic. The continuum models using level-set method and phase-field method feature the evolution equations for the kinetics and hence are the latter. Atomistic models using MC [84, 85] are probabilistic which means the equations do not depict the kinetics exactly but the probability of various events that lead to the kinetics. The time scale and length scale of the aforementioned models as well as ab initio, MD and finite element analysis (FEA) are shown in Fig. 3.1. The boundary of these modelling techniques are approximate and they overlap. MC particularly has the potential of expanding into both microscopic and mesoscopic scales to model not only the surface layers but also multiple grains and grain boundaries [86].

For thin film systems such as the vapour-deposited anatase-TiO_2 and the OAD-grown MgO films the dimensions of the features of the thin film morphologies range from 10 nm to several micros and are of several orders of magnitude larger than the lattice spacing. In such applications it is appropriate to choose continuum models.

3.2 Sharp interface models

In the sharp interface models the velocity of the interface front is explicitly specified as opposed to the diffuse interface model which is based on variational methods that approximates this interface motion. Furthermore the interface is considered sharp because the location of which is known and the thickness of which is zero. As seen in Sec. 2.1, accompanying the front velocity there are usually descriptions of an external field that provides the driving force to the front velocity. The external field can either be a heat or a concentration field subject to diffusion, or a concentration field that is being advected at some speed, depending on the physics of transport. The gradient of the field at the interface which gives the flux onto the interface, gives rise to the driving force.

3.2.1 Near-equilibrium conditions and growth

The equilibrium shape of a vapour grown crystal under near-equilibrium conditions can be determined analytically by the famous Wulff construction for which the computation is straightforward. However it is often desirable to model also the kinetics of the near-equilibrium growth. In Section 2.1 the classical ideas of phase transition involving a moving boundary were described in terms of solid-liquid system in which heat diffusion is the rate limiting step. Now consider a solid-vapour system having a number density field c in addition to the temperature field. Apart from particle diffusion in the vapour phase there are adsorption, desorption and diffusion taking place on the surface. If these surface reactions contributing to growth of the interface at speed v_n into V^v happen at a timescale τ_g much bigger than particle diffusion timescale τ_d (i.e. $\tau_d << \tau_g$) then c has sufficient time to relax to steady state value, that is

$$\nabla^2 c = 0 \qquad \text{in } V^v(t) \tag{3.1}$$

Because of the quasi-steady state diffusion, the vapour can be thought of as an ideal gas and therefore the Maxwell–Boltzmann distribution f_v applies:

$$f_v(\vec{v}) = \Big(\frac{m}{2\pi k_B T}\Big)^{3/2} \exp\Big(-\frac{m\vec{v}\cdot\vec{v}}{2k_B T}\Big) \tag{3.2}$$

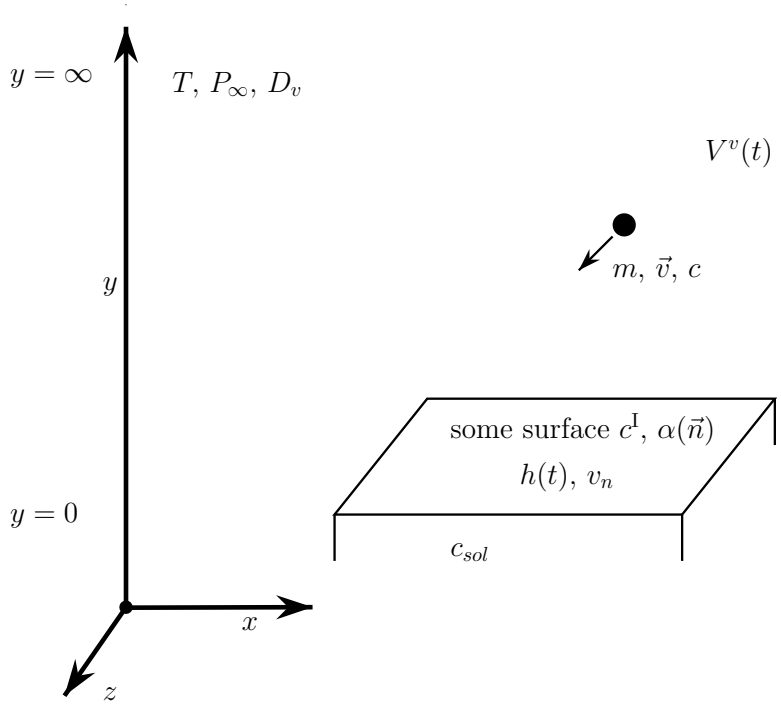

Figure 3.2: A sketch of a single gas-phase particle with velocity $\vec{v}$ that is representative of vapour of number density c.

Integrating along the -z axis from negative infinity to 0 (Fig. 3.2) where the surface locates we get the mean velocity of a molecule incident on a surface

$$\bar{v}_{-z} = \int_{-\infty}^{\infty} dv_x \int_{-\infty}^{\infty} dv_y \int_{-\infty}^{0} dv_z \cdot |v_z| f_v(\vec{v}) = \sqrt{\frac{k_B T}{2\pi m}} \tag{3.3}$$

The Hertz-Knudsen formula Eqn. 3.4 equating the rate of impingement normal to the surface (in terms of number per area N_A) to processing (ambient) temperature and pressure, is obtained by using the relationship for an ideal gas

$$N_v = \frac{N}{V} = \frac{P_\infty}{k_B T}$$

$$\frac{dN_A}{dt} = \bar{v}_{-z} \cdot N_v = \frac{P_\infty}{\sqrt{2\pi m k_B T}} \tag{3.4}$$

where the subscript ∞ indicates the processing parameter far from the interface. The vapour flux is uniform along the same facet [87] and the molecular incorporation mechanisms for crystallographically distinct facets are different due to surface processes [88]. Thus the final ingredient of the near-equilibrium growth can be expressed as the mass balance at the interface involving the diffusive flux:

$$D_v \nabla c \cdot \vec{n} = \alpha_i \frac{P_\infty}{\sqrt{2\pi m k_B T}} \qquad \text{on } h(t) \tag{3.5}$$

in which the symbol α_i represents the sticking coefficient of ith facet. This relationship requires that the incoming vapour flux at the interface is equal to the rate of molecular incorporation due to kinetics at the surface. α_i can be generalised to include all the missing orientations $\alpha_n = \alpha_n(\vec{n})$ and the normal velocity of the growing front can be expressed as

$$v_n = \alpha_i \frac{c^{\mathrm{I}} - c_{sat}}{c_{sol}} \cdot \bar{v}_{-z} = \alpha_n(\vec{n}) \frac{c^{\mathrm{I}} - c_{sat}}{c_{sol}} \sqrt{\frac{k_B T}{2\pi m}} \tag{3.6}$$

where $c_{sat}(T)$ is the equilibrium vapour number density above a planar interface and $c_{sol}(T)$ is the solid number density both of which are dependent on temperature.

In a model of ice crystal grown in water vapour [88] the vapour diffusivity for water molecules D_v^{water} is approximated by

$$D_v^{water}(T,P) = 2.0 \times 10^{-5} \sqrt{\frac{T}{T_m}} \frac{P_\infty}{P}$$

which can be experimentally determined for different materials and in the same paper the temperature variations at the surface are taken into consideration. However it is often assumed that for kinetics-limited growth the temperature does not restrict the growth as much as the concentration does [89] for the reason that the thermal conductivity of gas k^g is not comparable to k^s and the surface is thermally conductive. Thus the effect of latent heat is usually ignored and temperature is set to be constant everywhere (isothermal condition). Since the right hand side of Eqn. 3.5 is constant for the facet given a set of (T, P_∞) and molar mass m, it is said to exhibit scaling behaviour, i.e. $v_n = v_n(\vec{n})$.

3.2.2 Non-equilibrium conditions and growth

For the rapid growth scenario especially, when the supersaturation is large in the gas phase, diffusion plays a big role as the species needed for surface reactions have to be transported to the interface through gas and v_n is comparable with mass transport by diffusion. The supersaturation field for a single species is defined as $\sigma = {}^{(c\,-\,c_{sat})}/_{c_{sat}}$. It is also assumed that the heat transport in the gas phase V^v does not restrict the growth as much as the mass transport does (i.e. neglecting the diffusion and jump at the interface due to temperature field). Thus the net effect of the multi-species gas mixture may be characterised in the mesoscale model by the average supersaturation $\tilde{\sigma}$ and hereafter σ is used to denote $\tilde{\sigma}$. Although not much is known about the nature of the chemical reactions in the gas phase and on the surface, the system is modelled by σ which is subject to diffusion in V^v (shown in Fig. 3.3):

$$\dot{\sigma} = D_m \nabla^2 \sigma \qquad \text{in } V^v(t) \tag{3.7}$$

D_m is the diffusion coefficient and it is assumed to be constant, i.e. $D_m \neq D_m(\sigma)$. For $c_{sat} << c_{sol}$ and because of the zero diffusion flux out of the solid $\vec{J}_s = -D_m \nabla c = 0$, we have the mass balance at the interface $(\vec{J}_v - \vec{J}_s) \cdot \vec{n}|_h = (c_{sol} - c_{sat}) v_n \approx (c_{sol}) v_n$. Hence the generalised Stefan condition can be expressed as

$$c_{sol} v_n = D_m \nabla c \cdot \vec{n}|_h = c_{sat} D_m \nabla \sigma \cdot \vec{n}|_h \qquad \text{on } h(t) \tag{3.8}$$

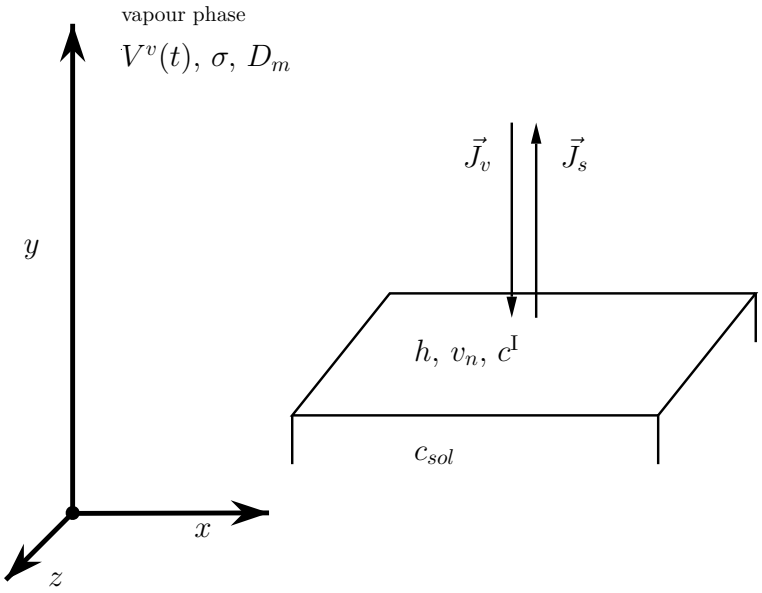

Figure 3.3: A sketch of the vapour phase and some surface.

Moreover if we rearrange Eqn. 3.6 into the form

$$c^{\mathrm{I}} = c_{sat}\left(1 + \frac{v_n c_{sol}}{\bar{v}_{-z}}\right) \tag{3.9}$$

and include the effect similar to surface tension undercooling introduced in Sec. 2.3.2 with $c_{sol}k_BT$ replacing volumetric latent heat $\rho^s L_f$ we get the modified Gibbs-Thomson expression (cf. [89], Eqn. [23])

$$c^{\mathrm{I}} = c_{sat}\left(1 - \frac{\gamma\kappa}{c_{sol}k_BT} + \frac{v_n c_{sol}}{\bar{v}_{-z}}\right) \tag{3.10}$$

It should be stressed here that the surface kinetics depicted in Eqn. 3.9 carries from Sec. 3.2.1 the assumption of ideal gas and thus only an approximation for the non-equilibrium vapour growth. However limitations should be considered in the continuum modelling of surface kinetics due to the fact that the competing processes such as deposition, dissociation, surface diffusion and adsorption/desorption mechanisms are of atomistic nature.

3.2.3 Kinetic Wulff shape and competitive growth

In Sec. 3.2.1 and 3.2.2 growth laws relating the physics of general growth conditions to the normal velocity of an interface v_n are introduced. Assuming that v_n is only dependent on the crystal orientation (as opposed to being controlled by diffusion as discussed by previous sections), a growth law $v_n = v_n(\vec{n})$ compactly models the zone II growth reviewed in Sec. 2.4.3. Analogous to the equilibrium Wulff shape governed by an orientation-dependent surface energy density $\gamma(\vec{n})$ (Sec. 2.3.4), the growth law prescribing a v_n of given orientation (specified by the interface normal $\vec{n}$) results in a growth shape that asymptotically approaches the kinetic Wulff Shape [90]. The kinetic Wulff shape is the inner convex hull of $v_n(\vec{n})$. A well-known geometric model for competitive growth according to the growth law of $v_n(\vec{n})$ is given by Taylor [91], who defined a normal velocity $v_n(\vec{n})$ to be a function of a tangential speed u and a normal speed ω_k to account for the problematic sharp corners that emerge during the growth:

$$v_n(\vec{n}) = \omega_k + u\sqrt{1 - (\vec{n} \cdot \vec{n}_k)^2} \tag{3.11}$$

The index k is determined by finding the closest facet normal, this is equivalent to finding the maximum angle between them where $\vec{n}_j$ denotes each facet normal of the crystal:

$$k = \arg\max_j (\vec{n} \cdot \vec{n}_j) \tag{3.12}$$

Under this growth law the texture formation happens upon **grain boundary impingement**, in accordance with the case (ii) of the van der Drift model (Sec. 2.4.2). It should be noted that this law does not describe the early stage roughening. A common practice for dealing with the early-time growth in these geometric models is to seed the substrate (see Fig. 3.4a), which ignores the nucleation. However the late stage morphology is well described by this model given that $v_n(\vec{n})$ is independent of time, i.e. as long as scaling behaviour holds. An example can be found in modelling the polycrystalline thin film growth with near-equilibrium conditions. In a study by Smereka [92], faceted crystals having random orientations are seeded at the beginning of the simulation and are allowed to evolve according to Eqn. 3.11 and 3.12. As shown in Fig. 3.4b the resulting fibre textured microstructure is governed by competitive growth in which the crystallites (coloured by blue in the figure) with orientations corresponding the fastest growth direction perpendicular to the substrate, outgrow others and define the texture.

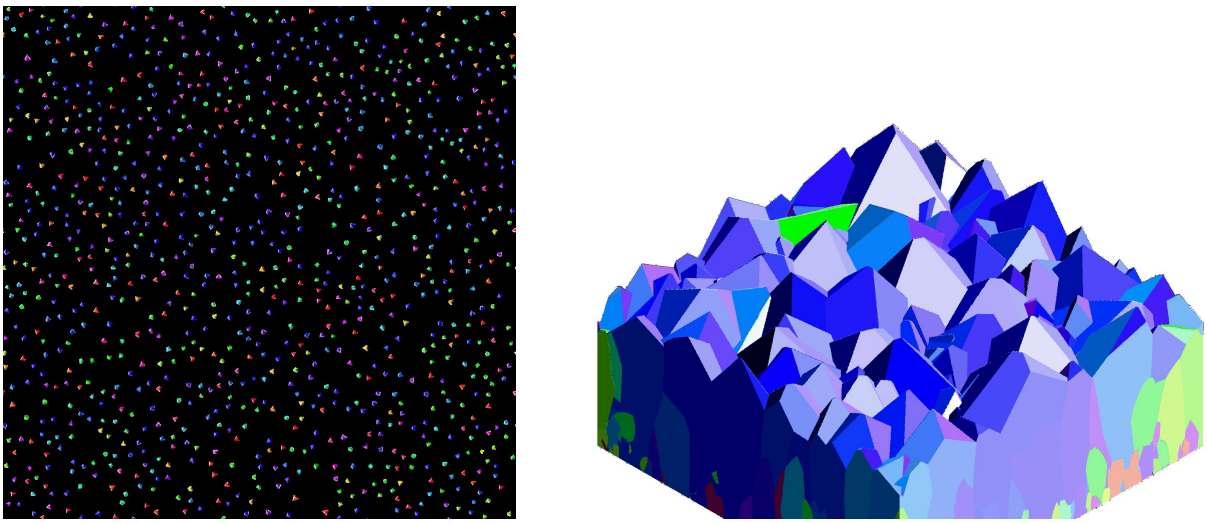

(a) (b)

Figure 3.4: Growth of polycrystalline thin film under near-equilibrium conditions reproduced from [92, 93, 67]. Top view of the seeding of crystallites with different colours representing different orientations (b) the side view of the late stage morphology.

Comparison can be made between this fully faceted, densely packed surface morphology and the one exhibited by anatase-TiO_2 nanocolumns (e.g. Fig. 1.7) or the biaxially textured nanocolumns (e.g. Fig. 1.2c). This simple geometric model cannot be used to describe the morphological development during the low-pressure deposition of nanocolumns, for which the growth of the interface does not solely depend on the orientation of the crystallite.

3.2.4 Surface diffusion

In Sec. 2.3.2 the driving force of the normal velocity v_n is attributed to the Stefan condition which requires the knowledge of the interface temperature. For a curved interface the interface temperature is dependent on the mean curvature (Eqn. 2.48). The formulation of the moving boundary problem in Sec. 2.3.2 is essentially the sharp interface description of motion by mean curvature[†]. For surface diffusion with isotropic surface energy the sharp interface model results in the volume/area-preserving mean curvature flow[‡] and in the case of surface diffusion with highly anisotropic surface energy in 2D,

$$v_n = \frac{\delta \int_s \gamma(\vec{\theta}) ds}{\delta s} = \nabla_s^2 \Big[M\big(\gamma + \gamma_{\theta\theta}\big)\kappa \Big] \tag{3.13}$$

where ∇_s^2 is the surface Laplacian, M the mobility of the flow and κ the mean curvature. When γ is strongly anisotropic the evolution of Eqn. 3.13 becomes unstable. In [94, 95] a regularised surface diffusion system $v_n = \dfrac{\delta \int_s \gamma + \frac{\tilde{\beta}}{2}\kappa^2 ds}{\delta s}$ is proposed which leads to

$$v_n = \nabla_s^2 M \left(\kappa_\gamma + \tilde{\beta} \left(\nabla_s^2 \kappa + \frac{1}{2}\kappa^3 - 2\kappa K \right) \right) \tag{3.14}$$

where $\tilde{\beta} > 0$ is a constant, $\kappa_\gamma = \nabla \cdot \vec{\xi}$ the weighted mean curvature and K is the Gaussian curvature. This notorious sixth-order sharp-interface evolution law poses severe numerical problems due to the moving meshes [95]. In Sec. 3.3.8 a phase field approximation will be reviewed which alleviates the problems greatly.

3.3 Diffuse interface models

3.3.1 Free energy functional

For a thermodynamic system held in constant temperature T that is free to exchange energy with a thermal reservoir, the entropy S and total energy U are no longer at their maximum and minimum in equilibrium as in an isolated system. The energy being minimised in the system under such isothermal condition is a certain type of free energy and in this specific case the Helmholtz Free Energy. The Helmholtz free energy $\mathcal{F}$ is the Legendre transform of U with respect to T:

$$\mathcal{F} \equiv U - TS \tag{3.15}$$

which is minimised in thermal equilibrium for a phase with phase field parameter ϕ, volume V and Helmholtz free energy density f:

$$\mathcal{F} = \int f(\phi) dV \tag{3.16}$$

[†]which can be seen later in the diffuse interface models as the $\mathcal{L}^2$ gradient flow of the corresponding free energy (e.g. Eqn. 3.29).

[‡]$\mathcal{H}^{-1}$ gradient flow of the corresponding free energy as in the diffuse interface models (e.g. Eqn. 3.32).

In general, ϕ can be any order parameter that changes across the interface: $\phi = \phi(x)$ in 1D. In the previous section ϕ is discontinuous across the interface while in diffuse interface model ϕ is a continuous function of x that takes constant value in the bulk phases and varies continuously across the interface.

3.3.2 Continuous spatial variation

In equation 3.16 it is seen that the value of $\mathcal{F}$ does not change in the bulk phases because of the atoms deep in the material have exactly the same neighbours, i.e. ϕ is identical at every point. But at the interface the neighbours are no longer of the same kind due to the compositional or structureal differences depending on the nature of the interface, so a correction is needed to include this finite atomic range interaction at the interface. Van der Waals' idea was that the free energy $\mathcal{F}$ is also dependent on the gradient of the order parameter ϕ such that this local gradient effect only takes place at the interface. Therefore an additional term was introduced that has only non-zero value at the interface, as shown below the ϵ is a coefficient and the square makes this change in ϕ always increase the free energy. For materials with isotropic surface energy, e.g. fluids or amorphous materials:

$$\mathcal{F} = \int \left[f(\phi) + \frac{1}{2}(\epsilon \nabla \phi)^2 \right] dV \tag{3.17}$$

To include anisotropy in gradient energy one of the conventional way is to add a $\nabla\phi$ dependent term:

$$\mathcal{F} = \int \left[f(\phi) + \frac{\epsilon^2}{2}\Gamma^2(\nabla \phi) \right] dV \tag{3.18}$$

where ϵ is the gradient energy coefficient and the function $\Gamma(\nabla\phi)$ contains the anisotropy of the excess surface free energy. To get the variational derivative or the functional derivative of $\mathcal{F}$ in Equation 3.17 for 1-D problem and no anisotropy, a more general case is first considered:

$$\mathcal{F} = \int_{x_0}^{x_1} F(x, \phi(x), \phi') dx \tag{3.19}$$

where $F(x, \phi(x), \phi') = [f(\phi) + {}^1\!/_2(\epsilon\phi')^2]$. x_0 and x_1 denote respectively $x|_{\phi=0}$ and $x|_{\phi=1}$ for values of x in the bulk. The prime notation denotes the derivative with respect to x, for instance $\phi' = {}^{d\phi}\!/_{dx}$. A family of comparison functions is constructed: $\Phi = \phi(x) + \xi\psi(x)$, such that $\psi(x_0) = \psi(x_1) = 0$. By replacing ϕ and ϕ' in Eqn. 3.19 by Φ and $\Phi' = \phi'(x) + \xi\psi'(x)$ respectively. $\mathcal{F}$ is a function of parameter ξ so that $\xi = 0$ minimises the functional $\mathcal{F}$:

$$\mathcal{F}(\xi) = \int_{x_0}^{x_1} F(x, \Phi(x), \Phi') dx \tag{3.20}$$

$$\frac{d\mathcal{F}}{d\xi} = \int_{x_0}^{x_1} \left(\frac{\partial F}{\partial \Phi}\frac{\partial \Phi}{\partial \xi} + \frac{\partial F}{\partial \Phi'}\frac{\partial \Phi'}{\partial \xi} \right) dx = \int_{x_0}^{x_1} \left(\frac{\partial F}{\partial \Phi}\psi + \frac{\partial F}{\partial \Phi'}\psi' \right) dx \tag{3.21}$$

setting ξ to zero $\iff$ replacing (Φ, Φ') by (ϕ, ϕ')

$$\begin{aligned}\mathcal{F}'(0) &= \int_{x_0}^{x_1} \left(\frac{\partial F}{\partial \phi}\psi + \frac{\partial F}{\partial \phi'}\psi'\right) dx \\ &= \frac{\partial F}{\partial \phi'}\psi\Big|_{x_0}^{x_1} + \int_{x_0}^{x_1} \left[\frac{\partial F}{\partial \phi} - \frac{d}{dx}\left(\frac{\partial F}{\partial \phi'}\right)\right]\psi dx \\ &= \int_{x_0}^{x_1} \left[\frac{\partial F}{\partial \phi} - \frac{d}{dx}\left(\frac{\partial F}{\partial \phi'}\right)\right]\psi dx\end{aligned}$$

As the choice of $\psi(x)$ is arbitrary, this can only be obtained when

$$\int_{x_0}^{x_1} \left[\frac{\partial F}{\partial \phi} - \frac{d}{dx}\left(\frac{\partial F}{\partial \phi'}\right)\right]\psi dx = 0 \qquad \Longleftrightarrow \qquad \frac{\partial F}{\partial \phi} - \frac{d}{dx}\left(\frac{\partial F}{\partial \phi'}\right) = 0 \tag{3.22}$$

$$\text{assuming } F = f(\phi) + \frac{1}{2}(\epsilon\phi')^2 \Rightarrow \tag{3.23}$$

$$\frac{\partial\left[f(\phi) + \frac{1}{2}(\epsilon\phi')^2\right]}{\partial \phi} - \frac{d}{dx}\left(\frac{\partial\left[f(\phi) + \frac{1}{2}(\epsilon\phi')^2\right]}{\partial \phi'}\right) = 0$$

$$\frac{\partial f(\phi)}{\partial \phi} - \epsilon^2\phi'' = 0 \tag{3.24}$$

Eqn. 3.24 is the Euler-Lagrange equation. Moreover, in equilibrium the variational derivative also equals to zero and therefore

$$\frac{\delta \mathcal{F}}{\delta \phi} = \frac{\partial f(\phi)}{\partial \phi} - \epsilon^2\nabla^2\phi = 0 \tag{3.25}$$

3.3.3 Diffuse interface profile

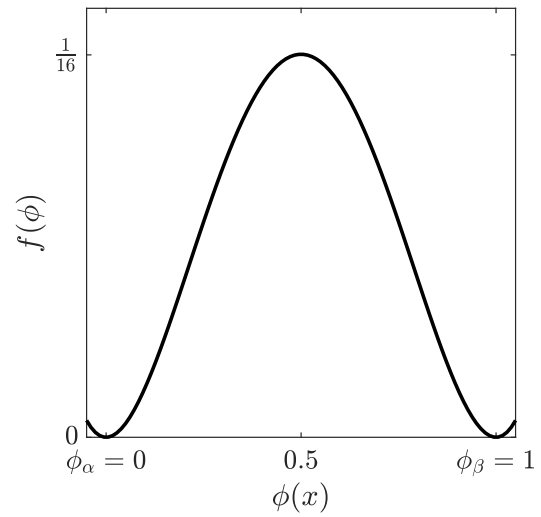

Figure 3.5: Double-well free energy density function with values $\phi = 0$ and $\phi = 1$ in phase α and β by convention.

As plotted in Fig. 3.5 a simple free energy density comprises two phases α, β and an energy barrier $1/16$ W and is of the form $f(\phi) = W\phi^2(1-\phi)^2$ [80]. The solution for this 1-D diffuse interface in terms of order the order parameter ϕ as a function of position x to the interface location where $\phi = 0.5$ requires the expansion of the total derivative of $F(\phi, \phi')$ with respect to x:

$$\begin{aligned} \frac{dF}{dx} &= \frac{\partial F}{\partial \phi}\frac{\partial \phi}{\partial x} + \frac{\partial F}{\partial \phi'}\frac{\partial \phi'}{\partial x} \\ \frac{dF}{dx} &= \frac{\partial F}{\partial \phi}\phi' + \frac{\partial F}{\partial \phi'}\phi'' \end{aligned} \tag{3.26}$$

Substituting the identity Eqn. 3.22

$$\frac{\partial F}{\partial \phi} = \frac{d}{dx}\left(\frac{\partial F}{\partial \phi'}\right)$$

into Eqn. 3.26 we get

$$\begin{aligned} \frac{dF}{dx} &= \frac{d}{dx}\left(\frac{\partial F}{\partial \phi'}\right)\phi' + \frac{\partial F}{\partial \phi'}\frac{d}{dx}(\phi') \\ \frac{dF}{dx} &= \frac{d}{dx}\left(\frac{\partial F}{\partial \phi'}\phi'\right) \\ \int dF &= \int d\left(\frac{\partial F}{\partial \phi'}\phi'\right) \end{aligned}$$

$$\Downarrow$$

$$F - \frac{\partial F}{\partial \phi'}\phi' = C_1$$

$$\begin{aligned} f(\phi) + \tfrac{1}{2}\epsilon^2(\phi')^2 - \left(\tfrac{1}{2}\cdot 2\cdot \epsilon^2\phi'\right)\phi' &= C_1 \\ f(\phi) &= \frac{1}{2}\epsilon^2\left(\frac{d\phi}{dx}\right)^2 + C_1 \\ \tfrac{\sqrt{2W}}{\epsilon}dx &= \frac{d\phi}{\phi(1-\phi)} + C_1 \\ \int \tfrac{\sqrt{2W}}{\epsilon}dx &= -2\int \frac{d\phi}{1-(1-2\phi)^2} \end{aligned}$$

Integrate both sides and use the fact that the derivative of a inverse hyperbolic tangent $\tanh^{-1}(\phi)$ is $1/(1-\phi)$, we then have

$$\tfrac{\sqrt{2W}}{\epsilon}x = -2\tanh^{-1}(1-2\phi) + C_2 \tag{3.27}$$

at interface $x = 0$, $\phi = 0.5 \quad \Longrightarrow \quad C_2 = 0$.

$$\phi(x) = \frac{1}{2}\left[1 + \tanh\left(\frac{x}{2l}\right)\right] \tag{3.28}$$

where $l = \epsilon/\sqrt{2W}$ determines the length scale of the width of the interface, both C_1 and C_2 are integration constants and that the double well potential of the form $f(\phi) = W\phi^2(1-\phi)^2$ is used. The integral of Eqn. 3.28 gives the interfacial energy $\gamma = \epsilon\sqrt{2W}/6$ in terms of gradient energy coefficient ϵ. This planar solution of Eqn. 3.25 is drawn in Fig. 3.6. It is a trade-off between the free energy density in the bulk of two phases that admits a discontinuous change in order to minimise $\mathcal{F}$ in Eqn. 3.17.

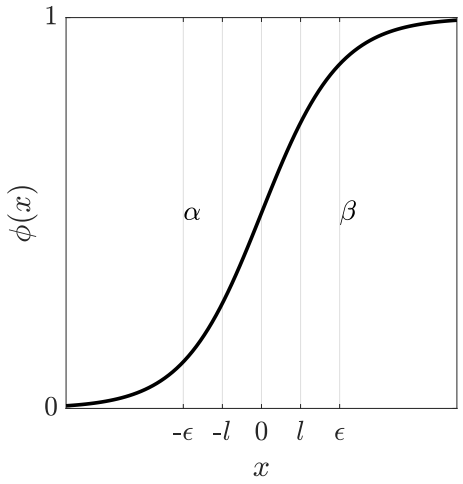

Figure 3.6: The exact solution of 1-D diffuse interface Eqn. 3.28 between phase α and β

3.3.4 Physical meaning of the phase-field parameter

The phase-field parameter ϕ in the diffuse interface model is an order paramter which varies in different phases. The physical representations of the underlying material properties can be interpreted as crystallinity [96]. $\phi = 1$, for example, represents that the probability of finding atoms on a specific lattice sites is 1, i.e. in the bulk phase of a crystalline solid. The localisation of atoms in solid is periodic in space, and a sinusoidal profile for simple crystals is expected as we move from solid to liquid, damped in the interfacial region and disappeared in the liquid where $\phi = 0$. Therefore ϕ in this context is the amplitude of the localisation function. In general the localisation function is a function of position $\vec{r}$ and in the theory of phase field crystal the free energy function is defined in terms of the localisation function [97, 98]. This allows for the incorporation of microscopic details in a continuum formulation. In 1D the localisation function is plotted in Fig. 3.7 with the dotted line representing the amplitude, equivalent to ϕ in a phase field model.

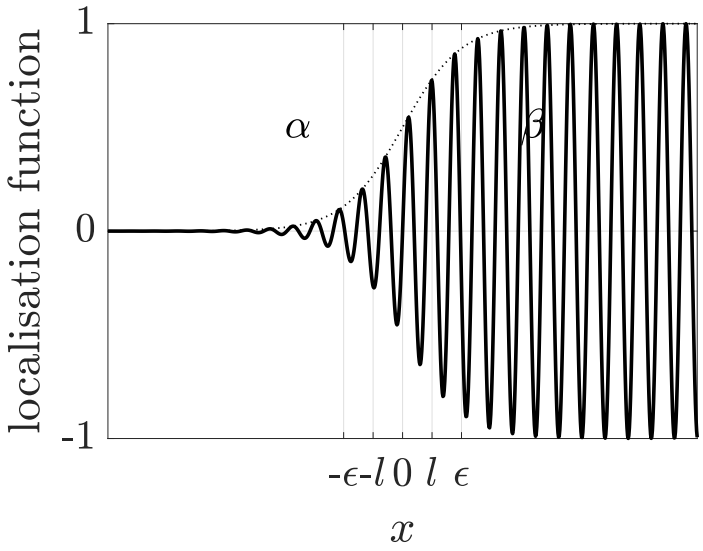

Figure 3.7: Possible physical meaning of ϕ in phase-field method ($\phi = 1$ the crystal phase and $\phi = 0$ the liquid or vapour phase)

3.3.5 Kinetics

Eqn. 3.25 assumes that the system has reached an equilibrium state. When it is in non-equilibrium state the temporal derivative $\partial\phi/\partial t$ must ensure that the total free energy $\mathcal{F}$ always decreases. Assuming a linear relationship and small departure from equilibrium:

$$\frac{\partial \phi}{\partial t} = -M_\phi \frac{\delta \mathcal{F}}{\delta \phi} \tag{3.29}$$

$$\Downarrow$$

$$\frac{\partial \phi}{\partial t} = -M_\phi \left[\frac{\partial f(\phi)}{\partial \phi} - \epsilon^2 \nabla^2 \phi \right] \tag{3.30}$$

Eqn. 3.30 is known as the Allen-Cahn equation [99, 100] for a non-conserved order parameter ϕ, M_ϕ is the positive mobility. Alternatively for conserved parameter, c, the continuity equation is applied:

$$\frac{\partial c}{\partial t} + \nabla \cdot J_c = 0 \tag{3.31}$$

and identifying

$$J_c = -M_c \nabla \frac{\delta \mathcal{F}}{\delta c}$$

The flux J_c [101] has negative mobility $-M_c$ to ensure the decrease in $\mathcal{F}$. Therefore, combining Eqns.3.31 and 3.25 we get:

$$\begin{aligned} \frac{\partial c}{\partial t} &= -\nabla \cdot J_c \\ &= -\nabla \cdot (-M_c \nabla \frac{\delta \mathcal{F}}{\delta c}) \\ &= M_c \nabla^2 \left[\frac{\partial f(c)}{\partial c} - \epsilon^2 \nabla^2 c \right] \end{aligned} \tag{3.32}$$

assuming a constant M_c and that F takes the form as in Eqn. 3.23. Eqn. 3.32 is the Cahn-Hilliard equation [102] of a conserved order parameter c (e.g. composition). Eqn. 3.28 is a non-trivial steady state solution of 3.32 in 1D.

3.3.6 General interface

The diffuse interface profile Eqn. 3.28, can be extended to multi-dimensional systems by replacing the x by the signed distance function $\mathcal{S}(\vec{x})$ defined as the shortest distance to the nearest point on the interface. Mathematically, this is to say that the gradient of ϕ everywhere outside of the interface is constant in the direction of the interface normal and the constant is usually set equal to 1, we have the Eikonal equation:

$$|\nabla \mathcal{S}(\vec{x})| = 1 \tag{3.33}$$

The initial condition of a phase-field calculation is usually given by the hyperbolic tangent function (akin to Eqn. 3.28 depending on the convention) of $\mathcal{S}$ that satisfies Eqn. 3.33. In addition to the initial profile and following on from the derivation of 1-D expression of the generalised chemical potential Eqn. 3.25, it is derived here the generalised chemical potential with isotropic gradient energy coefficient ϵ^2 in dimension $d > 1$. First by assuming the form of free energy functional as in Eqn. 3.17 and using the chain rule $\nabla \cdot (w\nabla\phi) = \nabla w \cdot \nabla\phi + w(\nabla^2\phi)$ as well as the divergence theorem to expand the integral below which will be used in the derivation of Eqn. 3.35

$$\begin{aligned}\int_V \nabla w \cdot \nabla\phi dV &= \int_V \nabla \cdot (w\nabla\phi) dV - \int_V w\nabla \cdot \nabla\phi dV \\ &= \int_{\partial V} w\nabla\phi \cdot \vec{n} dS - \int_V w\nabla^2\phi dV\end{aligned} \tag{3.34}$$

By definition we write down the functional derivative of the free energy in terms of $\tilde{\epsilon}$ an arbitrary small number and w a scaler field equal to 0 at the domain boundaries:

$$\begin{aligned}\delta\mathcal{F} &= \frac{d}{d\epsilon}\int_V \Big[f(\phi + \tilde{\epsilon}w) + \frac{\epsilon^2}{2}\nabla^2(\phi + \tilde{\epsilon}w)\Big] dV\Big|_{\tilde{\epsilon}=0} \\ &= \int_V \Big[\frac{\partial f(\phi + \tilde{\epsilon}w)}{\partial(\phi + \tilde{\epsilon}w)} w + \frac{\epsilon^2}{2} \cdot 2\nabla(\phi + \tilde{\epsilon}w) \cdot \frac{d}{d\epsilon}\nabla(\phi + \tilde{\epsilon}w)\Big] dV\Big|_{\tilde{\epsilon}=0} \\ &= \int_V \Big[\frac{\partial f(\phi)}{\partial\phi} w + \epsilon^2\nabla\phi \cdot \nabla w\Big] dV \\ &= \int_V \frac{\partial f(\phi)}{\partial\phi} w dV + \epsilon^2 \int_{\partial V} \cancelto{0}{w\nabla\phi \cdot \vec{n} dS} - \int_V w\epsilon^2\nabla^2\phi dV \\ &= \int_V w\Big[\frac{\partial f(\phi)}{\partial\phi} - \epsilon^2\nabla^2\phi\Big] dV\end{aligned} \tag{3.35}$$

If, $\mathcal{F}$ is at an extremum, set $\delta\mathcal{F}$ to zero and since the choice of w is arbitrary it follows that the integrand has to be zero:

$$\frac{\partial f(\phi)}{\partial \phi} - \epsilon^2 \nabla^2 \phi = 0 \tag{3.36}$$

3.3.7 The Kobayashi model

For crystalline materials having anisotropic surface energy the phase-field formulations usually get a bit involved. To model the anisotropy in surface tension Kobayashi[103] made the gradient energy coefficient ϵ and the function $\Gamma(\nabla\phi)$ in Eqn. 3.18 to be functions of the interface normal:

$$\epsilon = \epsilon(\nabla\phi)$$
$$\Gamma(\nabla\phi) = |\nabla\phi|$$

The anisotropic surface free energy $\mathcal{E}$ then becomes:

$$\mathcal{E}[\phi] = \int \left[f(\phi) + \frac{\epsilon^2(\nabla\phi)}{2} |\nabla\phi|^2 \right] dV \tag{3.37}$$

The variational derivative of which gives the Euler-Lagrange equation as in Eqn. 3.22 and follow the Allen-Cahn kinetics Eqn. 3.29 we need to find:

$$\frac{\partial \phi}{\partial t} = -M \frac{\delta \mathcal{F}}{\delta \phi} = -M \left(\frac{\partial f}{\partial \phi} - \nabla \cdot \frac{\partial \mathcal{E}}{\partial \nabla \phi} \right) \tag{3.38}$$

By noticing $\frac{d|\nabla\phi|}{d\phi} = \frac{\phi}{|\nabla\phi|}$ the second term in the bracket in 2D can be shown to be:

$$\begin{aligned}
\nabla \cdot \frac{\partial \mathcal{E}}{\partial \nabla \phi} &= \nabla \cdot \left(\epsilon^2 |\nabla\phi| \frac{\nabla\phi}{|\nabla\phi|} + \epsilon \frac{\partial \epsilon}{\partial \nabla \phi} |\nabla\phi|^2 \right) \\
&= \nabla \cdot \left(\epsilon^2 \nabla\phi \right) + \nabla \cdot \left(\epsilon \frac{\partial \epsilon}{\partial \nabla \phi} |\nabla\phi|^2 \right) \\
&= \nabla \cdot \left(\epsilon^2 \nabla\phi \right) + \frac{d}{dx} \left(\epsilon \frac{\partial \epsilon}{\partial \phi_x} |\nabla\phi|^2 \right) + \frac{d}{dy} \left(\epsilon \frac{\partial \epsilon}{\partial \phi_y} |\nabla\phi|^2 \right)
\end{aligned} \tag{3.39}$$

where ϕ_x and ϕ_y denote the derivatives of ϕ with respect to x and y respectively, and $|\nabla\phi|^2 = \phi_x^2 + \phi_y^2$. It follows that Kobayashi must have blended in 2D the terms $\frac{\partial \epsilon}{\partial \phi_x}$ and $\frac{\partial \epsilon}{\partial \phi_y}$ through the orientation angle $\theta = atan(\phi_y/\phi_x)$ so that:

$$\frac{\partial \epsilon}{\partial \phi_x} = \frac{\partial \epsilon}{\partial \theta} \frac{\partial \theta}{\partial \phi_x} = \frac{\partial \epsilon}{\partial \theta} \frac{1}{1 + \phi_y^2/\phi_x^2} \left(-\frac{\phi_y}{\phi_x^2} \right)$$
$$\frac{\partial \epsilon}{\partial \phi_y} = \frac{\partial \epsilon}{\partial \theta} \frac{\partial \theta}{\partial \phi_y} = \frac{\partial \epsilon}{\partial \theta} \frac{1}{1 + \phi_y^2/\phi_x^2} \left(-\frac{1}{\phi_x} \right)$$

Substitute these two terms in Eqn. 3.39 and make the last simplification before magically reaching Kobayashi's surface diffusion Eqn. 3.40

$$
\begin{aligned}
&\frac{d}{dx}\left(\epsilon\frac{\partial\epsilon}{\partial\theta}\frac{1}{1+\phi_y^2/\phi_x^2}\Big(-\frac{\phi_y}{\phi_x^2}\Big)|\nabla\phi|^2\right)+\frac{d}{dy}\left(\epsilon\frac{\partial\epsilon}{\partial\theta}\frac{1}{1+\phi_y^2/\phi_x^2}\Big(-\frac{1}{\phi_x}\Big)|\nabla\phi|^2\right)\\
=&\frac{d}{dx}\left(\epsilon\frac{\partial\epsilon}{\partial\theta}\frac{\phi_x^2+\phi_y^2}{1+\phi_y^2/\phi_x^2}\Big(-\frac{\phi_y}{\phi_x^2}\Big)\right)+\frac{d}{dy}\left(\epsilon\frac{\partial\epsilon}{\partial\theta}\frac{\phi_x^2+\phi_y^2}{1+\phi_y^2/\phi_x^2}\Big(-\frac{1}{\phi_x}\Big)\right)\\
=&-\frac{d}{dx}\left(\epsilon\frac{\partial\epsilon}{\partial\theta}\phi_y\right)+\frac{d}{dy}\left(\epsilon\frac{\partial\epsilon}{\partial\theta}\phi_x\right)
\end{aligned}
$$

$$
\frac{\partial\phi}{\partial t}=-M\left[\frac{\partial f}{\partial\phi}-\nabla\cdot\left(\epsilon^2\nabla\phi\right)+\frac{d}{dx}\left(\epsilon\frac{\partial\epsilon}{\partial\theta}\phi_y\right)-\frac{d}{dy}\left(\epsilon\frac{\partial\epsilon}{\partial\theta}\phi_x\right)\right] \tag{3.40}
$$

3.3.8 Regularisation

It is well-known that Eqn. 3.40 is ill-posed when the anisotropy function $\epsilon(\theta)$ is non-convex. The convexity is lost in the range of θ corresponding to the so-called missing orientations, the surface energy is said to be strongly anisotropic. This makes the evolution equation 3.40 backward parabolic. The identification of this range is straightforward in 2D owning to the analytic criterion $\epsilon+\epsilon_{\theta\theta}<0$ given by Herring [104]. In 3D a much more complicated method [64] is used to locate the non-convex regions of the anisotropy function as reviewed in Sec. 2.3.4. To overcome it Eggleston [105] used a common tangent construction to convexify $\epsilon(\theta)$. This method although enjoys the simplicity of still sticking to Eqn. 3.40 by convexifying ϵ, it however modifies the physics by suppressing the faceting in the region of the missing orientations. Wheeler [106] and Wise [107] circumvented this problem by introducing an additional energy $\mathcal{E}_r=\frac{\tilde{\beta}}{2}\int_\Omega\frac{1}{\epsilon^3}(\epsilon^2\nabla^2\phi)^2d\Omega$ in the free energy functional Eqn. 3.37. It is noticed by Torabi [62, 63] that they have problems with the rounding of corners and edges.

Another way to deal with the non-convex anisotropy function which renders the evolution backward parabolic is to regularise the free energy functional by adding a curvature-dependent term as first introduced by Herring [104] and later in a more rigorous treatment [108]. This curvature-dependent energy is termed Cahn-Hilliard-Willmore (CHW) energy and Torabi et al. [62, 63] developed a phase-field approximation for this regularisation. They started with the free energy Eqn. 3.41 in which the thickness of the diffuse interface is independent of the orientation as compared with Kobayashi's free energy.

$$
\mathcal{E}[\phi]=\int_\Omega\frac{\tilde{\gamma}(\vec{n})}{\epsilon}\Big(f(\phi)+\frac{\epsilon^2}{2}|\nabla\phi|^2\Big)+\frac{\tilde{\beta}}{2\epsilon^3}\big(f'(\phi)-\epsilon^2\nabla^2\phi\big)^2d\Omega \tag{3.41}
$$

The first in this energy can be seen as a surface delta function[†] $\delta=\frac{1}{\epsilon}[(f(\phi)+\frac{\epsilon^2}{2}|\nabla\phi|^2]$ acting on the dimensionless free energy density $\tilde{\gamma}=\gamma/\gamma_0$ function[‡] parametrised by the surface normal $\vec{n}=\frac{\nabla\phi}{|\nabla\phi|}$. The second term is the Willmore energy in which the regularisation coefficient $\tilde{\beta}>0$ introduces a new length scale for the sharp corners and edges.

$$
\frac{\delta\mathcal{E}}{\delta\phi}=\mu=\frac{1}{\epsilon}\Big(\tilde{\gamma}(\vec{n})f'(\phi)-\epsilon^2\nabla\cdot\vec{m}\Big)+\frac{\tilde{\beta}}{\epsilon^2}\Big(f''(\phi)\tilde{\omega}-\epsilon^2\nabla^2\tilde{\omega}\Big) \tag{3.42}
$$

The variational derivative of this energy μ Eqn. 3.42 the generalised chemical potential is given in [62, 63] in terms of the isotropic chemical potential $\tilde{\omega} = \frac{1}{\epsilon}[(f'(\phi) - \epsilon^2\nabla^2\phi]$ and the anisotropic gradient $\vec{m}(\phi)$:

$$\vec{m} = \tilde{\gamma}(\vec{n})\nabla\phi + \xi_t|\nabla\phi| \tag{3.43}$$

where ξ_t is the tangential component of the Cahn-Hoffman vector $\vec{\xi}$ (Sec. 2.3.3) and in the phase-field framework it is equal to the inner product of the tangential projection vector $\mathbf{P}$ and the ξ-vector

$$\xi_t = \mathbf{P}\vec{\xi} = \left(\mathbf{I} - \vec{n} \otimes \vec{n}\right) \cdot \vec{\xi}$$

[†]Both $f(\phi)$ and $|\nabla\phi|^2$ can be interpreted physically as to approximate the surface delta function, when at equilibrium $\frac{1}{4}\phi^2(1-\phi)^2 = \frac{\epsilon^2}{2}|\nabla\phi|^2$ can also be used as a surface delta function [109].

[‡]If $\tilde{\gamma}$ is a constant the surface delta function 'picks up' an isotropic interface as in the Hilliard-Cahn system [102].

4. Realistic materials

Under isothermal conditions crystals take on an equilibrium shape known as the Wulff shape that minimises the total surface free energy for a fixed volume. Faceting of the exposed surfaces naturally arise in crystalline materials due to the highly anisotropic surface energy. Material mass on facets having lower surface energy density tends to diffuse faster than that on high-energy facets and eventually outgrow them. Using the same construction method γ and $\vec{\xi}$ of a general crystalline material can be obtained as opposed to the toy-type anisotropies reviewed in Sec. 2.3.4, which relies on the particular symmetries. In this section the γ functions of two realistic ceramic materials anatase-TiO_2 and MgO are constructed using the Siem-Carter method [110, 111, 112, 113]. The significance of constructing such a function is that $\gamma(\vec{n})$ forms an essential part of the energy minimising calculation of realistic materials.

4.1 Anatase-TiO_2

4.1.1 Cohesive energy

It is known that the anatase phase is energetically preferable for TiO_2 nanoparticles of diameters smaller than 10 nm [114]. The equilibrium shape of a single crystal is equivalent to the convex hull (inner envelop) of the surface energy polar plot, commonly known as the equilibrium Wulff shape [81]. Among the experimentally observed surfaces of anatase TiO_2, {101} and {001} stick out to be of central importance as the Wulff shape is only dependent on these two surfaces, owing to the lattice parameters and tetragonal symmetry of anatase. {001} faceted anatase is known to have higher photocatalytic performance over {101}-type facets [115], and the relative exposed area of {001} facets is related to the surface energy ratio $\gamma_{\{101\}}/\gamma_{\{001\}}$. For clean surfaces the highly reactive {001} surfaces are found to be less than 10% of the total exposed area [116, 117]. However by doping with various species that have small bonding energy when adsorbed on anatase nanocrystals, increase in surface energy ratio can be achieved [118].

The cohesive energy is defined as the difference between the isolated gas-phase atoms and the same atoms in a crystal lattice. Consider a unit cell of anatase with only its motifs and one Ti atom residing in one of the lattice point shown in Fig. 4.1. The Ti and O atoms are six-fold and three-fold coordinated respectively. By applying periodic boundary conditions in space this will fill out the whole lattice with bulk configuration of anatase, with optimised lattice parameters A, C* and internal degrees of freedom defined by the apical and equatorial bond lengths d_a and d_e. These parameters can be determined experimentally at low temperature, however in this section the optimised ground state values of A, C and d are taken from [116] which are calculated by using Perdew–Burke–Ernzerhof (PBE) exchange-correlation functional.

*$B = C$ for tetragonal materials

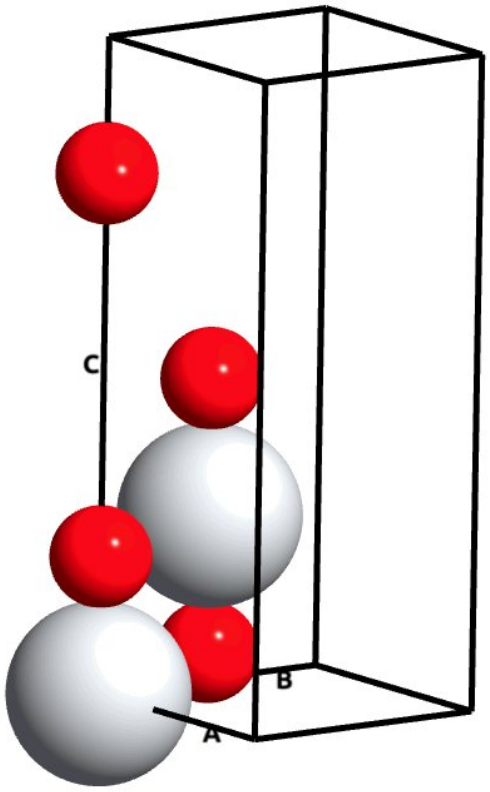

Figure 4.1: TiO_2 anatase unit cell with computed lattice parameters A, B and C ($A = B$ for tetragonal materials). Ti atoms are coloured in red and O atoms are in grey, visualised using OVITO [119].

The aim is to treat the surface the same way as the bulk system so the same cut-off energy of 350 eV is used. It is worth noting that convergence is not reached at this cut-off energy for isolated Ti and O atoms. Pseudopotentials with six valence electrons ($2s^2, 2p^4$) for Oxygen and 12 electrons ($3s^2, 3p^6, 3d^2, 4s^2$) for Ti are employed. PBE is known to be reliable for surface calculations so it is used here for the bulk system too for consistency. The result of the total energy of the four units of TiO_2 is calculated to be -106.35 eV and the energy associated with one unit is therefore $-106.35/4 = -26.6\,\text{eV}/TiO_2$. The literature values are $-21.44\,\text{eV}/TiO_2$ (PBE) and $-24.44\,\text{eV}/TiO_2$ (local-density approximation) for anatase [116, 117].

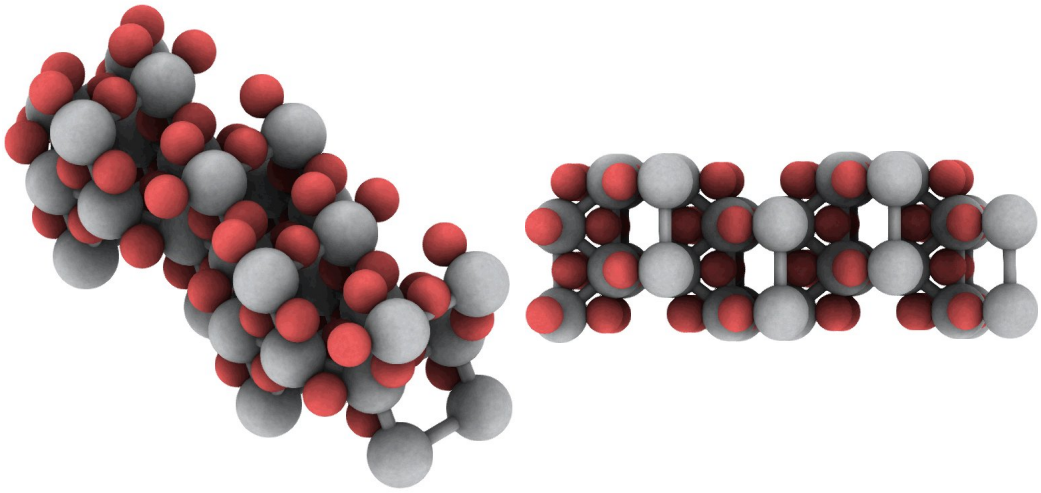

Figure 4.2: Ball and stick visualisation of the slab model of unrelaxed anatase {101} (2 × 4) with 4 Ti layers (Ti atoms are coloured in grey and O in red, visualised using OVITO [119])

4.1.2 Surface energy density

The surface excess energy is calculated from the cohesive energy of the bulk structure E_{bulk} and the total energy of the surface structure E^N_{slab}. The surface is modelled by an ultrathin film (UTF) of N layers of titanium. Fig. 4.2 shows a bulk-like slab model of a particular surface constructed from bulk structure by cleaving the corresponding planes. Then the slab is relaxed so that the stress of either of the principal axes is less than 0.02 GPa. A $N = 4$ layer slab consisting of 24 atoms is shown in Fig. 4.3 and the unrelaxed structure is used for electronic-structure calculation using density functional theory (DFT). The surface energy density γ is then calculated using Eqn. 4.1 proposed in [120].

$$\gamma = \lim_{N\to\infty} \frac{1}{2A}\left(E^N_{slab} - NE_{bulk}\right) \tag{4.1}$$

It is known that there are computational errors associated with γ that make it diverge linearly with N [121]. For a UTF approximation of Eqn. 4.1 a small number of N between $4-8$ is selected and an example calculation is shown below for a {101} (2×2) with 4 Ti layers:

$$\begin{aligned}
\gamma^{\{101\}} &= \frac{E_{slab} - N_{\mathrm{TiO_2}} \times E^{bulk}_{\mathrm{TiO_2}}}{\text{total exposed area}} \\
&= \frac{-201.3105 - 8 \times (-26.6)}{10.447 \times 24.352 \times 2} \\
&= \frac{11.4895\,\mathrm{eV}}{508.81\,\mathrm{\AA}^{-2}} \\
&= 0.022\,58\,\mathrm{eV\AA}^{-2} \\
&= 0.362\,\mathrm{Jm}^{-2}
\end{aligned}$$

Repeat the calculation for $N = 6$ we get $\gamma^{\{101\}} = 0.350\,\mathrm{Jm}^{-2}$. For comparison values of $\gamma^{\{101\}}$ in literature are less than $0.44\,\mathrm{Jm}^{-2}$ [116, 117].

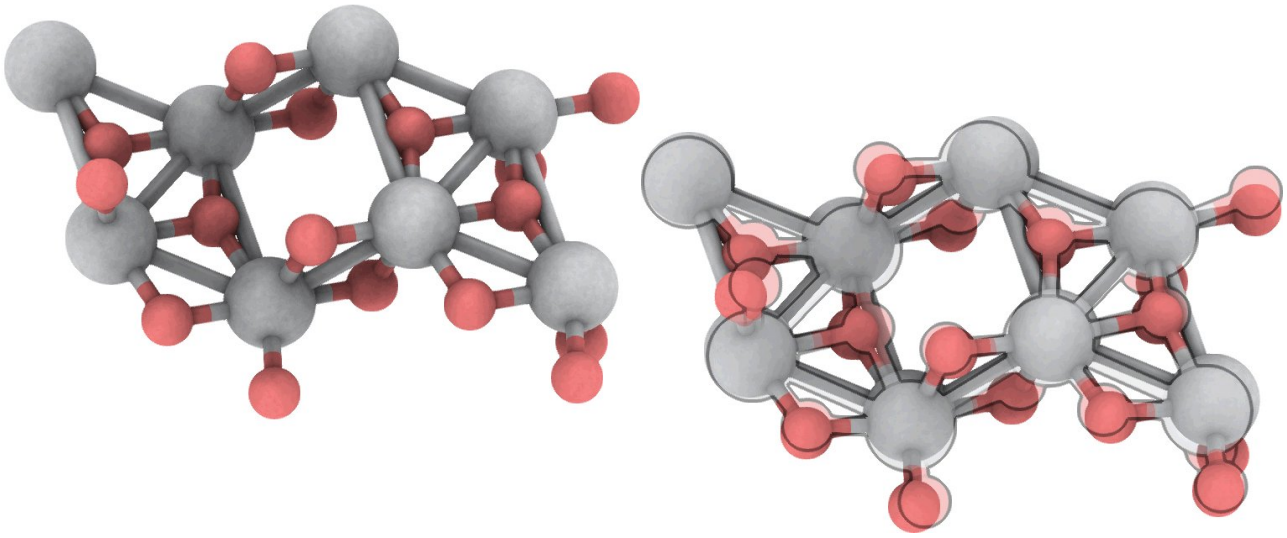

(a) (b)

Figure 4.3: Ball and stick models of (a) unrelaxed and (b) unrelaxed (coloured) and relaxed (transparent) anatase {101} (2×2) slabs superimposed showing bond expansion and displacements. In (b), the top left Ti atom is fixed for comparison. The visualisation is done in OVITO [119].

For non-stoichiometric surfaces such as {103} the literature values of γ at 0 K are found (cf. [116, 117]) and they are listed in Tab. 4.1.

Table 4.1: Surface energy values of various anatase-TiO_2 surfaces

families	$\{101\}$	$\{100\}$	$\{001\}$	$\{103\}_s$[1]	$\{103\}_f$[1]
surfaces	(101) (011) $(\bar{1}01)$ $(0\bar{1}1)$ $(01\bar{1})$ $(10\bar{1})$ $(\bar{1}0\bar{1})$ $(0\bar{1}\bar{1})$	$(0\bar{1}0)$ $(\bar{1}00)$ (100) (010)	(001) $(00\bar{1})$	$(0\bar{1}\bar{3})_s$ $(\bar{1}0\bar{3})_s$ $(10\bar{3})_s$ $(01\bar{3})_s$ $(0\bar{1}3)_s$ $(\bar{1}03)_s$ $(103)_s$ $(013)_s$	$(0\bar{1}\bar{3})_f$ $(\bar{1}0\bar{3})_f$ $(10\bar{3})_f$ $(01\bar{3})_f$ $(0\bar{1}3)_f$ $(\bar{1}03)_f$ $(103)_f$ $(013)_f$
γ literature [116, 117]	$0.44\,\mathrm{Jm}^{-2}$	$0.53\,\mathrm{Jm}^{-2}$	$0.90\,\mathrm{Jm}^{-2}$	$0.93\,\mathrm{Jm}^{-2}$	$0.83\,\mathrm{Jm}^{-2}$
γ literature [122][2]	$0.56\,\mathrm{Jm}^{-2}$	$0.74\,\mathrm{Jm}^{-2}$	$1.03\,\mathrm{Jm}^{-2}$	$1.11\,\mathrm{Jm}^{-2}$	$0.99\,\mathrm{Jm}^{-2}$
γ this work	$0.35\,\mathrm{Jm}^{-2}$	$0.45\,\mathrm{Jm}^{-2}$	$0.78\,\mathrm{Jm}^{-2}$		

[1] In [116, 117] the faceted (subscript f) and smooth (subscript s) $\{001\}$-type surfaces are distinguished depending on the termination.
[2] In [122] 4e pseudopotentials are used to compare with those obtained in [116, 117] using 12e pseudo-potentials.

4.1.3 γ construction for realistic materials

The γ function is then constructed by employing a computationally convenient function [112, 111, 113] Eqn. 4.2 that is equivalent to the Siem-Carter construction [110]:

$$\gamma(\vec{n}) = \gamma_0 \left(1 - \sum_{i=1}^{M} \alpha_i (\vec{m}_i \cdot \vec{n})^{w_i} \Theta(\vec{m}_i \cdot \vec{n}) \right) \tag{4.2}$$

where M is the total number of surfaces with miller index m_i converted to Cartesian coordinate, γ_0 sets the magnitude of the surface energy density and $\vec{n}$ is the surface normal. The value of γ_0 is greater than the surface energy density of the facets. α_i are values normalised by choosing γ_{ref} and α_{ref} according to Eqn. 4.3 as devised and extensively documented in [112, 111, 113]:

$$\alpha_i = 1 - \left(\frac{\gamma_i}{\gamma_{ref}} \right) (1 - \alpha_{ref}) \tag{4.3}$$

It is noted and emphasised below the implications of functions 4.2 and 4.3 by tuning the values of the coefficients α_i, w_i and plotting γ in Fig. 4.5.

1. This is formulation is equivalent to the Siem-Carter construction [110] but extended to incorporate the realistic material-specific surface energy density values.

2. γ_0 served as a scaling factor which does not appear in the normalisation of α Eqn. 4.3. However the relative depths of the local minima (set by α_i) to that of the value of the missing orientations (where $\gamma/\gamma_0 = 1$) is determined by γ_0. For example, in choosing α_{ref} and γ_{ref} to be $10/11$ and γ_{001} respectively, γ_0 is implicitly set to 1.1 times the value of γ_{001}. In an energy minimising calculation the local rate of change of energy is dependent on the relative decent of the potential energy surface. This means that the value of γ_0 together with the mobility in an energy minimising calculation set the timescale.

3. The surface energy density is usually made dimensionless in an energy minimisation calculation, i.e. defining $\tilde{\gamma} = \gamma/\gamma_0$. The physical value of γ_0 is linked to the isotropic surface energy which can be estimated for a specific system [111].

4. positive coefficients α_i and w_i determine the depth and the localisation of the energy minima. It is shown in Fig. 4.4 the effects of w and α taking on a single local minimum. For multiple minima the choice of w_i for each i has to ensure that the minima do not overlap as they will superimpose according to Eqn. 4.2.

5. The values of α_i obtained by Eqn. 4.3 for the three sets of surface energies (i.e. various literature values and calculations in this work) are close. It can be concluded that the difference of the γ functions constructed by using this method is small for different pseudopotentials of a particular DFT calculation.

6. The surface energies are evaluated at zero Kelvin. There are studies (e.g. [123]) that suggest small increase in surface energies for some finite temperature. By the same token, it can be assumed that the temperature dependence is insignificant when calculating α_i.

7. The inclusion of the Heaviside function $\Theta(\vec{m}_i \cdot \vec{n})$ has the effect of ensuring that an orientation specified by $\vec{m}_i$ in Cartesian coordinate is independent of its opposite -$\vec{m}_i$ (which is not necessarily the crystallographically equivalent facet).

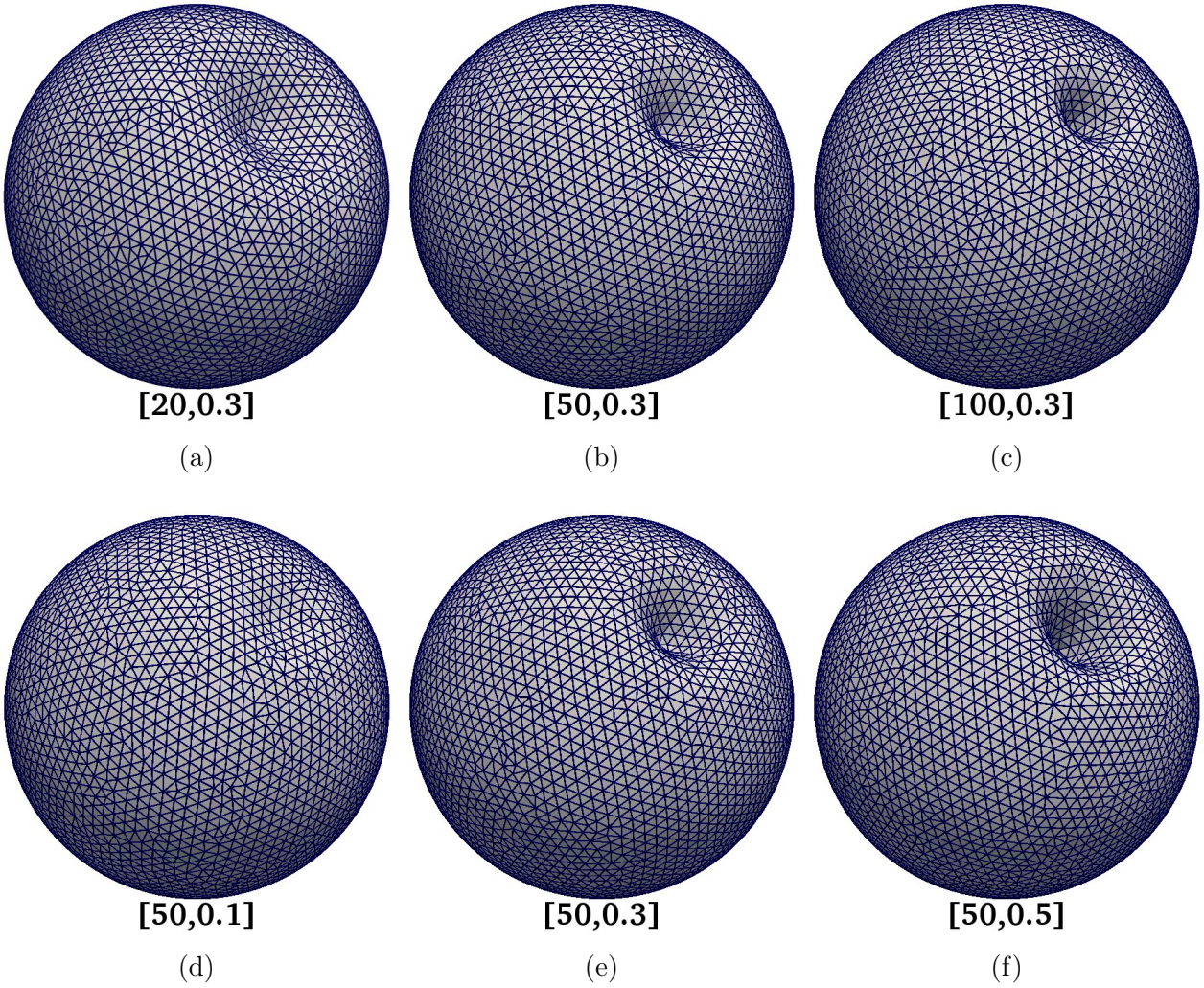

Figure 4.4: γ-plots showing local minima of arbiturary orientation constructed using Eqn. 4.2: (a)-(c) with different corfficients $[w_i, \alpha_i]$ keeping α the same and (d)-(f) keeping w unchanged. The surface mesh used is generated by using the package Meshlab [124].

4.2 Convexified ξ-plot

4.2.1 Anatase-TiO_2

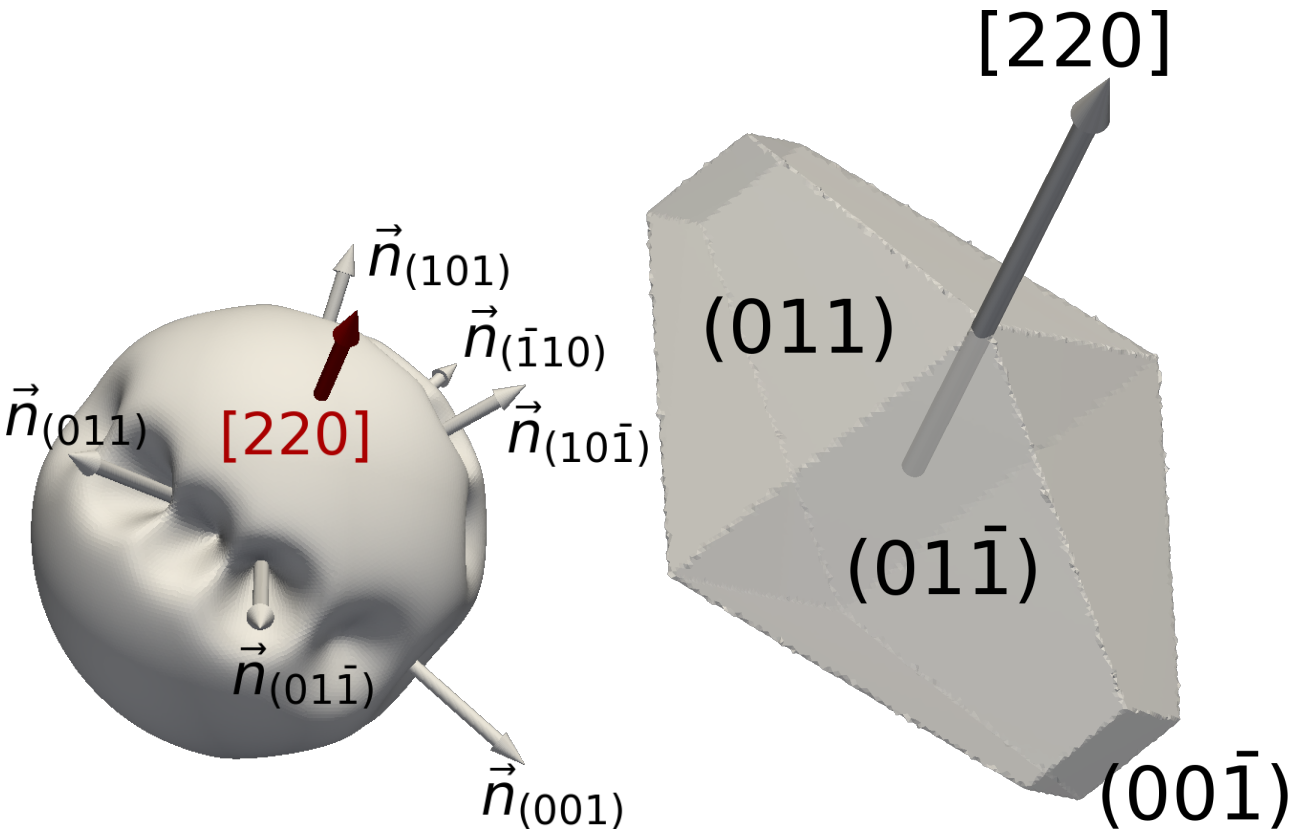

(a) (b)

Figure 4.5: γ-plot of anatase-TiO_2 (a) and the corresponding convexified ξ-plot (b), visualised in Paraview [125].

The γ-plot of anatase-TiO_2 using the values in Tab. 4.1 is shown in Fig. 4.5(a). The equilibrium shape, which is the inner convex hull[†] of the γ-plot is obtained by first identifying the missing orientations associated with the convex-to-concave transition in the $^1/\gamma$-plot due to a well-known criterion given by Sekerka [64]. These missing orientations correspond to the 'ears' and 'flaps' of the ξ-plot which are 'chopped' off, the remaining part of which gives the equilibrium shape and it is called the convexified ξ-plot shown in Fig. 4.5(b). The ξ-plot of anatase-TiO_2 is shown in Fig. 4.6(a) along with Fig. 4.6(b) the Wulff shape obtained by the slab model based on the surface energy ratio $\gamma_{\{101\}}/\gamma_{\{001\}}$ as explained earlier in this section. The artifacts around the ridges of Fig. 4.6(b) are due to insufficient number points specified by coordinates $[\xi_1 \quad \xi_2 \quad \xi_3]^{\ddagger}$ in those regions as a result of this convexifying ξ-plot approach [64] in which the recipe is given but not made efficient for computation.

*non-trivial in 3D as the analytical formula for finding missing orientations of the γ-plot is only available for 2D as reviewed in Sec. 2.3.4

†where ξ_1, ξ_2 and ξ_3 are components of the $\vec{\xi}$ vector in x, y and z respectively.

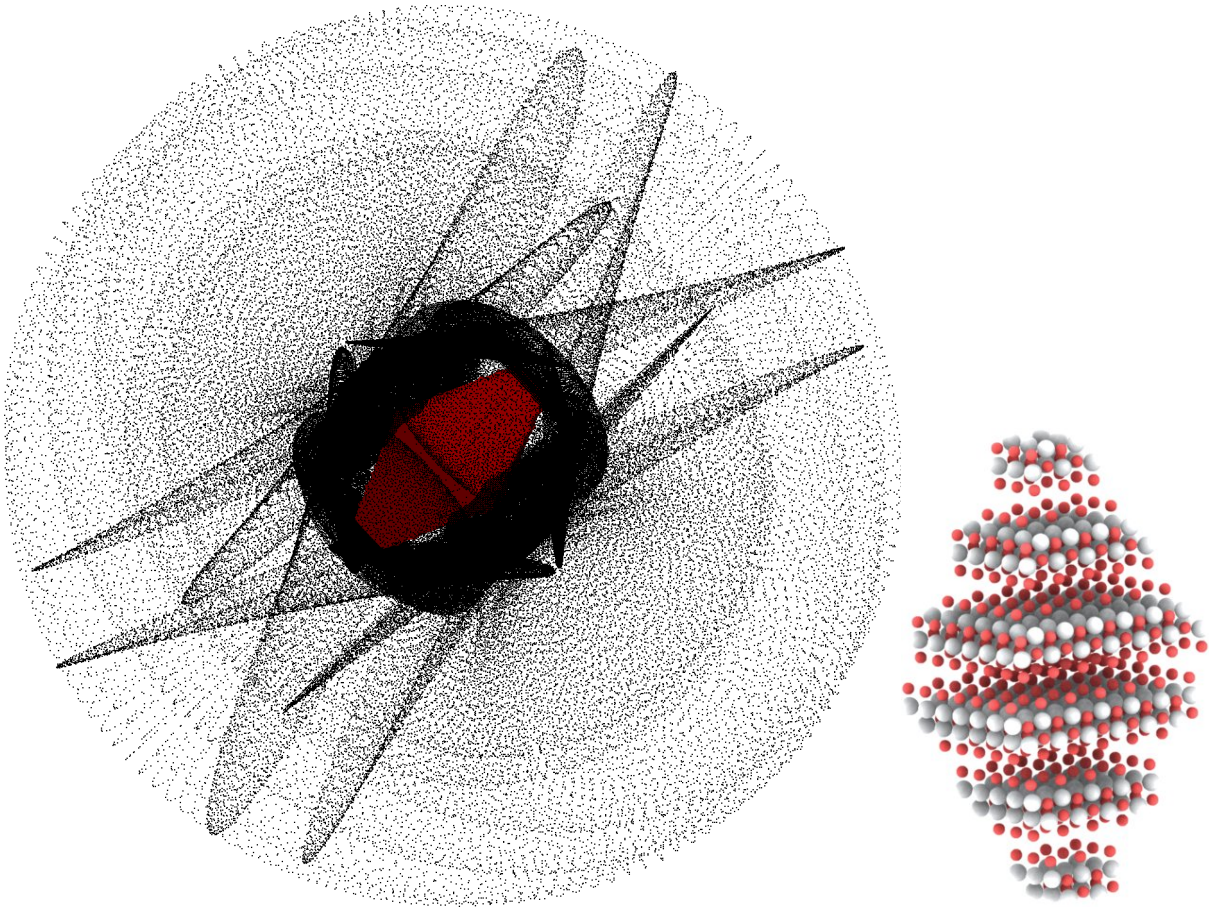

(a) (b)

Figure 4.6: Equilibrium shape of antase-TiO_2, also known as the convexified ξ-plot (red) is shown to be embedded in (a), the point cloud of $\vec{\xi}$ (black) visualised in Paraview [125] and (b), a slab model based on the surface energy ratio $\gamma_{\{101\}}/\gamma_{\{001\}}$ (Ti atoms are coloured in grey and O in red) visualised in OVITO [119].

4.2.2 MgO

Following on for a different material MgO, the surface energies of the low-index planes are reported in [126]. They are collected in Tab. 4.2. The crystal morphology in equilibrium state for MgO is determined by the ratio $\gamma_{\{100\}}/\gamma_{\{111\}}$, this is reflected on the convexified ξ-plot shown along side the γ-plot in Fig. 4.7 in which it can be seen that the equilibrium shape of MgO is mostly bounded by {100} surfaces.

Table 4.2: Surface energy values of various MgO surfaces

families	{111}	{110}	{100}
surfaces	$(\bar{1}\bar{1}\bar{1})$ $(1\bar{1}\bar{1})$ $(\bar{1}1\bar{1})$ $(11\bar{1})$ $(\bar{1}\bar{1}1)$ $(1\bar{1}1)$ $(\bar{1}11)$ (111)	$(0\bar{1}\bar{1})$ $(\bar{1}0\bar{1})$ $(10\bar{1})$ $(01\bar{1})$ $(\bar{1}\bar{1}0)$ $(1\bar{1}0)$ $(\bar{1}10)$ (110) $(0\bar{1}1)$ $(\bar{1}01)$ (101) (011)	$(00\bar{1})$ $(0\bar{1}0)$ $(\bar{1}00)$ (100) (010) (001)
$\gamma(\mathrm{Jm}^{-2})/(\times 10^{-2}\mathrm{eV\AA}^{-2})$	2.21/13.81	2.25/14.06	0.93/5.81

The values in Tab. 4.2 are evaluated at 0 K [126]. However following the same arguments as in the 6th implication of Eqns. 4.2 and 4.3, the difference between the equilibrium shapes is insignificant for DFT calculations of surface energy at 0 K and some other temperatures below the melting point.

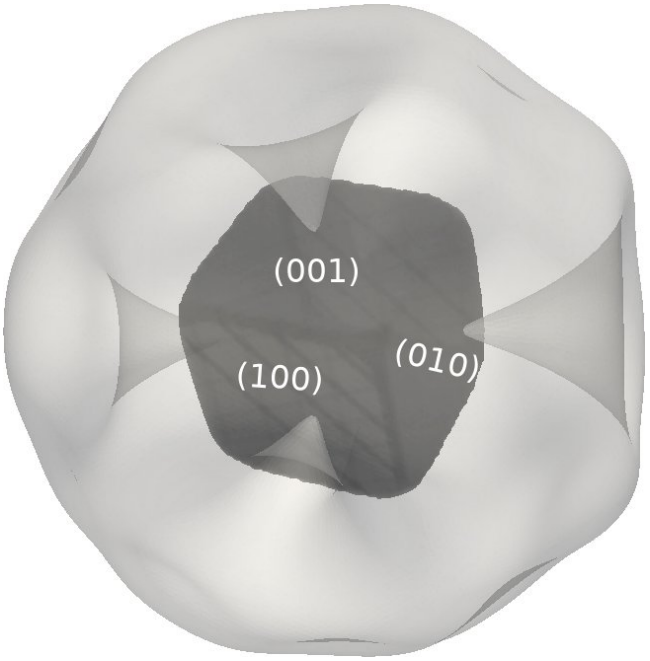

Figure 4.7: γ-plot of MgO (transparent) and its corresponding convexified ξ-plot (solid), visualised in Paraview [125].

4.3 Energy minimising calculation for realistic materials

4.3.1 Numerical methods and implementation

The geometric evolution law Eqn. 3.14 has important applications in modelling the surface diffusion. Its variational approximation - the conserved H^{-1} gradient flow of the CHW energy in Eqn. 3.42 as seen in Sec. 3.3.8 results in a high-order, stiff, highly nonlinear parabolic PDE:

$$\begin{aligned}\phi_t &= \nabla\cdot\Big(M(\phi)\nabla\mu\Big)\\ &= \nabla\cdot\left[M(\phi)\nabla\left(\frac{1}{\epsilon}\Big(\gamma(\vec{n})f'(\phi)-\epsilon^2\nabla\cdot\vec{m}\Big)+\frac{\tilde{\beta}}{\epsilon^2}\Big(f''(\phi)\tilde{\omega}-\epsilon^2\nabla^2\tilde{\omega}\Big)\right)\right] \quad \text{in} \quad \Omega\end{aligned} \tag{4.4}$$

subject to boundary conditions

$$\mathcal{B}\mu|_{\partial\Omega}=\mathcal{B}\phi|_{\partial\Omega}=\mathcal{B}\tilde{\omega}|_{\partial\Omega}=0 \tag{4.5}$$

which poses severe numerical issues for conventional explicit methods. $\mathcal{B}$ here is a linear operator. It is worth noting that this system is mass conservative, i.e.,

$$\frac{d}{dt}\int_\Omega \phi(\vec{x},t)d\vec{x}=0 \tag{4.6}$$

and energy dissipating

$$\frac{d\mathcal{E}}{dt}=-\int_\Omega M(\phi)|\nabla\mu|^2 d\vec{x} \tag{4.7}$$

It has been an ongoing research in designing a scheme that retains the above properties in a numerical sense as well as being unconditionally solvable [127], energy stable [128, 129, 130] and uniquely solvable [129]. In addition, the convergence analysis [131, 129] is of practical importance as accuracy and efficiency are essential in applying any numerical scheme to real-world materials science problems. In this chapter a particular discretisation scheme is reviewed that will be frequently mentioned in the following chapters.

Time integration scheme

The major difficulty of solving the six-order stiff Eqn. 4.4 is associated with the restriction of the time step $\delta t \sim \mathcal{O}\big((\delta x)^6\big)$. A semi-implicit scheme [12] removes the restriction and is implemented in an adaptive multigrid finite element toolbox [132]. It has been shown in [112, 111, 113] that it is computationally convenient to decompose Eqn. 4.4 into three coupled second-order PDEs. Based on a stabilised time discretisation method [133] Chen designed a semi-implicit scheme [134]:

$$\begin{aligned}\frac{\epsilon}{\delta t}\phi^{n+1}-M\nabla^2\mu^{n+1}&=\frac{\epsilon}{\delta t}\phi^n\\ \frac{1}{\tilde{\beta}}\mu^{n+1}-\frac{\tilde{s}\tilde{\omega}^{n+1}}{\epsilon^2}+\nabla^2\tilde{\omega}^{n+1}&=\frac{1}{\tilde{\beta}\epsilon}\Big(\gamma(\vec{n}^{\,n})f'(\phi^n)-\epsilon^2\nabla\cdot\vec{m}\Big)+\frac{1}{\epsilon^2}f''(\phi^n)\tilde{\omega}^n-\frac{\tilde{s}\tilde{\omega}^n}{\epsilon^2}\\ \frac{1}{\epsilon}\tilde{\omega}^{n+1}-\frac{s}{\epsilon^2}\phi^n+\nabla^2\phi^{n+1}&=-\frac{s}{\epsilon^2}\phi^n+\frac{1}{\epsilon^2}f'(\phi^n)\end{aligned} \tag{4.8}$$

where s and $\tilde{s}$ are stabilisation terms, n is the index of the time step, M is assumed to be constant and ϵ, $\tilde{\omega}$, μ follow the same meanings as in Sec. 3.3.8. The linear terms in system 4.8 are interpreted implicitely and the nonlinear terms are treated explicitly. It has been demonstrated that this scheme is stable even with $\delta t = 1 \times 10^{-3}$ but with an error that scales with δt as $\mathcal{O}(\frac{s\delta t}{\epsilon})$ [134].

Spatial discretisation

For the time integration scheme, system 4.8 with unknowns μ, ϕ, $\tilde{\omega}$, the constants on the LHS are denoted by a, b, $\tilde{a}$, $\tilde{c}$, $\tilde{b}$, d, $\tilde{\tilde{a}}$, $\tilde{\tilde{c}}$, $\tilde{\tilde{b}}$ and constants on the RHS f, g, h:

$$\begin{aligned} a\phi - b\nabla^2\mu &= f \\ \tilde{a}\phi + \tilde{c}\tilde{\omega} - \tilde{b}\nabla^2\phi &= g \qquad \text{in} \quad \Omega \\ d\mu + \tilde{\tilde{a}}\phi + \tilde{\tilde{c}}w - \tilde{\tilde{b}}\nabla^2\tilde{\omega} &= h \end{aligned} \tag{4.9}$$

A weighted integral projection of this system is taken with test functions w [135] using a Legendre-Gauss-Lobatto (LGL) quadrature rule for the coupled second-order equations subject to non-periodic boundary condition. Solving for the unknowns in each time step then becomes a linear algebra problem, i.e.,

$$\begin{aligned} a(\phi_N, w_1) - b(\nabla^2\mu_N, w_1) &= (\mathcal{I}_N f, w_1) \\ \tilde{a}(\phi_N, w_2) + \tilde{c}(\tilde{\omega}_N, w_2) - \tilde{b}(\nabla^2\phi_N, w_2) &= (\mathcal{I}_N g, w_2) \\ d(\mu_N, w_3) + \tilde{\tilde{a}}(\phi_N, w_3) + \tilde{\tilde{c}}(\tilde{\omega}_N, w_3) - \tilde{\tilde{b}}(\nabla^2\tilde{\omega}_N, w_3) &= (\mathcal{I}_N g, w_3) \end{aligned} \tag{4.10}$$

where $\mathcal{I}_N$ is the interpolation operator based on the LGL points and weights, and the subscripts on the three unknowns denote the N-mode spectral approximation of the trial functions, e.g. in 2D

$$\phi_N = \sum_{i=0}^{N-2}\sum_{j=0}^{N-2} \hat{\phi}_{ij}\psi_{ij}(x, y) \tag{4.11}$$

$$\psi_{ij} = \tilde{\phi}_i(x)\tilde{\tilde{\phi}}_j(y) \tag{4.12}$$

in which $\tilde{\phi}_i$ and $\tilde{\tilde{\phi}}_j$ are the modal basis functions composed of linear combinations of the Legendre polynomials L_k depending on the boundary conditions. Furthermore, with a special choice of the test function $w = \psi_{ij}$ and the trial function in Eqn. 4.11 the system 4.10 can be arranged into a system of matrix equations:

$$\begin{aligned} aMVM + b(MUS + SUM) &= F \\ \tilde{a}MVM + \tilde{c}MWM + b(MVS + SVM) &= G \\ dMUM + \tilde{\tilde{a}}MVM + \tilde{\tilde{c}}MWM + \tilde{\tilde{b}}(MWS + SWM) &= H \end{aligned} \tag{4.13}$$

where U, V, W denote the coefficient matrices of $\tilde{\mu}_{ij}$, $\tilde{\phi}_{ij}$, $\tilde{\omega}_{ij}$ respectively and M, S are the mass and stiffness matrices. F, G, H are the inner products on the RHS of system 4.10 and they can be evaluated via a nodal to modal transform using fast Legendre transform. Compared with the direct point-wise evaluation $\mathcal{O}(N^2)$ and fast Fourier transform (FFT) for periodic systems $\mathcal{O}(NlogN)$ this fast transform is a $\mathcal{O}(N(logN)^2/loglogN)$ algorithm [136] as illustrated in Fig. 4.8.

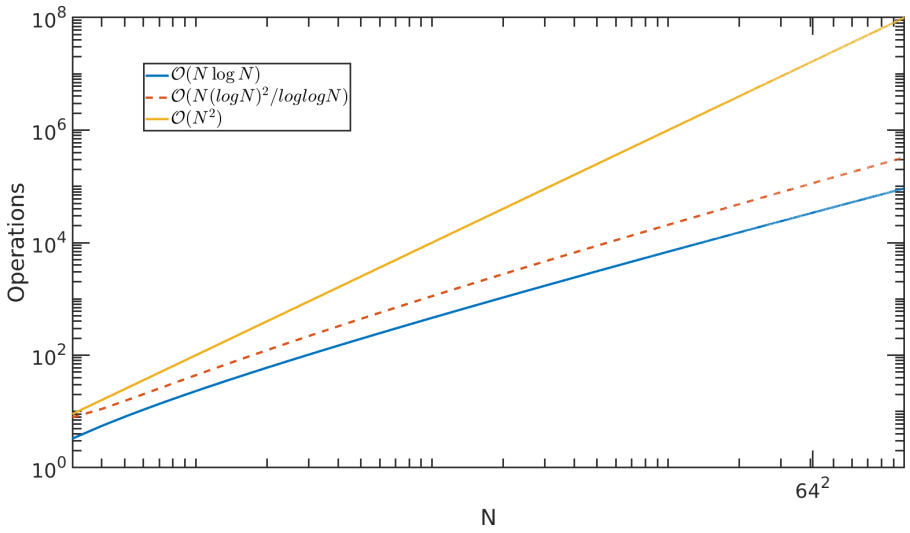

Figure 4.8: Operations versus number of modes N for three different algorithms: direct point-wise evaluation $\mathcal{O}(N^2)$, FFT for periodic systems $\mathcal{O}(NlogN)$ and the fast transform $\mathcal{O}(N(logN)^2/loglogN)$.

Robust direct solver

It is followed that by clearly setting the constants a_k and b_k of the orthogonal basis $\tilde{\tilde{\phi}}_k = L_k + a_k L_{k+1} + b_k L_{k+2}$ with the constraint $\mathcal{B}\tilde{\tilde{\phi}}_k|_{\partial\Omega} = 0$, the structure of M and S can be explored. In particular, for the homogeneous Dirichlet and Neumann boundary conditions M can be made symmetric positive definite and penta-diagonal and S an identity matrix [135]. This in turn makes the matrix system 4.13 solvable by matrix diagonalisation techniques, such as the partial or the full diagonalisation [127]. The precomputation involves the decomposition of M which is well conditioned thanks to its special structure. The solution process takes five steps, four of which are matrix multiplications that can be easily computed using a BLAS or equivalently the IMSL subroutine. Finally, a kernel function is required for solving the linear system and this can be done efficiently using matrix transposes [137].

4.3.2 Energy minimisation by surface diffusion

Lastly the calculations of minimising the total surface free energy defined by Eqn. 3.41 in Sec. 3.3.8 is carried out for a given shape using scheme 4.8. In this phase field approximation to the sharp interface description of surface diffusion (Eqn. 3.14) with constant mobility, the mass in the topmost layer of a particle diffuses onto energetically favourable sites, forming facets, sharp edges and corners. Firstly, the initial condition admits a hyperbolic profile Eqn. 4.14 of the signed distance function $d(\vec{r})$ to a sphere.

$$\phi(\vec{r}) = \frac{1}{2}\left(1 + \tanh\left(\frac{d(\vec{r})}{2\sqrt{2}\epsilon\tilde{\gamma}(\vec{n})}\right)\right) \tag{4.14}$$

Field variables ϕ, $\tilde{\omega}$, μ in the energy-minimising formulation Eqn. 4.4 are solved with relatively small time stepping using an first-order scheme Eqn. 4.8. In this scheme the linear terms are treated implicitly and nonlinear terms involve approximating spacial derivatives and therefore are treated explicitly. The stabilisation terms s and $\tilde{s}$ are added to allow large time stepping. The error associated with this stabilisation is of order $\mathcal{O}(\frac{s\delta t}{\epsilon})$. The spatial discretisation follows Eqns. 4.10 and 4.11 with boundary condition for the three unknowns $\nabla\mu|_{\partial\Omega} = \nabla\phi|_{\partial\Omega} = \nabla\tilde{\omega}|_{\partial\Omega} = \vec{0}$. The robust direct solver described in Sec. 4.3.1 is implemented.

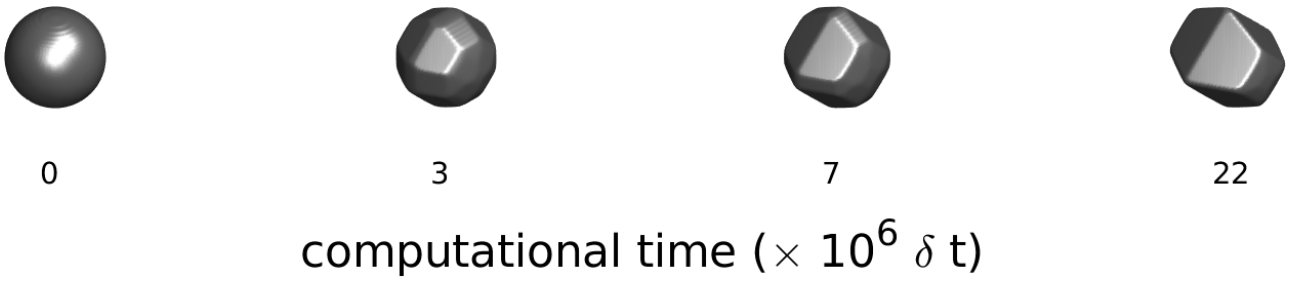

Figure 4.9: A time series of anatase-TiO_2 $\phi = 0.5$ iso-surface reached at 0, 3×10^6, 7×10^6 and 22×10^6 time step of the energy-minimising calculation. The parameters used in this calculation are $\epsilon = 0.02$, $\tilde{\beta} = 5 \times 10^{-3}$, $M = 1$, $s = \tilde{s} = 2$, $\delta t = 1 \times 10^{-7}$.

By allowing long enough evolution time the final minimum energy is reached and the corresponding interface for anatase-TiO_2 is shown in Fig. 4.9. The lowering of the CHW energy as the particle evolves starting from a sphere at $t = 0$ is plotted in Fig. 4.10. It can be seen that the bounding planes of the final shape are of {101} and {001}-type surfaces as according to the theory (Sec. 2.3.4) except at the sharp corners and edges. In Fig. 4.11a the equilibrium shape reached by energy-minimising calculation is compared with the analytical shape and it can be seen that the discrepancy occurs at the sharp corners and edges. The degree of which the corners and edges are rounded is controlled by the regularisation coefficient $\tilde{\beta}$ as discussed in Sec. 3.3.8. the effect of $\tilde{\beta}$ is illustrated in Fig. 4.11b-4.11c. A smaller $\tilde{\beta}$ gives sharper edges and corners.

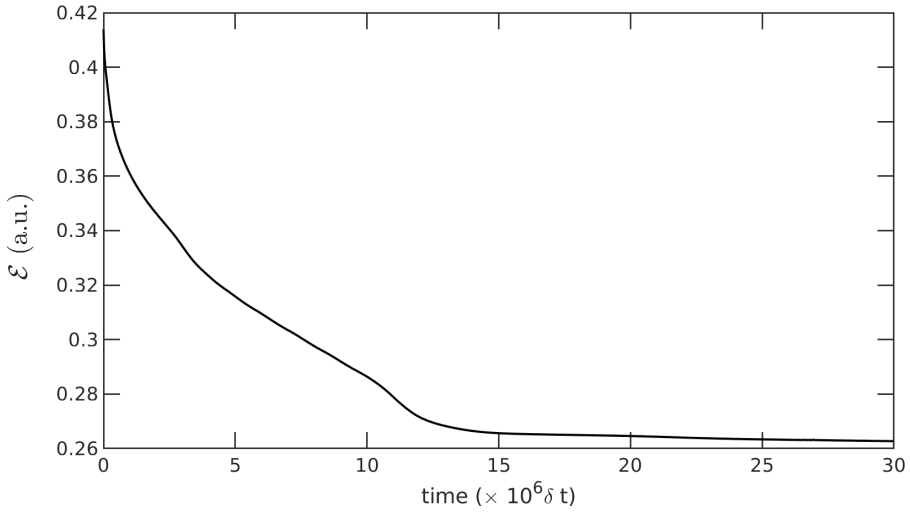

Figure 4.10: The lowering of the CHW energy $\mathcal{E}$ as the TiO_2 system evolves. The parameters used in this calculation are $\epsilon = 0.02$, $\tilde{\beta} = 5 \times 10^{-3}$, $M = 1$, $s = \tilde{s} = 2$, $\delta t = 1 \times 10^{-7}$.

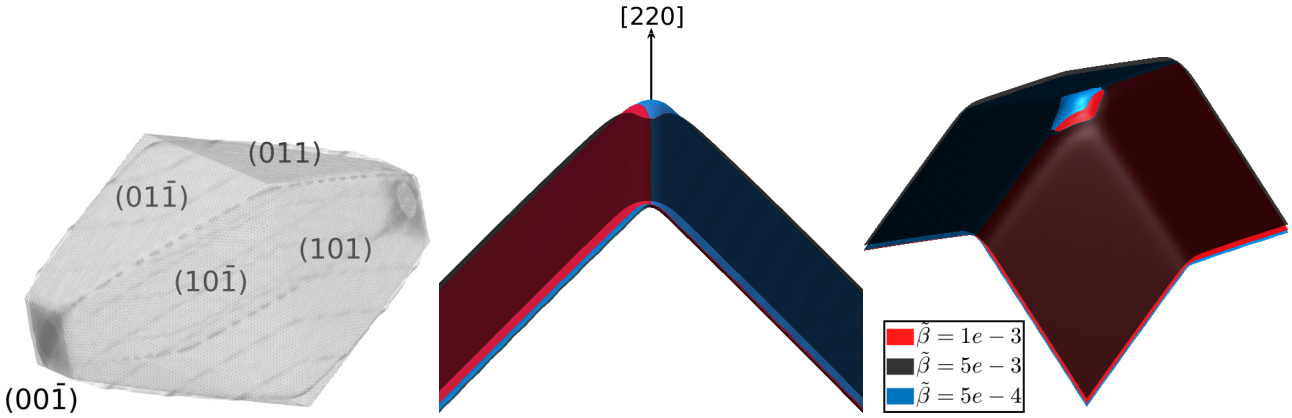

(a) (b) (c)

Figure 4.11: (a): the equilibrium shape reached by energy-minimising calculation using parameter $\tilde{\beta} = 5 \times 10^{-4}$ compared with the convexified ξ-plot. (b) and (c): the effect of coefficient $\tilde{\beta}$ on the sharpness of corners and edges, only one of the [220]-pointing corners is shown.

The same calculation is repeated for MgO using the γ values listed in Tab. 4.2. The time evolution of the shape of a particle is shown in Fig. 4.12 starting from an initial shape of a sphere to the final shape of a cube bounded by the {100} surfaces with 8 corners truncated by {111} surfaces.

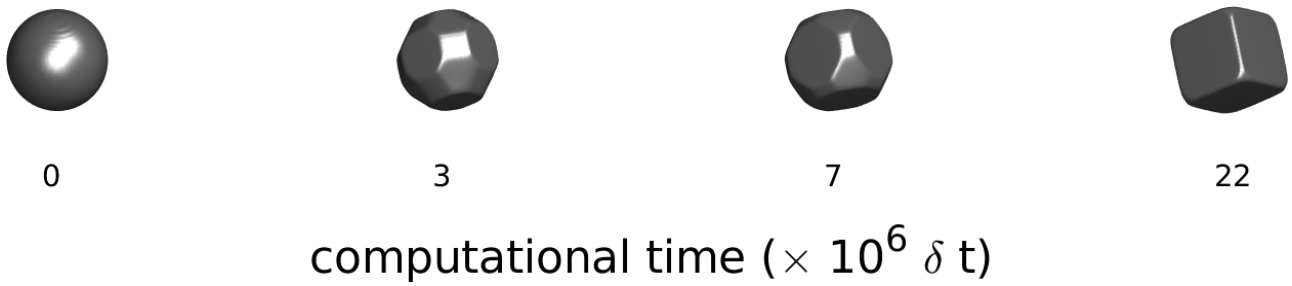

Figure 4.12: MgO $\phi = 0.5$ iso-surface plots of different stages of the energy-minimising calculation. The parameters used in this calculation are $\epsilon = 0.02$, $\tilde{\beta} = 5 \times 10^{-3}$, $M = 1$, $s = \tilde{s} = 2$, $\delta t = 1 \times 10^{-7}$.

5. Obliquely deposited MgO

5.1 Introduction

The technological importance of biaxially aligned polycrystalline thin films has attracted increasing attention to the characterisation and the study of the origin of texture formation, owing to the columnar microstructure developed during an OAD that shares many of the characteristics of single crystals. The film morphology resembles an array of aligned single crystals which enables the applications in preparing single-crystalline substrates [138, 139], coated-conductors [140, 141] and buffer layers [142, 143]. Both the out-of-plane and in-plane textures can be characterised by using XRD and RHEED surface pole figures [144]. It is found that the column tilt angle β and the degree of texturing are influenced by the vapour incident angle α [145, 146, 15]. In particular, negative β angles, indicating that the aligned single crystals are tilted away from the flux, are obtained for certain materials (e.g. MgO and CaF_2 films shown in Fig. 5.1) and α angles [15, 147]. This negatively valued β angle along with the relationship between α and β in these materials remain inconsistent with and unexplained by empirical laws [148, 149, 150] and existing theories [65, 75, 147, 151]. It does not come as a surprise because the material-specific crystal shapes are not accounted for in these works for a deposition process subject to complex geometric shadowing.

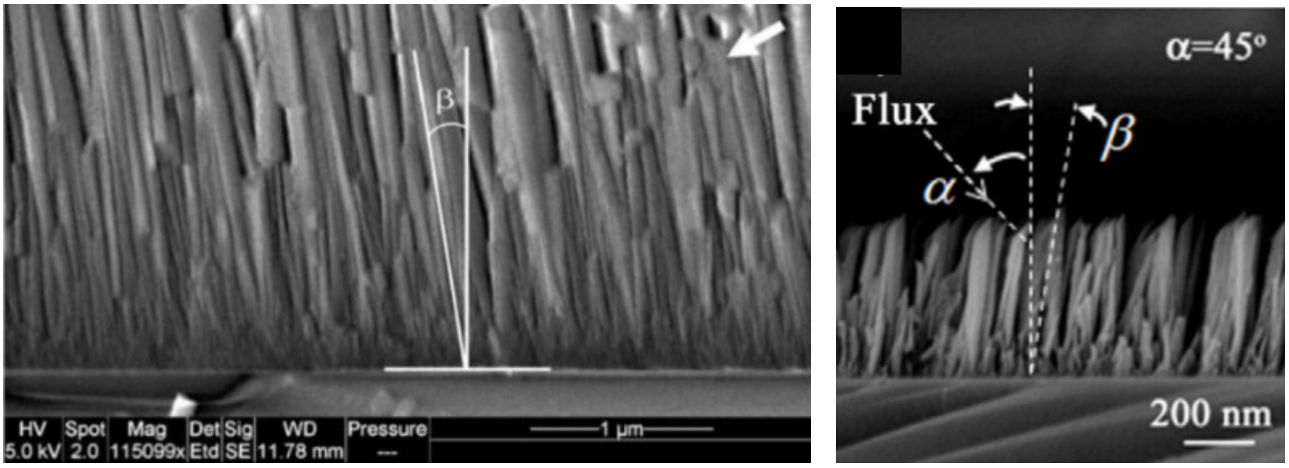

(a) (b)

Figure 5.1: SEM cross sections of the biaxially aligned (a) MgO (taken from [147]) and (b) CaF_2 (taken from [15]) nanocolumns grown by OAD with $\alpha = 55°$ and 45° respectively. The arrows indicate in-flux direction and β is the angle between the average growth direction of the nanocolumns and the substrate normal. β is measured at (a) -9° and (b) -10°. A negative β means the nanocolumns are tilted away from the materials flux.

The texture formation of polycrystalline thin films has been understood by competitive growth of the nanocolumns under shadowing effect imposed by the preferential deposition due to shadowing. A well-known orientation selection model of van der Drift's, termed principle of

evolutionary selection, has been used to predict the out-of-plane texture for various material symmetries subject to assumptions on the roles of surface diffusion, adparticle incorporation and grain impingement [65]. The in-plane texturing has been studied by Mahieu et al. in an extended structural zone model [75]. According to which, the in-plane alignment is attributed to a similar argument that for a predetermined out-of-plane texture, fully faceted grains oriented with geometrically fastest growing direction perpendicular to the substrate outgrow the neighbouring grains. The model also predicts, based on the concept of geometric capture length [151], the in-plane texture of cubic materials. Taking into account both the geometric shadowing and general equilibrium crystal shapes, the model has enjoyed varying degrees of success. Cubic materials with {111} or {110} faceted crystal habit* have one favourable in-plane orientation, e.g. the olique-angle-deposited yttria-stabilized zirconia (YSZ) [152] and Cr [18] thin films. However for materials with a {100} faceted crystal habit, the model predicts two preferential in-plane orientations. Only one in-plane texture is experimentally observed in TiN [153, 154, 155] and MgO [145, 156, 157, 158, 146] thin films.

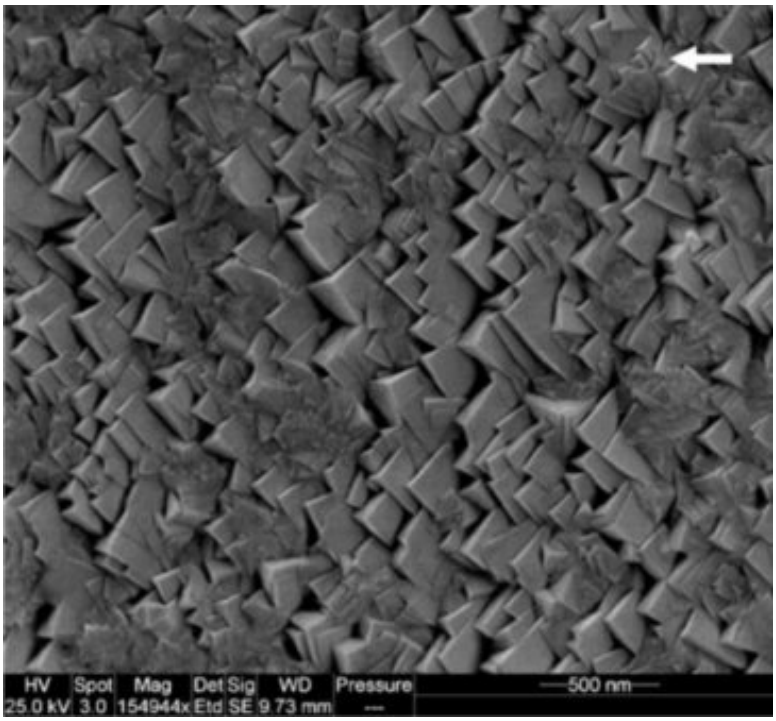

Figure 5.2: Plan view SEM image of the biaxially textured MgO thin film grown by OAD with $\alpha = 55°$ (taken from [147]). The arrow indicates in-flux direction.

Ghekiere et al. [147] addressed this discrepancy by adding the effect of self-shadowing of one of the {100} facets facing the atomic flux which overshadows the other facets. They showed that for $\alpha > 55°$ only one in-plane orientation has the fastest vertical growth rate. Fig. 5.2 shows the characteristic roof-tile surface morphology of the biaxially aligned MgO nanocolumns, the top exposed surfaces consist of a triangular surface which according to Ghekiere et al. [147] overshadows the adjacent surfaces of the same {100} family. Yet evidence suggests otherwise, there has been only one preferred in-plane orientation during the growth of biaxially textured MgO thin films, even for small α angles [145, 157, 146]. It is noted here that although this model considers quantitatively the preferential deposition induced by self-shadowing, the equilibrium crystal shape of MgO is used in the calculation, i.e. neglecting the presence of {110} and {111} surfaces and the relative surface diffusion, as opposed to a kinetically growing shape

*{111} or {110} being the lowest energy surface

during the orientation selection process of texture formation.

The existing theories assume the zone T growth conditions [75, 147], in which the surface diffusion on facets of a single grain is considered unlimited. This assumption means that once the adparticles are adsorped they diffuse instantly onto the facets already formed. It results in a fully faceted crystal shape that coarsens and the means by which the fastest growing grains are selected is through grain impingement. The nucleation and growth of new surfaces are not feasible in such growth models.

Experimental microscopy works show a different picture with all the biaxially textured thin films exhibiting a certain degree of porosity [14, 15]. For example, a large angle of incidence α grows nanocolumns of aligned single crystals that display large distance in between, as shown in the microstructures obtained with $\alpha = 45°$ (Fig. 5.1b) and $\alpha = 80°$ in [15]. Moreover the presence of low-angle grain boundaries owing to the biaxial alignment (as characterised by full width at half maximum (FWHM) of the X-ray phi-scans, also a measure of quality of the in-plane texturing, cf. [146] Fig. 5 & 6) suggests that the grain impingement is not the key effect in the competitive growth of these thin films.

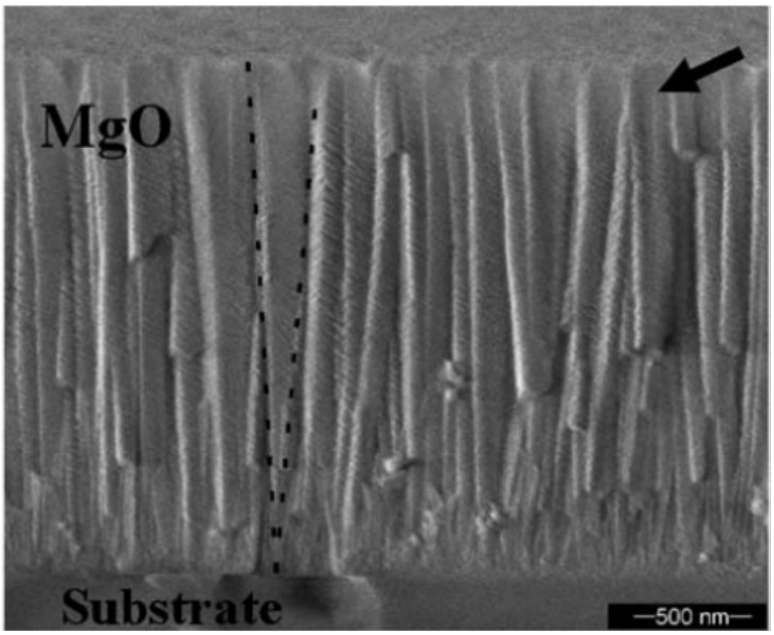

Figure 5.3: SEM cross sections of biaxially textured MgO thin film grown by OAD with $\alpha = 55°$ (taken from [18]). The dashed black lines outlines the shape of one of the crystallites. The laminar structure is visible on some of the crystallites.

In Fig. 5.3 the SEM image also reveals that the sides of the MgO nanocolumns are not fully faceted, but on which lateral instability develops resembling a laminar structure. A material-specific MD calculation shows that the sides of a single-crystal nanocolumn can be bounded by alternating surfaces and a 3-D Schwoebel–Ehrlich barrier may be responsible for the in-plane texture [159].

A big variety of the shapes of these single-crystal-like nanocolumns and their deviations from the equilibrium shapes cannot be explained by purely thermodynamic arguments. If the contributions to the single-crystal morphology from the kinetics are considered, the surface diffusion becomes finite and anisotropic. As a consequence, the out-of-equilibrium shapes are formed and they are controlled by the finite mobility and the surface energies. For an inverse problem a so-called polar v-plot has been constructed to perdict the kinetically frozen morphologies based on the crystal shapes obtained experimentally [160]. More directly a modified Wulff construction taking into consideration the kinetic parameters derived from atomistic information of the crystal lattice has explained a large number of out-of-equilibrium shapes of nanoparticles [161]. However these models assume an isolated single crystal with all its surfaces exposed to vapour or partially exposed due to the presence of substrate and therefore the preferential deposition is not accounted for.

In this work a continuum approach is adopted to include effects of both preferential deposition and the kinetics of surface diffusion. It is assumed that the effect of grain boundary impingement and the influence of substrate in the growth of biaxially textured polycrystalline thin films during OAD are negligible. The proposed model is assessed for an isolated single crystal of a prototype OAD-MgO system, which has been widely studied and characterised. Calculations of the vertical growth rates are carried out for model parameters shown consistent with experimental observations by the model assessment. The growth of crystallites with various out-of-plane and in-plane orientations are realised and evaluated alongside experimental characterisations. The model parameters that best reproduce the observed single-crystal morphology are identified.

5.2 Model description

5.2.1 Non-local shadowing

Shadowing is known to be a non-local effect which is more convenient to incorporate in geometric and atomistic models [6, 162, 8, 159]. However for the surface diffusion with highly anisotropic surface energy, it is desired to be realised in a continuum model. In the formalism of the surface diffusion Eqn. 4.4, the free energy functional $\mathcal{E}$ (defined in Eqn. 3.41) is independent of the interface topology, i.e., it is a local formulation. In the existing continuum models, the non-local shadowing have been modelled as flux decoupled from the surface effects, e.g. it can be included discretely in a line-of-sight approach [163, 164] or more recently a rigorous flux shielding algorithm is developed [12] in which the flux is represented by rays having prescribed trajectories.

A more natural way to incorporate the atomic flux in a continuum manner is to couple the dynamics of the local surface diffusion to the transport of the vapour field [165]. This approach has been widely used in modelling solidification in a convection field (e.g. the coupling of gas flow to a Cahn-Hilliard system [166]). The difference is that for the deposition processes taking place in low pressure environment, the adparticles follow some ballistic trajectories making an angle θ to the substrate normal, which can be conveniently modelled by the advection of a vapour field with some external velocity field. These process-specific velocity fields can then be linked to different deposition processes. The processes are usually modelled by different angular (cumulative) distribution function $\mathcal{P}(\theta)$ and the corresponding probability density function ${}^{d\mathcal{P}}/_{d\theta}$ [162]. For the OAD process there is only one possible incoming angle, i.e. α and therefore $\mathcal{P}$ can be modelled by a Heaviside step function $\mathcal{P} = H(\theta - \alpha)$ and the corresponding probability density function as a Dirac delta function ${}^{d\mathcal{P}}/_{d\theta} = \delta(\theta - \alpha)$. The choice of such a $\mathcal{P}$ results in a constant velocity field.

5.2.2 Formulation

The model is based on the surface diffusion Eqn. used in Sec. 4.3 and a linear advection equation. Two scaler fields are introduced and coupled through the source and sink terms in the diffusion and advection equations respectively.

$$\frac{\partial \phi}{\partial t} = \nabla \cdot \left(M \nabla \frac{\delta \mathcal{E}}{\delta \phi} \right) + \mathcal{A}(\nabla \phi)^2 g \qquad \text{in} \quad \Omega \tag{5.1}$$

$$\frac{\partial g}{\partial t} = -\vec{R} \cdot \nabla g - B(\nabla \phi)^2 g \qquad \text{in} \quad \Omega \tag{5.2}$$

The vapour field, denoted by order parameter $g(\vec{r}, t)$ in the model, takes on value $g = 1$ in the vapour and $g = 0$ in the solid. Similarly the phase field parameter $\phi(\vec{r}, t)$ of the diffusion Eqn. 5.1, has value 1 in the solid and 0 in the vapour. In Eqn. 5.2 the ballistic transport is modelled by the advection of the vapour field g with an external velocity field $\vec{R}$, plus a sink term that is made operative only in the interfacial 'skin' region by a surface delta function $(\nabla \phi)^2$. The magnitude of the sink term B is set sufficiently large[†] for an effective consumption of the g field in the interfacial region. This way the non-local shadowing is naturally incorporated by the coupling of the dynamics of the ϕ field and g field.

[†]It is set to $B = |\vec{R}|$ so that all adatoms that arrive at the interface are consumed.

where M is the mobility, $\mathcal{E}$ and $\frac{\delta\mathcal{E}}{\delta\phi}$ are the CHW energy and the generalised chemical potential, defined by Eqn. 3.41 and 3.42 respectively. One may recognise that the coupled Eqns. 5.1 and 5.2 form the deterministic part of the Keblinski model [165] in which the interfacial region characterised by $(\nabla\phi)^2$ grows at the expense of the g field. The isotropic energy in the original Keblinski model is replaced by the anisotropic CHW energy. The growth is enabled by adding a source term $\mathcal{A}$ to the diffusion Eqn. 5.1. To suit a realistic, process-specific deposition, modification is made so that not all adatoms arriving at the surface are incorporated, but that the relative abundance of acceptance is dependent on the angle between the unit normal of the surface $\vec{n} = \frac{\nabla\phi}{|\nabla\phi|}$ and $\vec{R}$.

$$\mathcal{A}(\vec{n}, \vec{R}, \eta) = (1-\eta)\vec{R}\cdot\vec{n} + \eta\|\vec{R}\times\vec{n}\| \tag{5.3}$$

Akin to an angle-dependent coefficient called acceptance introduced by van der Drift [65], in Eqn. 5.3 the coefficient $\mathcal{A}(\vec{n})$ is composed of two terms that correspond to the normal $\vec{R}\cdot\vec{n}$ and lateral $\|\vec{R}\times\vec{n}\|$ adsorption modes. The adsorption modes dictate the acceptance of adatoms incorporated into the interface. This differs from Keblinski model as $\mathcal{A} \neq B$, i.e. the coefficient is not a constant. η is a parameter controlling the relative contribution of these two modes to the incorporation. $\eta = 1$ and $\eta = 0$ correspond to the sine and cosine dependence of the acceptance function respectively.

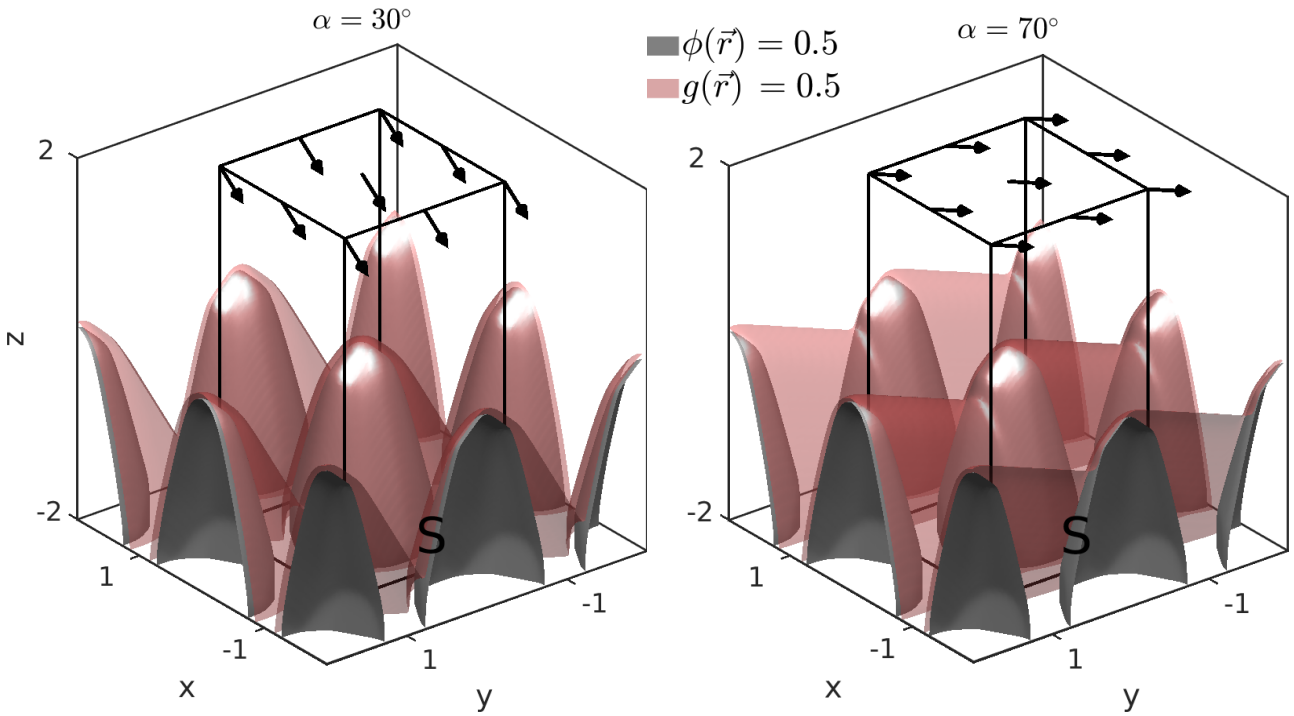

(a) (b)

Figure 5.4: The simulation cell as highlighted by the inner wireframes, of which periodic boundary conditions are considered for the lateral boundaries. Different angles of incidence $\alpha = \angle(\vec{R}, \vec{n}_{sub})$ can be distinguished by the visualisation of the 0.5 iso-surface of the g field. The grey protrusions in the figures stand for the $\phi = 0.5$ iso-surface. Rain vectors $\vec{R}$ associated with (a) $\alpha = 30°$ and (b) $\alpha = 70°$ are plotted with rescaled magnitude.

The domain is taken to be $\Omega = [\text{-}1, 1]^2 \times [\text{-}2, 2]$, as shown by the inner wireframe in Fig. 5.4. For simplicity the generalised chemical potential $\frac{\delta \mathcal{E}}{\delta \phi}$ is denoted by μ. Periodic boundary conditions along x and y directions are applied for ϕ, μ and g to allow for inter-columnar shadowing, whereas Neumann boundary conditions $\nabla\mu|_{z=\pm 2} = \nabla\phi|_{z=\pm 2} = 0$ are employed in z. The inflow boundary condition at $z = 2$ for the g field is set to $g = 1$, i.e. to maintain a constant supply of the vapour. No outflow boundary condition is imposed at domain boundary $z = \text{-}2$.

5.2.3 Link to deposition parameters of an OAD system

The model parameters can be linked to some of the deposition parameters of the thin film system in a laboratory frame. Firstly, the constant velocity field as represented by the rain vector $\vec{R}$ makes an angle to the substrate normal $\vec{n}_{sub}$ and this is known experimentally as the angle of incidence $\alpha = \angle(\vec{R}, \vec{n}_{sub})$. Secondly, the magnitude of the rain vector $|\vec{R}|$ is associated with the deposition rate. Thirdly, $\phi = 0.5$ iso-surface is defined to be the material interface that separates the solid from the vapour.

For a demonstration, an arbitrary sinusoidal interface is illustrated in Fig. 5.4 in grey. Two different g fields are evolved to steady state with two sets of α angles and the corresponding rain vectors $\vec{R}$. For the same site S, marked in Fig. 5.4 and their periodic images, they are overshadowed by nearby protrusions in Fig. 5.4b with a larger α value compared with smaller α value in Fig. 5.4a. Lastly, the shapes reached at the stage also make a few characteristic angles to the substrate normals which are defined and discussed in Sec. 5.3. A list of symbols used in this chapter is included in Tab. 10.3.

5.3 Model assessment

For the MgO polycrystalline thin film, the development of film structure is considered to be independent of the nature of the substrate, i.e. no external force acting on the crystals. This is generally the case for systems under conditions of low substrate temperature and/or high deposition rate, whose surface mobility is limited [20]. Assuming this is true for a typical OAD-MgO system, and given the evidence of negligible grain boundary impingement* and the biaxially textured microstructure of well-aligned single crystals, the microstructural development of the film can be simplified by the growth of an isolated single crystal. The single-crystal morphologies reached by long-time evolution according to Eqns. 5.1 and 5.2, is subsequently explored with some pre-defined M and $\vec{R}$ values.

5.3.1 Model setup

The growth of an isolated MgO crystallite is simulated by solving ϕ, μ on a $128 \times 128 \times 256$ Fourier-LGL grid for each time step $\delta t = 1 \times 10^{-5}$ using the time integration scheme adapted from Eqn. 4.8 and a Fourier-Legendre-Galerkin solver built on top of the weak formulation of 4.10 (Sec. 4.3.1). g is solved by numerically integrating Eqn. 5.2 using the LGL quadrature rule†. The inflow boundary condition for the g field at $z = 2$ is imposed strongly.

*evident in the low grain boundary angle as discussed in Sec. 5.1

†as opposed to the exact integration property that the matrix equation 4.10 uses. The schemes used are varied depending on the stability of the hyperbolic equation 5.2.

Nucleation is not modelled, and the simulation is begun with spherical nucleus (seeds) with radius 0.5 centered at (x, y, z) = (0, 0, -1). The crystallographic orientations of the seeds were varied. The initial configuration for ϕ takes on the equilibrium hyperbolic profile 4.14 of signed distance function to an isolated sphere of radius 0.5. The initial configuration of the g field is obtained using the initial condition for ϕ and allowing g to evolve in order to reach steady state.

$$\phi(x,y,z) = \frac{1}{2}\left[1 + \tanh\left(\frac{\sqrt{x^2+y^2+(z+1)^2} - 0.5}{2\sqrt{2}\epsilon\tilde{\gamma}(\vec{n})}\right)\right] \tag{5.4}$$

5.3.2 The MgO-OAD system

The anisotropic surface energy density function $\tilde{\gamma}(\vec{n})$ appearing in the initial condition 5.4 and the CHW energy $\mathcal{E}$ in Eqn. 3.41, is constructed using Eqn. 4.2 based on *ab initio* results of surface energies in Tab. 4.2. In all the simulations same values are used for the phase field parameters, and they are $\epsilon = 0.02$ and $\tilde{\beta} = 0.005$ to ensure relatively sharp facets. Similarly, the free energy density parameter α_0, γ_{ref}, γ_0 and w_i in Eqn. 4.2, are chosen to be 0.1, $\gamma_{\{110\}}$, $1.1 \times \gamma_{\{110\}}$ and 100 respectively. All simulations are run using the same set of these parameters. The values of the parameters used in this chapter are summarised in Tab. 10.2.

For an oblique angle deposited MgO system [1 1 1] is usually considered as the preferred growth direction. However it has been shown in [157, 147, 18, 146] that [1 1 1] is tilted away from the substrate normal, depending on the incident angle α. Subsequently a local coordinate system x', y', z' is defined for the crystal, so that they match the crystallographic directions [0 $\bar{1}$ 1], [2 $\bar{1}$ $\bar{1}$], [1 1 1] and a substrate normal [1 1 n] where n is varied depending on the angle γ between [1 1 n] and [1 1 1]. $\vec{R}$ is set to:

$$\vec{R} = |\vec{R}| \cdot \begin{bmatrix} 0 \\ -sin(\alpha) \\ -cos(\alpha) \end{bmatrix} \tag{5.5}$$

The y-component of $\vec{R}$ is negatively signed by the default in-plane orientation relative to the flux. As will be explored in Sec. 5.6, the sign of which can be changed in order to configure a different in-plane orientation. In Fig. 5.5 the crystal coordinate system, $\vec{R}$ and the characteristic angles are marked on a single-crystal nanocolumn having a {100} crystal habit. ω is the angle between [0 0 1] and [1 1 n] that characterises the in-plane orientation. The values of γ together with ω define the orientation relationship between the crystal and the substrate and they are varied between simulations so that a tilt angle β of the nanocolumn is obtained.

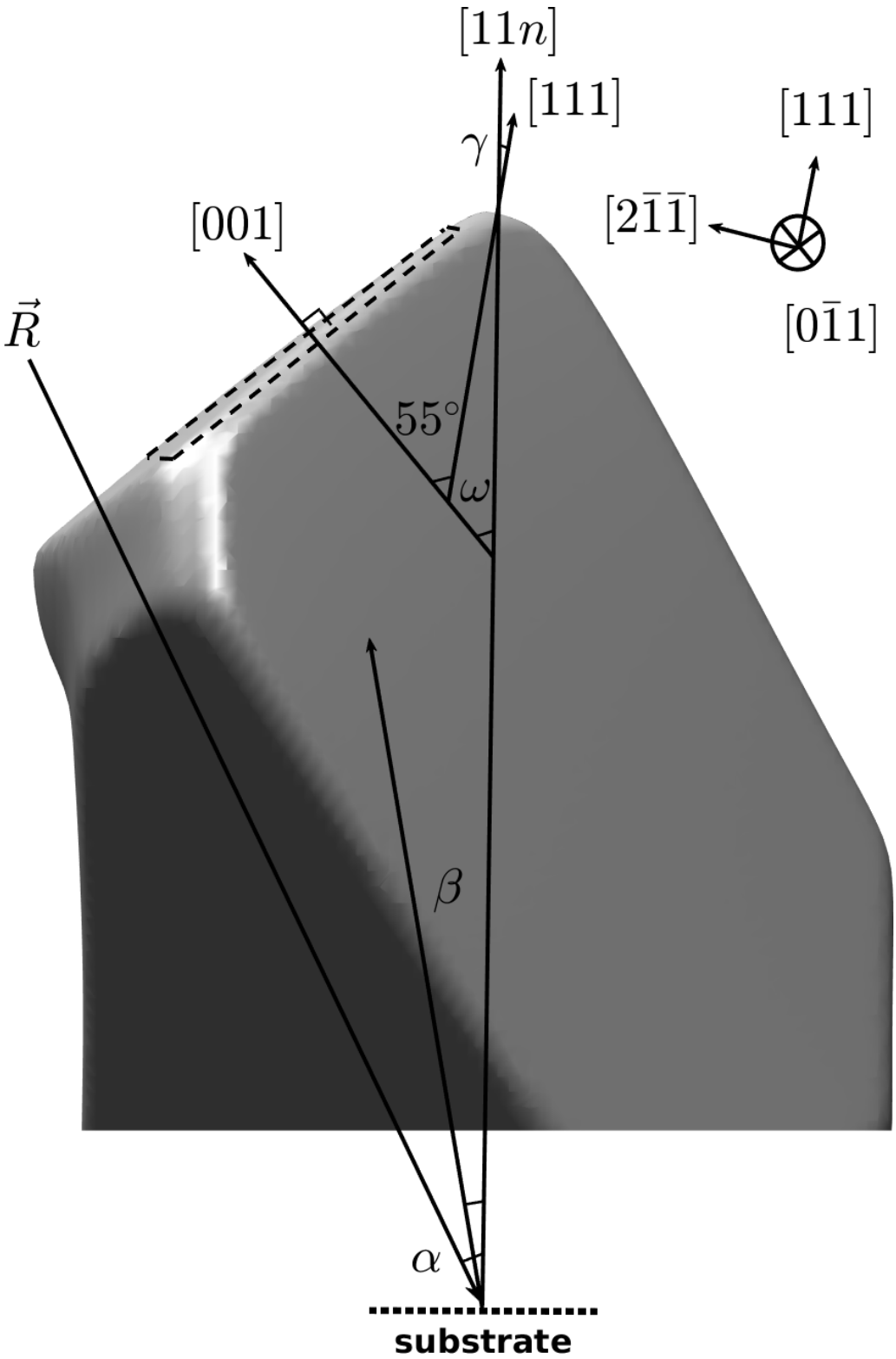

Figure 5.5: A single-crystal nanocolumn having a {100}-habit and the schematics marking the angles α, β, γ, ω.

The exact angle between [1 1 1] and [0 0 1] of cubic symmetry is $54.7356° \approx 55°$ and Xu et. al. [146] used the [100] tilt angle $\beta = 55° - \gamma$ to characterise the growth angle of biaxially aligned MgO nanocolumns. A relationship between this angle and α termed 'two third rule' is therefore obtained and compared with existing empirical tangent law [148] and cosine law [149]. However this angle is not equivalent to the physical tilt angle of the nanocolumns, i.e. $\beta \neq 55° - \gamma$, that the empirical laws predict. As a matter of fact, this column tilt angle β can be negatively valued [147, 18] to which all empirical laws and existing theories do not apply. This suggests that the nanocolumns are not bounded by facets of minimum surface energy only, in which case there should be a linear dependence of the column tilt angle on the crystal orientation. Hence it is hypothesised that this is due to the growth regime in which these nanocolumns develop a biaxial texture and nano-faceted morphologies is controlled by kinetics.

5.4 Growth regimes

In an experimental work [146], biaxially aligned nanocolumns were deposited at different α angles 0°, 25°, 35°, 57°. The preferred out-of-plane orientations γ are reported to be 0°, 39°, 32°, 19° respectively. Given these sets of discrete deposition parameters α and γ, long-time evolution of the systems with various model parameters M, $\vec{R}$, η is performed. For all simulations, $|\vec{R}|$ is kept constant so that the value of M controls the growth.

As far as modelling is concerned, a quantitative description of an OAD system requires detailed measurements of the flux density and surface diffusion mobility. Unfortunately their values are not accessible in the known experimental works. Instead, processing parameters such as chamber pressure, source-to-substrate distance and substrate temperature are given which vary from process to process. Some MD models (e.g. [159]) assume physical values of deposition rate and the kinetic energy of incident atoms but they are not derived from the actual processing parameters of the experimental system. In addition, the nature of the growth for a solid-vapour interface is much more complex than the mechanisms upon which the existing atomistic models are built. Similar to those considered previously in continuum approaches of thin film growth under shadowing [6, 12] and within the framework of the phase field model Eqns. 5.1 and 5.2, a non-dimensional parameter is identified for controlling the growth regime, i.e. the ratio between surface diffusion mobility M and the deposition rate $|\vec{R}|$. The physical relevance of model parameters M and $|\vec{R}|$ can be linked to processing parameters, e.g. temperature and vapour pressure, but the one-to-one relationship is unknown.

The column tilt angle β reached in a long-time evolution is used to characterise nano-columnar morphologies and hence the magnitude of the model parameters. To this end and following e.g. [14, 15] for the measurement of β, the value is given by the angle between $[1\,1\,n]$ and the average growth direction. A summary of input parameters described in this section is given in Tab. 5.1. β was determined for each set of the input parameters.

Table 5.1: A summary of input parameters described in this section.

	model input parameters			
	α	γ	η	$M/\lvert\vec{R}\rvert$
values	0°	0°	0, 1	10^{-4}, 10^{-3}, 10^{-2}, 10^{-1}, 1
	25°	39°		
	35°	32°		
	57°	19°		

It has been observed that there are three distinct regimes of film growth whose late-stage microstructures are reflected by the morphologies of the individual isolated crystallites. For a large $M/\lvert\vec{R}\rvert$ value the influence of the preferential deposition due to shadowing can be neglected, and the crystallites grow into their fully faceted, near-equilibrium shapes. A column tilt angle is dependent on the crystallographic orientation in this instance, and the tilt angle of the (100) plane $\omega = 54.7° - \gamma$ is used to distinguish morphologies obtained by different α and γ values, as shown in Fig. 5.6 on the right y-axis. The resulting microstructure development therefore follows case (i) or (ii) of the van der Drift model, according to which out-of-plane texturing happens upon grain boundary impingement and there is no in-plane texture. By contrast, a small $M/\lvert\vec{R}\rvert$ value results in negligible surface diffusion and the crystal is not bounded by crystalline planes. Every accepted adatom stays where it was incorporated, and by virtue of a preferential incident flux the column tilt angle is equal to α, as evident in Fig. 5.6 for small $M/\lvert\vec{R}\rvert$ values. This regime is described by case (iv) of the van der Drift model.

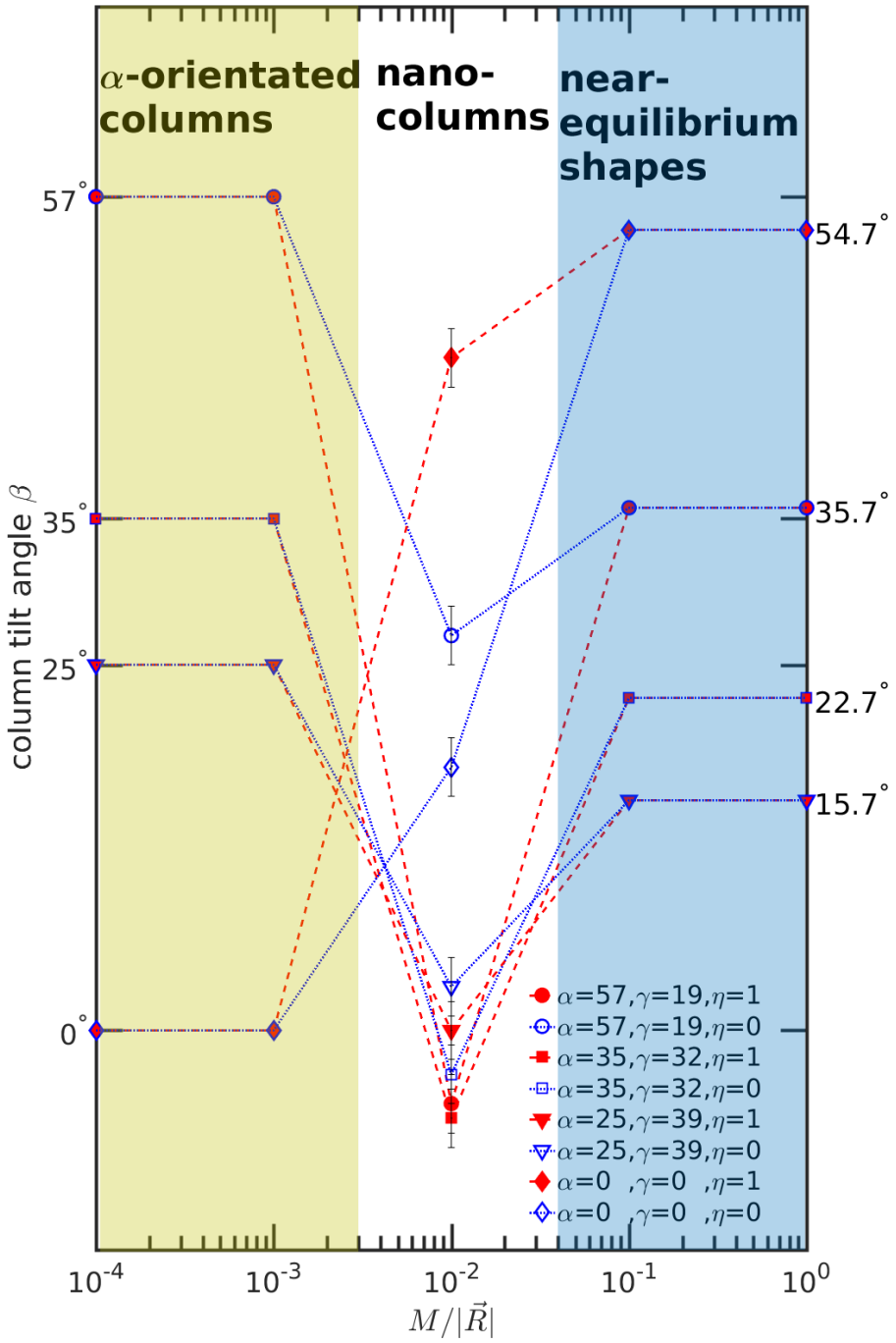

Figure 5.6: Three distinct regimes characterised by the $^{M}/_{|\vec{R}|}$ values. The $\pm 2°$ error bars for the measurement of column tilt angles are only applicable in the nano-columnar regime as the angles are exact in the other two regimes.

There exists an intermediate regime marked by a finite diffusion for which it is hypothesised to be the necessary condition for the biaxial texture formation. It has been found that above around $^{M}/_{|\vec{R}|} = 0.03$ the coarsening due to surface diffusion onto all facets makes an average growth direction hard to determine, the shapes resemble that of an fully faceted near-equilibrium shape. Whereby below around $^{M}/_{|\vec{R}|} = 0.002$ the typical faceted shape is lost. In between $^{M}/_{|\vec{R}|} = 0.03$ and $^{M}/_{|\vec{R}|} = 0.002$, nanocolumns are developed. The angle measurement of β involves drawing of trendlines (e.g. in Fig. 5.1) which is subject to a human error. This random error is estimated to be around $\pm 2°$ across various morphologies of the nanocolumns in the nano-columnar regime. The estimated error bars for β are only applicable in this regime because they are non-exact as opposed to the tilt angles in the other two regimes. Thus far

and to the best of the author's knowledge, statistical analysis of β in relation to α has not been reported in the literature for an OAD-MgO system. What have been systematically analysed are the tilt angles of the MgO (100) plane ω, evaluated using XRD pole figures [146]. ω should be distinguished from the column tilt angle β. In Fig. 5.6 there are a few β values below 0° in the nano-columnar regime. The nanocolumn with parameters $\alpha = 57°$, $\gamma = 19°$, $\eta = 1$ in particular has a β value -5° $\pm$ 2° that is comparable to a reported values in the range of -10° to 0° for biaxially aligned MgO nanocolumns [147, 18].

5.4.1 Characteristic energy, length and time

Recall Eqn. 5.1 and denote the dimensional energy, displacements in x, y, z and time by $\bar{E}$, $\bar{L}$ and $\bar{t}$, where

$$\bar{E} = \frac{\mathcal{E}}{E_0} \qquad \bar{L} = \frac{L}{l_0} \qquad \bar{t} = \frac{t}{\tau_0}$$

and similarly assume the dimensional coefficients $\bar{M}$ [$\mathrm{m^5 J^{-1} s^{-1}}$], $\bar{\mathcal{A}}$ [$\mathrm{m^2\, s^{-1}}$], the gradient operator $\bar{\nabla}$ [$\mathrm{m^{-1}}$] and the chemical potential $\frac{\delta \bar{E}}{\delta \phi}$ [$\mathrm{J/m^3}$] by the following forms:

$$\bar{M} = \frac{E_0 \tau_0}{l_0^5} \cdot M \qquad \bar{\mathcal{A}} = \frac{\tau_0}{l_0^2}\mathcal{A} \qquad \bar{\nabla} = l_0 \nabla \qquad \frac{\delta \bar{E}}{\delta \phi} = \frac{l_0^3}{E_0}\frac{\delta \mathcal{E}}{\delta \phi}$$

The dimensional form of Eqn. 5.1 therefore becomes:

$$\frac{1}{\tau_0}\frac{\partial \phi}{\partial \bar{t}} = \frac{\cancel{l_0^5}}{\cancel{E_0}\tau_0}\frac{\cancel{E_0}}{\cancel{l_0^2} \cdot \cancel{l_0^3}}\bar{M}\bar{\nabla}^2\frac{\delta \bar{E}}{\delta \phi} + \frac{\cancel{l_0^2}}{\tau_0 \cancel{l_0^2}}\bar{\mathcal{A}}(\bar{\nabla}\phi)^2 g \tag{5.6}$$

By the same token, if the dimensional rain vector $\bar{\vec{R}}$ [$\mathrm{m\, s^{-1}}$] and coefficient $\bar{B}$ [$\mathrm{m^2\, s^{-1}}$] take the forms:

$$\bar{\vec{R}} = \frac{\tau_0}{l_0}\vec{R} \qquad \bar{B} = \frac{\tau_0}{l_0^2}B$$

the dimensional form of Eqn. 5.2 becomes:

$$\frac{1}{\tau_0}\frac{\partial g}{\partial \bar{t}} = -\frac{\cancel{l_0}}{\tau_0}\frac{1}{\cancel{l_0}}\bar{\vec{R}} \cdot \bar{\nabla} g - \frac{\cancel{l_0^2}}{\tau_0 \cancel{l_0^2}}\bar{B}(\bar{\nabla}\phi)^2 g \tag{5.7}$$

In order to examine a realistic system, the numerical values of the model parameters used are required to match the orders of magnitudes of those found in an experimental system. In other words, the characteristic energy, length and time E_0, l_0 and τ_0 set by the model parameters should be comparable to their corresponding values of a physical system. The interrelationships between E_0, l_0, τ_0 and those of a realistic system have not been explored or proposed in any of the existing works [165, 62, 63, 12, 111, 112, 113].

In the simulations, the magnitude of the rain vector $|\vec{R}|$ is kept constant while the phenomenological mobility M is varied. This is equivalent to say that $|\vec{R}|$ sets the characteristic time. For a characteristic energy, recalling the non-dimensional form of the CHW energy introduced in Sec. 3.3.8, the units of both terms of the integrand are carried by $\frac{\tilde{\gamma}(\vec{n})}{\epsilon}$ and $\frac{\tilde{\beta}}{2\epsilon^3}$. The dimensional forms of these two terms have the unit of $\mathrm{J\,m^{-3}}$, because $\mathcal{F} = f(\phi) + \frac{\epsilon^2}{2}|\nabla\phi|^2$ is dimensionless. In addition, the dimensional surface energy density γ [$\mathrm{J\,m^{-2}}$] is constructed using the formula:

$$\gamma(\vec{n}) = \gamma_0\left(1 - \sum_{i=1}^{M}\alpha_i(\vec{m}_i\cdot\vec{n})^{w_i}\Theta(\vec{m}_i\cdot\vec{n})\right)$$
$$\alpha_i = 1 - \left(\frac{\gamma_i}{\gamma_{ref}}\right)(1-\alpha_{ref}) \tag{5.8}$$

in which the surface energy density values of specific facets γ_i [$\mathrm{J\,m^{-2}}$] are normalised by γ_{ref}. In the simulations, the reference is chosen to be the facets having the largest surface energy density and $\gamma_0 = 1.1 \times \gamma_{ref}$. Assuming $l_0 = 100\,\mathrm{nm}$ and γ_{ref} sets the characteristic energy, i.e. $E_0 = \gamma_{ref} \times l_0^2 = 2.25 \times 10^{-14}\mathrm{J}$. As for a characteristic time, a reasonable choice has the order of magnitude of 1 s. Assuming these characteristic energy, length and time, $|\vec{R}|$ and $\bar{M}$ can be shown to have the value of $1 \times 10^7 \times |\vec{R}|$ [$\mathrm{m\,s^{-1}}$] and $2.25 \times 10^{21} \times M$ [$\mathrm{m^5 J^{-1} s^{-1}}$]. Because the exact values for E_0, l_0 and τ_0 are unknown to specific experimental systems, the dimensionless energy, length, time and the dimensionless forms of the parameters are used throughout the following sections.

5.5 Preferred out-of-plane orientation for film growth

According to the principle of evolutionary selection, the crystallites with the fastest growth direction perpendicular to the substrate ($\beta = 0°$) outgrow the neighbouring grains and hence define the texture [65]. The out-of-plane orientation giving rise to this fastest growth is considered the preferred out-of-plane orientation. The underlying assumption for this theory is that the surface diffusion is infinite and the kinetics is not taken into consideration. For a finite surface diffusion in the nano-columnar regime, the anisotropic growth must be considered, as crystallites of different growth directions in this regime can develop different growth rates. Therefore the criterion can be boiled down to the out-of-plane orientation that yields the fastest vertical rate of growth, which in turns defines the out-of-plane texture in the nano-columnar regime. Hence it is useful to test the model against experimentally determined out-of-plane orientation reported in [146]. The calculations are limited to $\alpha = 57°$ incident angle, because β has only been reported around this deposition angle [147, 18]. The effect of model parameter η is also investigated. The vertical growth rates are determined by the z-coordinate of the

top surface of the interface during the growth of a nanocolumn, which is plotted against the deposition time in Fig. 5.7. A summary of input parameters used in this numerical experiment is given in Tab. 5.2.

Table 5.2: A summary of input parameters described in this section.

	model input parameters			
	α	γ	η	$M/\lvert\vec{R}\rvert$
values	57°	9°	0, 0.5, 1	0.01
	57°	19°		
	35°	29°		

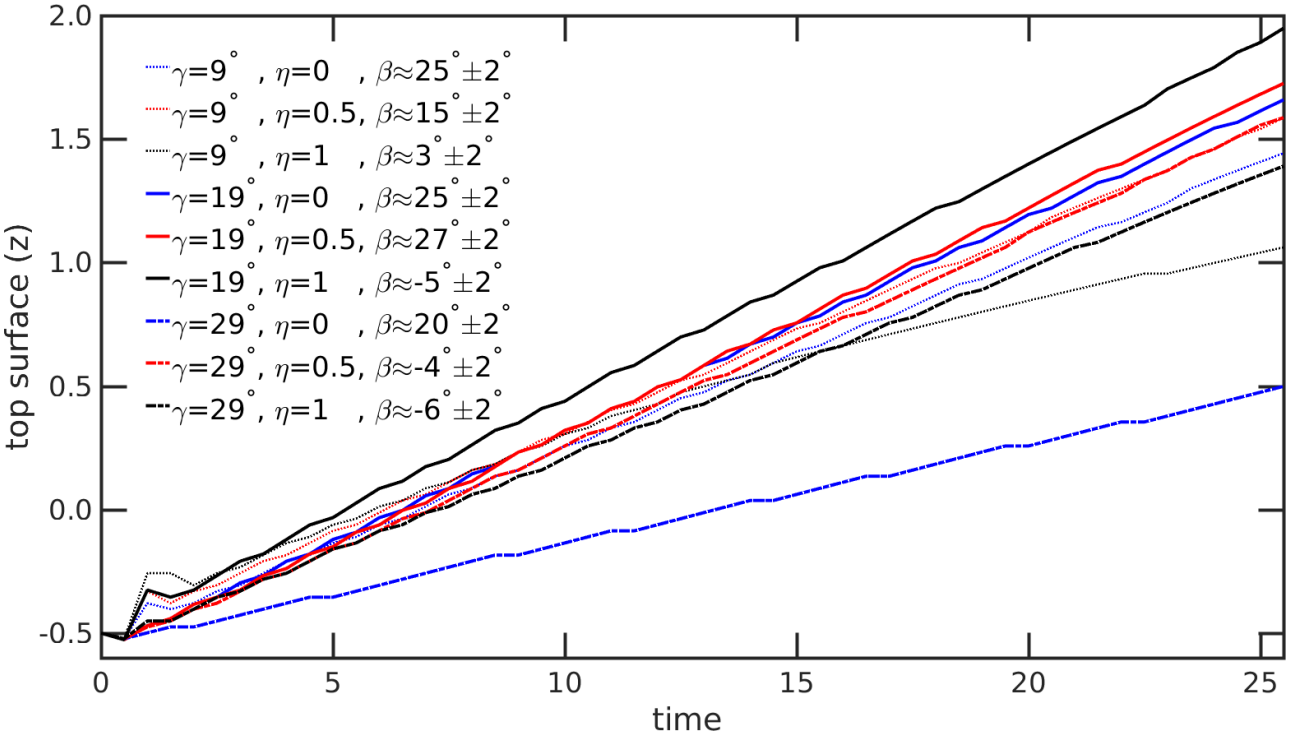

Figure 5.7: z coordinate of the top surface (sampled every interval $\Delta t = 0.5$) of nanocolumns grown under vapour incidence angle $\alpha = 57°$, $\delta t = 1 \times 10^{-5}$, $M/\lvert\vec{R}\rvert = 0.01$ and the corresponding γ, η and β values.

For $\alpha = 57°$ depositions in Fig. 5.7, the nanocolumns having an out-of-plane orientation $\gamma = 19°$ outgrow the others. In particular, the one with model parameter $\eta = 1$ happens to yield not only the fastest vertical growth rate but also a negative β angle that is within the range -10° $< \beta < 0°$ in agreement with the experiment [147, 18]. It has also been shown feasible for $\gamma = 29°$ to have a negative β angle with the same $\eta = 1$ setting, but more tilted away from the substrate normal compared with $\gamma = 19°$. In fact, it has been experimentally observed not only for MgO but also other biaxially textured thin films to have a negative column tilt angle, i.e. fastest growth direction is tilted away from incoming flux [14, 15], though not addressed in terms of a growth model. Some suggest that this is due to the anisotropy in adsorption energies of the surfaces [15]. It is reasonable to attribute this nonintuitive result to the model parameter $\eta = 1$

which signifies the sine dependence of the acceptance function, i.e. $\mathcal{A} \sim sin\big(\angle(\vec{R}, \vec{n})\big)$, from a continuum standpoint. Physically, this may suggest that the microscopic/atomistic growth mechanisms (e.g. adsorption, desorption and step bunching) favour the step flow growth mode [167].

For an offset angle as much as 10° the nanocolumns can develop vastly different β angles ranging from -9°±2° to 27°±2°. The average growth directions are determined at the late stage of growth. In the early stage, unphysical structuring of the initial spherical shape occurs due to the seeding necessary in a simulation, as detailed by the initial condition Eqn. 5.4 in Sec. 5.3. This is reflected by the bumps in the z v.s. t curves for $t < 2.5$ in Fig. 5.7. It may be appealing to find an empirical law for these curves (e.g. a linear fit), but it should be noted that the vertical component of the anisotropic growth rate in 3D is not only dependent on α and model parameters ${}^{M}/_{|\vec{R}|}$, η but also the crystallographic orientation, i.e. γ and ω. To model the vertical growth rate by an empirical law that universally applies to all systems is to oversimplify the problem, though it is possible from a modelling standpoint to construct sharp-interface growth laws for the growth rate $v_n = v_n(\alpha, \vec{n})$, cf. [164]. On the other hand, for simplicity only the height of the nanocolumn tip is monitored here. In order to get an idea of the late-stage roughening behaviour of the thin film, e.g. the growth exponent, it must be taken into account the topographical surface of the single-crystal nanocolumn with preferred orientation as well as the variation in the orientation of these aligned crystallites which contribute to the surface roughness calculation.

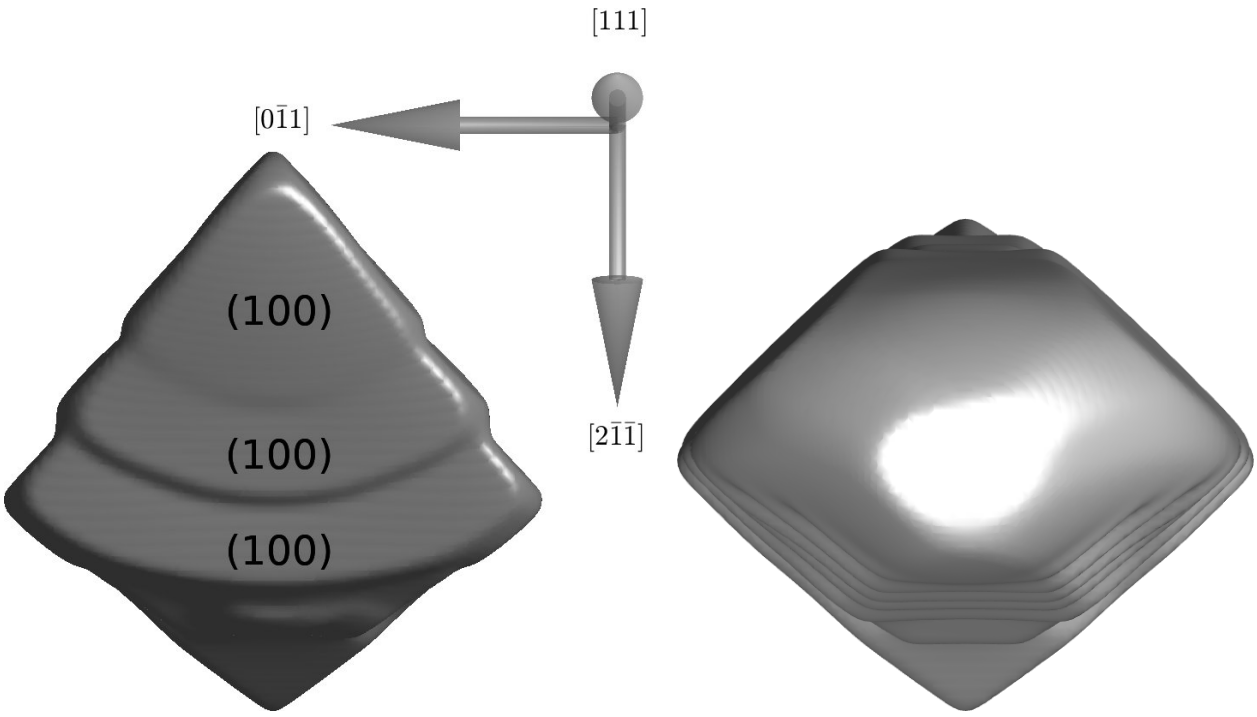

(a) $\eta = 1$, β = -6° (b) $\eta = 0$, β = -3°

Figure 5.8: The influence η on β as well as surface morphology in the nano-columnar regime: (a) exposed {100} top surfaces and (b) no {100} facet formed on the top surface . Other deposition parameters used for the two nanocolumns include: $\alpha = 35°$, $\gamma = 32°$ and ${}^{M}/_{|\vec{R}|} = 0.01$. The [111] arrow is pointing out of the page.

The model parameter η also has considerable influence on the surface morphology of the nanocolumns. For some deposition parameters the growth of trianglar {100} facets on the top are favoured by the deposition process with model parameter $\eta = 1$. This is shown in Fig.

5.8 in comparison with $\eta = 0$ where the formation of {100} facet on the tip of the nanocolumn is not favoured by the preferential deposition. The morphologies of the nanocolumns in the late stage should be discussed on an individual basis, e.g. some are more or less bounded by the {100} planes on the sides and some develop a triangular top surface, as will be discussed in Sec. 5.7.2. A selection of the morphologies of the nanocolumns are shown in Fig. 5.9 with model parameters as well as the measured β angles. The morphologies are discussed in details in Sec. 5.7.

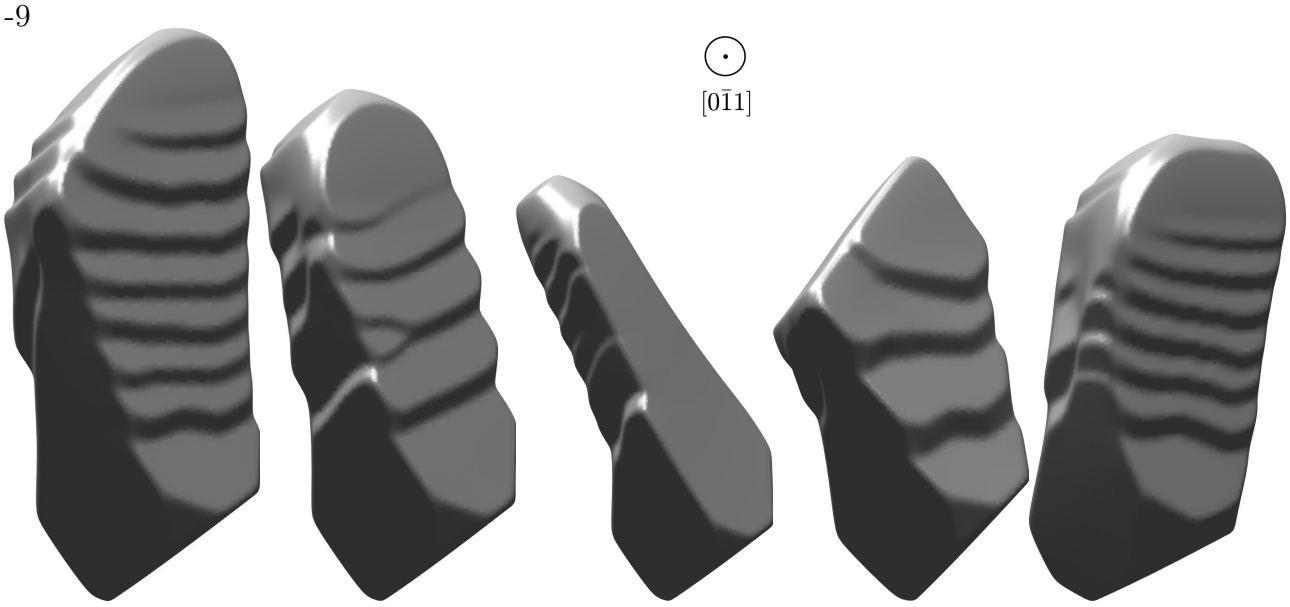

(a) $\gamma = 19°$, $\eta = 1$ β = -5° ± 2° (b) $\gamma = 19°$, $\eta = 0.5$ $\beta = 15° \pm 2°$ (c) $\gamma = 19°$, $\eta = 0$ $\beta = 27° \pm 2°$ (d) $\gamma = 9°$, $\eta = 1$ $\beta = 6° \pm 2°$ (e) $\gamma = 29°$, $\eta = 1$ β = -9° ± 2°

Figure 5.9: Nanocolumns grown under vapour incidence angle $\alpha = 57°$, mobility to flux magnitude ratio $^{M}/_{|\vec{R}|} = 0.01$, orientation angle γ and η specified in the captions of the subfigures. The crystallites share a common substrate normal but with different local coordinates all orientated with [0$\bar{1}$1] pointing out of the page. The morphologies shown correspond to simulation time reached when either dimensions in x or y exceeds 1.9.

5.6 In-plane texture selection

By the same token, given an out-of-plane texture those with the fastest vertical growth rate are favoured by competitive growth in the nano-columnar regime. For a {001}-faceted crystal habit there are two different in-plane orientations that are favoured by the growth, as per the extended structural zone model [75]*. These two favourable in-plane orientations are described in [147] and [146] as configurations of a (100) plane and an edge of the {100} planes (marked by letter E in Fig. 5.10) orienting towards the in-flux direction. The two configurations are reproduced here, as shown in Fig. 5.10a the configuration I and Fig. 5.10b the configuration II. The 0.5 iso-surface of the g field illustrates the self-shadowing effect: configuration I is characteristic of a (100) plane being shadowed and an edge E facing the flux for all $\alpha > 55°$; while configuration II has a non-shadowed (100) plane†. This way the two possible in-plane orientations for multiple out-of-plane orientations are simplified. According to the setup of the model geometry (Fig. 5.4) the two can be easily specified by the sign of the y-component

*They are specified by the in-plane orientation angle $\omega \approx 35°$ and $\omega \approx 55°$ corresponding to the [111] tilt angle.

†For $\alpha < 55°$ however, none of the (100) planes of the two configurations are shadowed.

of the rain vector: a positive y-component of $\vec{R}$ corresponds to configuration I, whereas a negative y-component of $\vec{R}$ corresponds to configuration II. For both of these configurations, the x-component and z-component of $\vec{R}$ are kept the same, thanks to the setup of the model geometry.

In Tab. 5.3 the observed out-of-plane orientations and in-plane orientations are summarised, as well as the corresponding configurations for the experimentally observed in-plane texture [146] and various existing model predictions [75, 147]. There has been only one in-plane texture that is experimentally observed, yet the models [75, 147] predict a mixed in-plane texture consisting of the two configurations for various α angles.

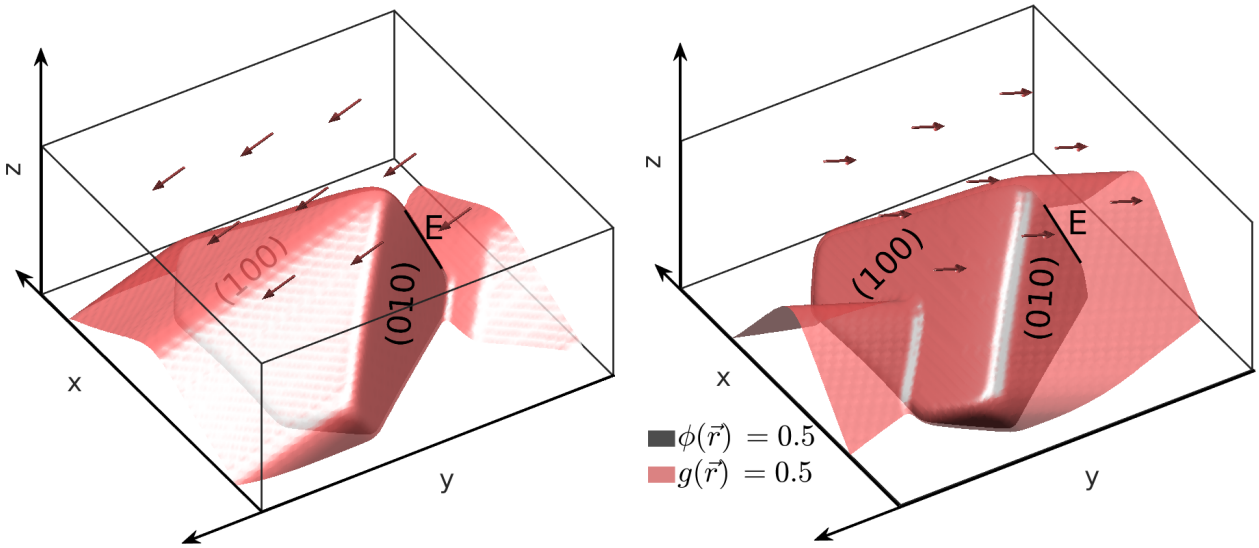

(a) Conf. I, with a positive y-component of $\vec{R}$, i.e., $|\vec{R}|[0\ sin(\alpha)\ -cos(\alpha)]$.

(b) Conf. II, with a negative y-component of $\vec{R}$, i.e., $|\vec{R}|[0\ -sin(\alpha)\ -cos(\alpha)]$.

Figure 5.10: Schematics of the two different configurations of the in-plane orientation which the extended structural zone model predicts to be equally favourable [75]. Ghekiere et. al. predicts that for $\alpha > 55°$ only one of them is favourable (configuration II) and for $\alpha < 55°$ both are favourable [147]. However only one in-plane texture has been experimentally observed [146]. In this figure different $\vec{R}$ vectors corresponding to the same $\alpha = 57°$ angle and the $g = 0.5$ iso-surface are visualised (rescaled).

Table 5.3: Comparison of experimental in-plane texture [146] (as specified by the two different types of configurations) and literature model perdictions [75, 147].

incident angle α	out-of-plane texture $[1\,1\,n]$	out-of-plane orientation γ	in-plane orientation ω	exp. conf. [146]	model conf. [75]	model conf. [147]
57°	[1 1 2]	19°	35.7°	II	I, II	II
35°	[1 1 3.5]	32°	22.7°	II	I, II	I, II
25°	[1 1 5]	39°	15.7°	II	I, II	I, II
0°	[1 1 1]	0°	54.7°	II	I, II	I, II

Next, the simulations are carried out in the nano-columnar regime for different in-plane orientations. For the same deposition parameters α, γ two separate runs are performed with negatively and positively valued y-component of the rain vector $\vec{R}$ to realise the two configurations.

As shown previously in Fig. 5.6 the $\alpha = 57°$ system with model parameter $\eta = 1$, $^{M}/_{|\vec{R}|} = 0.01$ develops a negative β in the nano-columnar regime which is in agreement with the known experimental result for column tilt angle. Other η values yield either positive β angles or non-faceted top surface as seen in Fig. 5.8. To simplify the picture $\eta = 1$ is used for all simulations hereafter.

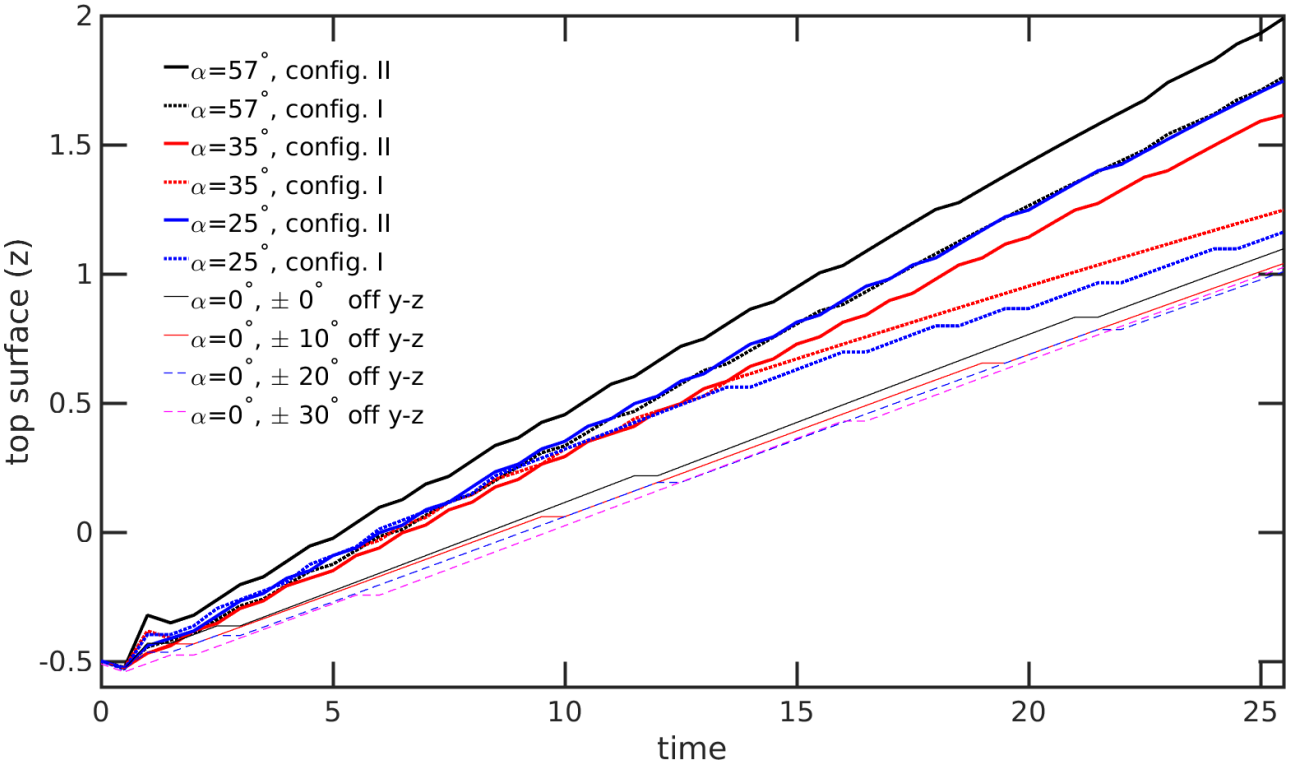

Figure 5.11: z coordinate of the top surface (sampled every interval $\Delta t = 0.5$) of nanocolumns grown under vapour incidence angle $\alpha = 57°$, $35°$, $25°$, $0°$ with different in-plane orientations. Other model parameters include $\eta = 1$, $^{M}/_{|\vec{R}|} = 0.01$, $\delta t = 1 \times 10^{-5}$.

The locations of the top surface in z reached at a particular time in the simulation are plotted against t in Fig. 5.11. For $\alpha = 35°$, $25°$ the initial vertical growth for the two configurations are comparable, but configuration II outgrows configuration I in late stage. Whereas for $\alpha = 57°$ the configuration II always stays on top of configuration I. Since vector $\vec{R}$ for $\alpha = 0°$ has a zero valued y-component, y' of the local coordinates of the crystal is rotated about the substrate normal so that $y\prime = [2\,\bar{1}\,\bar{1}]$ is at an angle to the y-z plane. Because of the symmetry of the system and the nature of a deterministic model the growth rates for a negatively and positively signed angle off the y-z plane are the same. Once again the configuration II corresponding to the observed in-plane texture develops a higher vertical growth rate. As a consequence of the type II configuration relative to the in-flux direction for various in-plane orientations, one of the planes of reflection of the $m\bar{3}m$ point group is preserved, i.e. the $(0\bar{1}1)$ mirror plane. It is also worth noting that these in-plane orientations are less affected by the (unphysical) seeding, as compared with Fig. 5.7 in Sec. 5.5, due to the favourable out-of-plane orientations on which they are taken.

In this section, it is demonstrated by means of the numerical experiment that the model is capturing the observed in-plane orientation for all out-of-plane textures. This is in contrast to the existing model predictions. In Sec. 5.7, the model is used to study the nanocolumn morphologies. Special attention will be paid to the nature of the free surface that the nanocolumns expose.

5.7 Nanocolumn morphology

5.7.1 Symmetry reduction and colour mapping

In Sec. 5.5 and 5.6 the resulting nanocolumns with prefered out-of-plane orientations and type II configuration relative to the flux preserve the $(0\bar{1}1)$ mirror plane. To simplify the representation and to illuminate the nature of the exposed surfaces of the resultant single-crystal morphologies, it is helpful to employ a meaningful colour scheme. MgO has a point group symmetry $m\bar{3}m$ that can be exploited to simplify the colouring of the facets. In this section, a colour scheme is adapted based on the concept of inverse pole figure (IPF) that reduces the surfaces of the same family to a so-called fundamental sector [168]. The difference between the IPF colour mapping and the adaptation here is that, the crystallographic orientations of crystallites in an orientation map is replaced by Miller indices representing the normal to the surfaces. A stereographic projection of an upper hemisphere coloured by this scheme is shown in Fig. 5.12a. It is only necessary to show one hemisphere thanks to the antipodal symmetry. This can be further reduced to a triangle by IPF mapping of the Miller indices, as shown in Fig. 5.12b.

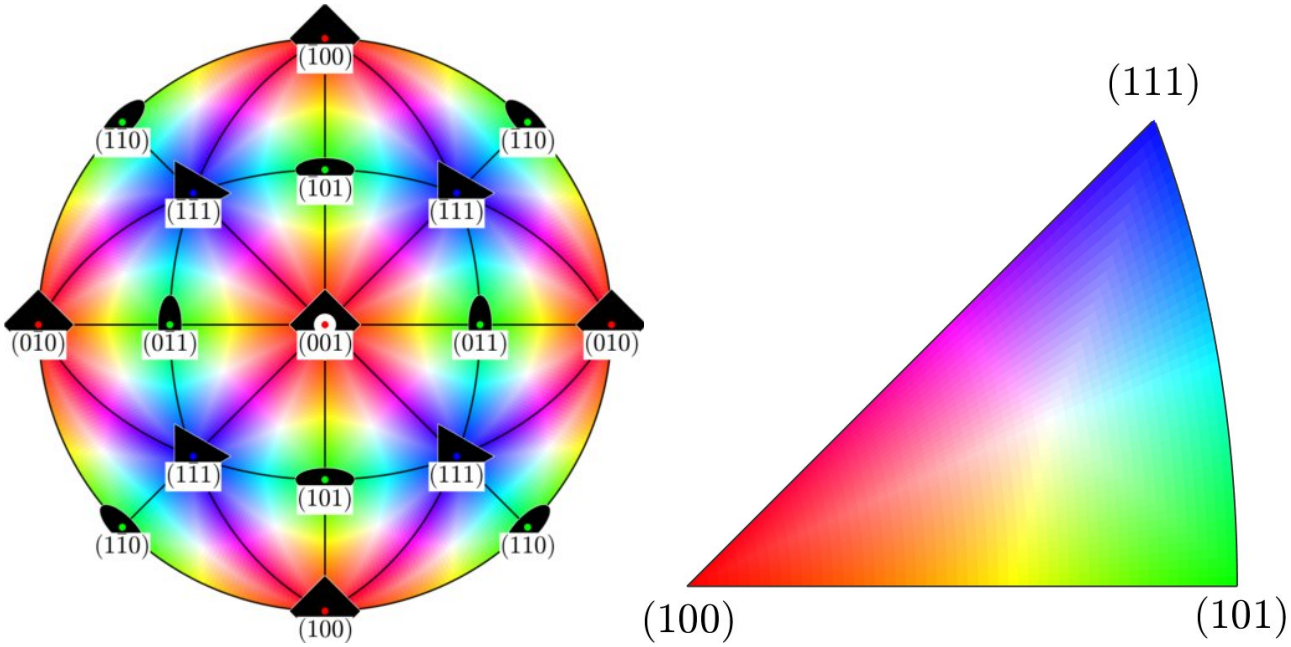

Figure 5.12: (a) Stereographic projection of the upper hemisphere coloured by the Miller indices of the normals which can be reduced to (b) the stereographic triangle for the point group $m\bar{3}m$

The shapes in an energy minimising calculation for a MgO particle are used to benchmark this colouring scheme. As shown in Fig. 5.13 the sphere corresponding to $t = 0$ has a stereographic projection equivalent to Fig. 5.12a. The shape at late stage is predominately bounded by six facets of the {100} family, all coloured red according to the stereographic triangle Fig. 5.12b. Furthermore, eight truncation {111} planes in blue on the corners and 12 edges in green belonging to the {101} family are also correctly coloured.

Figure 5.13: MgO $\phi = 0.5$ iso-surface plots at $t = 0, 0.3, 0.7, 2.2$ of the energy-minimising calculation, reproduced from Fig. 4.12 using $\delta t = 1 \times 10^{-7}$ and $M = 1$. Surfaces are coloured using the IPF stereographic triangle for MgO shown in Fig. 5.12b

5.7.2 Surface morphology

To make a meaningful comparison between the film morphology observed in the laboratory frame and the single-crystal morphology obtained in the simulation, it is necessary to make some assumptions. Firstly, the origin of texture formation is considered independent of the influence of the substrate and the effect of grain boundary impingement. Secondly, the processing parameters of the system reside in the range and scope that the model parameters cover. It is hypothesised that the in-plane texturing occurs in the nano-columnar regime where the single-crystal morphologies of interest develop a column tilt angle β that is independent of the crystallographic orientation of the crystallite. This implies that the nanocolumns in this regime are not fully faceted as one would expect from various existing theories. Lastly, it is assumed here that certain values of the model parameters best reproduce the true single-crystal morphology.

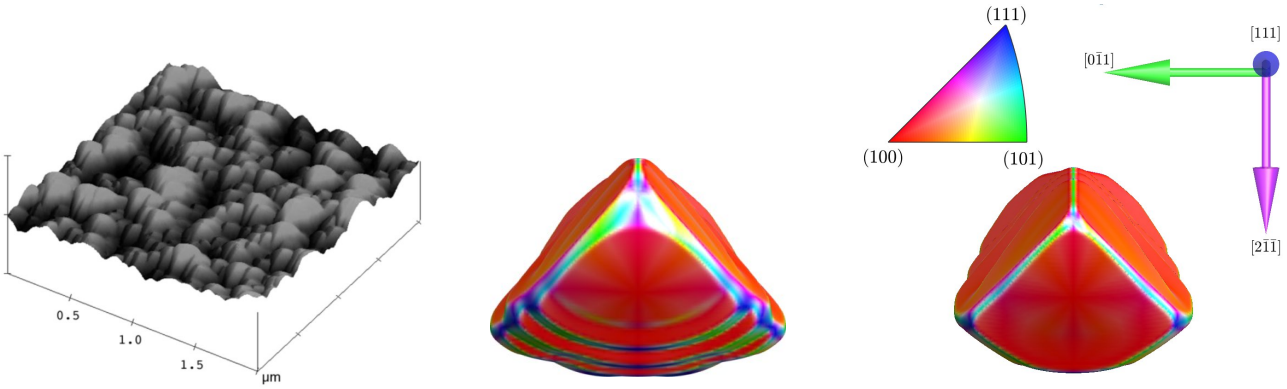

(a) $\alpha = 57°$ [158] (b) $\frac{M}{|\vec{R}|} = 0.01$, β = -5° ± 2° (c) $\frac{M}{|\vec{R}|} = 0.02$, β= -5° ± 2°

Figure 5.14: (a) AFM surface topography of the biaxially textured MgO thin film (from [158]). (b) and (c) top view of the late stage shapes deposited at $\alpha = 57°$ with $\gamma = 19°$ and configuration II relative to the flux. The [111] arrow in (c) is pointing out of the page.

In addition to the parameters used throughout this chapter which are listed in Tab. 10.2, the values of model parameters chosen for reproducing the nanocolumn morphologies include $0.002 \leq {}^{M}/_{|\vec{R}|} \leq 0.03$, $\eta = 1$ and type II in-plane configuration. Under these settings of model parameters, the resulting nanocolumns preserve one of the reflection symmetries of the point group with mirror plane $(0\bar{1}1)$, as noted in Sec. 5.6. It has been observed in this 3-D numerical simulations that, the model parameter ${}^{M}/_{|\vec{R}|}$ in this range reproduce the characteristic triangular roof-tile surface morphology of a typical OAD-MgO thin film, as shown by an atomic force microscopy (AFM) surface topography of such thin film in Fig. 5.14a. The triangular

top surfaces are of the {100} family facing the flux, according to the results of the simulations. As a general trend, {100} facets become sharper the larger the $^{M}/_{|\vec{R}|}$ value, as can be seen by comparison with shapes reached at the same simulation time, shown in Fig. 5.14b and Fig. 5.14c. Moreover, the triangular top surface develops overhangs bounded by {100}-{101} surfaces for $^{M}/_{|\vec{R}|} \leq 0.01$. The bounding surfaces of the two symmetric sides of the nanocolumns are not clearly visible from this top view.

5.7.3 Side profile

A nano-faceted, branched structure on the sides of the nanocolumns has been observed and described colloqually as laminar 'notchy side' in an experimental work [18], shown in Fig. 5.15a. As noted earlier, unlimited surface diffusion cannot explain the secondary structure. In Fig. 5.15b the simulations show that the two symmetric sides of the nanocolumns are bounded by {100}-{111} alternating surfaces resulting in well-aligned overhangs. The development of such bounded surfaces from kinetics perspective is due to the fact that in the nano-columnar regime, surface diffusion is not fast enough for all mass to diffuse onto the more energetically favoured {100} surfaces. As a consequence, {111} surfaces grow in favour of this imbalance, in combination with the preferential flux.

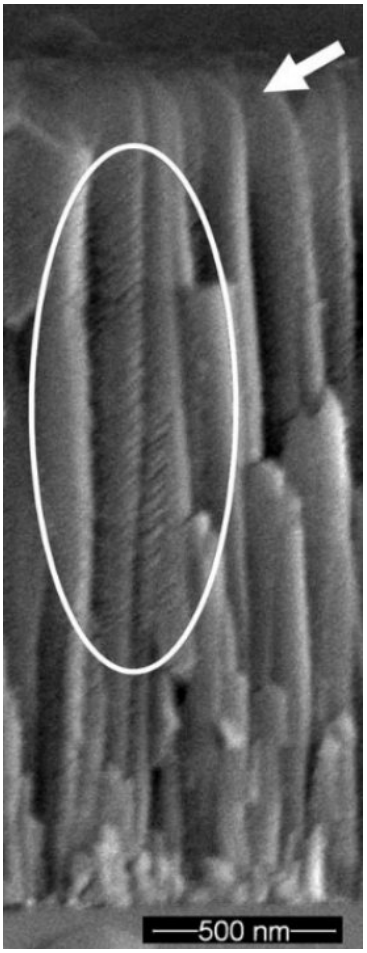

(a) $\alpha = 55°$, β = -10° ∼ 0° [147]

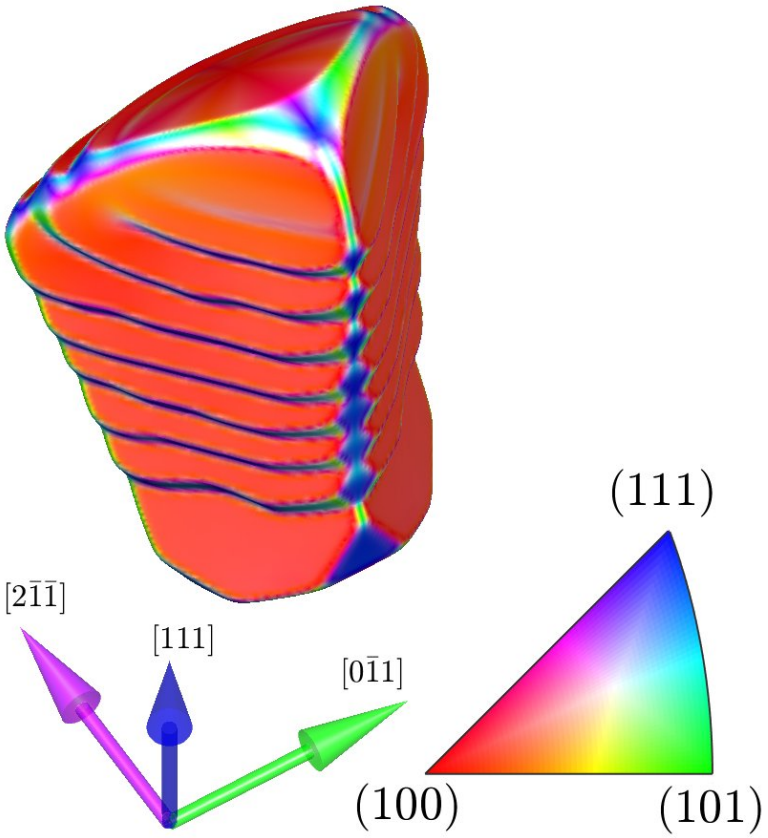

(b) $^{M}/_{|\vec{R}|} = 0.01, \alpha = 55°, \beta$ = -6° ± 2°

Figure 5.15: (a) SEM image of the side profile of biaxially textured MgO thin film grown by OAD with $\alpha = 55°$ and β measured at -10° ∼ 0° (from [147]). The white ellipse highlights the branched structures. (b) The sides of a nanocolumn, bounded by {100}-{111} alternating nano-faceted surfaces with column tilt angle β =-6° ± 2°.

5.7.4 Growth exponent

A series of side profiles corresponding to different time during a long-time-scale evolution are shown in Fig. 5.16. The nanocolumn width W is found to grow as a function of the nanocolumn length d. For this particular morphology reproduced using the aforementioned model parameters, W is defined to be the distance between the two $(0\bar{1}1)$ in-plane bounding planes and d the distance between two (111) out-of-plane bounding planes, as illustrated in Fig. 5.17a. The measurement of W and d is consistent with the method used in [10, 11]. At some time intervals, measurements are taken for both W and d. The first such measurement is taken when the alternating surfaces start to develop. The last measurement is done when the d reaches 87% of the simulation cell. The scaling in time is found to follow a power law $W \sim d^p$ with growth exponent p, as plotted in Fig. 5.17b for various ${}^{M}/_{|\vec{R}|}$ values.

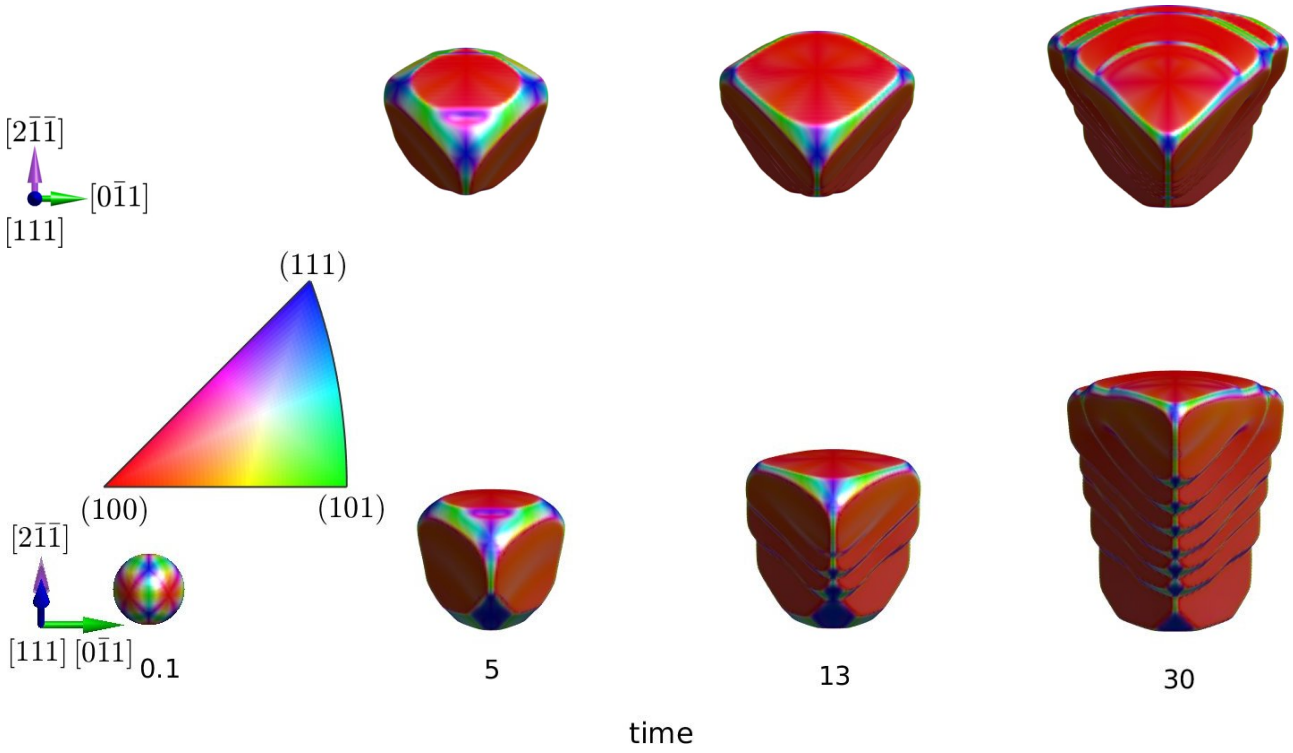

Figure 5.16: The evolution of a nanocolumn with type II in-plane texture grown in the nanocolumnar regime using model parameters ${}^{M}/_{|\vec{R}|} = 0.01$, $\alpha = 57°$, $\delta t = 1 \times 10^{-5}$. The visualisation shows two different views, the upper row shows the top view and the bottom row shows the side profile.

There are two limiting cases for the varying values of ${}^{M}/_{|\vec{R}|}$ controlling the growth regime. For a negligibly small ${}^{M}/_{|\vec{R}|}$ the nanocolumns grow towards the incoming flux, as discussion in Sec. 5.4. As a result the late-stage orientations are tilted in alignment with the in-flux direction, i.e. $\beta = \alpha$. The width W in this case saturates in the late stage and consequently W does not depend on d, i.e. W is constant at late stage and $p = 0$. One can draw parallel between this growth scenario and the case iv of the van der Drift's model, reviewed in Sec. 2.4.2.

For unlimited diffusion, in which case ${}^{M}/_{|\vec{R}|}$ is large, each crystallite grows in a manner that preserves the equilibrium crystal shape. The fully faceted crystallite in this case coarsens with time and one expects W to be a linear function of d, i.e., $W \sim d$ and $p = 1$. In between the two limiting cases, it is found in the 3-D numerical simulations that the growth exponent p increases as ${}^{M}/_{|\vec{R}|}$ increases.

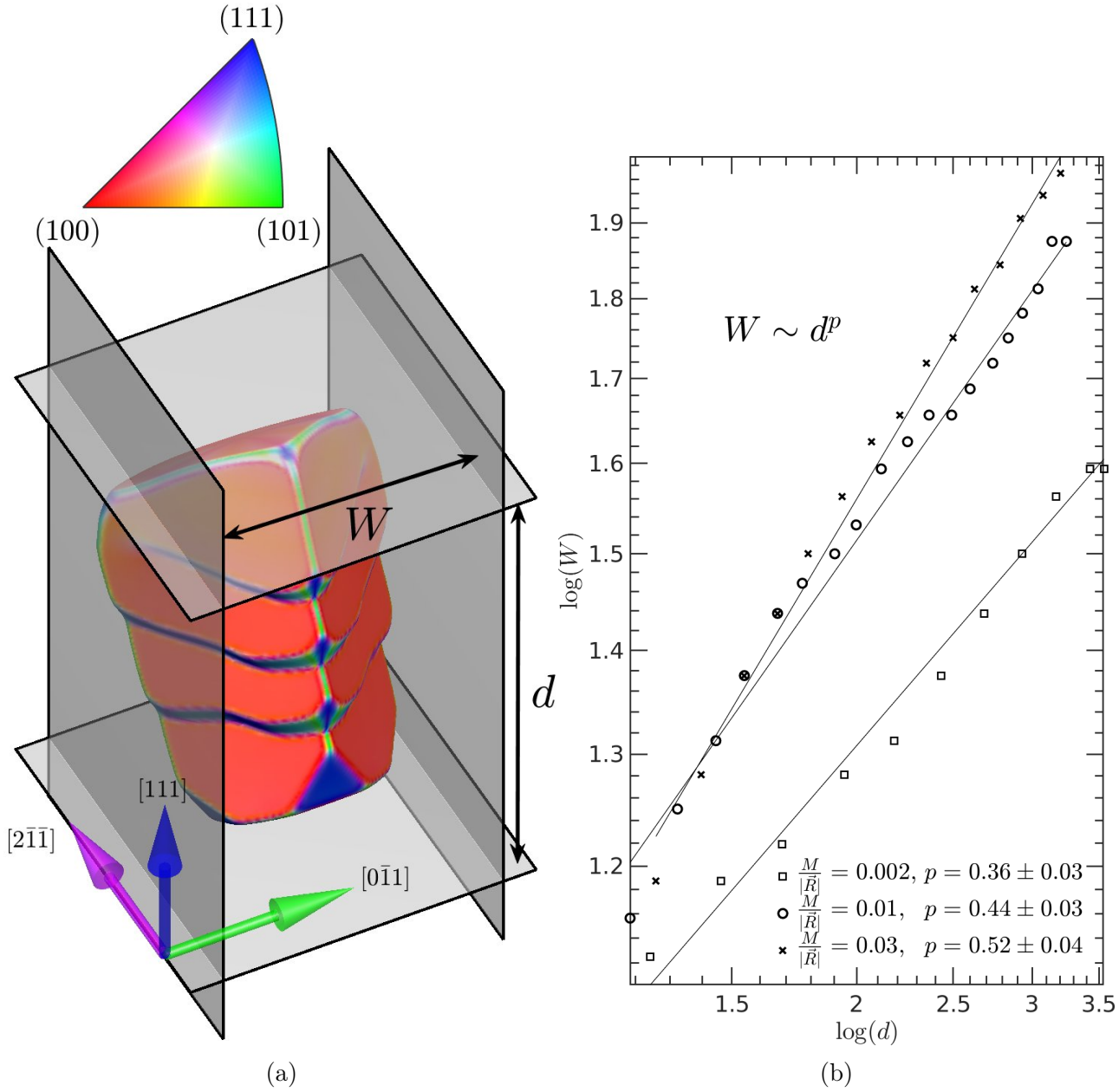

Figure 5.17: (a) Schematics showing the bounding planes coloured in gray and the convention of the dimensions defined for W and d. (b) Power law scaling and growth exponents for various $^{M}/_{|\vec{R}|}$ values.

This scaling behaviour is opposite to that reported in [10], in which p decreases as diffusion rate increases. It has also been reported in [11] a value $p = 0.37 \pm 0.02$ for experimentally grown, isolated Si nanocolumns. It should be noted here that in [10, 11] the isolated nanocolumns are deposited using OAD with substrate rotation, whereas in this model the directional flux is featured with no substrate rotation. Another difference is that both these works [10, 11] consider isotropic transport of surface diffusion, as opposed to the material-specific, material-specific surface diffusion for nano-structured MgO columns considered in this model.

5.7.5 Overhangs formed by alternating surfaces

The spacing of the overhangs formed by nano-faceted {100}-{111} surfaces on the two symmetric sides of the nanocolumns is sensitive to the model parameter $^{M}/_{|\vec{R}|}$. Physically, surface diffusion is a thermally activated process driven by the tendency of minimising the total surface energy. A temperature dependence on the mobility M is expected. A small enough M value would hinder the surface diffusion in regions of high surface energy (the edges and corners). This in turn contributes to the appearance of kinetically-frozen nano-facets of high-energy {111} surfaces, with edges freezing them and separating them from the more energetically favourable {100} surfaces. On the other hand, $|\vec{R}|$ controls the deposition rate, which can be linked to processing parameters such as vapour pressure and source-to-substrate distance depending on the specific technique used for an OAD system. A larger $|\vec{R}|$ means that more mass is brought to some preferred sites, which induces an imbalance of the mass being diffused between these regions and regions where no mass is brought to the surface by vapour flux (shadowed regions).

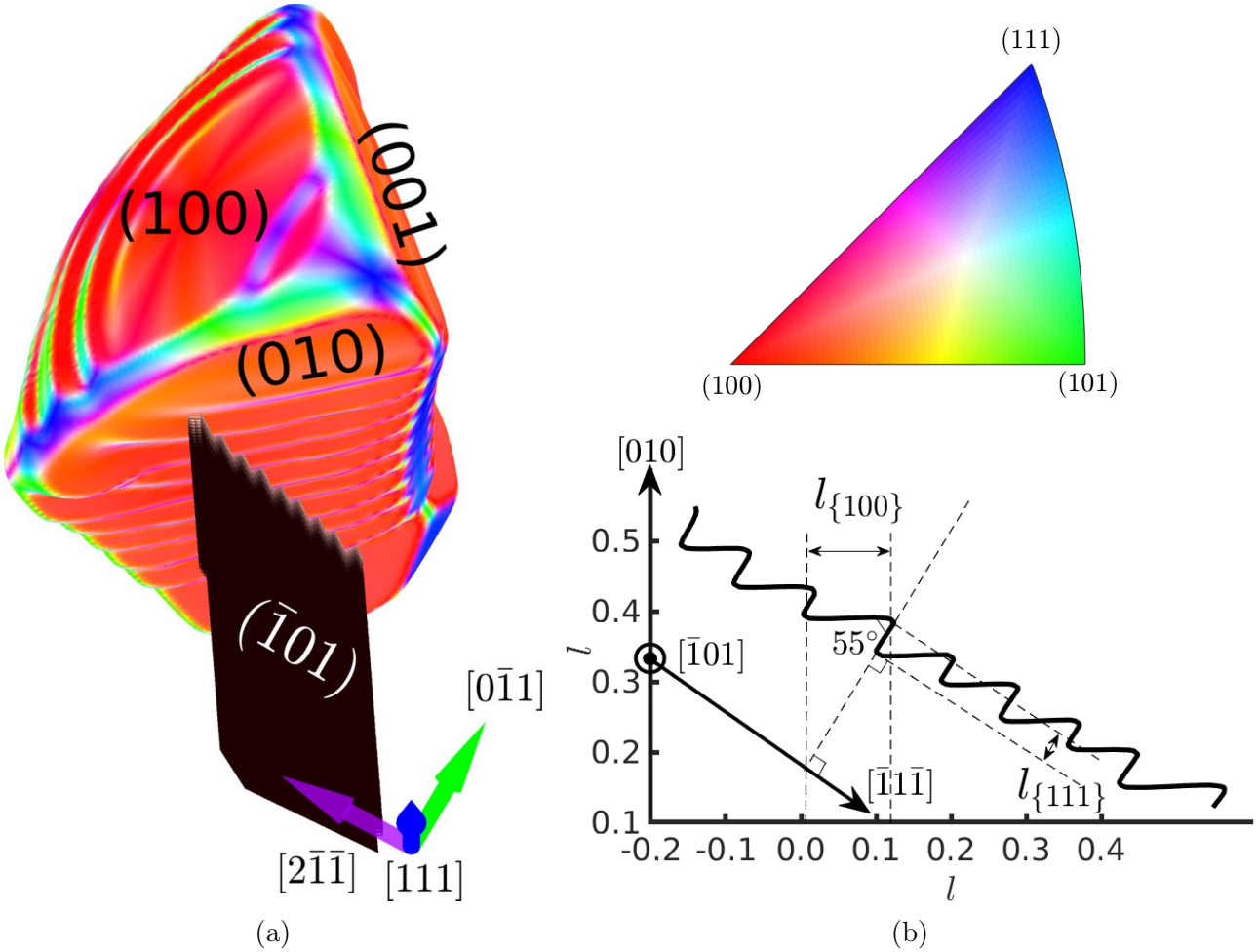

Figure 5.18: (a) A slice parallel to the $(\bar{1}01)$ plane is taken at a time interval of a simulation for the measurement of overhang length. (b) The profile of the (010)-$(\bar{1}1\bar{1})$ alternating nano-faceted surfaces with annotations for some important directions, angle and dimensions.

It is found in the 3-D numerical simulations that the ratio between the average lengths of {100} and {111} nano-facets, i.e. $\bar{l}_{\{100\}}/\bar{l}_{\{111\}}$ approaches a constant value at late stage of growth. To examine this observation, a slice along the $(\bar{1}01)$ plane is taken at a time interval $\Delta t = 2$ during the nanocolumnar growth. As shown in Fig. 5.18a, the intersection between the $(\bar{1}01)$ plane and the material interface picks up the features terminated by (010)-$(\bar{1}1\bar{1})$ alternating nano-facets. Or equivalently on the other side the (001)-$(\bar{1}\bar{1}1)$ alternating nano-facets by symmetry, if a $(1\bar{1}0)$ slice is taken. One of these profiles is plotted in Fig. 5.18b, in which the directions as well as one of such measurements for $l_{\{100\}}$ and $l_{\{111\}}$ are annotated.

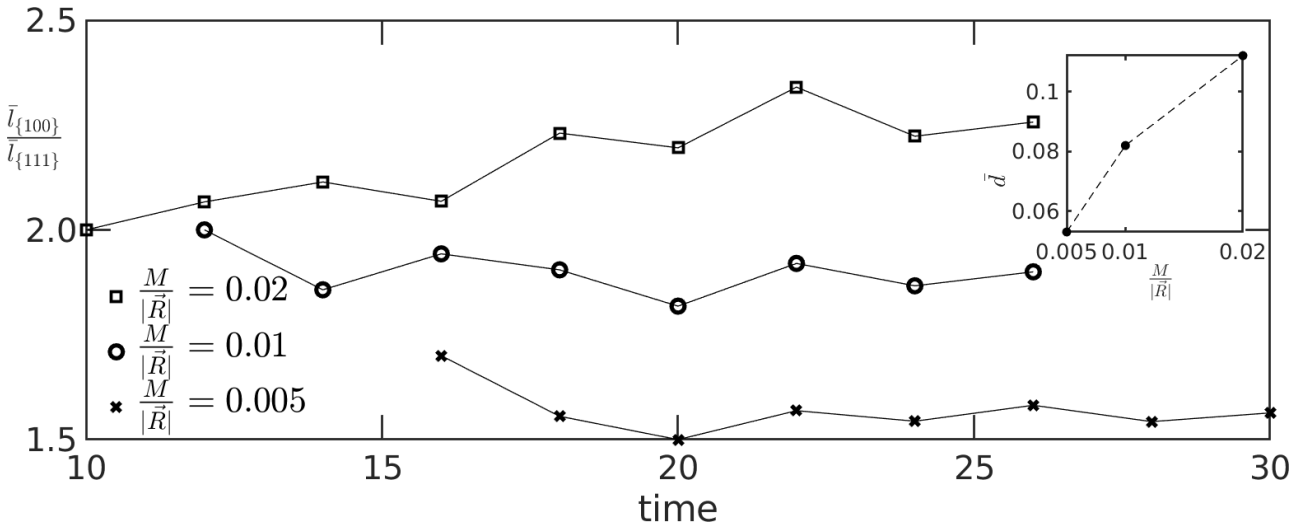

Figure 5.19: The ratio of lengths $\bar{l}_{\{100\}}/\bar{l}_{\{111\}}$ plotted against time for three different $M/|\vec{R}|$ values, for which the overhangs develop during the growth of nanocolumns. The inset shows the mean spacing of secondary features (overhangs) versus $M/|\vec{R}|$.

Overhangs are formed according to these profiles with a characteristic angle equal to 55° between the (010)-$(\bar{1}1\bar{1})$ alternating nano-facets irrespective of the $M/|\vec{R}|$ values. The ratio of lengths $\bar{l}_{\{100\}}/\bar{l}_{\{111\}}$ at late stage saturates during a long-time-scale evolution. This may suggest that the overhangs grow in a self-similar fashion in late stage. The ratio is found to increase as $M/|\vec{R}|$ increases, as evident in Fig. 5.19. This can be understood by taking the same energetics argument as used eariler. An increase in $M/|\vec{R}|$ would allow for more mass to diffuse from the {111} surfaces to the more favourable {100} surfaces. The mean spacing $\bar{d}$ was measured at simulation time corresponding to the stop criterion[‡]. The value of $\bar{d}$ shown in the inset of Fig. 5.19 is given by the total distance along $[\bar{1}1\bar{1}]$ divided by number of overhangs. An increase in $\bar{d}$ was observed for a bigger $M/|\vec{R}|$ value, which is expected given that the rate of energy minimising is controlled by M.

[‡]The simulations are stopped when largest dimension of the nanocolumn reaches 87% of one of the dimensions of simulation cell

5.8 Discussion

5.8.1 Key assumptions and results

Before reaching the conclusions of this chapter, there are a number of assumptions that are essential to reaching the results. These have been more or less introduced and repeated in the text. For the purpose of examining them alongside the key results, they are summarised as follows:

1. Texturing of an typical OAD-MgO system does not depend on the nature of the substrate.
2. Texturing does not happen upon grain boundary impingement and the film morphology can be explored by studying the growth of an isolated single crystal.
3. Crystallites with the fastest vertical growth rate determine the film texture.
4. The length scale and timescale underlying the model formulation based on established non-dimensional models match those of a typical experimental system.
5. The material-specific surface diffusion can be modelled by the energy minimising calculation of the CHW energy, with $\tilde{\gamma}(\vec{n})$ constructed using discrete surface energy density values given by the *ab initio* calculations.
6. The acceptance of the incoming adatoms is a function of the surface normal $\vec{n}$ and rain vector $\vec{R}$.

The key observations and results of this chapter are listed below for a summary:

- β is not related to either α or γ by an empirical law.
- The OAD-grown MgO nanocolumns are not bounded by lowest energy surfaces only.
- A negatively tilted nanocolumn ($\beta < 0°$) is possible considering the nano-columnar growth regime in which the surface diffusion is limited.
- Three distinct growth regimes characterised by the model parameter $\frac{M}{|\vec{R}|}$ are identified.
- β is found to be equal to α in the regime where surface diffusion is negligible.
- β in the nano-columnar regime is determined by the interplay between the limited surface diffusion and the preferential deposition.
- The roof-tile surface morphology is obtained with model parameter $\eta = 1$, which implies $\mathcal{A} \sim sin\big(\angle(\vec{R}, \vec{n})\big)$ growth.
- $\eta = 1$ gives rise to a preferred growth for experimentally observed out-of-plane orientations.
- Model parameter $\eta = 1$ may suggest that the microscopic/atomistic growth mechanisms (e.g. adsorption, desorption and step bunching) favour the step flow growth mode.
- There is only one preferred in-plane configuration for various out-of-plane orientations and α angles. This configuration is characterised by the (100) facet facing the in-flux direction.

- Considering the material-specific CHW energy of MgO and preferred in-plane configuration, the resulting nanocolumn morphology preserves the mirror plane $(0\bar{1}1)$ of the $m\bar{3}m$ point group.
- The nanocolumns are bounded by {100}-{111} alternating nano-facets.
- Anomalous scaling behaviour for the growth of isolated, nano-structured MgO nanocolumns in the nanocolumnar regime is observed. The exponent of the power law scaling $W \sim d^p$ is found to be $0.36 < p < 0.52$.
- 55° overhangs are formed on the two symmetric side of the nanocolumns deposited at $\alpha = 57°$ in the nanocolumnar regime.
- The ratio $\bar{l}_{\{100\}}/\bar{l}_{\{111\}}$ saturates at late stage of growth and is found to be dependent on $M/|\vec{R}|$. This suggests a self-similar growth of the overhangs at late stage.

5.8.2 Conclusions and remarks

In this work a continuum model has been adapted and assessed for a prototype OAD system. The critical interplay between limited surface diffusion and preferential deposition owing to non-local shadowing effects plays a central role in the development of morphology and texture of biaxially aligned single crystals. The arguments of the origin of the biaxial texture formation based on experimental evidence have led to the assumptions that allow for simplifying the thin film system to the growth of a single-crystal nanocolumn. Moreover, kinetics has been attributed to the nano-columnar morphology and consequently the in-plane texturing. By selecting a suitable model geometry and surface energy function, the simulated crystal growth is used to make meaningful comparison with the nanocolumn growth of MgO during OAD. A model parameter $M/|\vec{R}|$ has been identified to be the determining factor for the growth regime, the range of which has been evaluated. The nano-columnar growth is found to reside in $0.002 < M/|\vec{R}| < 0.03$.

There has been a long-standing discrepancy regarding the preferred in-plane texture for cubic nanocolumns having a {100}-faceted crystal habit, between the established theory and experimental evidence. A 2-D growth model [75, 147] based on a simple calculation of the capture length cannot account for the complex shadowing effects involved in the 3-D competitive growth during OAD, as well as the material-specific surface diffusion. For the same reason, a negative-valued column tilt angle remained unexplained. It has been demonstrated for the prototype system that a negative-valued column tilt angle can develop for the given preferred orientation. It is also shown that only one in-plane texture is favourable for all given α angles, the orientations of which match those of the experimentally observed in-plane texture. In addition, the model provides insight into the origin of biaxial texture formation, the unusual far-from-equilibrium shapes and the nature of bounding surfaces of the single-crystal nanocolumns. In particular, the single-crystal morphology resembling a nano-faceted laminar structure observed on the sides of MgO nanocolumns, as well as the triangular roof-tile surface morphology characteristic of biaxially textured MgO thin films can be reproduced in the modelling framework.

The modelling parameters used to reproduce the characteristic morphology are discussed. Recommendations of the future experimental work are given. Lastly, from a modelling perspective this is the first continuum model incorporating limited, material-specific surface diffusion and non-local shadowing. It provides detailed description of a process-specific prototype system and the expected time evolution of a realistic prototype material. The framework under

which the model was developed is modular. It can be adapted in terms of model geometry and boundary conditions to suit other deposition systems of interest. Other materials, including but not limited to cubic materials, can also be met with the construction of the relevant surface energy function. In Ch. 6, the modelling framework is adapted and applied to CVD-grown anatase-TiO_2 nanocolumns.

5.8.3 Recommendations

Following the model results, a more in-depth study is needed for morphology of an isolated MgO nanocolumn, using e.g. focused ion beam and high resolution TEM, or ideally direct surface characterisation techniques. The anisotropic overhangs found in the existing TEM work [147] would be very valuable to examine. An investigation into, for example, the porosity of these intra-columnar, secondary structures and their evolution in time would be of great contribution to the understanding of this common feature prevalent in low-pressure vapour-deposited, nano-structured thin films. The study of growth exponent as well as overhang spacing can also be developed further in the future experimental work. The experimental techniques suitable for this kind of work include ultrasmall-angle X-rays scattering analysis (USAXS) [169, 170], which enables the study of pore formation, pore morphology and statistical analysis on the pore size distribution on nano-structured columns; X-ray nanobeam diffraction imaging (XRNDI) [171] and more recently the nano-focused X-ray imaging (NFXRI) [172] technique which allow for direct surface mapping and surface indexing of the nanocolumns.

Looking ahead, the array of overhangs terminated by alternating nano-faceted surfaces is common in low-pressure-deposited thin films, including but not limited to OAD systems. An example is shown in Fig. 5.20, for the ⟨001⟩-fibre-textured, rutile-TiO_2 nanocolumns deposited in low pressure [173, 174]. The authors identified the bounding surfaces to be $(\bar{1}1\bar{1})$ and $(\bar{1}10)$, with the help of a single SAED pattern shown in Fig. 5.20(b) inset. However it should be noted that this method of indexing the terminating planes only works if the zone axis of which the SAED pattern is taken happens to be parallel to planes marking these features. In the next chapter, the model developed in this chapter is adapted and studied to provide insight into the free surfaces of anatase-TiO_2 nanocolumns.

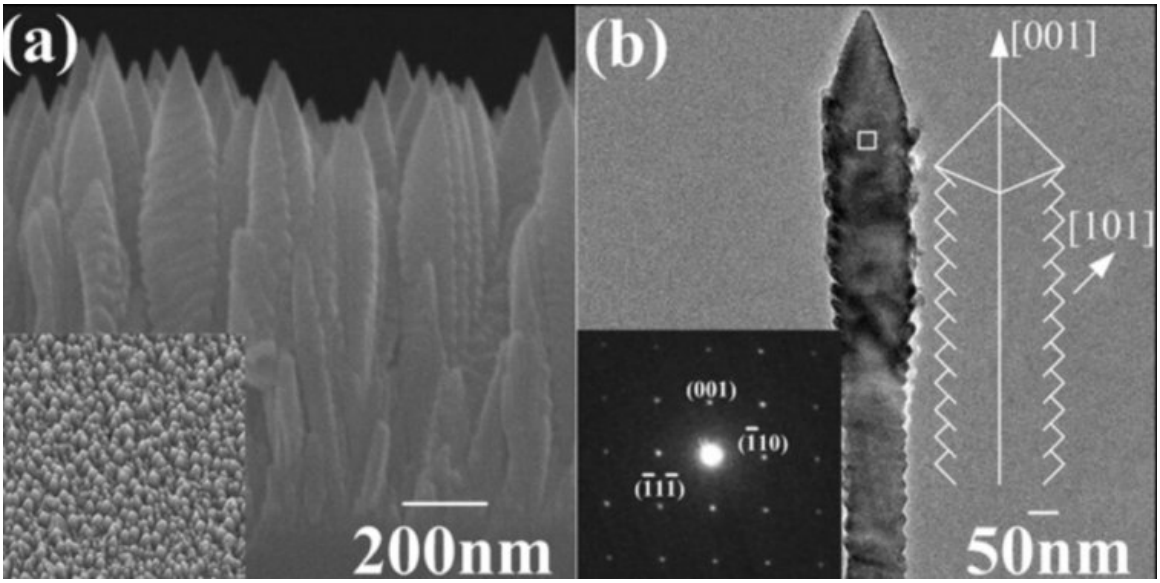

Figure 5.20: (a) SEM images of rutile-TiO_2 nanocolumns grown by vertical-flow CVD (b) TEM image and SAED pattern (inset) of a single-crystal rutile nanocolumn with schematics depicting the outline of the nanostructure (taken from [174]).

6. Application to anatase-Titania nanocolumns

6.1 Experimental system

The unusual microstructure of nano-faceted anatase-TiO_2 (A-TiO_2) nanocolumns as reviewed in Sec. 1.3, have been observed in other thin film systems operating at low pressure. Notably, A-TiO_2, β-Al_2TiO_5 and YSZ films prepared by laser CVD [175, 176]; YSZ thermal barrier coatings deposited by electron beam PVD [177, 178, 169, 170]; and the A-TiO_2 nano-structured films deposited by MOCVD [24, 25, 26, 40, 27, 1], to name but a few. The difference when comparing them with OAD systems is that the columnar microstructures are fibre textured, owing to a range of incident angles covered. These angles consist of a polar component θ ranging from 0° to 90° and an azimuthal component ψ covering all 360° angles, despite the vastly different deposition techniques used. Furthermore, the fibre texture implies an average column tilt angle $\beta \approx 0°$. No in-plane alignment of the polycrystalline nanocolumns is observed.

The commonality, other than the low vapour pressure in which these deposition processes are operated, is the high volume fraction of both inter-columnar gaps and intra-columnar voids. The voids in particular, formed in between the array of secondary columns, are inclined at an angle with respect to the average growth direction of the nanocolumns, varying among different materials, shown in Fig. 6.1 for an example. The technological relevance of this common feature lies in the nature of the exposed surfaces of anisotropic, nano-faceted secondary columns, which has inspired applications exploiting the thin film properties such as thermal conductivity [177, 178, 170], photoconductivity [26, 27, 28, 29] and antimicrobial property [1].

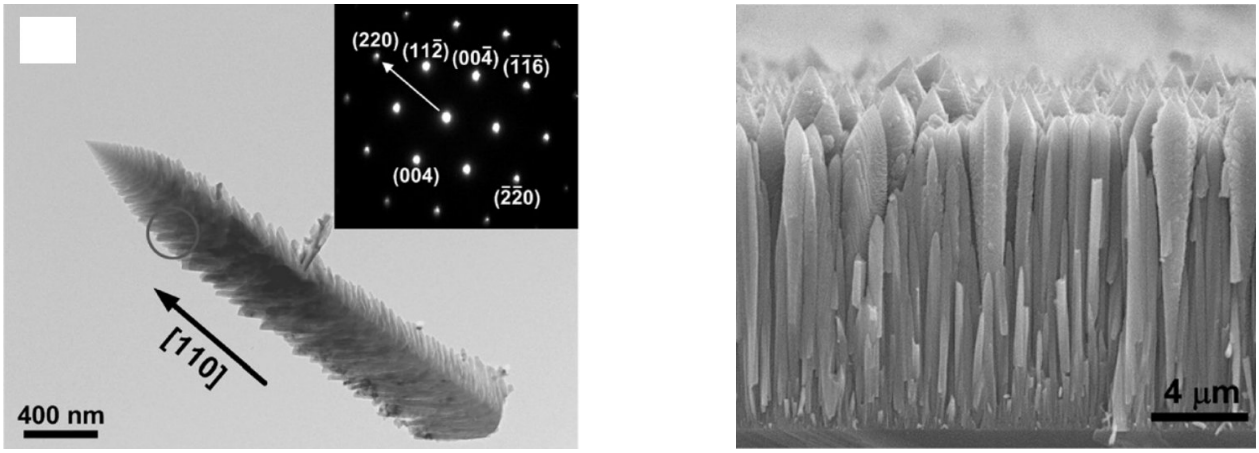

(a) (b)

Figure 6.1: (a) TEM of a single-crystal anatase-TiO_2 nanocolumn with arrow showing the growth direction and (b) SEM side profile of fibre-textured microstructure (taken from [27])

The microstructural characterisations done to the nano-structured A-TiO_2 thin film systems are limited to confirming the phase and fibre texture using Raman spectroscopy and XRD θ-2θ scan, qualitative imaging using TEM and SEM, and SAED that provides indirect hints on possible bounded surfaces [40, 27]. Glancing angle XRD (e.g. the phi-scan and omega-scan) and RHEED surface pole figure measurements, which are frequently used in the characterisation of biaxially textured thin films, have not been done to A-TiO_2 thin film systems.

The RHEED surface pole figure measurement is a surface technique that is helpful in understanding the crystallographic orientation distribution at top surface of the thin film [144]. It facilitates *in-situ* study of the texture evolution, especially at the early stage of growth [16]. The common understanding in the literature is that the fibre textured thin films are grown under zone T condition with no biased in-flux direction, where surface diffusion on a single grain is unlimited and that texturing happens upon grain boundary impingement. Although it is true that under these assumptions the grains develop an out-of-plane texture, the formation of anisotropic voids and gaps which are technologically important in these thin film applications, cannot be explained by existing theory on the origin of texture formation.

Insight into similar microstructures is given by a surface technique called USAXS, which has been used to investigate the statistical size distribution of the inter-columnar gaps and intra-columnar voids for electron beam PVD grown YSZ TBCs [169, 170]. A summary of the study includes the identification of three distinct microstructures, characterised by different populations of both inter-columnar gaps and intra-columnar voids. The formation of the three microstructures are found to be sensitive to processing parameters. It has been found the interrelation between population of anisotropic voids, and desired material property for TBCs, thermal conductivity [169, 170].

For properties such as photoconductivity, photocatalysis and antimicrobial property, of A-TiO_2 thin films [40, 27, 1], it is desired from a research perspective to elucidate the nature of the exposed surfaces. Unfortunately, techniques used in conventional surface science, such as scanning tunneling microscope (STM) and AFM, are too challenging to apply here due to the difficulties involved in sample preparation of surfaces of a 3-D nanocolumn. However, direct surface imaging techniques such as NFXRI have been proven to be applicable to nano-structured single-crystal arrays, in particular it allows for facet indexing [172]. By NFXRI analysis the surface distributions are also readily available to link to the desired material property. Thus far and to the best of the author's knowledge, study using direct surface techniques has not been conducted on antase-TiO_2 nano-structured thin films and the only quantitative characterisation work done regarding the exposed surfaces are limited to TEM and SAED that have not been done systematically.

In this chapter, attention is paid to the exposed surfaces of nano-structured A-TiO_2 thin films. Given the lack of experimental work on indexing of the free surfaces the thin films expose, the goal of the modelling work is to suggest the candidates of the exposed surfaces, based on continuum theories of the material-specific thermodynamics of faceting and the process-specific preferential deposition. The existing characterisations [24, 25, 26, 40, 27, 1] have reported a common $\langle 110 \rangle$ fibre texture. The microscopy characterisations undertaken in these works have shown qualitatively the morphology of isolated single-crystal nanocolumn, with some suggestions of the free surfaces by SAED. The growth regions of interest are the sides of the nanocolumns, surrounded by a network of well-aligned secondary columns, which contribute to most of the exposed surface area. A prediction as such would be helpful to explain the extraordinary properties that nano-structured A-TiO_2 thin films possess and to give insight

into engineering of free surfaces. The continuum model developed for the prototype OAD-MgO system in Ch. 5 is employed here, with a few modifications.

6.2 The model

6.2.1 Theme

As seen in Ch. 5, the surface diffusion alone is not sufficient to explain the formation of an in-plane texture of the biaxialled textured MgO thin film. Similarly, for ⟨110⟩-textured A-TiO_2 nanocolumns the unlimited surface diffusion on a single crystal, as per the zone T growth condition, cannot account for the formation of well-aligned secondary columns. In [40] an alternative theory based on oriented attachment using peridoc boundary chain (PBC) theory is held to explain the formation of secondary columns. But the PBC theory as adopted by the authors has only enjoyed success in explaining the self-assembly and coarsening of nano-particles under hydrothermal conditions [41] and recrystallisation [179]. For kinetically grown thin films by vapour deposition in low pressure, it is generally recognised that the non-local shadowing is the cause of the interface instability [180, 7, 8, 6, 9], which in the case of polycrystalline thin films results in the branching of the primary nanocolumns. A high resolution TEM image in Fig. 6.2 shows the branching of primary columns which gives rise to the secondary columns. The tilt angle of these secondary columns, for a typical A-TiO_2 nanocolumn, with respect to the average growth direction, β', is measured between $25° - 30°$ on the TEM micrographs reported in [40, 27].

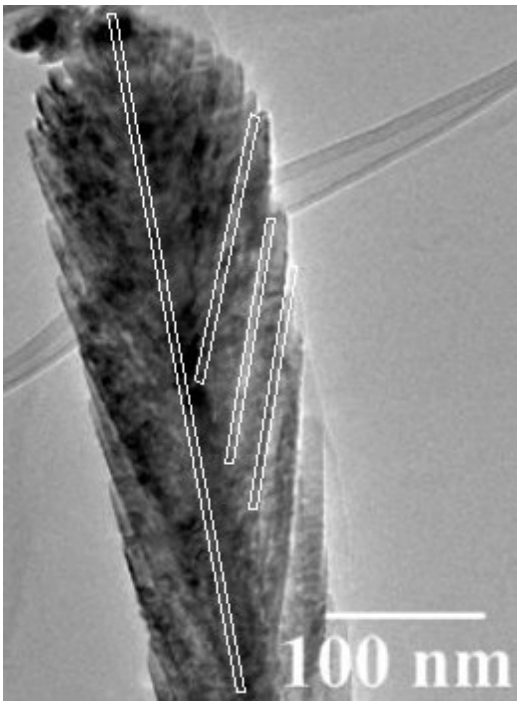

Figure 6.2: High resolution TEM side profile of an isolated A-TiO_2 nanocolumn (image from [40]). The secondary columns on the TEM micrographs in [40, 27] are inclined at an angle $25° - 30°$ with respect to the average growth direction.

The study of instability of an interface during the growth of a particle was pioneered by Mullins and Sekerka in their seminar paper [45] titled 'Morphological Stability of a Particle Growing by Diffusion or Heat Flow'. In this paper a classic stability analysis is developed to understand the interplay between the point effect of heat diffusion and surface diffusion. The

point effect causing the perturbation to amplify due to the bunched iso-concentrates above the protuberances, is balanced by the smoothing process of surface diffusion which has the role of carrying away the mass. The regulation by surface diffusion controls the break-up of the interface.

The instability analysis was adopted by Coriell and Parker [181] for the growth of an infinite cylinder controlled by mass diffusion. Experimental technique for studying such growth instabilities is limited, consequently the basic understanding of the phenomena of such systems relies very much on the Mullins-Sekerka type instability analysis.

For the growth of a realistic vapour-solid interface under effects of ballistic transport and surface diffusion, where the break-up of the interface is controlled by the complex interplay between surface diffusion and non-local shadowing, the analytical instability analysis becomes impracticable. The so-called shadowing instability is said to associate with this type of growth [7]. Bales and Zangwill carried out the stability analysis for idealised shadowing scenarios with isotropic surface diffusion. For a directional shadowing, i.e. OAD or the deposition techniques having a complex flux distribution, e.g. CVD, there lacks a theoretical study on systems featuring highly anisotropic surface energy.

6.2.2 Relevant surfaces

The excellent photocatalytic activity reported in the various applications of ⟨110⟩-textured A-TiO_2 nanocolumn has been attributed to large exposed surface areas [1, 24, 40, 27]. Apart from the surface area, the nature of the free surfaces is also critical for the photocatalytic, photoconductive and antimicrobial properties. Some high-energy surfaces, e.g. {001}, {111}, {107}, are considered more reactive than others [182, 183, 184, 185]. However, experimental characterisation work on indexing the free surfaces is difficult, as discussed in Sec. 6.1. The conclusion reached by Chen [40, 27] using high resolution TEM and SAED pattern overlooks the fact that, the surfaces associated with the terminating features can have surface normals that are not perpendicular to the zone axis. As discussed at the end of Sec. 5.7.5, zone axis has to be parallel to the bounding planes in order to ensure that the features marking the terminating planes are indeed applicable on a SAED pattern. Experimentally, this might mean that a series of high resolution TEM images and SAED patterns with different zone axes have to be undertaken and analysed in a systematical way, in order to align the zone axis with the crystallographic axis of A-TiO_2 nanocolumn precisely.

The material-specific $\tilde{\gamma}(\vec{n})$ construction introduced in Ch. 4 requires the surface energy density values for selected surfaces. In performing the energy minimisation calculation, a function of the inner product of these values with $\vec{n}$ is integrated over all selected surfaces (Eqn. 4.2). For example, there are in total 24 such terms if only {101}, {103} and {107} are considered. Therefore for the purpose of an efficient computation, it is helpful to identify first the important surfaces of A-TiO_2 that are most likely to yield an accurate presentation of the true $\tilde{\gamma}(\vec{n})$.

Luckily, there are a few clues at my disposal provided by the microscopy works (e.g. the TEM micrographs shown in Fig. 6.1 and Fig. 6.2, as well as the characterisation works in [40, 27, 1]) that can be used to narrow all possible surfaces down to a few of them. These clues are summarised as follows:

1. The average growth direction of the nanoclumns is $\langle 110 \rangle$, as identified by SAED [40, 27] and XRD analysis.
2. The secondary columns are well-aligned and inclined at an angle β' with respect to $\langle 110 \rangle$. β' is measured at $25° - 30°$ from the TEM micrographs.
3. The SAED analysis suggests that the average growth direction of secondary columns $\vec{n}_{C3}$ is perpendicular to $[\bar{1}10]$ [1].
4. $C2$ surface is faceted, as suggested by SEM micrographs such as the one shown in Fig. 1.5.

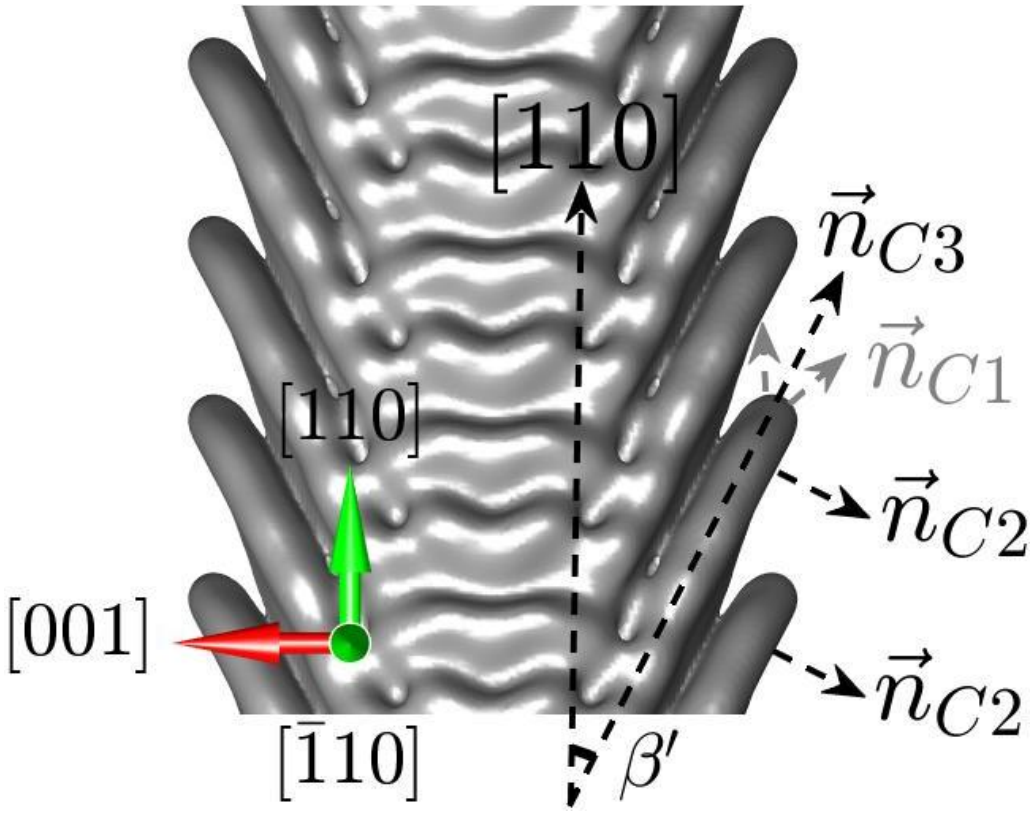

Figure 6.3: Schematics showing some of the directions, angles and candidate surfaces.

To facilitate the discussion, some of the directions and angles are labelled in Fig. 6.3. The secondary columns are predominantly bounded by $C2$ plane and the edges of them are partially bounded by $C1$ and $C3$ planes. It is therefore reasonable to suggest from these observations that an infinite cylindrical geometry, aligned with $\langle 110 \rangle$ for the initial condition, is best suited to capture the most abundant $C2$ planes, as far as the exposed free surfaces are concerned. In this geometry, it can be seen that $C1/C3$ planes and $C2$ planes reside on the upper and lower hemisphere respectively, on a (110) pole figure. Furthermore, it can be estimated from this geometry that some of the candidates of $C1/C3$ planes make an right angle with $C2$ plane, that

is $\angle(\vec{n}_{C1/C3}, \vec{n}_{C2}) = 90°$. Some of the pairs of candidate planes that form an angle $90.0° \pm 2°$ are joined by double arrow on (110) pole figure, shown in Fig. 6.4. The Miller indices of these candidate planes and the characteristic β' angle are listed in Tab. 6.1.

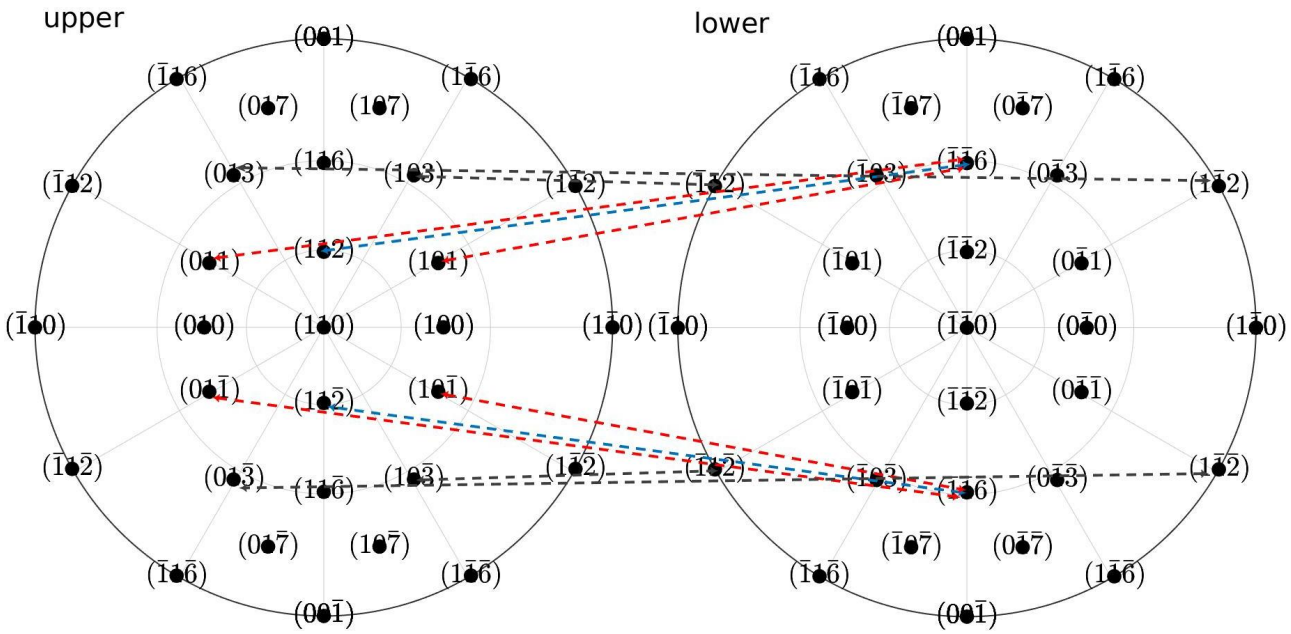

Figure 6.4: (110) pole figure of A-TiO_2. Some of the pairs of candidate planes forming approximately 90.0° angle are joined by dotted double arrows.

Table 6.1: The example pairs of candidate planes that make up $90 \pm 2°$ angles. These pairs are joined by double arrows on a (110) pole figure in Fig. 6.4 with colours specified in the table.

C1/C3 (upper)	C2 (lower)	$\angle(\vec{n}_{C1/C3}, \vec{n}_{C2})$	arrow color on pole figure 6.4
(013)	$(1\bar{1}2)$	91.15°	grey
(103)	$(\bar{1}12)$	91.15°	grey
$(01\bar{3})$	$(1\bar{1}\bar{2})$	91.15°	grey
$(10\bar{3})$	$(\bar{1}1\bar{2})$	91.15°	grey
(112)	$(\bar{1}\bar{1}6)$	91.29°	blue
$(11\bar{2})$	$(\bar{1}\bar{1}\bar{6})$	91.29°	blue
(011)/(101)	$(\bar{1}\bar{1}6)$	90.97°	red
$(01\bar{1})$/$(10\bar{1})$	$(\bar{1}\bar{1}\bar{6})$	90.97°	red
{101}	{001}	90.00°	not drawn

$\vec{n}_{C3}$ is the average (fastest) growth direction of the secondary columns. $C3$ candidate planes listed in Tab. 6.1 are examined in conjunction with Clue 2. The angles between $\vec{n}_{C3}$ and [110], i.e. $\beta' = \angle(\vec{n}_{C3}, [110])$, are listed in Tab. 6.2. It can be seen that β' associated with candidates (112) and (11$\bar{2}$) falls within the range that Clue 2 specifies. At the same time, candidates (112) and (11$\bar{2}$) agree with Clue 3, that is $\angle(\vec{n}_{(112)/(11\bar{2})}, \vec{n}_{(\bar{1}10)}) = 90°$.

Table 6.2: The candidate C3 surfaces, the angles between $\vec{n}_{C3}$ and [110] and the range of angles given by Clue 2.

C3	β'	Clue 2
(013)	63°	25° – 30°
(103)	63°	25° – 30°
(01$\bar{3}$)	63°	25° – 30°
(10$\bar{3}$)	63°	25° – 30°
(112)	29°	25° – 30°
(11$\bar{2}$)	29°	25° – 30°
(011)/(101)	49°	25° – 30°
(01$\bar{1}$)/(10$\bar{1}$)	49°	25° – 30°

Based on the above arguments, {103}, {112} and {116}-type surfaces are included in the construction of $\tilde{\gamma}(\vec{n})$, along with other commonly observed free surfaces {101}, {100}, {001} and {107}, which A-TiO_2 particles expose [183, 184, 185]. The surface energy density values in Jm^{-2} are calculated with the surfaces used in the construction and their surface energy density values listed in Tab. 6.3. The calculations of the surface energy density follow the methodology laid out in Sec. 4.1. It is found that the values are relatively lower than the literature values for some surfaces. But to the best of the author's knowledge, the value for candidate {116} has not been previously reported in the literature. For consistency, values of common surfaces given in Tab. 6.3, instead of the literature values, are used in the $\tilde{\gamma}(\vec{n})$ construction.

The same energy minimisation calculation as the one used in Sec. 4.3.2 is performed using the newly constructed $\tilde{\gamma}(\vec{n})$. The equilibrium shape reached at late stage is plotted in Fig. 6.5a together with the $\tilde{\gamma}$-plot. The final shape reached by the energy minimising calculation agrees with the Wulff's theorem, which states that the terminating planes of an equilibrium shape are those that form the convex hull of the planes perpendicular to $\vec{n}\gamma(\vec{n})$. The surfaces are coloured accordingly for A-TiO_2, using the scheme introduced in Sec. 5.7. The corresponding IPF stereographic triangle is given in Fig. 6.5b and it applies to all coloured morphologies in the following sections. Literature values [116] for the lattice parameters ($a = 3.782$, $c = 9.502$) are employed for both the construction and the colouring scheme. The shape is mostly bounded by eight {101} surfaces and the other two ends are truncated and partially bounded by {107} and {001} surfaces. This equilibrium shape differs from the one in Fig. 4.5 and Fig. 4.6 because in the previous chapters only {101}, {100}, {103} and {001} are considered (Tab. 4.1).

Table 6.3: DFT calculations of the surface energy density for various A-TiO_2 planes used to construct $\tilde{\gamma}(\vec{n})$ in this chapter.

family	surface energy density (Jm^{-2})	family	surface energy density (Jm^{-2})
{101}	0.35	{100}	0.45
{001}	0.78	{103}	0.66
{107}	0.74	{112}	0.73
{116}	0.75		

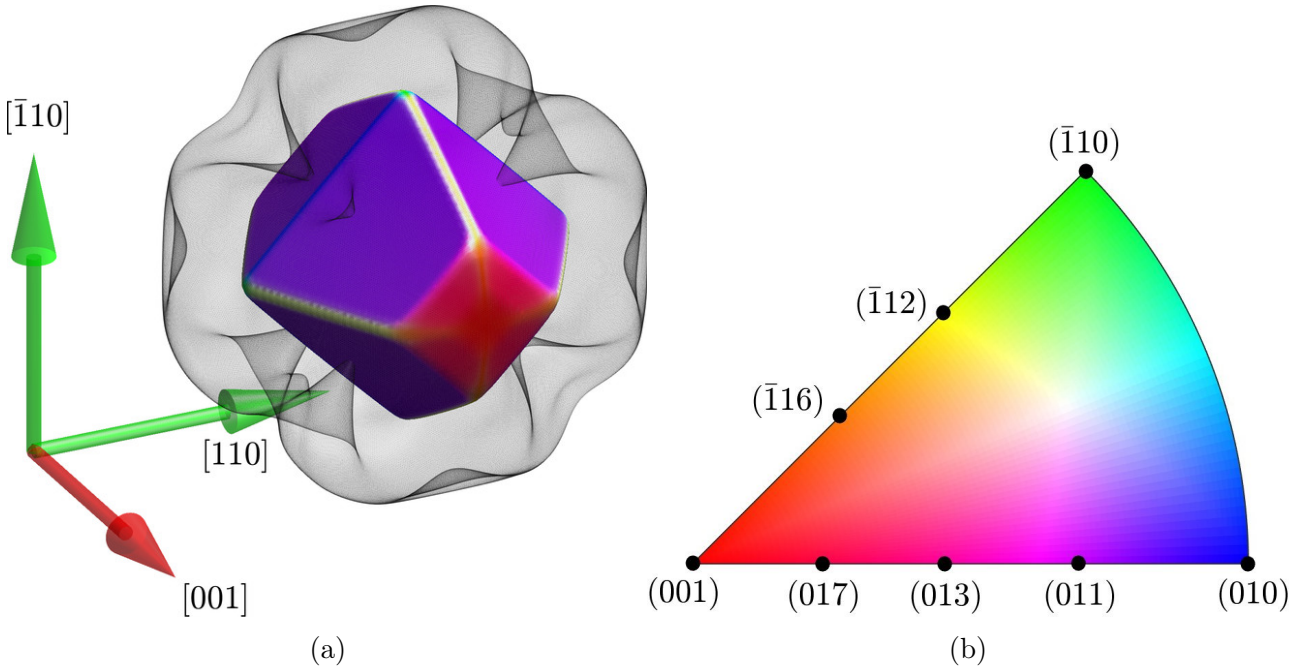

(a) (b)

Figure 6.5: (a) The equilibrium shape of an A-TiO_2 particle and its $\tilde{\gamma}$-plot, with axes drawn to represent the crystal coordinate system. (b) The corresponding IPF colour key.

6.2.3 Phase field model

The modelling approach to the material interface described here follows the one developed in Ch. 5, which can be categorised into a special class of phase field models based on a phenomenological description of an interfacial growth problem [186]. Used as a computational tool this approach keeps track of the interface implicitly, in the sharp interface limit the solution of which converges to that of the underlying moving boundary problem. In this section for the growth of an interface, the ballistic transport characteristic of a CVD process has been included. This is modelled by an array of g fields being advected in various directions following the concept first introduced by Keblinski [165]. The adaptation of the Keblinski model occurs in the incorporation of the g_i fields into the material interface, as specified by an acceptance function characteristic of CVD processes.

It is commonly expected in LPCVD processes that the species are transported to the material interface following some trajectories with an angular cumulative distribution function $\mathcal{P}$ [162]. $\mathcal{P}$ can be modelled by a Maxwellian distribution as a function of polar angle θ and normalised velocity $\tilde{v}$ of the incident adparticles [187]:

$$\mathcal{P}(\theta,\,\tilde{v}) = 1 - cos(\theta)\frac{exp\big(\tilde{v}^2\,cos^2(\theta)\big)\big[1 + erf\big(\tilde{v}\,cos(\theta)\big)\big]}{exp(\tilde{v}^2)\big[1 + erf(\tilde{v})\big]} \tag{6.1}$$

It can be shown that the corresponding probability density function is given by:

$$\frac{d\mathcal{P}}{d\theta} = sin(\theta)\frac{\big(1 + 2cos^2(\theta)\big)exp\big(\tilde{v}^2\,cos^2(\theta)\big)\big[1 + erf\big(\tilde{v}\,cos(\theta)\big)\big] + \frac{2}{\sqrt{\pi}}\tilde{v}\,cos(\theta)}{exp(\tilde{v}^2)[1 + erf(\tilde{v})]} \tag{6.2}$$

The normalised velocity $\tilde{v}$ depends on the average velocity of the incoming adparticles and temperature, which is usually determined for each particular LPCVD processes by the direct simulation Monte Carlo (DSMC) modelling of specific reactors [188]. For simplicity and because of the continuum approach adopted herein*, a simple cosine law 6.3 is used to model the CVD process following [189]. This approximation is made due to the lack of known DSMC modelling of the reactors and deposition systems that have been reported to give rise to the ⟨110⟩-fibre-textured, nano-structured A-TiO_2 nanocolumns.

$$\frac{d\mathcal{P}}{d\theta} = cos(\theta) \tag{6.3}$$

Similar to the approach used in Ch. 5 based on the deterministic part of the Keblinski model [165], the transport of the vapour field is coupled to the diffusion Eqn. 5.1. For the CVD process with an angular distribution function of the incoming flux following Eqn. 6.3, the transport dynamics now consists of the advection of multiple g fields. The different g fields are not coupled to each other, i.e. they do not have interactions following the assumption of ballistic transport. Each g field features a different rain vector $\vec{R}_{\psi,\theta}$ specified by the azimuthal and polar angles ψ and θ defined relative to the crystal coordinate system.

$$\frac{\partial\phi}{\partial t} = \nabla\cdot\left(M\nabla\frac{\delta\mathcal{E}}{\delta\phi}\right) + (\nabla\phi)^2\int_0^{2\pi}\int_0^{\frac{\pi}{2}}\mathcal{A}_{\psi,\theta}\,g_{\psi,\theta}\,d\theta d\psi \qquad \text{in} \quad \Omega \tag{6.4}$$

$$\frac{\partial g_{\psi,\theta}}{\partial t} = -\vec{R}_{\psi,\theta}\cdot\nabla g_{\psi,\theta} - B(\nabla\phi)^2 g_{\psi,\theta} \qquad \text{in} \quad \Omega \tag{6.5}$$

The meanings of the parameters M, $\mathcal{E}$, $\mathcal{A}$, B, η, Ω follow the same as those in Ch. 5, a list of which is given in Tab. 10.3. The subscripts specify the azimuthal and polar angles associated with each g, $\vec{R}$ and $\mathcal{A}$. For example, $\mathcal{A}_{\psi,\theta}$ stands for the acceptance of the flux with azimuthal angle ψ and polar angle θ. The acceptance function $\mathcal{A}$ now also has to consider the polar and azimuthal contributions:

*Complications associated with CVD, e.g. re-emission and thermal decomposition of precursor molecules are not modelled using the continuum approach.

$$\mathcal{A}_{\psi,\theta}(\vec{n}, \vec{R}_{\psi,\theta}) = \frac{d\mathcal{P}}{d\theta}\left((1-\eta)\vec{R}_{\psi,\theta}\cdot\vec{n} + \eta\|\vec{R}_{\psi,\theta}\times\vec{n}\|\right) \tag{6.6}$$

Following the same design as in Eqn. 5.3 in Ch. 5, η controls the contribution of each of the two adsorption modes, with the limiting case of $\eta = 0$ for all normal growth and $\eta = 1$ for all lateral growth.

For a CVD process, it is expected that the flux comes from all possible angles ranging from 0° to 360° for ψ and from 0° to 90° for θ, the contributions of which have to be integrated as shown by the double integral in Eqn. 6.4. The convention and range of the polar and azimuthal angles are illustrated in Fig. 6.6 with arrows representing the corresponding rain vectors

$$\vec{R}_{\psi,\theta} = |\vec{R}|\cdot\begin{bmatrix}\cos\psi & 0 & \sin\psi\\ 0 & 1 & 0\\ -\sin\psi & 0 & \cos\psi\end{bmatrix}\begin{bmatrix}0\\ -sin(\theta)\\ -cos(\theta)\end{bmatrix} \tag{6.7}$$

While each $\vec{R}_{\psi,\theta}$ is associated with a different pair of ψ and θ angles, the magnitude is set to the same value, i.e. $|\vec{R}|$.

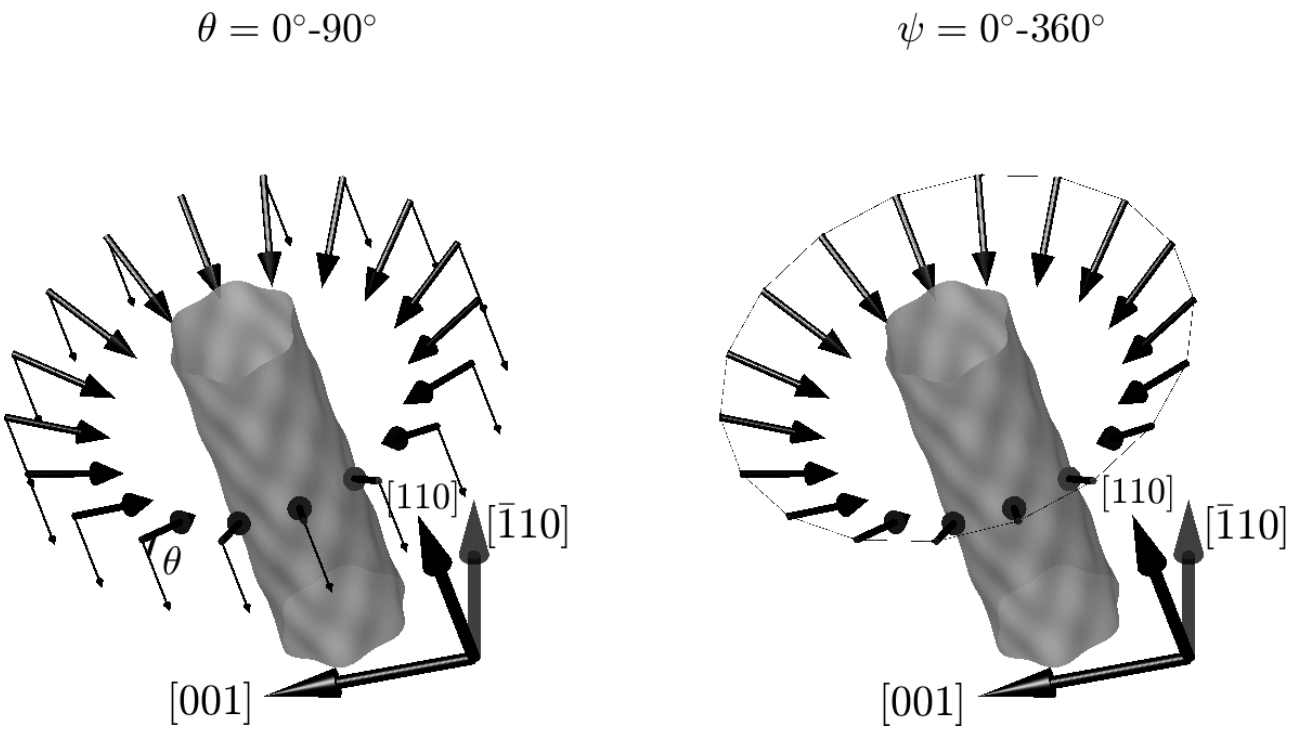

Figure 6.6: Schematic depiction of the geometries of simulation cell visualised by the wireframe. A selection of rain vectors of some g_i fields and their range are represented by the arrows (rescale). The convention of the crystal coordinate system for the A-TiO_2 nanocolumn shown by the three mutually orthogonal arrows.

Following sections 5.2 and 5.3 the same spectral solver for system of Eqns. 6.4 and 6.5 is used. The domain is chosen to be $\Omega = [-1, 1]^3$ with a $256 \times 256 \times 256$ Fourier-LGL grid. The surface energy $\tilde{\gamma}(\vec{n})$ is constructed in such a way that the same method outlined in Sec.

4.1.3 and values given in Tab. 6.3 are employed to yield the correct equilibrium shape. The relevant parameters used in the construction, i.e., γ_{ref}, γ_0 and α_{ref} in Eqn. 4.2 and 4.3, are assigned the values $\gamma_{\{001\}}$, $1.1 \times \gamma_{\{001\}}$ and 0.1 respectively. The gradient energy coefficient ϵ and the Willmore regularisation coefficient $\tilde{\beta}$ in Eqns. 3.41 and 3.42, are given the values 0.02 and 0.005 following Sec. 5.3. As before, these values are fixed for all simulations to ensure that the length scale and timescale are constant throughout the simulations. Following the same arguments made in Sec. 5.4.1, and assuming $l_0 = 100\,\text{nm}$ and γ_{ref} sets the characteristic energy, i.e. $E_0 = \gamma_{ref} \times l_0^2 = 0.78 \times 10^{-14}\text{J}$ and $\tau = 1\,\text{s}$, $|\bar{\vec{R}}|$ equals to $1 \times 10^7 \times |\vec{R}|$ $[\text{m}\,\text{s}^{-1}]$ and $\bar{M}$ becomes $7.8 \times 10^{20} \times M$ $[\text{m}^5\text{J}^{-1}\text{s}^{-1}]$. Because the exact values for E_0, l_0 and τ_0 are unknown to the A-TiO_2 system, the dimensionless energy, length, time and the dimensionless forms of the parameters are used throughout the following sections.

The growth region subject to the examination here is the region that receives the flux coming from all possible ψ, θ angles, assuming no inter-columnar shadowing of the neighbouring nanocolumns. The growth morphology of the secondary columns are numerically exploring by varying the value of $^M/_{|\vec{R}|}$. The initial surface profile of the $\phi = 0.5$ iso-surface is a perturbed cylinder having a radial component $r = r(R,\, \delta_{\psi,z},\, k_\psi,\, \psi,\, z,\, \lambda_z)$:

$$r = R + \delta_{\psi,z}\, cos(k_\psi \cdot \psi)\, cos(\frac{2\pi z}{\lambda_z}); \tag{6.8}$$

where R is the mean radius of the cylinder. $\delta_{\psi,z}$, k_ψ and λ_z are the amplitude, wave number in ψ and wave length in z. The initial condition of the ϕ field is given by the hyperbolic function 6.9 of a numerical approximation to the signed distance function $d = d(r)$. While the initial profile conditions for g_i are obtained by fixing the initial value of ϕ and allowing g_i to evolve in order to reach steady state.

$$\phi(r) = \frac{1}{2}\left(1 + \tanh\left(\frac{d(r)}{2\sqrt{2}\epsilon\tilde{\gamma}(\vec{n})}\right)\right) \tag{6.9}$$

A crystal coordinate system x', y', z' corresponding to [001], [110], [$\bar{1}$10] directions is chosen, as shown in Fig. 6.6, for $\langle 110\rangle$-textured A-TiO_2 nanocolumns. The boundary conditions are specified as follows: ϕ is periodic in z and homogeneous Neumann boundary condition is applied at $x = y = \pm 1$; each g_i field has an in-flow Dirichlet boundary condition $g = 1$ imposed at the x-z and y-z planes to ensure constant supply of vapour. The double integral in Eqn. 6.5 is approximated by using the trapezoidal rule with a resolution of 10°. A factor of $\pi(\pi - 2)$ is used to normalise the probability density function so that the volume under which is equal to 1.

A quasi-steady pressure is assumed in the assignment of in-flow condition for g_i fields. This is based on the observation that similar $\langle 110\rangle$-fibre-textured A-TiO_2 nanocolumns obtained using various techniques [1, 24, 40, 27] share the same feature, that is a low pressure processing parameter the reactors are operated in. A review of these systems are given in Sec. 1.3.2 of Ch. 1. The commonality is the ballistic transport of vapour species in low pressure, regardless of the variants of the processes, either with a time-dependent supply [1] or constant supply [24, 40, 27] of the species.

Due to the scope of this modelling work, it is not desirable in this chapter to explore the entire parameter space of the initial profile, i.e. the four-dimensional space of R, $\delta_{\psi,z}$, k_ψ and λ_z, in order to map out the stability criteria for perturbations as a function of radius, wavenumber and wavelength. Instead, the values of these parameters are fixed and the favourable exposed surfaces during a long-time-scale evolution according to system of Eqns. 6.4 and 6.5 are studied. Likewise, some other model parameters are kept the same as the ones used in Ch. 5, shown in Tab. 10.2. $M/|\vec{R}|$ is varied between 0.001 to 1. All notations used in this chapter are summarised in Tab. 10.3.

6.2.4 Surface indexing

In Sec. 5.7.1 a facet mapping scheme was used to simplify the colouring of the exposed surfaces by symmetry. The same method was applied for an A-TiO_2 particle, shown in Fig. 6.5a. It is worth noting that although this representation of the exposed surfaces gives visually the perception of which surfaces are of the same family, it has to be compared side-by-side with the IPF stereographic triangle (Fig. 6.5b) in order to identify the Miller indexes of the bounding planes. Further complication arises when a 3-D morphology is visualised by using for example a ray-tracing algorithm. The shading and hence the perception of the colour depends on positioning of the surfaces relative to and the type of the light source. It is therefore imprecise and insufficient to disclose the results using this representation. Secondly, unlike a cubic system, the $\{\bar{1}10\}$ and $\{101\}$ surfaces are of different families for a tetragonal symmetry. As a consequence, the colour assigned to the lowest energy surfaces, i.e. $\{101\}$-type surfaces, does not correspond to any of the red, green and blue (RGB) colours located at the corners of the stereographic triangle. Instead, they appear to be purple in the visualisation such as Fig. 6.5a, which is a mix of the RGB colours. For the same reason, the colours of some of the surfaces, e.g. $\{103\}$ and $\{107\}$ surfaces, are very close to each other which make them visually indistinguishable.

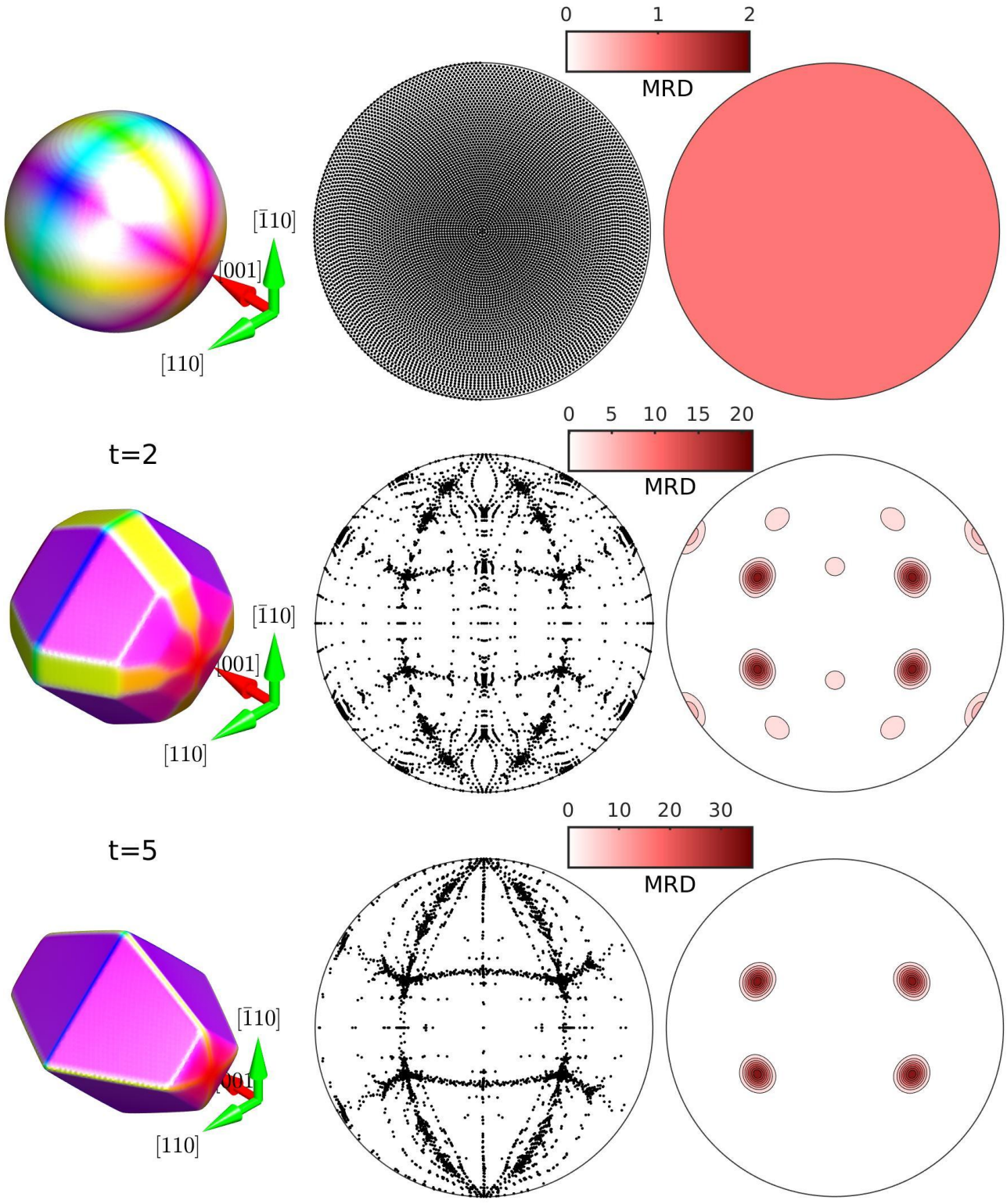

Figure 6.7: The coloured morphologies and their corresponding (110) RSPFs during the time evolution of an A-TiO_2 particle at various intervals of an energy minimising calculation using very small time step $\delta t = 10^{-7}$.

To this end, a suitable way of representing the exposed surfaces based on the concept of pole figure common in EBSD orientation mapping, is adopted with a slight modification. Instead of the crystal orientations, here the stereographic projection of the direction vectors normal to a crystallographic plane $\vec{n}_{(hkl)}$, as specified by a set of Miller indices hkl, is shown on the pole figure. This way each exposed surface with an unique $\vec{n}_{(hkl)}$ is mapped onto a point on the pole figure and this type of pole figure is referred to here as the reciprocal space pole figure (RSPF).

On the implementation side, all the surface patches that give rise to a projection point on the RSPF have to be of equal area. Only the upper RSPF is shown, with the equivalent planes from the lower RSPF projected onto the upper, thanks to the antipodal symmetry. The coloured morphology is complemented by RSPF representation of the exposed surfaces when a result is shown in this chapter and the IPF stereographic triangle is not given in all figures for brevity.

The time evolution of an A-TiO_2 particle in an energy minimising calculation is used for a benchmark. As shown in Fig. 6.7 the initial shape of a sphere corresponding to $t = 0$ has uniformly distributed exposed surfaces on the RSPF, indicated by the intensity in units of multiples of random distribution (MRD). A (110) pole is chosen for the illustration. The non-random patterns appearing in the scatter (middle) and contour (right) representations of the RSPF for the sphere are due to the equal-distance projection. As the energy minimisation progresses, the projection of $\vec{n}_{(hkl)}$ of the exposed surfaces converges to a few definite spots. For this particular benchmark, the maximum intensity increases as more missing orientations become present.

The RSPF of the equilibrium shape in Fig. 6.7 shows {101} poles with intensity of around 35 MRD, which suggest that it is largely bounded by {101}-type surfaces. By choosing different scales for the colourbar, as shown in Fig. 6.8 for the equilibrium morphology of an A-TiO_2 particle, {107} poles become visible. This suggests, similar to the result reached in Sec. 6.2.2, that the equilibrium shape is an octahedron bounded by predominantly eight {101} planes, truncated at two ends by {107}. Furthermore, the scatter plot in Fig. 6.7 indicates that there are eight ridges (corresponding to the light yellow fibres between {101} and {112} in Fig. 6.7), that are enclosed by surfaces with energy density γ_0. It is also noticed by this benchmark that the projection of the exposed surfaces are subject to a numerical error, introduced from the meshing of $\phi = 0.5$ iso-surface in the post-processing[†].

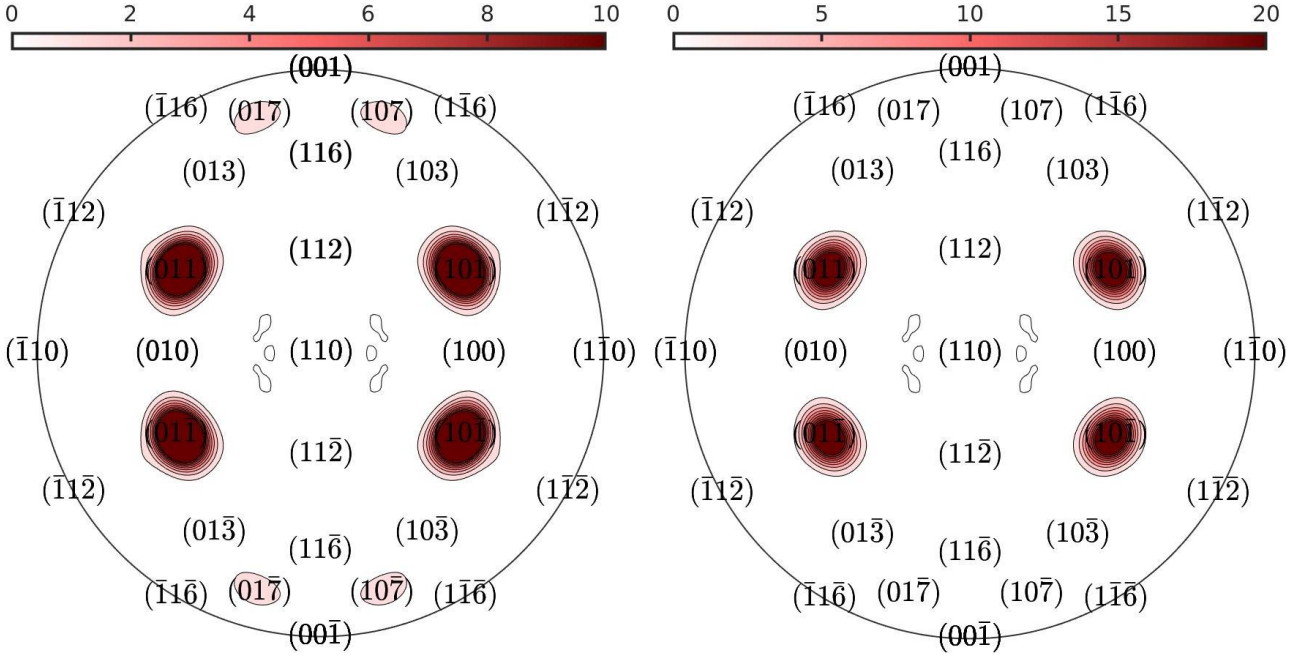

Figure 6.8: RSPF for exposed surfaces of the equilibrium morphology of an A-TiO_2 particle.

[†]Unlike the colouring of the surface which uses the unit normal calculated directly from the phase field $\vec{n} = {}^{\nabla\phi}/_{|\nabla\phi|}$, the normals of the equal-area patches are obtained through the conformal meshing of the implicit surface $\phi = 0.5$, which is subject to errors. Consequently, the centers of the concentrated spots on RSPF are slightly off their corresponding $\vec{n}_{(hkl)}$.

6.3 Long-time-scale evolutions

A long-time evolution for a given initial profile, specified by Eqns. 6.8 and 6.8, is followed. The scale of the colourbars are set to the same range to allow for comparison. During the evolution, the initial shape of a slightly perturbed cylinder gradually approaches a nonrandom morphology at late stage. In Sec. 5.4 it was hypothesised and shown that the growth regime is controlled by the model parameter $^{M}/_{|\vec{R}|}$. By the same token, it is assumed and shown here that $^{M}/_{|\vec{R}|}$ controls the nanocolumnar morphologies corresponding to the LPCVD-grown A-TiO_2 columns. It is therefore varied in order to explore the late-stage morphologies.

For the purpose of a demonstration, an initial profile with parameters listed in Tab. 7.1 is shown in Fig. 6.9. It can be seen on the RSPF that the initial distribution of $\vec{n}_{(hkl)}$ are close to poles perpendicular to (110). This is no coincidence, as the perturbation to a cylinder is small. The degree of spreading is determined by R and $\delta_{\psi,z}$. The larger the ratio $^{\delta_{\psi,z}}/_{R}$ the more spread-out the projection of $\vec{n}_{(hkl)}$ is on RSPF[‡].

Table 6.4: Parameters used for the initial profile shown in Fig. 6.9.

parameter	R	$\delta_{\psi,z}$	k_ψ	λ_z
meaning	radius	amplitude	wave number in ψ	wave length in z
value	0.3	0.02	6	0.5

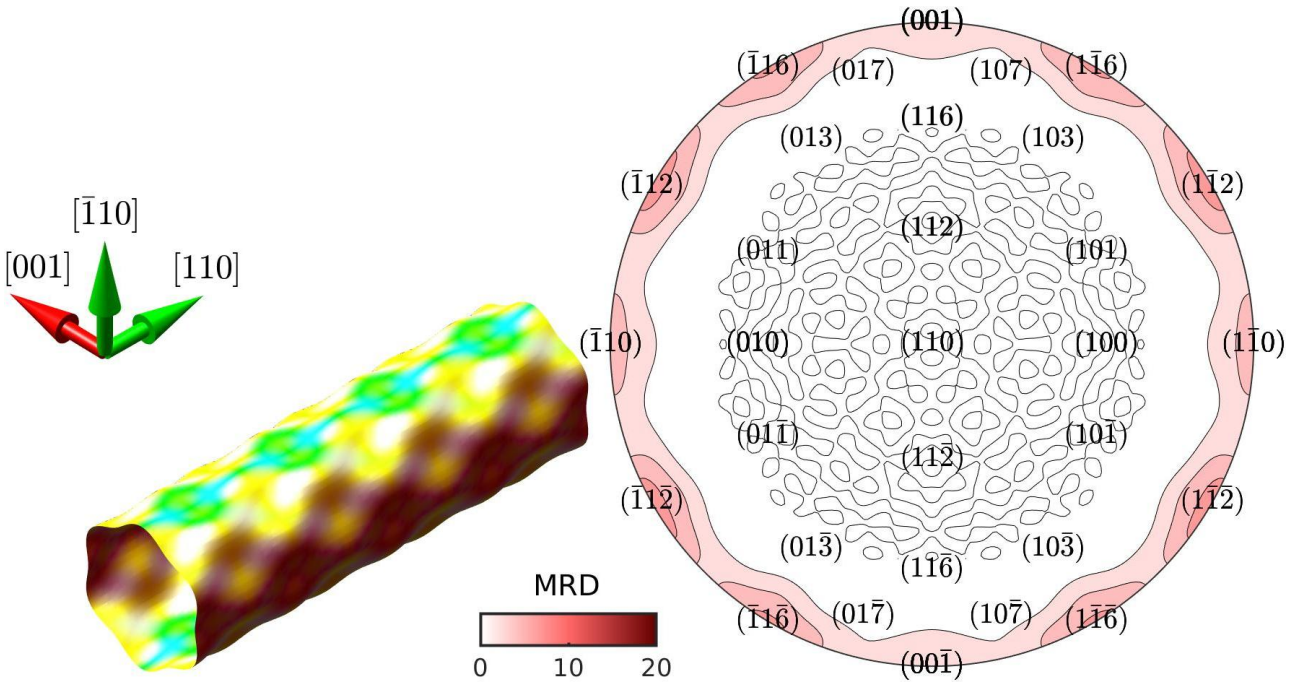

Figure 6.9: Initial surface profile of the material interface at $t = 0$ given by Eqn. 6.9 and the corresponding RSPF.

[‡]It can be shown that, the (110) pole figure has an antipodal symmetry for this initial profile.

It is found that for a $^{M}/_{|\vec{R}|}$ equal to 1, the initial surface profile reduces all its sinusoidal irregularities during the evolution. The morphology approaches its minimum energy configuration, regardless of the η value. Once the equilibrium configuration is reached the column grows in such a way that it keeps its shape and coarsens over time. It can be seen in Fig. 6.10 that the equilibrium shape is bounded largely by $(\bar{1}12)$, $(1\bar{1}2)$, $(\bar{1}1\bar{2})$ and $(1\bar{1}\bar{2})$ surfaces that are again, perpendicular to (110), as indicated by the four intense poles on the RSPF in Fig. 6.10.

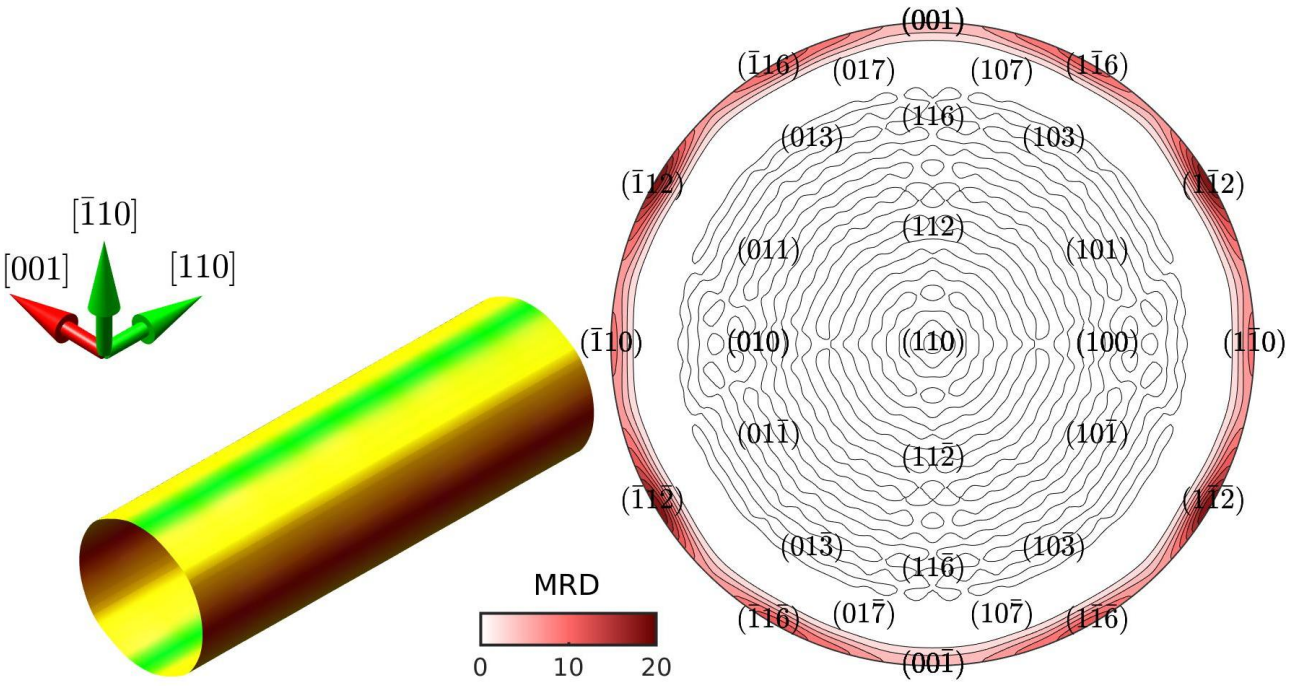

Figure 6.10: Late stage morphology of the column at $t = 1$ with parameter $^{M}/_{|\vec{R}|} = 1$.

For a small $^{M}/_{|\vec{R}|}$ value the long-time evolution of the interface is stopped when the maximum distance of a surface to the centerline $x = y = 0$ exceeds 0.95. The evolution time at which the final morphology is recorded hereafter corresponds to time reached at $r_{max} = 0.95$ and it varies across different $^{M}/_{|\vec{R}|}$ values. Since the structures have an antipodal symmetry with respect to the (110) pole, only the upper part of the (110) RSPF is shown. As can be seen in Fig. 6.11 for $^{M}/_{|\vec{R}|} = 0.001$ and $\eta = 1$, four ring-like protuberances are formed with no fully faceted terminating planes, indicated by the low intensity of the poles. The $\vec{n}_{(hkl)}$ on RSPF are largely scattered but with visible poles around $\{112\}$ and $\{103\}$. The number of the periodic structures, i.e. four in this case, is found to be related to the wavelength in z of the initial perturbation λ_z, i.e. $^{2}/_{\lambda_z} = 4$.

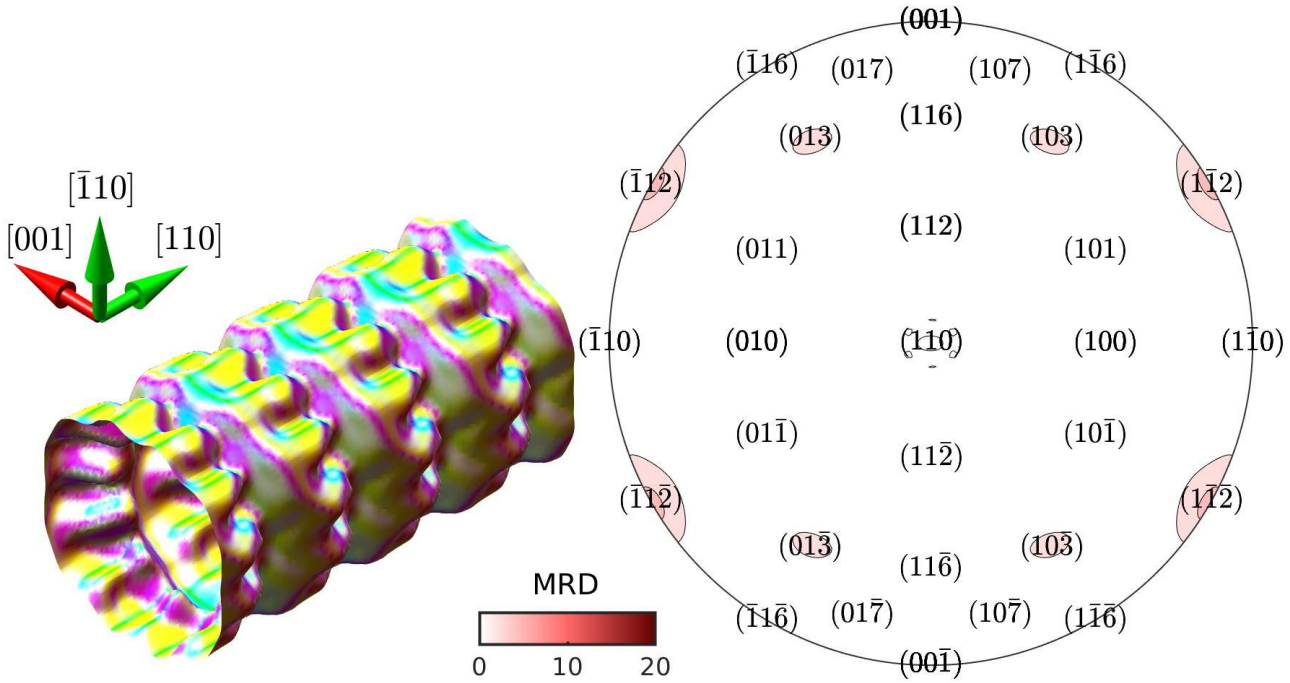

Figure 6.11: Nanocolumn morphology reached at $r_{max} = 0.95$ and $t = 21.5$ with parameters ${}^{M}/_{|\vec{R}|} = 0.001$ and $\eta = 1$.

An interesting morphology is obtained with ${}^{M}/_{|\vec{R}|} = 0.01$ and $\eta = 1$, as shown in Fig. 6.12. Under this growth condition, neither does the column coarsen in a self-similar way nor does it grow with no major facet formed, as in the cases of ${}^{M}/_{|\vec{R}|} = 1$ and ${}^{M}/_{|\vec{R}|} = 0.001$ respectively. The anisotropic growth for ${}^{M}/_{|\vec{R}|} = 0.01$ results in a set of four secondary columns that face upwards in Fig. 6.12. They are bounded partially by {112}, {103}, {110} and {116}-type planes, which are evident on the RSPF, shown in Fig. 6.12. It should be noted that the resulting {110} surfaces which are not included in the $\tilde{\gamma}$-construction have an energy density value equal to γ_0.

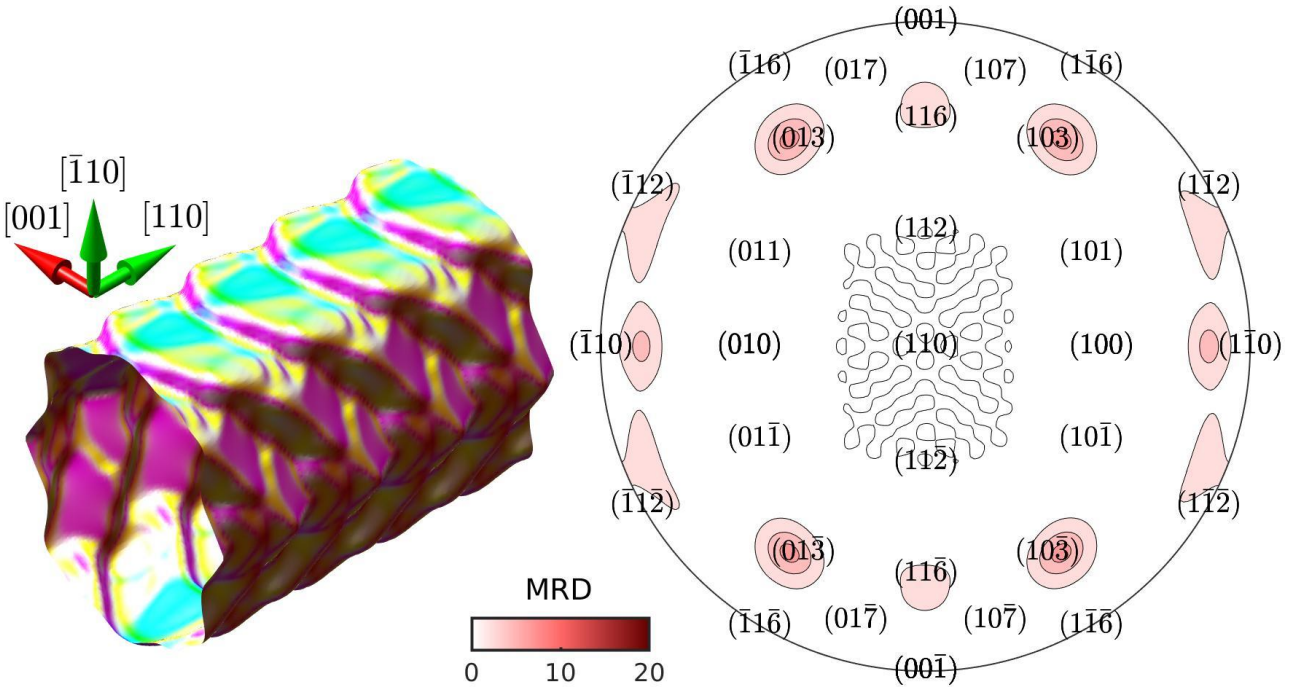

Figure 6.12: Nanocolumn morphology reached at $r_{max} = 0.95$ and $t = 23.7$ with parameters ${}^{M}/_{|\vec{R}|} = 0.01$ and $\eta = 1$.

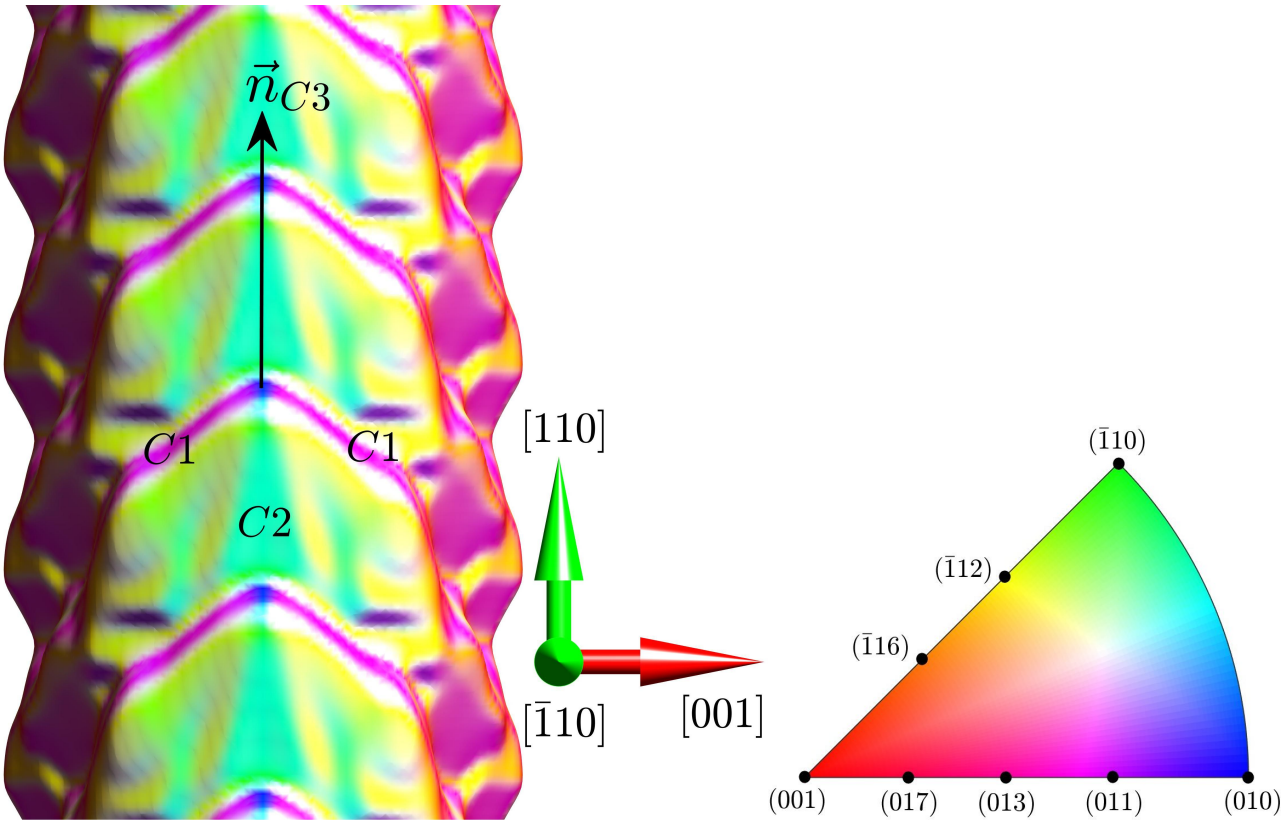

Figure 6.13: The side view of the nanocolumn in Fig. 6.12, reached at $r_{max} = 0.95$ and $t = 23.7$ with parameters ${}^{M}/_{|\vec{R}|} = 0.01$ and $\eta = 1$.

The anisotropic morphology with ${}^{M}/_{|\vec{R}|} = 0.01$ shown in Fig. 6.12 is somewhat expected under this growth condition. The highly anisotropic surface energy of A-TiO_2 is expected to take effect in forming certain facets but not strong enough to counter the preferential deposition in order to maintain the shape. The resultant morphology is found to be symmetric, i.e. it preserves the two-fold rotational symmetry about $\langle 110 \rangle$ of the point group.

As marked on Fig. 6.13, the characteristic features of this morphology can be summarised as follows:

- C1 is bounded by a mixture of $(011)/(01\bar{1})$ and $(013)/(01\bar{3})$ surfaces.
- C2 is not fully faceted.
- $\vec{n}_{C3}$ is found to be close to $\vec{n}_{(010)}$ which makes an β' angle equal to 45°.

These together with how the secondary columns are orientated contradict with the experimental observations, such as the ones given by Clues 2, 3 and 4 in Sec. 6.2.2.

6.3.1 {116} exposed surfaces

It has been shown above that the morphologies obtained with parameter $0.001 < {}^{M}/_{|\vec{R}|} < 1$ are inconsistent with the target nanocolumn morphology detailed in Sec. 6.2.2. A different initial profile given by Eqn. 6.10 is adopted here to replace Eqn. 6.8 for the initial condition. The same parameters listed in Tab. 6.4 are used. This surface profile, as shown in Fig. 6.14, is biased towards the ⟨001⟩ directions, with the superposition of a second sinusoidal perturbation having an amplitude in ⟨001⟩ that is equal to 0.1. The scatter RSPF and the contour RSPF with a different colourbar of this initial profile is shown in Fig. 6.15.

$$r = R + \delta_{\psi,z}\, cos(2k_{\psi} \cdot \psi)\, cos(\frac{4\pi z}{\lambda_z}) + 0.1\, cos(\psi)\, cos(\frac{2\pi z}{\lambda_z}); \tag{6.10}$$

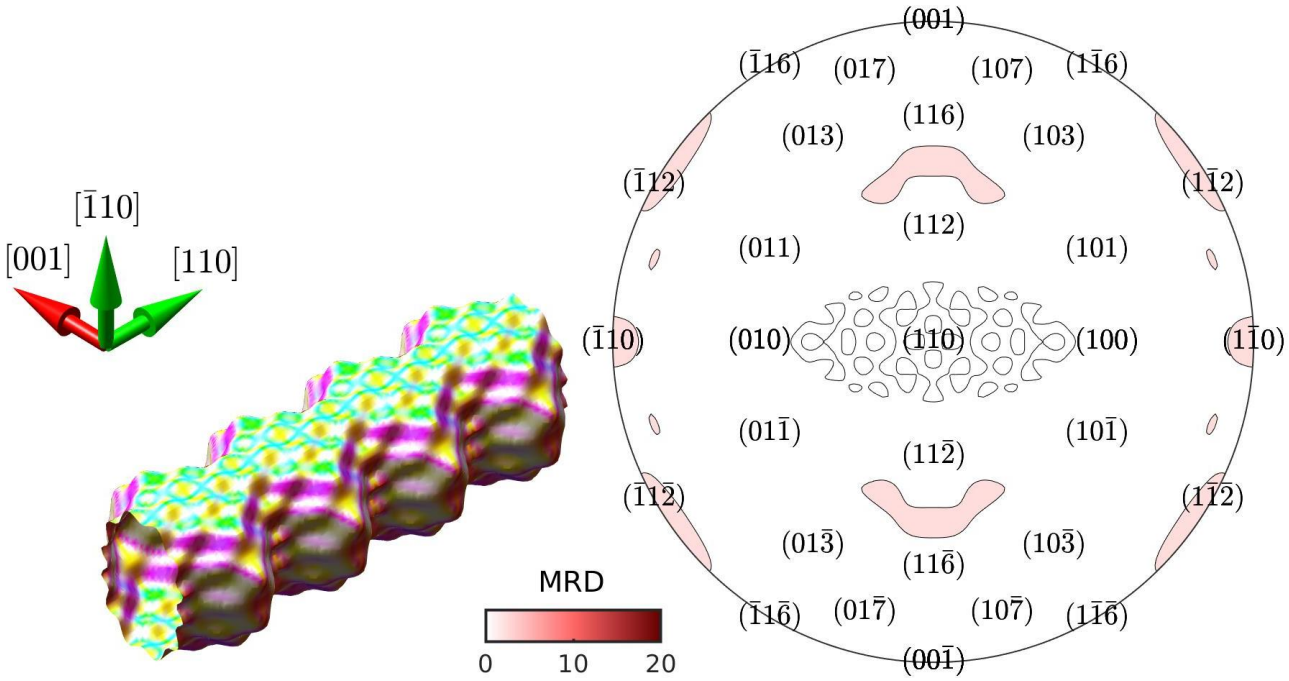

Figure 6.14: Initial surface profile of the material interface at $t = 0$ given by Eqn. 6.10 and the corresponding RSPF.

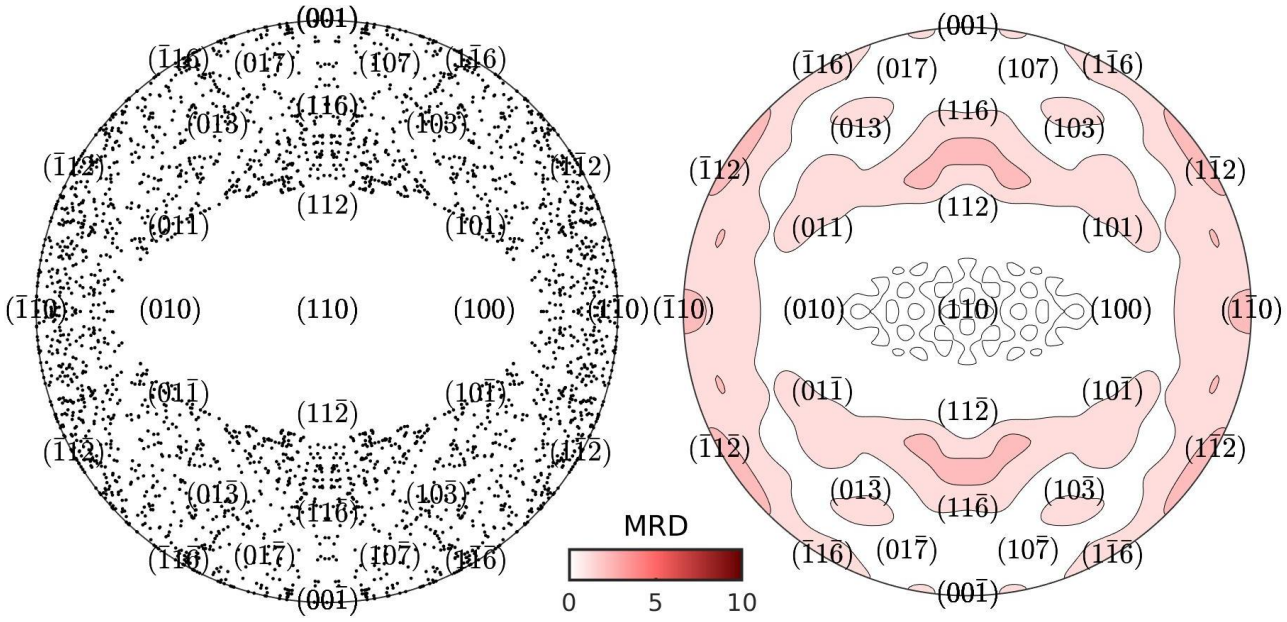

Figure 6.15: The scatter RSPF and contour RSPF of the initial surface profile of the material interface at $t = 0$ given by Eqn. 6.10.

For $M/|\vec{R}| = 1$, the same late-stage morphology is obtained as the one shown in Fig. 6.10, regardless of the η value. This is expected because the thermodynamics of surface diffusion dominate under this growth condition.

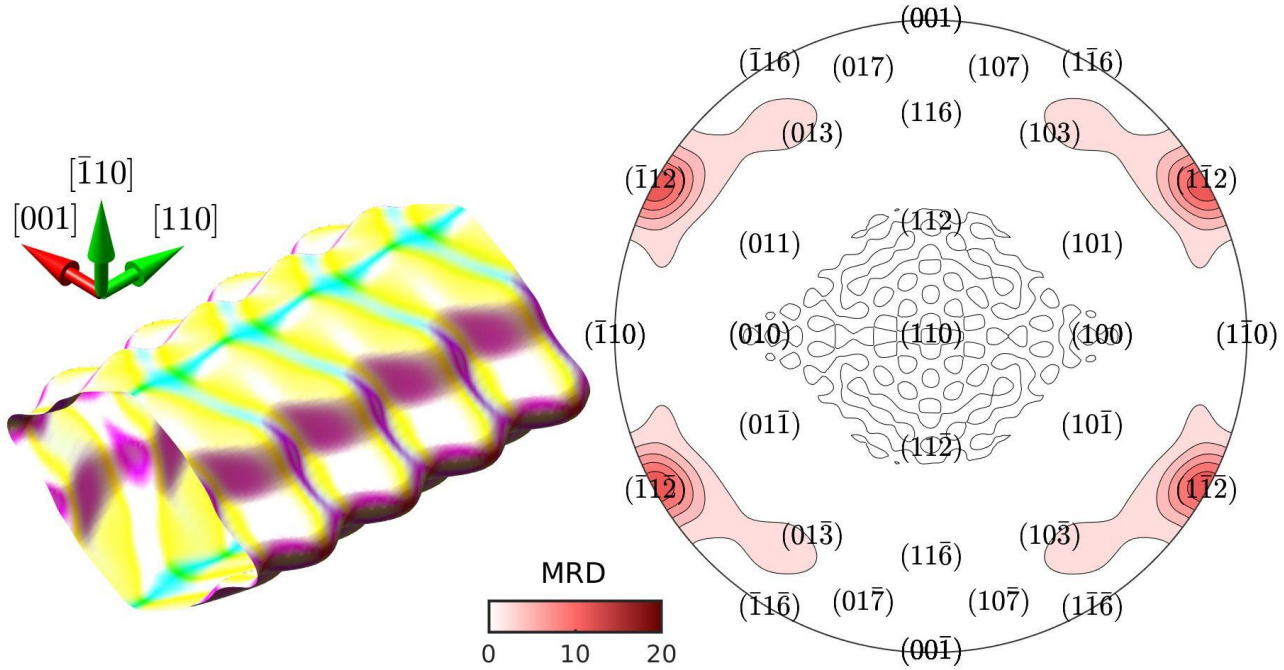

Figure 6.16: Nanocolumn morphology reached at $r_{max} = 0.95$ and $t = 8.0$ with parameters $M/|\vec{R}| = 0.1$ and $\eta = 1$.

For a smaller $M/|\vec{R}|$ equal to 0.1, the morphology obtained when r_{max} reached 0.95 is shown in Fig. 6.16. The perturbation with amplitude $\delta_{\psi,z}$ is found to be stable. However the newly added perturbation with amplitude equal to 0.1 is unstable. Compared with the RSPF in Fig. 6.10, the four high-intensity {112} poles are more spread-out and some intensity has migrated to the nearby eight {103} poles. The morphology is still largely bounded by the four {112}-type surfaces that are perpendicular to (110).

With $^{M}/_{|\vec{R}|} = 0.01$ and $\eta = 1$, an interesting morphology was developed as shown in Fig. 6.17. High-intensity poles around (116), (11$\bar{6}$), ($\bar{1}\bar{1}\bar{6}$) and ($\bar{1}\bar{1}$6) are found, suggesting that the faceted C2 planes for this morphology are of the {116} family. The C2 planes are indexed on the 3-D morphology. It can seen that, the perturbation with amplitude $\delta_{\psi,z}$ became unstable under this growth condition, compared with $^{M}/_{|\vec{R}|} = 0.1$. The poles around (116), (11$\bar{6}$), ($\bar{1}\bar{1}\bar{6}$) and ($\bar{1}\bar{1}$6) are spread out and the centers are slightly off them. This means that although C2 planes are largely bounded by {116} facets, they are not fully faceted. On the other hand, C1 planes consist of a mix of surfaces. $\vec{n}_{C3}$ is identified to be close to $\vec{n}_{(112)}$ and $\vec{n}_{(11\bar{2})}$.

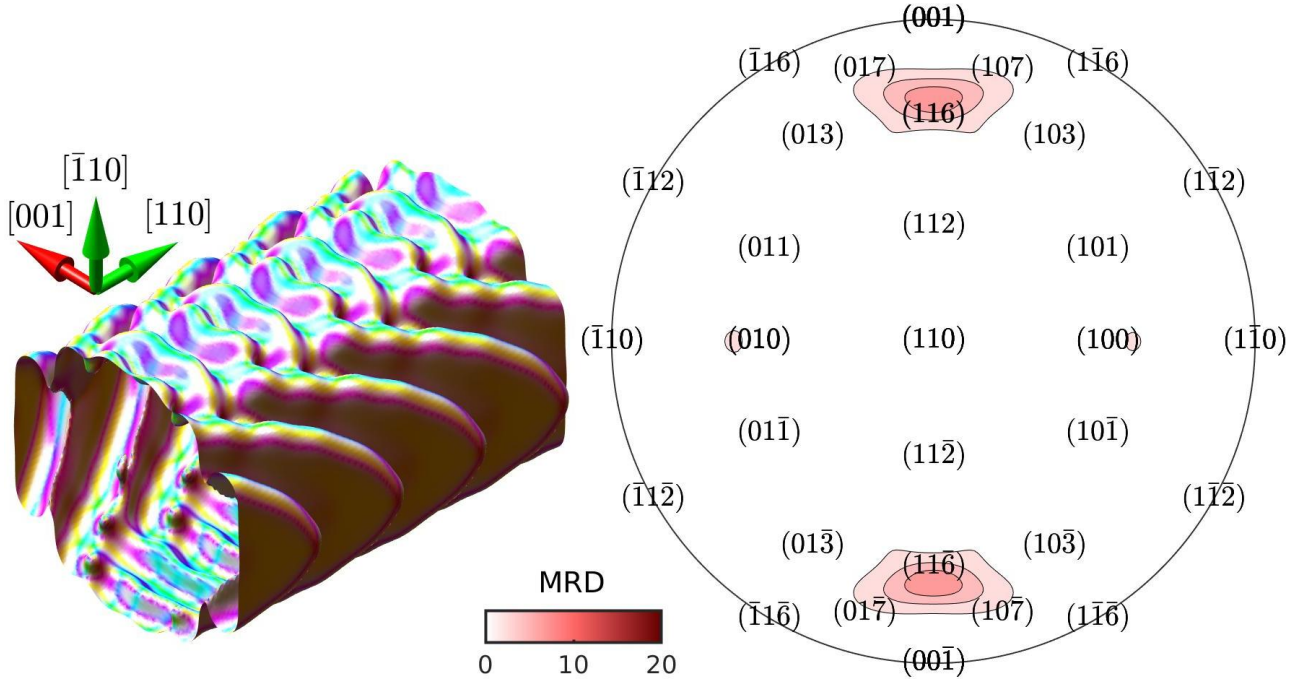

Figure 6.17: Nanocolumn morphology reached at $r_{max} = 0.95$ and $t = 22.3$ with parameters $^{M}/_{|\vec{R}|} = 0.01$ and $\eta = 1$.

The antipodal symmetry with respect to the (110) pole is broken for this morphology and therefore in Fig. 6.18, both upper and lower pole figures are shown. The scale of the colorbar is also changed in Fig. 6.18 to allow for the visualisation of the less intense poles. The areas {101} and {100} poles cover in the lower pole figure are large, suggesting that the anisotropy of {101} and {100} bounding plane distribution is weak. A slice through the ($\bar{1}$10) plane is taken and the profile with a bright-field colourmap is plotted in Fig. 6.19. As marked on the plot, β' is measured at 26.5°, which is in agreement with Clue 2.

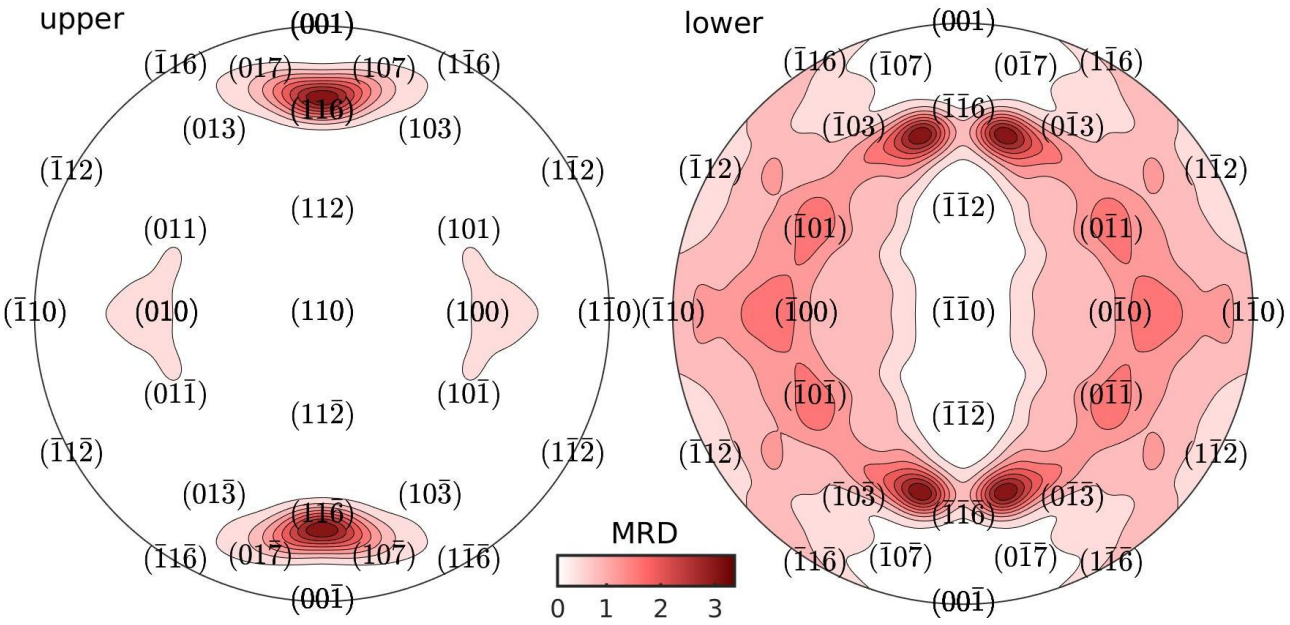

Figure 6.18: Upper RSPF and lower RSPF of the same morphology in Fig. 6.17 with a different colourbar.

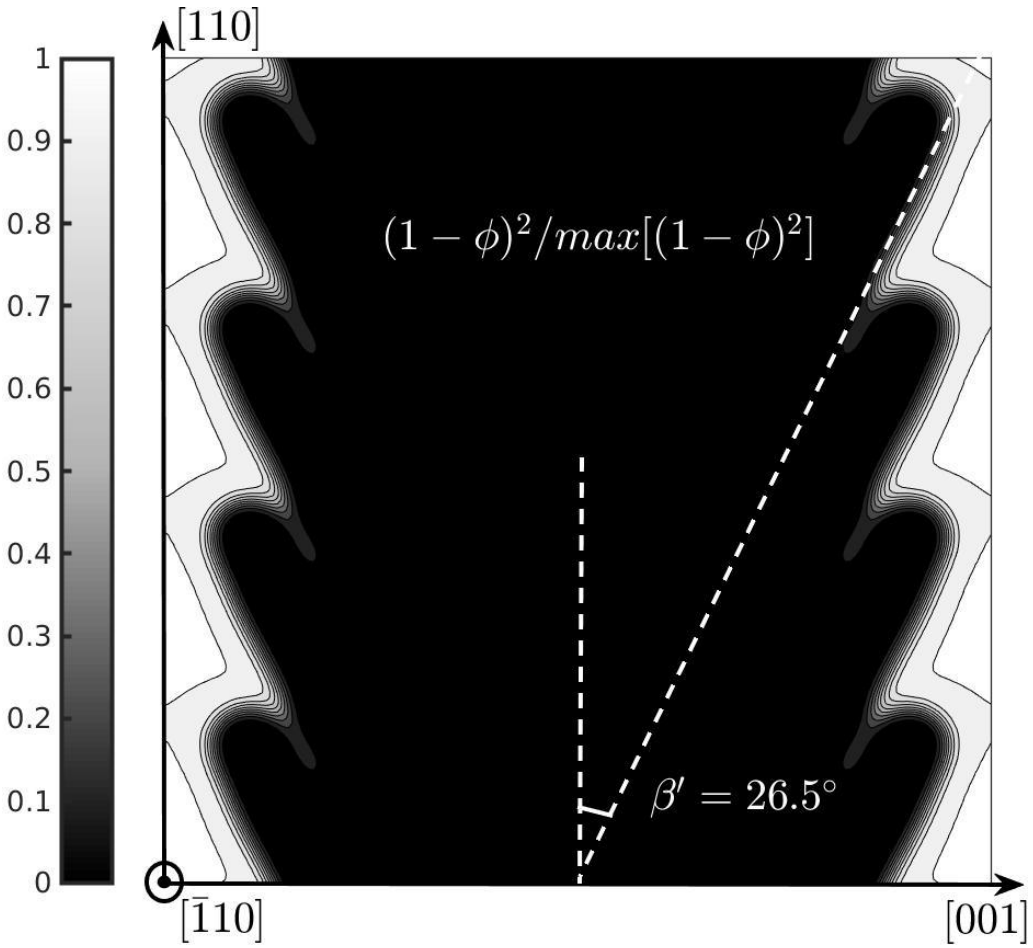

Figure 6.19: A slice of the morphology reached at $r_{max} = 0.95$ and $t = 22.3$ with parameters $^{M}/_{|\vec{R}|} = 0.01$ and $\eta = 1$.

6.4 Discussion

Before making comparisons between the microstructure of the A-TiO_2 thin films and the morphology of the periodic columns described in Sec. 6.3, it is necessary to re-examine the assumptions and simplifications which led to the results. These are summarised as follows:

1. Ballistic transport of the gas species in the reactors is assumed to grow nano-structured A-TiO_2.
2. A quasi-steady pressure is assumed, which translates to the Dirichlet in-flow boundary condition of the g fields.
3. The effect of grain boundary impingement is negligible in the formation of the $\langle 110 \rangle$ fibre texture.
4. Negligible inter-columnar shadowing occurs during the development of secondary morphology.
5. The crystallites grow under condition close to $^{M}/_{|\vec{R}|} = 0.01$, a commonality shared among various deposition techniques reviewed in Sec. 1.3.2.
6. Only the anatase phase of TiO_2 is considered.
7. The variation in the choice of substrate materials is assumed to have no effect on the growth of late stage nanocolumnar morphology.
8. Surface diffusion of A-TiO_2 can be modelled by Eqn. 4.4 using a highly anisotropic $\tilde{\gamma}(\vec{n})$ constructed with discrete physical values given in Tab. 6.3.

With the above assumptions and simplifications made, one can draw parallels, using the resultant morphology that is consistent with experimental observations, in hope of providing insight into the nature of the free surface. To support the following conclusions, the simulated microstructure (Fig. 6.20a) is compared with the SEM micrograph of an A-TiO_2 thin film (Fig. 6.20b).

- The surface energy density values associated with specific planes affect the details of the resulting morphologies.
- A nano-structured morphology consistent with observations made in Sec. 6.2.2, is developed with initial profile specified by Eqn. 6.10 and parameters $^{M}/_{|\vec{R}|} = 0.01$ and $\eta = 1$.
- The biased perturbation for an initial profile, as specified by Eqn. 6.10, results in periodic secondary structures that are largely bounded by C2, {116}-type free surfaces.
- The resultant microstructure, predominantly bounded by C2 surfaces, is controlled by the interplay between the thermodynamics of faceting and the shadowing due to ballistic transport.
- {116}-type surfaces are technologically important reactive facets that have superior electrochemical properties, and have only been reported in synthesised nanoparticles using doping [190].
- The fastest growth directions of the secondary structures $\vec{n}_{C3}$ are close to $\vec{n}_{(112)}$ and $\vec{n}_{(11\bar{2})}$.
- The tilt angle of the secondary structures $\beta' \approx 26.5°$ is smaller than the theoretical angle 29° between $\vec{n}_{(112)}/\vec{n}_{(11\bar{2})}$ and $\langle 110 \rangle$. This means that $\vec{n}_{C3}$ are slightly off $\vec{n}_{(112)}$ and $\vec{n}_{(11\bar{2})}$

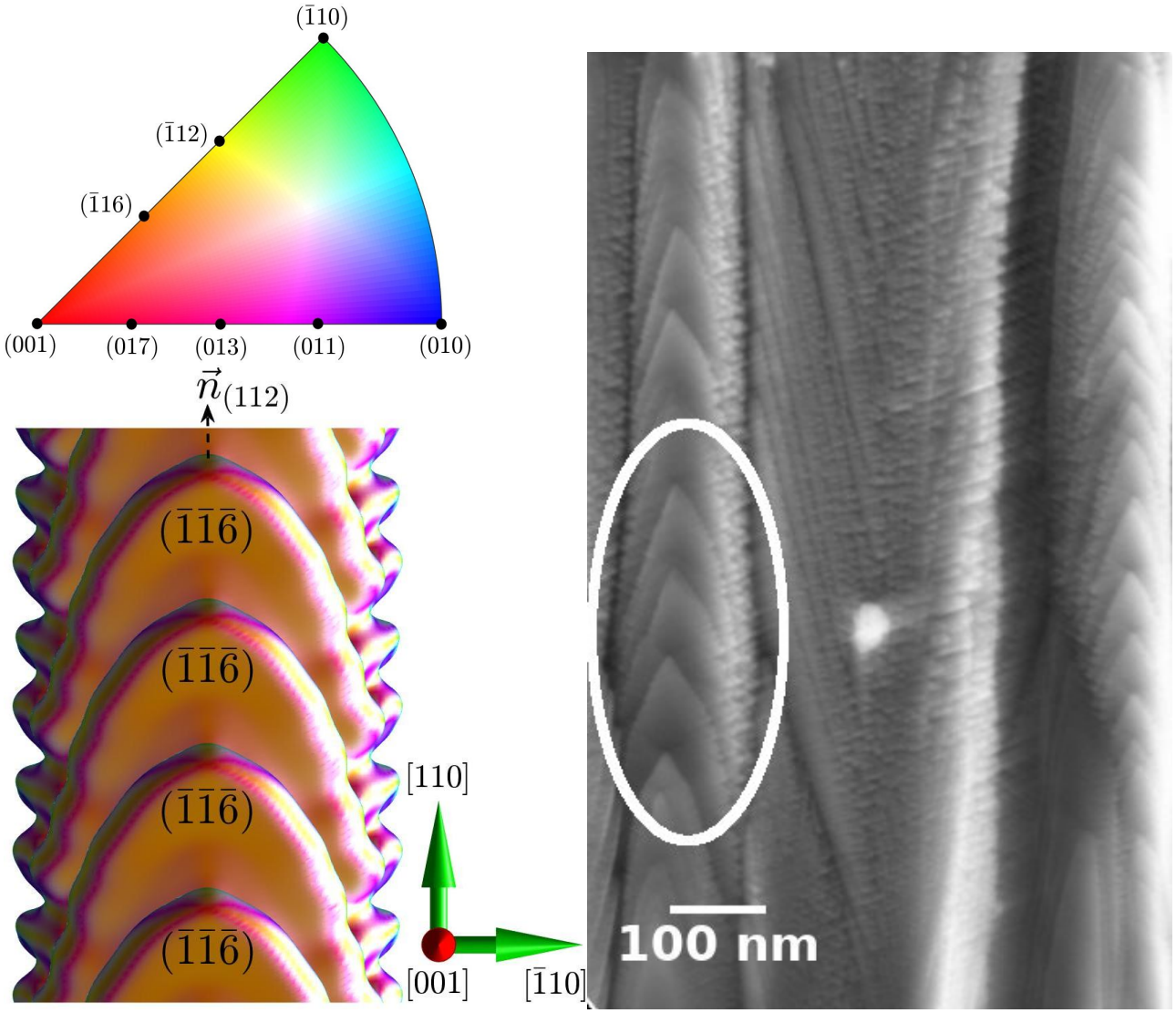

(a) (b)

Figure 6.20: (a) A side profile of the morphology in Fig. 6.17 reached from the initial profile Eqn. 6.10 with parameters $^{M}/_{|\vec{R}|} = 0.01$ and $\eta = 1$. The relavant terminations in the discussion are annotated and an IPF stereographic triangle for A-TiO_2 is given on the top left. (b) SEM side view of pp-MOCVD grown TiO_2 thin film on fused silica substrate (image from [1]). The white oval highlights a nanocolumn orientated for comparison to the simulation with a set of secondary plates and tertiary instability.

6.5 Final remarks and outlook

In Sec. 5.7.5, the array of overhangs around the primary MgO nanocolumn is bounded by two alternating surfaces, resulting in high exposed surface area. The pertinent experimental characterisation techniques for the study of such intra-columnar interface were suggested in Sec. 5.8.3. The same techniques, e.g. USAXS [169, 170], XRNDI [171] and NFXRI [172], can be used to unravel the nature of the free surfaces and to validate the model predictions for A-TiO_2.

The secondary structures are commonly observed in the nano-structured A-TiO_2 thin films [1, 24, 40, 27]. The origin of the well-aligned secondary structures can be attributed to the self-shadowing of surface protuberances, which under growth condition ${}^{M}/_{|\vec{R}|} = 0.01$ cannot be compensated by the local surface diffusion. It can be argued that the details of such secondary structures are not captured by means of numerical simulation used in this chapter, such as the non-symmetric shapes of the secondary columns evident in Fig. 6.20b. One may ask the question if this is due to the fact that inter-columnar shadowing in fact plays the role of controlling the morphologies of the secondary structures. What is the origin of this anisotropy as the symmetries which $\tilde{\gamma}(\vec{n})$ and $\vec{R}_{\psi,\theta}$ possess are broken? These are detailed questions which can only be answered by a model taking into account additional effects.

Only a selected set of parameters, R, $\delta_{\psi,z}$, k_ψ, λ_z and η are explored in this study. Initial profiles are assumed the forms of Eqn. 6.8 and Eqn. 6.10. A further study of this model can be based on the variation in these parameters, in order to seek for the existence of e.g. a critical radius or wavelength. For a complex system such as Eqns. 6.4 and 6.5 the conventional, analytical stability analysis seems impractical if not at all feasible, as discussed in Sec. 6.2.1. Numerical study of such a realistic system remains the only practical way.

In addition, the surface energy density values for the surfaces, the types of surfaces being included and the $\tilde{\gamma}$-construction parameters, may be of importance in determining the details of morphologies reached at late stage. In the construction of $\tilde{\gamma}(\vec{n})$, interfacial energies of stoichiometric surfaces of pure anatase are used. A natural question is to ask if any contaminants reported, such as amorphous carbon [1] would have any effects on the growth. The adsorption energies of the carbon adsorbed surfaces would differ from those of the clean facets. If this effect is present among the growth of A-TiO_2 thin films, how would it change the crystallography of the nano-structured morphology? How does the model parameter η which is related to the mechanisms of incorporating materials on the diffuse interface change if there was such effect? These are the questions that a future atomistic modelling work will be able to answer.

To improve on top of the current model, which assumed no inter-columnar shadowing, the model formulation can be extended to include the growth of neighbouring nanocolumns. The details of the morphology are affected by preferential deposition due to inter-columnar shadowing, depending on the nature of the neighbouring grains. In particular, it is useful to know how the distance of separation between grains affects the late-stage morphologies. Other than the separation, the neighbouring grains take on different in-plane orientations for the $\langle 110 \rangle$-fibre-textured A-TiO_2 thin film. The variation in in-plane orientations, or the misorientation in neighbouring nanocolumns, is also expected to influence the details of the morphology, compared with those of the perfectly aligned (periodic) nanocolumns. Therefore, a systematic study based on the variations in orientation for nanocolumns growing competitively can be helpful in understanding some of the details of the nanocolumnar morphologies of A-TiO_2 nanocolumns.

7. Conclusions

7.1 Review

Starting from modelling an experimental system of OAD, the deterministic part of the Keblinski model [165] is adapted for a regularised CHW energy functional, targeting realistic materials. The process-specific preferential deposition is realised by the introduction of an incident angle-dependent acceptance function. The proposed model is used to examine an alternative theory for the origin of texture formation in biaxially aligned MgO nanocolumns. Assumptions are made to enable the simplification of the model domain and geometry, which in turn allows for 3-D numerical simulation of the nanocolumn morphology. A growth regime is hypothesised to be responsible for the formation of biaxial texture. Under the assumptions and the hypothesis, the model has demonstrated that the alternative theory of texture formation produces nanocolumn morphologies and crystallography as well as the preferred column tilt angles, that are more agreeable with the experimental results than the existing theory predictions.

The growth of secondary structures on nano-structured A-TiO_2 columns has been examined using the same model, extended to a wide range of incident angles characteristic of a CVD system. The free surface such nanostructure exposes is technologically important in photoconductive and photocatalytic applications. The nature of the exposed surfaces are crucial in determining the overall property and performance of the particular application. By performing 3-D numerical experiments with various prescribed parameters, it was suggested in Sec. 6.3 that the relevant morphology is largely bounded by {116}-type surfaces of the secondary structures, with the fastest growth direction close to $\vec{n}_{(112)}/\vec{n}_{(11\bar{2})}$.

Energy minimisation calculations [62, 63] are undertaken to benchmark the highly anisotropic energies constructed for MgO and A-TiO_2, which employ *ab initio*-derived energies in the Siem-Carter construction [110] for realistic materials [111]. The highly nonlinear model formulation is studied numerically and implemented using an efficient stabilised time integration scheme [191, 127] in combination with a Fourier-Legendre-Galerkin solver tailored for the targeted model geometries. The implementation of the fast direct solver allows for the resultant complex 3-D morphologies to be accessed at various stages of nanocolumn growth during long-time-scale evolutions.

Focus was given on the formation of kinetically frozen facets. The MgO nanocolumns are found to be surrounded by a network of overhangs composed of alternating nano-facets, as a consequence of nanocolumns growing in the hypothesised growth regime. The model is extended to a more complex CVD system in order to index the exposed surfaces of A-TiO_2 nanocolumns, the nature of which are linked to the technologically important material properties. Based on similar assumptions and model setup, the candidate terminations for secondary columns of an A-TiO_2 nanocolumn are analysed and visualised, using RSPF representation developed for the 3-D numerical simulations undertaken.

7.2 Historical perspective

The concept of competitive growth in the context of texture formation was pioneered by van der Drift [65]. Following the success of this theory, particularly in the general results for a class of crystals based on simplistic geometric arguments, a large number of models have been proposed. These include the structural zone models (e.g. [70, 71, 72, 73, 74]), which assume ideal or extreme cases for the growth mechanisms involved in the microstructural development of the thin film. The extended structural zone model [75] took the non-local shadowing into account and explained the biaxial texture formation based on the calculation of geometric capture length [151]. Ghekiere improved on the extended structural zone model with the addition of a self-shadowing effect and gave a more accurate prediction [147]. Paritosh [8] for the first time took explicitly the shadowing effect of directional flux into the growth dynamics and argued that the formation of porosity is a result of facet splitting and the preferred orientation of nanocolumns can be related to α. However these geometric models overlooks the growth regime in which the surface diffusion is limited on a single-crystal nanocolumn.

A group of models featuring the Mullins' diffusion [192] as well as the deposition term as a function of the non-local morphology facilitate the study of the interplay between finite surface diffusion (finite adparticle mobility) and shadowing. These include, notably, models for sputtering deposition [193] and kinetic roughening of columnar surface morphology [194]. The mound formation in a typical columnar morphology is attributed to the so-called shadowing instability [7]. 3-D surface morphologies are accessible to the study in this class of small-slope models, owing to the single-valued height function. The drawback is that with the small-slope approximation in these models, some realistic effects and features, such as surface diffusion with anisotropic surface energy and the formation of overhangs are neglected.

From a modelling perspective, the model proposed in this work belongs to a class of models called diffuse interface model. This approach allows for an implicit representation of the interface and it facilitates the complex topological changes of interface common in a moving boundary problem. Eggleston first extended the Kobayashi model [103] to accommodate highly anisotropic surface energy, but this approach of convexifying the energy in the non-convex regions modifies the physics within those regions, which makes it unsuitable for realistic materials. Torabi et al. [62, 63] circumvented the ill-posedness of the Kobayashi formulation associated with highly anisotropic systems by proposing a regularised formulation. Salvalaglio et al [111, 112, 113] applied this model to material-specific systems using a large-scale finite element code [132]. The computational work involved in this type of simulations of 3-D realistic materials is usually very demanding. To include the physics of non-local shadowing into the formulation, this established computational approach does not readily apply. Salvalaglio in a recent work implemented an idealised deposition system featuring shadowing effect in a phase field model [12], but only isotropic energy was considered.

The model proposed in this thesis incorporates both material-specific anisotropic energy and process-specific deposition terms. The concept of an acceptance function in the original van der Drift theory [65] is extended to incorporate the process-specific features of a prototype MgO-OAD system, including a local coordinate system for the crystal orientation, a global coordinate system for the substrate as well as the boundary conditions rendering the shadowing naturally. The physics of an incident angle-dependent acceptance of the adparticles is examined

and it is found that the sine dependence of the acceptance function is responsible for some experimentally observed morphologies. Such study of a realistic system has not been reported previously in the literature. In addition, an efficient solver optimised for this type of modelling is adapted and is able to handle 3-D realistic materials and complex deposition setup. In Tab. 7.1, different features of the model proposed in this thesis is summarised and compared with some of the existing continuum models mentioned above.

Table 7.1: The features of the new model compared with those of the existing models.

model type	continuum models \ model features	surface diffusion			deposition kinetics			dimension	topology	
		finite	anisotropic transport	material-specific	nonlocal shadowing	incident angle-dependent acceptance	process-specific deposition	$2+1$	overhang	efficient solver
geometric	van-der-Drift [65]		✗			✗				
	extended SZM [75]		✗				✗			
	Ghekiere et al. [147, 151]		✗		✗		✗			
	Paritosh et al. [8]		✗		✗		✗		✗	
small-slope	Bales & Zangwill [193]	✗			✗		✗			
	Lichter & Chen [195]	✗			✗					
	Karunasiri et al. [194]	✗			✗		✗			
	Yao & Guo [7]	✗			✗		✗	✗		✗
	small world model [196]	✗			✗		✗	✗		✗
diffuse-interface	Keblinski et al.[165]	✗			✗				✗	
	Eggleston et al. [197]	✗							✗	
	Torabi et al. [62, 63]	✗	✗					✗	✗	✗
	Salvalaglio et al. [112, 113, 111]	✗	✗	✗				✗	✗	✗
	Salvalaglio et al. [12]	✗			✗			✗	✗	
	this work	✗	✗	✗	✗	✗	✗	✗	✗	✗

7.3 Key contributions

The modelling and analysis undertaken in this thesis enable engineering of film growth conditions to obtain optimal performance of a thin film system. The work has provided insight into the controlling processes that result in active surfaces. This novel modelling approach can be readily extended to other thin film vapour growth processes such as sputtering, plasma and rotating-substrate depositions of nano-structured materials. The main contributions of this thesis are chronologically listed as follows:

- A 1-D deposition model for the pulsing pressure process (Sec. 2.2).
- Material-specific surface energy density functions constructed for MgO and A-TiO_2 (Ch. 4), benchmarked and tested in energy minimisation calculations against the corresponding convexified ξ-plots (Ch. 4).
- A continuum model proposed for the study of a process-specific thin film system (Ch. 5).
- An alternative theory for the origin of texture formation in biaxially aligned nanocolumns. This theory is demonstrated and examined using the proposed continuum model (Ch. 5).
- Model parameters controlling the growth regime in this theory are identified. The nanocolumnar regime is hypothesised to be the condition necessary for the growth of biaxially textured MgO thin films (Ch. 5).
- 3-D numerical simulations undertaken for the study of highly anisotropic systems of realistic materials, optimised for different model geometries and process-specific deposition terms (Chapters 5 and 6).
- An extension of the model to CVD deposited A-TiO_2 nanocolumns (Ch. 6).
- Exposed surface representations developed for: the meaningful colouring of nano-structured morphologies (Ch. 5); and the RSPF of nanocolumnar morphologies (Ch. 6).
- A model prediction of the growth exponent and overhang spacing of the biaxially textured MgO nanocolumns (Ch. 5).
- A model prediction of the exposed surfaces of a A-TiO_2 nanocolumn grown from a special initial conditions (Ch. 6).

As a final remark, many nanostructured materials with interesting morphologies and free-surface-related properties are made using low pressure chemical or physical vapour deposition. By varying the model parameters the same work can be carried out for different materials and low pressure processes. The model developed here can be applied to understand how to select processing parameters such as temperature and pressure in order to control the resultant morphologies and engineering properties.

9. Bibliography

[1] S. Krumdieck et al. 'Nanostructured TiO2 anatase-rutile-carbon solid coating with visible light antimicrobial activity'. In: *Scientific Reports* 9.1 (2019), pp. 1–11. DOI: 10.1038/s41598-018-38291-y.

[2] Z. Aabdin et al. 'Growth Behavior of $DyBa_2Cu_3O_7$-δ Thin Films Deposited by Inclined Substrate Deposition for Coated Conductors'. In: *Physics Procedia* 36 (2012), pp. 1445 –1449. DOI: 10.1016/j.phpro.2012.06.240.

[3] F. Tang et al. 'Texture evolution during shadowing growth of isolated Ru columns'. In: *Phys. Rev. B* 72.16 (16 Oct. 2005), p. 165402. DOI: 10.1103/physrevb.72.165402.

[4] M. Hilse et al. 'Ferromagnet-semiconductor nanowire coaxial heterostructures grown by molecular-beam epitaxy'. In: *Appl. Phys. Lett.* 95.13 (2009), p. 133126. DOI: 10.1063/1.3240405.

[5] S. P. Stagon and H. Huang. 'Controllable growth of aluminum nanorods using physical vapor deposition'. In: *Nanoscale Res Lett* 9.1 (Aug. 2014), p. 400. DOI: 10.1186/1556-276x-9-400.

[6] M. Pelliccione et al. 'Mound formation in surface growth under shadowing'. In: *Phys. Rev. B* 74 (12 2006), p. 125420. DOI: 10.1103/PhysRevB.74.125420.

[7] J. H. Yao and H. Guo. 'Shadowing instability in three dimensions'. In: *Phys. Rev. E* 47 (2 1993), pp. 1007–1011. DOI: 10.1103/PhysRevE.47.1007.

[8] Paritosh and D. J. Srolovitz. 'Shadowing effects on the microstructure of obliquely deposited films'. In: *Journal of Applied Physics* 91.4 (2002), pp. 1963–1972. DOI: 10.1063/1.1432125.

[9] J. Yu and J. G. Amar. 'Dynamical scaling behavior in two-dimensional ballistic deposition with shadowing'. In: *Phys. Rev. E* 66 (2 2002), p. 021603. DOI: 10.1103/PhysRevE.66.021603.

[10] T. Karabacak et al. 'Scaling during shadowing growth of isolated nanocolumns'. In: *Phys. Rev. B* 68 (12 2003), p. 125408. DOI: 10.1103/PhysRevB.68.125408.

[11] E. Main, T. Karabacak, and T.-M. Lu. 'Continuum model for nanocolumn growth during oblique angle deposition'. In: *Journal of Applied Physics* 95.8 (2004), pp. 4346–4351. DOI: 10.1063/1.1687033.

[12] M. Salvalaglio, R. Backofen, and A. Voigt. 'Thin-film growth dynamics with shadowing effects by a phase-field approach'. In: *Phys. Rev. B* 94 (23 2016), p. 235432. DOI: 10.1103/PhysRevB.94.235432.

[13] L. Chen, T.-M. Lu, and G.-C. Wang. 'Incident flux angle induced crystal texture transformation in nanostructured molybdenum films'. In: *Journal of Applied Physics* 112.2 (2012), p. 024303. DOI: 10.1063/1.4737403.

[14] H.-F. Li et al. 'Biaxially oriented CaF2 films on amorphous substrates'. In: *Journal of Crystal Growth* 310.15 (2008), pp. 3610 –3614. DOI: 10.1016/j.jcrysgro.2008.04.040.

[15] C. Gaire et al. 'Morphology and texture evolution of nanostructured CaF2 films on amorphous substrates under oblique incidence flux'. In: *Nanotechnology* 21.44 (2010), p. 445701. DOI: 10.1088/0957-4484/21/44/445701.

[16] F Tang et al. 'Surface texture evolution of polycrystalline and nanostructured films: RHEED surface pole figure analysis'. In: *Journal of Physics D: Applied Physics* 40.23 (2007), R427–R439. DOI: 10.1088/0022-3727/40/23/r01.

[17] F. Tang et al. 'Unusual Magnesium Crystalline Nanoblades Grown by Oblique Angle Vapor Deposition'. In: *J. Nanosci. Nanotech.* 7.9 (Sept. 2007), pp. 3239–3244. DOI: 10.1166/jnn.2007.665. URL: https://doi.org/10.1166/jnn.2007.665.

[18] P. Ghekiere et al. 'Structure evolution of the biaxial alignment in sputter-deposited MgO and Cr'. In: *Thin Solid Films* 515.2 (2006). Proceedings of the Eighth International Conference on Atomically Controlled Surfaces, Interfaces and Nanostructures and the Thirteenth International Congress on Thin Films, pp. 485 –488. DOI: 10.1016/j.tsf.2005.12.266.

[19] M. Pelliccione and T.-M. Lu. *Evolution of Thin Film Morphology*. Springer-Verlag, 2004. DOI: 10.1007/978-0-387-75109-2.

[20] G.-C. Wang and T.-M. Lu. 'RHEED transmission mode and pole figures: thin film and nanostructure texture analysis'. English. In: New York: Springer, 2013. Chap. 6. DOI: 10.1007/978-1-4614-9287-0.

[21] W. Prusseit et al. 'Working Around HTS Thickness Limitations–towards 1000+A/cm–Class Coated Conductors'. In: *Physics Procedia* (2012).

[22] T. W. and. 'The EcoSwing Project'. In: *IOP Conference Series: Materials Science and Engineering* 502 (2019), p. 012004. DOI: 10.1088/1757-899x/502/1/012004.

[23] H. Zhang, G. Chen, and D. W. Bahnemann. 'Photoelectrocatalytic materials for environmental applications'. In: *J. Mater. Chem.* 19 (29 2009), pp. 5089–5121. DOI: 10.1039/B821991E.

[24] S.-C. Jung and N. Imaishi. 'Preparation, crystal structure, and photocatalytic activity of TiO2 films by chemical vapor deposition'. In: *Korean Journal of Chemical Engineering* 18.6 (2001), pp. 867–872. DOI: 10.1007/BF02705610.

[25] S.-C. Jung et al. 'Effect of TiO2 thin film thickness and specific surface area by low-pressure metal-organic chemical vapor deposition on photocatalytic activities'. In: *Applied Catalysis B: Environmental* 55.4 (2005), pp. 253 –257. DOI: 10.1016/j.apcatb.2004.08.009.

[26] S.-C. Jung. 'Photocatalytic activities and specific surface area of TiO2 films prepared by CVD and sol-gel method'. In: *Korean Journal of Chemical Engineering* 25.2 (2008), pp. 364–367. DOI: 10.1007/s11814-008-0060-z.

[27] R.-S. Chen et al. 'Photoconductivities in anatase TiO2 nanorods'. In: *Applied Physics Letters* 105.15 (2014), p. 153107. DOI: 10.1063/1.4898004.

[28] S. Krumdieck et al. 'Characterization of photocatalytic, wetting and optical properties of TiO2 thin films and demonstration of uniform coating on a 3-D surface in the mass transport controlled regime'. In: *Surface and Coatings Technology* 326.Part B (2017). Surface Engineering at the International Vacuum Congress-20, pp. 402 –410. DOI: 10.1016/j.surfcoat.2016.11.064.

[29] S. Krumdieck et al. 'Titania-based photocatalytic coatings on stainless steel hospital fixtures'. In: *Physica Status Solidi (c)* 12.7 (2015), pp. 1028–1035. DOI: 10.1002/pssc.201510040.

[30] K. Pomoni et al. 'Electrical conductivity studies of anatase TiO2 with dominant highly reactive 001 facets'. In: *Journal of Alloys and Compounds* 548 (2013), pp. 194 –200. DOI: 10.1016/j.jallcom.2012.08.136.

[31] S. Mukherjee et al. 'Tuning the Band Gap in Titanium Dioxide Thin Films by Surfactant-Mediated Confinement and Patterning of Gold Nanoparticles'. In: *The Journal of Physical Chemistry C* 121.39 (2017), pp. 21311–21323. DOI: 10.1021/acs.jpcc.7b04964.

[32] A. J. Gardecka et al. 'Growth stages of nano-structured mixed-phase titania thin films and effect on photocatalytic activity'. In: *Thin Solid Films* 685 (2019), pp. 136 –144. DOI: doi.org/10.1016/j.tsf.2019.06.018.

[33] D. Lee, S. Krumdieck, and S. D. Talwar. 'Scale-up design for industrial development of a PP-MOCVD coating system'. In: *Surface and Coatings Technology* 230 (2013). 19th European Conference on Chemical Vapor Deposition (EuroCVD19), Varna, Bulgaria, 1st - 6th September 2013, pp. 39 –45. DOI: 10.1016/j.surfcoat.2013.06.064.

[34] M. Patil, S. Shaikh, and G. Ibram. 'Recent Advances on TiO2 Thin Film Based Photocatalytic Applications (A Review)'. In: *Current Nanoscience* 11 (2015). DOI: 10.2174/1573413711666150212235054.

[35] S. Krumdieck et al. 'Titania Solid Thin Films Deposited by pp-MOCVD Exhibiting Visible Light Photocatalytic Activity'. In: *physica status solidi (a)* 215.2 (2018), p. 1700578. DOI: 10.1002/pssa.201700578.

[36] S. Krumdieck et al. 'Expansion transport regime in pulsed-pressure chemical vapor deposition'. In: *Chemical Engineering Science* 62.22 (2007), pp. 6121 –6128. DOI: 10.1016/j.ces.2007.07.003.

[37] B. J. Blackburn et al. 'In situ mass spectrometry analysis of chemical vapour deposition of TiO2 thin films to study gas phase mechanisms'. In: *RSC Adv.* 6 (113 2016), pp. 111797–111805. DOI: 10.1039/C6RA22801A.

[38] R. Boichot and S. Krumdieck. 'Numerical Modeling of the Droplet Vaporization for Design and Operation of Liquid-pulsed CVD'. In: *Chemical Vapor Deposition* 21.10-11-12 (2015), pp. 385–386. DOI: 10.1002/cvde.201571015.

[39] J.-J. Wu and C.-C. Yu. 'Aligned TiO2 Nanorods and Nanowalls'. In: *The Journal of Physical Chemistry B* 108.11 (2004), pp. 3377–3379. DOI: 10.1021/jp0361935.

[40] C.-A. Chen et al. 'Synthesis and characterization of well-aligned anatase TiO2 nanocrystals on fused silica via metal–organic vapor deposition'. In: *Cryst. Eng. Comm.* 11 (2009), pp. 2313–2318. DOI: 10.1039/B909433D.

[41] R. L. Penn and J. F. Banfield. 'Imperfect Oriented Attachment: Dislocation Generation in Defect-Free Nanocrystals'. In: *Science* 281.5379 (1998), pp. 969–971. DOI: 10.1126/science.281.5379.969.

[42] L. Meng, T. Ren, and C. Li. 'The control of the diameter of the nanorods prepared by dc reactive magnetron sputtering and the applications for DSSC'. In: *Applied Surface Science* 256.11 (2010), pp. 3676 –3682. DOI: 10.1016/j.apsusc.2009.12.169.

[43] S. Gupta. *The Classical Stefan ProblemBasic Concepts, Modelling and Analysis*. Vol. 45. North-Holland Series in Applied Mathematics and Mechanics. North-Holland, 2003, p. ii. DOI: 10.1016/S0167-5931(13)70019-6.

[44] E. Javierre et al. 'A comparison of numerical models for one-dimensional Stefan problems'. In: *Journal of Computational and Applied Mathematics* 192.2 (2006), pp. 445 –459. DOI: 10.1016/j.cam.2005.04.062.

[45] W. W. Mullins and R. F. Sekerka. 'Morphological Stability of a Particle Growing by Diffusion or Heat Flow'. In: *Journal of Applied Physics* 34.2 (1963), pp. 323–329. DOI: 10.1063/1.1702607.

[46] L. Brush and R. Sekerka. 'A numerical study of two-dimensional crystal growth forms in the presence of anisotropic growth kinetics'. In: *Journal of Crystal Growth* 96.2 (1989), pp. 419 –441. DOI: 10.1016/0022-0248(89)90541-1.

[47] A. W. Date. 'Novel Strongly Implicit Enthalpy Formulation for Multidimensional Stefan Problems'. In: *Numerical Heat Transfer, Part B: Fundamentals* 21.2 (1992), pp. 231–251. DOI: 10.1080/10407799208944918.

[48] J. CRANK. 'Two Methods for the Numerical Solution of Moving-boundary Problems in Diffusion and Heat Flow'. In: *The Quarterly Journal of Mechanics and Applied Mathematics* 10.2 (1957), pp. 220–231. DOI: 10.1093/qjmam/10.2.220.

[49] M. N. Koleva. 'Numerical Solution of the Heat Equation in Unbounded Domains Using Quasi-uniform Grids'. In: *Large-Scale Scientific Computing*. Ed. by I. Lirkov, S. Margenov, and J. Waśniewski. Berlin, Heidelberg: Springer Berlin Heidelberg, 2006, pp. 509–517. DOI: 10.1007/11666806_58.

[50] R. Fazio and A. Jannelli. 'Finite difference schemes on quasi-uniform grids for BVPs on infinite intervals'. In: *Journal of Computational and Applied Mathematics* 269 (2014;2012;), pp. 14–23. DOI: 10.1016/j.cam.2014.02.036.

[51] S. Mitchell and M. Vynnycky. 'Finite-difference methods with increased accuracy and correct initialization for one-dimensional Stefan problems'. In: *Applied Mathematics and Computation* 215.4 (2009). Physics and Computation, pp. 1609 –1621. DOI: 10.1016/j.amc.2009.07.054.

[52] S. H. Davis. *Theory of Solidification*. Cambridge Monographs on Mechanics. Cambridge University Press, 2001. DOI: 10.1017/CBO9780511546747.

[53] D. A. Porter, K. E. Easterling, and M. Y. Sherif. *Phase transformations in metals and alloys*. English. 3rd. CRC Press, 2009.

[54] W. W. Mullins. 'Solid Surface Morphologies Governed by Capillarity'. In: *Metal Surfaces: Structure, Energetics and Kinetics* ASM (1963), p. 17.

[55] D. W. Hoffman and J. W. Cahn. 'A Vector Thermodynamics for Anisotropic Surfaces I. Fundamentals and Application to Plane Surface Junctions'. In: *The Selected Works of John W. Cahn* (1972), pp. 293–313. DOI: 10.1002/9781118788295.ch28.

[56] J. Cahn and D. Hoffman. 'A vector thermodynamics for anisotropic surfaces II. Curved and faceted surfaces'. In: *Scripta Metallurgica* 8.5 (1974), p. xxiii. DOI: 10.1016/0036-9748(74)90074-x.

[57] R. F. Sekerka. *Thermal Physics - Thermodynamics and Statistical Mechanics for Scientists and Engineers*. 1st ed. Amsterdam: Elsevier, 2016, pp. 589 –. DOI: 10.1016/B978-0-12-803304-3.09981-6.

[58] Wheeler and McFadden. 'A ξ vector formulation of anisotropic phase-field models'. In: (1994). DOI: 10.6028/nist.ir.5505.

[59] J. W. Barrett, H. Garcke, and R. Nurnberg. 'A variational formulation of anisotropic geometric evolution equations in higher dimensions'. In: *Numerische Mathematik* 109.1 (2008), pp. 1–44. DOI: 10.1007/s00211-007-0135-5.

[60] J. W. Barrett and Garcke. 'On stable parametric finite element methods for the Stefan problem and the Mullins-Sekerka problem with applications to dendritic growth'. In: *Journal of Computational Physics* 229.18 (2010), pp. 6270–6299. DOI: 10.1016/j.jcp.2010.04.039.

[61] S. BJ. 'Asymptotic solutions for the equilibrium crystal shape with small corner energy regularization'. English. In: *Physical Review E* 69.1 (2004), p. 011603. DOI: 10.1103/PhysRevE.69.011603.

[62] S. Torabi et al. 'A new phase-field model for strongly anisotropic systems'. In: *Proceedings of the Royal Society of London A: Mathematical, Physical and Engineering Sciences* 465.2105 (2009), pp. 1337–1359. DOI: 10.1098/rspa.2008.0385.

[63] S. Torabi and J. Lowengrub. 'Simulating interfacial anisotropy in thin-film growth using an extended Cahn-Hilliard model'. In: *Phys. Rev. E* 85 (4 2012), p. 041603. DOI: 10.1103/PhysRevE.85.041603.

[64] R. F. Sekerka. 'Analytical criteria for missing orientations on three-dimensional equilibrium shapes'. en. In: *Journal of Crystal Growth* 275.1-2 (2005), pp. 77–82. DOI: 10.1016/j.jcrysgro.2004.10.069.

[65] A. van-der Drift. 'Evolutionary Selection, A principle Governing Growth Orientation in Vapor-Deposited Layers'. English. In: *Philips Research Reports* 22.3 (1967), pp. 267–267.

[66] P. Smereka et al. 'Simulation of faceted film growth in three dimensions: microstructure, morphology and texture'. In: *Acta Materialia* (2005). DOI: 10.1016/j.actamat.2004.11.013.

[67] C. Ophus, E. Luber, and D. Mitlin. 'Simulations of faceted polycrystalline thin films: Asymptotic analysis'. In: *Acta Materialia* (2009). DOI: 10.1016/j.actamat.2008.11.014.

[68] S. Liu et al. 'Three-dimensional Schwoebel–Ehrlich barrier'. In: *Journal of Computer-Aided Materials Design* 7.3 (2000), pp. 195–201. DOI: 10.1023/A:1011832828818.

[69] C. Tang et al. 'Scaling theory for the growth of amorphous films'. In: *Phys. Rev. Lett.* 64 (7 1990), pp. 772–775. DOI: 10.1103/PhysRevLett.64.772.

[70] B. Movchan and A. Demchishin. 'Growth and structure of thin solid films'. In: *Phys. Met. Metallogr., 28, p. 83* (1969).

[71] J. A. Thornton. 'Influence of apparatus geometry and deposition conditions on the structure and topography of thick sputtered coatings'. In: *Journal of Vacuum Science and Technology* 11.4 (1974), pp. 666–670. DOI: 10.1116/1.1312732.

[72] R. Messier, A. P. Giri, and R. A. Roy. 'Revised structure zone model for thin film physical structure'. In: *Journal of Vacuum Science & Technology A* 2.2 (1984), pp. 500–503. DOI: 10.1116/1.572604.

[73] Y. Kajikawa, S. Noda, and H. Komiyama. 'Comprehensive perspective on the mechanism of preferred orientation in reactive-sputter-deposited nitrides'. In: *Journal of Vacuum Science & Technology A* 21.6 (2003), pp. 1943–1954. DOI: 10.1116/1.1619414.

[74] E. Mirica, G. Kowach, and H. Du. 'Modified Structure Zone Model to Describe the Morphological Evolution of ZnO Thin Films Deposited by Reactive Sputtering'. In: *Crystal Growth & Design* 4.1 (2004), pp. 157–159. DOI: 10.1021/cg025596b.

[75] S. Mahieu et al. 'Biaxial alignment in sputter deposited thin films'. In: *Thin Solid Films* 515.4 (2006), pp. 1229 –1249. DOI: 10.1016/j.tsf.2006.06.027.

[76] L.-Q. Chen. 'A novel computer simulation technique for modeling grain growth'. In: *Scripta Metallurgica et Materialia* (1995). DOI: 10.1016/S0956-716X(99)80022-3.

[77] Z. Bi and R. F. Sekerka. 'Phase-field model of solidification of a binary alloy'. In: *Physica A: Statistical Mechanics and its Applications* (1998). DOI: 10.1016/S0378-4371(98)00364-1.

[78] A. F. Ferreira et al. 'Simulation of the Microstructural Evolution of Pure Material and Alloys in an Undercooled Melts via Phase-field Method and Adaptive Computational Domain'. In: *Materials Research* (2005). DOI: 10.1590/1516-1439.293514.

[79] J. A. Warren et al. 'Extending phase field models of solidification to polycrystalline materials'. In: *Acta Materialia* (2003). DOI: 10.1016/S1359-6454(03)00388-4.

[80] W. J. Boettinger et al. 'Phase-Field Simulation of Solidification'. In: *Annual Review of Materials Research* (2002). DOI: 10.1146/annurev.matsci.32.101901.155803.

[81] S. Osher and B. Merriman. 'The Wulff shape as the asymptotic limit of a growing crystalline interface'. In: *Asian Journal of Mathematics* (1997).

[82] C. C. Battaile and D. J. Srolovitz. 'Kinetic Monte Carlo Simulation of Chemical Vapor Deposition'. In: *Annual Review of Materials Research* (2002). DOI: 10.1146/annurev.matsci.32.012102.110247.

[83] H. V. Atkinson. 'Theories of normal grain growth in pure single phase systems'. In: *Acta Metallurgica* 3 (1988). DOI: 10.1016/0001-6160(88)90079-X.

[84] C. C Battaile, D. J Srolovitz, and J. E Butler. 'Atomic-scale simulations of chemical vapor deposition on flat and vicinal diamond substrates'. In: *Journal of Crystal Growth* (1998). DOI: 10.1016/S0022-0248(98)00685-X.

[85] M. Schroeder, P. Smilauer, and D. E. Wolf. 'Bond counting in a simulation model of epitaxial growth'. In: *Physical Review B* (1997). DOI: 10.1103/PhysRevB.55.10814.

[86] L. A. Zepeda-Ruiz. 'Surface morphology evolution during sputter deposition of thin films - lattice Monte Carlo simulations'. In: *Journal of Crystal Growth* (2009). DOI: 10.1016/j.jcrysgro.2009.12.035.

[87] J. Nelson. 'a Theoretical Study of Ice Crystal Growth in the Atmosphere'. PhD thesis. University of Washington, 1994.

[88] S. E. Wood, M. B. Baker, and D. Calhoun. 'New model for the vapor growth of hexagonal ice crystals in the atmosphere'. In: *Journal of Geophysical Research: Atmospheres* 106.D5 (2001), pp. 4845–4870. DOI: 10.1029/2000jd900338.

[89] K. Libbrecht. 'The physics of snow crystals'. In: *Rep. Prog. Phys.* 68 (Apr. 2005). DOI: 10.1088/0034-4885/68/4/R03.

[90] S. Osher and B. Merriman. 'The Wulff shape as the asymptotic limit of a growing crystalline interface'. In: *Asian J. Math* 1 (1997), pp. 560–571. DOI: 10.4310/AJM.1997.v1.n3.a6.

[91] J. Taylor, J. Cahn, and C. Handwerker. 'Overview No. 98 I — Geometric models of crystal growth'. In: *Acta Metallurgica et Materialia* 40.7 (1992), pp. 1443 –1474. DOI: 10.1016/0956-7151(92)90090-2.

[92] P. Smereka et al. 'Simulation of faceted film growth in three dimensions: microstructure, morphology and texture'. In: *Acta Materialia* 53.4 (2005), pp. 1191 –1204. DOI: 10.1016/j.actamat.2004.11.013.

[93] G. Russo and P. Smereka. 'A Level-Set Method for the Evolution of Faceted Crystals'. In: *SIAM Journal on Scientific Computing* 21.6 (2000), pp. 2073–2095. DOI: 10.1137/S1064827599351921.

[94] M. Siegel, M. Miksis, and P. Voorhees. 'Evolution of material voids for highly anisotropic surface energy'. In: *Journal of the Mechanics and Physics of Solids* 52.6 (2004), pp. 1319 –1353. DOI: 10.1016/j.jmps.2003.11.003.

[95] F. Haußer and A. Voigt. 'A discrete scheme for regularized anisotropic surface diffusion: A 6th order geometric evolution equation'. In: *Interfaces and Free Boundaries* 7 (2005), pp. 353–370. DOI: 10.4171/IFB/129.

[96] W. J. Boettinger and J. A. Warren. 'The phase-field method: simulation of alloy dendritic solidification during recalescence'. In: *Metallurgical and Materials Transactions A* 27.3 (1996), pp. 657–669. DOI: 10.1007/BF02648953.

[97] K. R. Elder et al. 'Modeling Elasticity in Crystal Growth'. In: *Phys. Rev. Lett.* 88 (24 2002), p. 245701. DOI: 10.1103/PhysRevLett.88.245701.

[98] K.-A. Wu and A. Karma. 'Phase-field crystal modeling of equilibrium bcc-liquid interfaces'. In: *Phys. Rev. B* 76 (18 2007), p. 184107. DOI: 10.1103/PhysRevB.76.184107.

[99] S. M Allen and J. W Cahn. 'Ground state structures in ordered binary alloys with second neighbor interactions'. In: *Acta Metallurgica* (1972). DOI: 10.1016/0001-6160(72)90037-5.

[100] S. M. Allen and J. W. Cahn. 'A correction to the ground state of FCC binary ordered alloys with first and second neighbor pairwise interactions'. In: *Scripta Metallurgica* (1973). DOI: 10.1016/0036-9748(73)90073-2.

[101] W. C. Carter, J. E. Taylor, and J. W. Cahn. 'Variational methods for microstructural-evolution theories'. In: *Journal of the Minerals, Metals & Materials Society* (1997). DOI: 10.1007/s11837-997-0027-2.

[102] J. W. Cahn and J. E. Hilliard. 'Free energy of a nonuniform system. I. Interfacial free energy'. In: *The Journal of Chemical Physics* (1958). DOI: 10.1063/1.1744102.

[103] R. Kobayashi. 'Modeling and numerical simulations of dendritic crystal growth'. In: *Physica D: Nonlinear Phenomena* 63.3 (1993), pp. 410 –423. DOI: 10.1016/0167-2789(93)90120-P.

[104] C. Herring. 'Some Theorems on the Free Energies of Crystal Surfaces'. In: *Phys. Rev.* 82 (1 1951), pp. 87–93. DOI: 10.1103/PhysRev.82.87.

[105] J. Eggleston, G. McFadden, and P. Voorhees. 'A phase-field model for highly anisotropic interfacial energy'. In: *Physica D: Nonlinear Phenomena* 150.1 (2001), pp. 91–103. DOI: 10.1016/S0167-2789(00)00222-0.

[106] A. Wheeler. 'Phase-field theory of edges in an anisotropic crystal'. In: *Proceedings of the Royal Society A: Mathematical, Physical and Engineering Sciences* 462.2075 (2006), pp. 3363–3384. DOI: 10.1098/rspa.2006.1721.

[107] S. Wise, J. Kim, and J. Lowengrub. 'Solving the regularized, strongly anisotropic Cahn-Hilliard equation by an adaptive nonlinear multigrid method'. In: *Journal of Computational Physics* 226.1 (2007), pp. 414 –446. DOI: 10.1016/j.jcp.2007.04.020.

[108] A. Di Carlo, M. Gurtin, and P. Podio-Guidugli. 'A Regularized Equation for Anisotropic Motion-by-Curvature'. In: *SIAM Journal on Applied Mathematics* 52.4 (1992), pp. 1111–1119. DOI: 10.1137/0152065.

[109] H. G. Lee and J. Kim. 'Regularized Dirac delta functions for phase field models'. In: *International Journal for Numerical Methods in Engineering* 91.3 (2012), pp. 269–288. DOI: 10.1002/nme.4262.

[110] E. J. Siem and W. C. Carter. 'Orientation-dependent surface tension functions for surface energy minimizing calculations'. In: *Journal of Materials Science* 40.12 (2005), pp. 3107–3113. DOI: 10.1007/s10853-005-2671-7.

[111] M. Salvalaglio et al. 'Morphological Evolution of Pit-Patterned Si(001) Substrates Driven by Surface-Energy Reduction'. en. In: *Nanoscale Research Letters* 12.1 (2017). DOI: 10.1186/s11671-017-2320-5.

[112] M. Salvalaglio et al. 'Faceting of Equilibrium and Metastable Nanostructures: A Phase-Field Model of Surface Diffusion Tackling Realistic Shapes'. In: *Crystal Growth & Design* 15.6 (2015), pp. 2787–2794. DOI: 10.1021/acs.cgd.5b00165.

[113] M. Salvalaglio et al. 'Phase-field simulations of faceted Ge/Si-crystal arrays, merging into a suspended film'. In: *Applied Surface Science* 391 (2017). European Conference on Surface Science 2015, pp. 33 –38. DOI: 10.1016/j.apsusc.2016.05.075.

[114] W. Li et al. 'Size dependence of thermal stability of TiO_2 nanoparticles'. In: *Journal of Applied Physics* 96.11 (2004), pp. 6663–6668. DOI: 10.1063/1.1807520.

[115] Y. Lu et al. 'Meaningful comparison of photocatalytic properties of {001} and {101} faceted anatase TiO2 nanocrystals'. In: *Science Bulletin* 61.13 (2016), pp. 1003–1012. DOI: 10.1007/s11434-016-1109-8.

[116] M. Lazzeri, A. Vittadini, and A. Selloni. 'Structure and energetics of stoichiometric TiO_2 anatase surfaces'. In: *Phys. Rev. B* 63.15 (2001), p. 155409. DOI: 10.1103/PhysRevB.63.155409.

[117] M. Lazzeri. 'Erratum: Structure and energetics of stoichiometric TiO_2 anatase surfaces'. In: *Phys. Rev. B* 65 (2002), p. 119901. DOI: 10.1103/PhysRevB.65.119901.

[118] H. G. Yang et al. 'Anatase TiO_2 single crystals with a large percentage of reactive facets'. In: *Nature* 453.7195 (2008), pp. 638–641. DOI: 10.1038/nature06964.

[119] A. Stukowski. 'Visualization and analysis of atomistic simulation data with OVITO–the Open Visualization Tool'. In: *Modelling and Simulation in Materials Science and Engineering* 18.1 (2009), p. 015012. DOI: 10.1088/0965-0393/18/1/015012.

[120] V. Fiorentini and M Methfessel. 'Extracting convergent surface energies from slab calculations'. In: *Journal of Physics: Condensed Matter* 8.36 (1996), p. 6525. DOI: 10.1088/0953-8984/8/36/005.

[121] J. C. Boettger. 'Nonconvergence of surface energies obtained from thin-film calculations'. In: *Phys. Rev. B* 49 (23 1994), pp. 16798–16800. DOI: 10.1103/PhysRevB.49.16798.

[122] X.-Q. Gong et al. 'Steps on anatase $TiO_2(101)$'. en. In: *Nature Materials* 5.8 (2006), pp. 665–670. DOI: 10.1038/nmat1695.

[123] S. Bebelis and P. Nikolopoulos. 'Temperature Dependence of the Surface Energy of the Low-index Planes of CaF2, BaF2 and SrF2'. In: *Journal of Materials Engineering and Performance* 26.3 (2017), pp. 1223–1228. DOI: 10.1007/s11665-017-2560-7.

[124] P. Cignoni et al. 'MeshLab: an Open-Source Mesh Processing Tool'. In: *Eurographics Italian Chapter Conference*. Ed. by V. Scarano, R. D. Chiara, and U. Erra. The Eurographics Association, 2008.

[125] J. Ahrens, B. Geveci, and C. Law. 'ParaView: An end-user tool for large-data visualization, Visualization Handbook'. In: Elsevier, 2005.

[126] A. Sternig et al. 'Phase Separation at the Nanoscale: Structural Properties of BaO Segregates on MgO-Based Nanoparticles'. In: *The Journal of Physical Chemistry C* 115.32 (2011), pp. 15853–15861. DOI: 10.1021/jp204043g.

[127] F. Chen and J. Shen. 'Efficient spectral-Galerkin methods for systems of coupled second-order equations and their applications'. In: *Journal of Computational Physics* 231.15 (2012), pp. 5016 –5028. DOI: 10.1016/j.jcp.2012.03.001.

[128] R. Guo, Y. Xu, and Z. Xu. 'Local Discontinuous Galerkin Methods for the Functionalized Cahn–Hilliard Equation'. In: *Journal of Scientific Computing* 63.3 (2015), pp. 913–937. DOI: 10.1007/s10915-014-9920-3.

[129] W. Feng et al. 'A Uniquely Solvable, Energy Stable Numerical Scheme for the Functionalized Cahn–Hilliard Equation and Its Convergence Analysis'. In: *Journal of Scientific Computing* 76.3 (2018), pp. 1938–1967. DOI: 10.1007/s10915-018-0690-1.

[130] Y. Chen et al. 'Efficient energy stable schemes for isotropic and strongly anisotropic Cahn-Hilliard systems with the Willmore regularization'. In: *Journal of Computational Physics* 365 (2018), pp. 56 –73. DOI: 10.1016/j.jcp.2018.03.024.

[131] A. Christlieb et al. 'High accuracy solutions to energy gradient flows from material science models'. In: *Journal of Computational Physics* 257 (2014), pp. 193 –215. DOI: 10.1016/j.jcp.2013.09.049.

[132] S. Vey and A. Voigt. 'AMDiS: adaptive multidimensional simulations'. In: *Computing and Visualization in Science* 10.1 (2007), pp. 57–67. DOI: 10.1007/s00791-006-0048-3.

[133] X. Y. Jie Shen. 'Numerical approximations of Allen-Cahn and Cahn-Hilliard equations'. In: *Discrete & Continuous Dynamical Systems - A* 28 (2010), p. 1669. DOI: 10.3934/dcds.2010.28.1669.

[134] F. Chen and J. Shen. 'Efficient Energy Stable Schemes with Spectral Discretization in Space for Anisotropic Cahn-Hilliard Systems'. In: *Communications in Computational Physics* 13.5 (2013), 1189–1208. DOI: 10.4208/cicp.101111.110512a.

[135] J. Shen. 'Efficient Spectral-Galerkin Method I. Direct Solvers of Second- and Fourth-Order Equations Using Legendre Polynomials'. In: *SIAM Journal on Scientific Computing* 15.6 (1994), pp. 1489–1505. DOI: 10.1137/0915089.

[136] N. Hale and A. Townsend. 'A fast FFT-based discrete Legendre transform'. In: *arXiv e-prints* (2015). DOI: 10.1093/imanum/drv060.

[137] F. Chen. 'A New Framework of GPU-Accelerated Spectral Solvers: Collocation and Glerkin Methods for Systems of Coupled Elliptic Equations'. In: *Journal of Scientific Computing* 62.2 (2015), pp. 575–600. DOI: 10.1007/s10915-014-9868-3.

[138] H. Li et al. 'Biaxially Textured Al Film Growth on CaF2 Nanostructures toward a Method of Preparing Single-Crystalline Si Film on Glass Substrates'. In: *ACS Nano* 4.10 (2010), pp. 5627–5632. DOI: 10.1021/nn1011978.

[139] C. Gaire et al. 'Small angle grain boundary Ge films on biaxial CaF2/glass substrate'. In: *Journal of Crystal Growth* 312.4 (2010), pp. 607 –610. DOI: 10.1016/j.jcrysgro.2009.11.051.

[140] Beihai Ma et al. 'Biaxially aligned template films fabricated by inclined-substrate deposition for YBCO-coated conductor applications'. In: *IEEE Transactions on Applied Superconductivity* 13.2 (2003), pp. 2695–2698. DOI: 10.1109/TASC.2003.811959.

[141] S Piñol et al. 'Preparation of biaxially cube textured Cu substrate tapes for HTS coated conductor applications'. In: *Superconductor Science and Technology* 14.1 (2000), pp. 11–15. DOI: 10.1088/0953-2048/14/1/303.

[142] L. Chen et al. 'Heteroepitaxy of large grain Ge film on cube-textured Ni(001) foils through CaF2 buffer layer'. In: *Thin Solid Films* 603 (2016), pp. 428 –434. DOI: 10.1016/j.tsf.2016.03.007.

[143] R. J. Lord et al. 'Biaxially oriented CdTe films on glass substrate through nanostructured Ge/CaF2buffer layers'. In: *Materials Research Express* 2.9 (2015), p. 095017. DOI: 10.1088/2053-1591/2/9/095017.

[144] G.-C. Wang and T.-M. Lu. *RHEED transmission mode and pole figures: thin film and nanostructure texture analysis*. English. New York: Springer, 2013. DOI: 10.1007/978-1-4614-9287-0.

[145] M. P. Chudzik et al. 'Mechanism and processing dependence of biaxial texture development in magnesium oxide thin films grown by inclined-substrate deposition'. In: *IEEE Transactions on Applied Superconductivity* 11.1 (2001), pp. 3469–3472. DOI: 10.1109/77.919810.

[146] Y Xu et al. 'Growth of textured MgO through e-beam evaporation and inclined substrate deposition'. In: *Superconductor Science and Technology* 19.8 (2006), pp. 835–843. DOI: 10.1088/0953-2048/19/8/026.

[147] P. Ghekiere et al. 'Scanning electron microscopy study of the growth mechanism of biaxially aligned magnesium oxide layers grown by unbalanced magnetron sputtering'. In: *Thin Solid Films* 493.1 (2005), pp. 129 –134. DOI: 10.1016/j.tsf.2005.07.314.

[148] H. B. H. J. M. Nieuwenhuizen. 'Microfractography of thin films'. In: *Philips Tech. Rev.* 27 (1966), pp. 87–91.

[149] R. Tait, T. Smy, and M. Brett. 'Modelling and characterization of columnar growth in evaporated films'. In: *Thin Solid Films* 226.2 (1993), pp. 196 –201. DOI: 10.1016/0040-6090(93)90378-3.

[150] B. Tanto, G. Ten Eyck, and T.-M. Lu. 'A model for column angle evolution during oblique angle deposition'. In: *Journal of Applied Physics* 108.2 (2010), p. 026107. DOI: 10.1063/1.3465296.

[151] O. P. Karpenko, J. C. Bilello, and S. M. Yalisove. 'Growth anisotropy and self-shadowing: A model for the development of in-plane texture during polycrystalline thin-film growth'. In: *Journal of Applied Physics* 82.3 (1997), pp. 1397–1403. DOI: 10.1063/1.365916.

[152] S. Mahieu et al. 'Mechanism of in-plane alignment in magnetron sputtered biaxially aligned yttria-stabilized zirconia'. In: *Journal of Crystal Growth* 290.1 (2006), pp. 272 –279. DOI: 10.1016/j.jcrysgro.2005.12.093.

[153] J. W. Gerlach et al. 'Biaxial alignment of TiN films prepared by ion beam assisted deposition'. In: *Applied Physics Letters* 68.17 (1996), pp. 2360–2362. DOI: 10.1063/1.115858.

[154] M. Zeitler et al. 'Evolution of texture at growth of titanium nitride films prepared by photon and ion beam assisted deposition'. In: *Applied Physics Letters* 70.10 (1997), pp. 1254–1256. DOI: 10.1063/1.118544.

[155] R. Hühne, S. Fähler, and B. Holzapfel. 'Thin biaxially textured TiN films on amorphous substrates prepared by ion-beam assisted pulsed laser deposition'. In: *Applied Physics Letters* 85.14 (2004), pp. 2744–2746. DOI: 10.1063/1.1802385.

[156] B. Ma and U. B. Balachandran. 'Prospects for the fabrication of low aspect ratio coated conductors by inclined substrate deposition'. In: *Superconductor Science and Technology* 19.6 (2006), pp. 497–502. DOI: 10.1088/0953-2048/19/6/015.

[157] K. K. Uprety et al. 'Growth and properties of YBCO-coated conductors on biaxially textured MgO films prepared by inclined substrate deposition'. In: *Superconductor Science and Technology* 18.3 (2005), pp. 294–298. DOI: 10.1088/0953-2048/18/3/015.

[158] B. Ma et al. 'Growth and properties of YBCO-coated conductors fabricated by inclined-substrate deposition'. In: *IEEE Transactions on Applied Superconductivity* 15.2 (2005), pp. 2970–2973. DOI: 10.1109/TASC.2005.848684.

[159] C. G. Johansen, H. Huang, and T.-M. Lu. 'Effects of three-dimensional Ehrlich-Schwoebel barrier on texture selection during Cu nanorod growth'. In: *Applied Physics Letters* 91.12 (2007), p. 121914. DOI: 10.1063/1.2771525.

[160] Q. Sun et al. 'Understanding nonpolar GaN growth through kinetic Wulff plots'. In: *Journal of Applied Physics* 104.9 (2008), p. 093523. DOI: 10.1063/1.3009969.

[161] E. Ringe, R. P. Van Duyne, and L. D. Marks. 'Kinetic and Thermodynamic Modified Wulff Constructions for Twinned Nanoparticles'. In: *The Journal of Physical Chemistry C* 117.31 (2013), pp. 15859–15870. DOI: 10.1021/jp401566m.

[162] M. Pelliccione and T.-M. LU. 'Non-local Effects in Thin Film Growth'. In: *Modern Physics Letters B* 21.19 (2007), pp. 1207–1225. DOI: 10.1142/S0217984907013638.

[163] Y. Wang. 'Phase Field Modeling of the Physical Vapor Deposition of Thin Film Microstructures'. In: *Theses and Dissertations Available from ProQuest* (2013), pp. 1–104. URL: https://docs.lib.purdue.edu/dissertations/AAI10155421.

[164] O. Ertl and S. Selberherr. 'Three-dimensional level set based Bosch process simulations using ray tracing for flux calculation'. In: *Microelectronic Engineering* 87.1 (2010), pp. 20 –29. DOI: 10.1016/j.mee.2009.05.011.

[165] P. Keblinski et al. 'Continuum model for the growth of interfaces'. In: *Phys. Rev. E* 53 (1 1996), pp. 759–778. DOI: 10.1103/PhysRevE.53.759.

[166] C. G. Gal and M. Grasselli. 'Asymptotic behavior of a Cahn–Hilliard–Navier–Stokes system in 2D'. In: *Annales de l'Institut Henri Poincare (C) Non Linear Analysis* 27.1 (2010), pp. 401 –436. DOI: 10.1016/j.anihpc.2009.11.013.

[167] J. Krug. 'Four lectures on the physics of crystal growth'. In: *Physica A: Statistical Mechanics and its Applications* 313.1 (2002), pp. 47 –82. DOI: 10.1016/S0378-4371(02)01034-8.

[168] G. Nolze and R. Hielscher. 'Orientations – perfectly colored'. In: *Journal of Applied Crystallography* 49.5 (2016), pp. 1786–1802. DOI: 10.1107/S1600576716012942.

[169] R Ochrombel, V Rykhtin, and A Wiedenmann. 'Analysis of Anisotropic Void System in Electron Beam Physical Vapour Deposited (EB-PVD) Thermal Barrier Coatings'. In: 6 (2009). DOI: 10.1002/adem.200800329.

[170] A. Renteria et al. 'Application of USAXS analysis and non-interacting approximation to determine the influence of process parameters and ageing on the thermal conductivity of electron-beam physical vapor deposited thermal barrier coatings'. In: *Surface and Coatings Technology* 201.8 (2007), pp. 4781 –4788. DOI: 10.1016/j.surfcoat.2006.10.020.

[171] T. U. Schülli and S. J. Leake. 'X-ray nanobeam diffraction imaging of materials'. In: *Current Opinion in Solid State and Materials Science* 22.5 (2018). Advanced characterization of nanomaterials, pp. 188 –201. DOI: 10.1016/j.cossms.2018.09.003.

[172] M.-I. Richard et al. 'Crystallographic orientation of facets and planar defects in functional nanostructures elucidated by nano-focused coherent diffractive X-ray imaging'. In: *Nanoscale* 10 (10 2018), pp. 4833–4840. DOI: 10.1039/C7NR07990G.

[173] C. A. Chen et al. 'Growth and characterization of well-aligned densely-packed rutile TiO2 nanocrystals on sapphire substrates via metal–organic chemical vapor deposition'. In: *Nanotechnology* 19.7 (2008), p. 075611. DOI: 10.1088/0957-4484/19/7/075611.

[174] C. Chen et al. 'Growth and characterization of the coexistence of vertically aligned and twinned V-shaped RuO2 nanorods on nanostructural TiO2 template'. In: *Journal of Alloys and Compounds* 485.1 (2009), pp. 524 –528. DOI: 10.1016/j.jallcom.2009.06.017.

[175] T. KIMURA. 'High-Speed Deposition of Yttria-Stabilized Zirconia and Titania Films by Laser Chemical Vapor Deposition'. In: *Journal of the Ceramic Society of Japan* 114.1326 (2006), pp. 161–166. DOI: 10.2109/jcersj.114.161.

[176] A. Ito, S. Nishigaki, and T. Goto. 'A feather-like structure of β-Al2TiO5 film prepared by laser chemical vapor deposition'. In: *Journal of the European Ceramic Society* 35.7 (2015), pp. 2195 –2199. DOI: 10.1016/j.jeurceramsoc.2015.01.027.

[177] D. D. Hass, P. A. Parrish, and H. N. G. Wadley. 'Electron beam directed vapor deposition of thermal barrier coatings'. In: *Journal of Vacuum Science & Technology A* 16.6 (1998), pp. 3396–3401. DOI: 10.1116/1.581492.

[178] J. R. Vargas Garcia and G. Takashi. 'Thermal Barrier Coatings Produced by Chemical Vapor Deposition'. In: *Science and Technology of Advanced Materials* 4 (2003), 397–402. DOI: 10.1016/S1468-6996(03)00048-2.

[179] P. Hartman and H.-K. Chan. 'Application of the Periodic Bond Chain (PBC) Theory and Attachment Energy Consideration to Derive the Crystal Morphology of Hexamethylmelamine'. In: *Pharmaceutical Research* 10.7 (1993), pp. 1052–1058. DOI: 10.1023/A:1018927109487.

[180] D. D. Hass, Y. Y. Yang, and H. N. G. Wadley. 'Pore evolution during high pressure atomic vapor deposition'. In: *Journal of Porous Materials* 17.1 (2010), pp. 27–38. DOI: 10.1007/s10934-008-9261-4.

[181] S. R. Coriell and R. L. Parker. 'Stability of the Shape of a Solid Cylinder Growing in a Diffusion Field'. In: *Journal of Applied Physics* 36.2 (1965), pp. 632–637. DOI: 10.1063/1.1714041.

[182] H. Xu et al. 'Anatase TiO2 Single Crystals Exposed with High-Reactive 111 Facets Toward Efficient H2 Evolution'. In: *Chemistry of Materials* 25.3 (2013), pp. 405–411. DOI: 10.1021/cm303502b.

[183] O. M. Ishchenko et al. 'Highly Reactive TiO2 Anatase Single Crystal Domains Grown by Atomic Layer Deposition'. In: *Crystal Growth & Design* 18.9 (2018), pp. 4929–4936. DOI: 10.1021/acs.cgd.8b00170.

[184] T.-Y. Lee, C.-Y. Lee, and H.-T. Chiu. 'Enhanced Photocatalysis from Truncated Octahedral Bipyramids of Anatase TiO2 with Exposed 001/101 Facets'. In: *ACS Omega* 3.8 (2018), pp. 10225–10232. DOI: 10.1021/acsomega.8b01251.

[185] C. Z. Wen et al. 'Synthesis of high-reactive facets dominated anatase TiO2'. In: *J. Mater. Chem.* 21 (20 2011), pp. 7052–7061. DOI: 10.1039/C1JM00068C.

[186] H. Emmerich. *The Diffuse Interface Approach in Materials Science*. English. Springer, 2003. DOI: 10.1103/PhysRevE.71.036110.

[187] A. Yanguas-Gil et al. 'Influence of the Angular Distribution Function of Incident Particles on the Microstructure and Anomalous Scaling Behavior of Thin Films'. In: *Phys. Rev. Lett.* 96 (23 2006), p. 236101. DOI: 10.1103/PhysRevLett.96.236101.

[188] D. J. Economou et al. 'Two-dimensional direct simulation Monte Carlo (DSMC) of reactive neutral and ion flow in a high density plasma reactor'. In: *IEEE Transactions on Plasma Science* 23.4 (1995), pp. 581–590.

[189] T.-M. Lu et al. '"Novel Mechanisms on the Growth Morphology of Films"'. In: *MRS Proceedings* 749 (2002), W1.2. DOI: 10.1557/PROC-749-W1.2.

[190] F. Li et al. '116 faceted anatase single-crystalline nanosheet arrays: facile synthesis and enhanced electrochemical performances'. In: *Nanoscale* 6 (21 2014), pp. 12434–12439. DOI: 10.1039/C4NR04248D.

[191] F. Chen and J. Shen. 'Efficient spectral-Galerkin methods for systems of coupled second-order equations and their applications'. In: *Journal of Computational Physics* 231.15 (2012), pp. 5016 –5028. DOI: 10.1016/j.jcp.2012.03.001.

[192] W. W. Mullins. 'Theory of Thermal Grooving'. In: *Journal of Applied Physics* 28.3 (1957), pp. 333–339. DOI: 10.1063/1.1722742.

[193] G. S. Bales and A. Zangwill. 'Macroscopic model for columnar growth of amorphous films by sputter deposition'. In: *Journal of Vacuum Science & Technology A* 9.1 (1991), pp. 145–149. DOI: 10.1116/1.577116.

[194] R. P. U. Karunasiri, R. Bruinsma, and J. Rudnick. 'Thin-Film Growth and the Shadow Instability'. In: *Phys. Rev. Lett.* 62 (7 1989), pp. 788–791. DOI: 10.1103/PhysRevLett.62.788.

[195] S. Lichter and J. Chen. 'Model for Columnar Microstructure of Thin Solid Films'. In: *Phys. Rev. Lett.* 56 (13 1986), pp. 1396–1399. DOI: 10.1103/PhysRevLett.56.1396.

[196] M. Pelliccione and T.-M. Lu. 'Small World Growth Model'. In: *Evolution of Thin Film Morphology*. Springer-Verlag, 2004, pp. 79–90. DOI: 10.1007/978-0-387-75109-2.

[197] J. Eggleston, G. McFadden, and P. Voorhees. 'A phase-field model for highly anisotropic interfacial energy'. English (US). In: *Physica D: Nonlinear Phenomena* 150.1-2 (2001), pp. 91–103. DOI: 10.1016/S0167-2789(00)00222-0.

[198] B. J. Palmer and R. G. Gordon. 'Local equilibrium model of morphological instabilities in chemical vapor deposition'. In: *Thin Solid Films* 158.2 (1988), pp. 313 –341. DOI: 10.1016/0040-6090(88)90034-X.

[199] B. J. Palmer and R. G. Gordon. 'Kinetic model of morphological instabilities in chemical vapor deposition'. In: *Thin Solid Films* 177.1 (1989), pp. 141 –159. DOI: 10.1016/0040-6090(89)90563-4.

Appendix

Nomenclature

Notes on the notations

- The superscript is reserved for the name of phase, e.g. V^s denotes the domain of the solid phase or simply V^- because there is always two phases involved in a moving boundary problem. In general superscript $^-$ means inside of the boundary and $^+$ means outside. For the subscripts, if one is not a constant such as T_m or further specified in the table of symbols below, it is referred to partial derivative notation convention.

- In the one spatial and one temporal dimensions concise notations can be adopted, e.g. $c_{xx} = {}^{\partial^2 c}/_{\partial x^2}$ reads 'the second derivative of c with respect to x'.

- When dealing with discretisations the superscripts are reserved for time increments and subscripts for spatial increments; Otherwise for a constant or non-spatial-varying vector the superscript denotes the power as what it would normally mean.

- Accents such as $\widehat{v}_n$ hat and $\tilde{\zeta}$ twiddle and some of the Greek letters represent the dimensionless forms of its counterparts.

List of abbreviations

OAD	oblique angle deposition
RHEED	reflection high-energy electron diffraction
SEM	scanning electron microscope
CVD	chemical vapour deposition
MOCVD	metal-organic CVD
pp-MOCVD	pulsed pressure MOCVD
MBE	molecular beam epitaxy
TEM	transmission electron microscopy
TTIP	titanium isopropoxide
LPMOCVD	low pressure MOCVD
SAED	selected area electron diffraction
XRD	X-ray diffraction
PBC	periodic boundary chain
PVD	physical vapour deposition
1-D	one-dimensional
2-D	two-dimensional
3-D	three-dimensional
PDE	partial differential equation
BIM	boundary immobilisation method
MD	molecular dynamics
MC	Monte Carlo
FEA	finite element analysis
CHW	Cahn-Hilliard-Willmore
PBE	Perdew–Burke–Ernzerhof
UTF	ultrathin film
DFT	density functional theory
LGL	Legendre-Gauss-Lobatto
FFT	fast Fourier transform
FWHM	full width at half maximum
IPF	inverse pole figure
USAXS	ultrasmall-angle X-rays scattering analysis
XRNDI	X-ray nanobeam diffraction imaging
NFXRI	nano-focused X-ray imaging
TBCs	thermal barrier coatings
A-TiO_2	anatase-TiO_2
YSZ	yttria-stabilized zirconia
STM	scanning tunneling microscopy
AFM	atomic force microscopy
RGB	red, green and blue
RSPF	reciprocal space pole figure
MRD	random distribution

Table of symbols

Table 10.1: Symbols and their meanings

Symbol	Meaning	Notation in the literature (Unit)
$\vec{N}$	general position vector	$\mathbf{r}$ [55], $\mathbf{P}$ [57]
$h(t)$	interface height function	ζ [198, 199]
$\dot{h}$	front speed	$dh(t)/dt$
η_h	scaled interface location	$h(t)/2\sqrt{Dt}$
$\vec{n}$	normal vector	$\mathbf{n}$[198, 199]
v_n	normal velocity	$(\mathrm{m\,s^{-1}})$
$\widehat{v}_n$	scaled front speed	$h(t)/2\sqrt{\alpha' t}$
α	thermal diffusivity	$(\mathrm{m^2 s^{-1}})$
k	thermal conductivity	$(\mathrm{W\,K^{-1}\,m^{-1}})$
D	diffusion coefficient	$(\mathrm{m^2 s^{-1}})$
T	temperature	(K)
T_∞	processing temperature	(K)
P	pressure	(Pa)
P_∞	processing pressure	(Pa)
P_{max}	maximum pulsing pressure	(Pa)
P_{min}	minimum pulsing pressure	(Pa)
c	number density	$(\mathrm{m^{-3}})$
Δc	negative supersaturation	$c_{sat} - c_0$
$c_{sat}(T)$	equilibrium vapour density	$(\mathrm{m^{-3}})$
$c_{sol}(T)$	solid number density	ρ_{sol}/m
σ	supersaturation	$c - c_{sat}/c_{sat}$
ΔT	undercooling	$T_m - T_\infty$
S	Stefan number	$L_f/c_p^s \Delta T$
$\mathcal{S}_d$	dep. number	$c_{sol}/(c_0 - c_{sat})$
$\mathcal{S}'_d$	primed dep. number	$c_{sol}/\delta(c_0 - c_{sat})$
P_e	Péclet number	v/D
N_A	number per unit area	$(\mathrm{m^{-2}})$
$\alpha_n(\vec{n})$	sticking coefficient	
$v_{\vec{n}}$	anisotropic mobility	$M(\mathbf{n})$[91]
γ	surface energy density	$(\mathrm{Jm^{-2}})$
$\tilde{\gamma}$	dimensionless surface energy density	$\tilde{\gamma} = \gamma/\gamma_0$
$\vec{\xi}$	capillarity vector	$\boldsymbol{\xi}$[55]
κ	mean curvature	$\nabla \cdot (\nabla c/\lvert\nabla c\rvert)$
κ_γ	weighted mean curvature	$\nabla \cdot \vec{\xi}$
∇_s	surface gradient operator	
T_p	pulse time	(s)
d_a	apical bond length	(nm)
d_e	equatorial bond length	(nm)
σ_m	moment	$(\mathrm{kgm^2 s^{-2}})$
$\mathcal{B}$	boundary operator	
L_k	Legendre polynomial of order k	

Table 10.2: A list of values of the parameters used in Ch. 5 and Ch. 6.

fixed model parameters	value	changing parameters	value
$\|\vec{R}\|$, B	1	M	$10^{-4} - 1$
$\tilde{\beta}$	0.005	α	$0° - 57°$
α_{ref}	0.1	γ_{ref} for MgO	$\gamma_{\{110\}}$
w_i	100	γ_{ref} for A-TiO_2	$\gamma_{\{001\}}$
γ_0	$1.1 \times \gamma_{ref}$	γ	$0° - 39°$
ϵ	0.02	η	$0 - 1$
δt[1]	10^{-5}	in-plane conf. relative to flux	I, II

[1] except in energy minimising calculation of the equilibrium shape where $\delta t = 10^{-7}$

Table 10.3: Symbols and their meanings in Chapters 5 and 6

Symbol	Meaning	Symbol	Meaning
β	column tilt angle	α	vapour incident angle for OAD
γ	orientation angle	ω	(100) tilt angle
$\mathcal{E}$	CHW energy	$\mathcal{P}$	probability density function
$\vec{r}$	position vector	g	vapour-field order parameter
ϕ	order parameter	μ	generalised chemical potential
$\vec{R}$	rain vector	$(\nabla\phi)^2$	surface delta function
N_v	adparticle number density	ψ	azimuthal angle
θ	polar angle	$\mathcal{A}_{\psi,\theta}$	acceptance function
$\vec{n}$	surface (unit) normal $\vec{n} = {}^{\nabla\phi}/_{\|\nabla\phi\|}$	η	a coefficient
$\vec{n}_{sub}$	substrate normal	$\tilde{v}$	normalised adparticle velocity
δt	time step	ϵ	gradient energy coefficient
$\tilde{\gamma}(\vec{n})$	surface energy function	w_i	free energy parameter in Eqn. 4.2
$\tilde{\beta}$	regularisation coefficient	γ_0	isotropic energy coefficient
$H(\theta)$	Heaviside step function	$\delta(\theta)$	Dirac delta function
r	radial component of a cylinder	R	mean radius of the cylinder
$\delta_{\psi,z}$	amplitude of perturbation	k_ψ	wavenumber in ψ
Ω	domain	λ_z	wavelength in z
r	radial component in a cylindrical coordinates system	l_0	characteristic length scale
$d(r)$	signed distance function to r	τ_0	characteristic time scale
W	nanocolumn width	d	nanocolumn length
p	growth exponent	$\bar{l}_{\{hkl\}}$	average length of the $\{hkl\}$ nano-facets
β'	tilt angle of the secondary structures	r_{max}	the maximum in r